CRANFIELD UNIVERSITY

TOMASZ BRZEZINKA

DEVELOPMENT OF LOW FRICTION COATINGS FOR ALSI
MILLING

School
SCHOOL OF AEROSPACE TRANSPORT AND MANUFACTURING

PhD
Academic Year: 2016 - 2019

Supervisor: Jose Luis Endrino
Associate Supervisor: Jeff Rao
APRIL 2019

CRANFIELD UNIVERSITY

SCHOOL OF AEROSPACE, TRANSPORT AND MANUFACTURING

PhD in Manufacturing

Academic Year 2016 – 2019

TOMASZ BRZEZINKA

DEVELOPMENT OF LOW FRICTION COATINGS FOR ALSI MILLING

Supervisor: Jose Luis Endrino
Associate Supervisor: Jeff Rao
APRIL 2019

This thesis is submitted in partial fulfillment of the requirements for the degree of Doctor of Philosophy

To my father Adam and mother Gabriela Brzezinka

ABSTRACT

Aluminium silicon (AlSi) alloys play an essential role in many industries because of their good machinability characteristics. However, their low degree of plasticity promotes adhesion at the tool edge during machine cutting, leading to a built-up edge (BUE) which reduces tool lifetimes, and the silicon content leads to tool abrasion. Currently, cemented carbide mill inserts coated with titanium diboride (TiB_2) offer the prospects of machining an array of structural metallic alloys including AlSi. However, the brittle nature of TiB_2 leaves it prone to extensive surface damage, particularly during the running-in stage of machining when tool adaptation takes place. An additional coating addressing abrasive wear and preventing BUE could limit TiB_2 damage.

Fabricating coatings of TiB_2 using arc evaporation remains challenging as an extensive cathode fracture occurs. Thus, the present work aims to address the drawbacks associated with TiB_2 by the deposition of a thin lubricious coating on top of the TiB_2. Secondly, the development of a new cathode, which would allow the deposition of TiB_2 by arc evaporation is investigated.

A hybrid Physical Vapor Deposition system combining Filtered Cathodic Vacuum Arc (FCVA) and Magnetron Sputtering was developed for this study. Three lubricious coating systems of Ti-MoS_2, single layer DLC and DLC-WS_2 were investigated as a top layer. Ti-MoS_2 was optimised for dry machining applications, and a Ti:MoS_2 ratio around 0.39 was found to prevent Al from sticking to the tool edges. The DLC and DLC-WS_2 coatings were designed for machining with coolant. In comparison to the performance of a TiB_2 benchmark, the monolayer DLC coating improved the machining length by ~60% and a two-layer DLC-WS_2 coating decreased wear rate by ~75%, having a measured coefficient of friction of 0.05.

The development of TiB_2 cathodes for FCVA required a modification of the chemical composition to improve it's sinterability and prevent cathode fracture during arc operation. A TiB_2-$TiSi_2$ (5 wt%) cathode ensured the best balance between arc stability and cathode utilisation while TiB_2-C (1 wt%) has provided exceptional arc stability, although the cathode utilisation was less due to the constant generation of cathode flakes.

Keywords:

ACKNOWLEDGEMENTS

TABLE OF CONTENTS

LIST OF FIGURES

LIST OF TABLES

Page No

LIST OF EQUATIONS

LIST OF ABBREVIATIONS

Abbreviation	Meaning
A_b/A_c	Cross section area of the backing plate/cathode
a-C	Amorphous Carbon
AE	Acoustic emission
AES	Atomic emission spectroscopy
At%	Atomic ratio
B	Magnetic field
BSE	Back-scattered electrons detector (on SEM)
BUE	Build-up of material
CAD	Cathodic Arc Deposition
CoF	Coefficient of Friction
CVD	Chemical Vapour Deposition
DLC	Diamond-Like Carbon
EDX/EDS	Energy Dispersive X-ray Spectroscopy
EELS	Electron Energy Loss Spectroscopy
FCVA	Filtered Cathodic Vacuum Arc
FIB	Focused Ion Beam
I_{arc}	Arc current (FCVA- deposition)
I_{coil1}/FoC	Focusing coil current (FCVA- deposition)
I_{coil3}/FtC	Filtering coil current (FCVA- deposition)
IPA	Isopropyl alcohol
J	Current density
k_b/k_c	Thermal conductivity of the backing plate/cathode
L_b/L_c	Height of the backing plate/cathode
MoS_2	Molybdenum Disulphide
MS	Magnetron sputtering
P_{arc}	Thermal power generated by the arc
P_{cath}	Net thermal power transferred by the arc to the cathode
PVD	Physical Vapour Deposition
R_b	Thermal resistance of the backing plate
R_c	Thermal resistance of the cathode
R_{it}	Thermal resistance of the interface backing plate-cathode
R_w	Thermal resistance of the interface backing plate-cooling water
SE	Secondary electrons detector (in SEM)
SEM	Scanning Electron Microscopy
ta-C	Tetrahedral Amorphous Carbon

$T_{cathode}$	Cathode temperature
TD	Theoretical density
TiB_2	Titanium diboride
TiB_2-C	Titanium diboride with 1 wt% of carbon (cathode)
TiB_2-$TiSi_2$	Titanium diboride with 5 wt% of titanium disilicide (cathode)
T_w	Cooling water temperature
V_{cs}	Arc spot velocity
WS_2	Tungsten Disulphide
Wt%	Weight ratio
XPS	X-ray Photoelectron Spectroscopy
XRD	X-Ray Diffraction
τ	Arc duration

1 Introduction

1.1 Motivation

Aluminium alloys are widely used in various industries such as aerospace, military and automotive [1,2]. Generally, they are considered to have good machinability [3], although their low degree of plasticity can cause adhesion to the cutting tool resulting in the built-up edge (BUE) [4]. The BUE increases cutting forces, reduces tool lifetimes and results in a poor surface finish [5]. Machining of aluminium silicon (AlSi) alloy used primarily in automotive applications [6] combines the BUE effect, with abrasion caused by silicon particles. Therefore, to improve the tool life and reduce friction, the cutting tools are coated. Currently, cemented carbide mill inserts coated with TiB_2 offer the possibility of machining a large variety of structural metallic alloys especially AlSi [7]. Titanium diboride (TiB_2) has a hexagonal structure with boron atoms being covalently bonded within the titanium matrix [8]. Properties such as high hardness (up to 30 GPa) [9], high chemical stability at elevated temperatures, and inertness to liquid aluminium [10] makes it an ideal material for coating tools to address both high abrasion resistance and machined material effect [11,12]. Commercial sputtered TiB_2 has high hardness (25 GPa), provides excellent wear characteristics and, a low coefficient of friction. However, its brittleness makes it prone to extensive surface damage during the running-in stage of the machining when tool adaptation takes place [13]. Typically TiB_2 is deposited by magnetron sputtering (MS), which ensures uniformity of the coatings and has low deposition temperature [14–16], although it has lower deposition rates comparing to other deposition methods, e.g. cathodic arc. Low deposition rates are a challenge for industry who wish for ever-increasing manufacturing yields, therefore enhancing TiB_2 for deposition rates by arc evaporation is of value. The reports describing successful and reproducible attempts of cathodic arc evaporation of TiB_2 are limited [17]. One of the problems with arc-evaporating TiB_2 is the tendency of the cathode spot to remain at a single specific location on the cathode surface, resulting in local overheating and cracking of the cathode [18,19]. Appropriate sintering additions

to the TiB_2 cathodes could possibly help to overcome those challenges, though only a few attempts were made by other researchers to investigate this route [18].

Regardless of the deposition method, the brittleness of TiB_2 can limit tool longevity; this may be overcome by implementing a "smart coating" concept [13]. In the running-in phase of the machining, the tool-workpiece adaptation takes place, and this is associated with extensive tool wear [20]. The addition of an antifriction thin coating with self-lubricating properties deposited on top of the hard layer can prevent intensive surface damage of the hard coating and also promote the formation of the stable protective compound in the running-in phase [13]. Such an approach was already proposed; soft lubricious MoST® coating was deposited on top of hard TiN and TiCN to improve drilling and punching performance of the tools [21–23]. This solution was not fully explored for milling applications, thus in this work TiB_2 was combined with lamellar solids to improve tool-chip area lubrication. Lamellar structure solid coatings such as tungsten disulfide (WS_2) and molybdenum disulfide (MoS_2) are commonly used for lubricating applications because of their low friction coefficient [24,25]. However, it has been already found by other researchers that in the presence of oxygen, the lifetime of lamellar coatings is significantly decreased [26,27]. It can be improved by combining the layers with metal (the most successful is Ti [28,29]) or another hard coating (e.g. Diamond-like carbon (DLC) [30]) which increases the time to failure and decreases the wear. Also, DLC monolayers have been successfully combined with TiB_2 into a multilayer coating; limiting its hardness while maintaining good tribological properties for high-temperature applications [15]. Filtered cathodic vacuum arc (FCVA) is the preferred and only method to deposit hydrogen-free diamond-like coatings which can provide extremely high wear resistance [31–34], while MS allows deposition of a wide range of materials [35] especially solid lubricant coatings: MoS_2 and WS_2 [27,36]. Hence the hybrid FCVA and MS system which is available for this project give impressive possibilities for developing new "smart" coatings combining both self-lubrication and wear resistance.

The research gap addressed in this project concerns the application of cathodic arc deposition for improving the lifetime of the tools for machining of Al alloys. The overall motivation is to employ cathodic arc deposition to improve the existing mill inserts coating solution for AlSi machining application. If the additional hard lubricious layer deposited on top of commercially available TiB_2 can improve the tool lifetime, it would allow tailoring the tool more precisely for AlSi machining without investing in new coating architecture. The project also determines if a sintering additive can facilitate TiB_2 for arc evaporation while maintaining the exceptional tribological of the TiB_2 coating.

1.2 Aims and objectives

This PhD thesis aim is to research on materials and technology of filtered cathodic vacuum arc and its combination with magnetron sputtering to produce hard, low friction coatings to provide increased tool lifetime during lightweight alloy machining.

The following objectives have been set:

I. In regard to low friction (below 0.5), good wear resistance and the possibility of deposition by FCVA and MS identify the coating candidates to improve the existing TiB_2 coated tools.

II. Recognise and apply the upgrades necessary to adapt hybrid FCVA – MS deposition system for sequential multilayer and composite coatings deposition of hard, lubricious coatings.

III. Using hybrid FCVA-MS system produce mono-layer as well as multilayered coatings providing both wear resistance and low friction coefficients.

IV. Perform initial evaporation trials with monolithic TiB_2 to identify the factors preventing TiB_2 from being deposited by FCVA and propose chemical/physical modifications to overcome the limitations.

V. Assess the arc stability and arc spot movement by optical observations and measurements of ion voltage and optimise the deposition parameters such as magnetic field distribution, gas composition, arc current to allow coating deposition from manufactured TiB_2 cathodes.

VI. Analyse the tribological properties of produced coatings by sliding tests and structure by SEM, FIB and optical microscopy.

VII. Test coated milling inserts in real-life applications by face milling of AlSi alloys and comparison with commercial TiB_2 coated tools.

The quantitative goal of 50 % tool flank wear reduction in comparison with commercial TiB_2 coated tool during the first 30 meters of machining was set. For arc evaporation of TiB_2 improving the time between following arc triggering actions above one minute would be considered as a success – this is the average time for non-metallic cathodes such as graphite.

1.3 Project methodology

To meet the above objectives, the project was divided into seven stages. The stages do not represent chronological order rather than the logical progress of the proposed concepts. The following stages are:

I. Evaluating the problems associated with TiB_2 coated tools for AlSi machining. After careful literature research, it has been found that due to the low ductility of TiB_2 the coating experiences wear in the running-in stage. The starting point was to improve the existing solution by depositing an additional thin layer on top of TiB_2 as illustrated in Figure 1-1

Lubricious layer or multilayered coating

TiB_2 coating

WC substrate
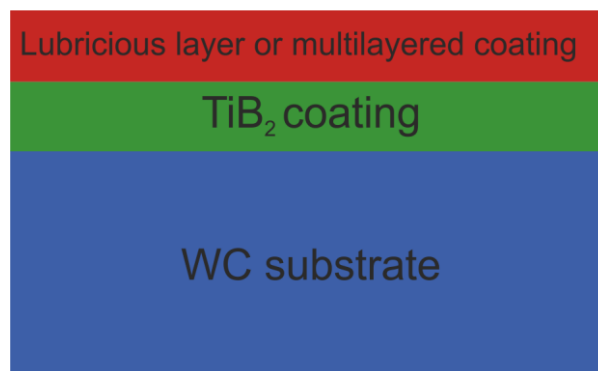
Figure 1-1 Schematic diagram of the arrangement of the coatings on the tool cross-section.

This layer would provide both lubrication and wear resistance. The proposed candidate coatings included titanium-molybdenum disulphide (Ti-MoS$_2$) known under commercial name MoST®, diamond-like carbon

coating (DLC) which would benefit from FCVA available for this project and diamond-like carbon – tungsten disulphide (DLC-WS$_2$).

II. Adaptation of the filtered vacuum cathodic arc - magnetron sputtering system. This system has been initially assembled during the preceding MSc thesis [37]. Although it required a number of upgrades over the 3 years of PhD project to ensure reliability and allow depositing coatings onto milling tools. The proposed improvements were based on industrial solutions. Studies of chambers manufactured by Platit and TecVac were carried out in terms of substrate holder design, allowing to coat milling inserts, applying substrate bias and substrate temperature monitoring. Therefore, to coat the complex shape of milling inserts the rotating substrate holder with an individual rotation of each sample (planetary rotation), which could alternate between the FCVA and magnetron was designed and assembled. To allow substrate biasing the substrate holder was insulated with ceramic tubes while the pneumatic socket connecting the substrate holder to bias power supply was installed in front of both MS and FCVA. Many other improvements enabled: ion current-voltage measurements (connectors to VersaStat potentiostat), substrate temperature monitoring (insulated thermocouple), reactive depositions (new gas flow controllers, and cold cathode full range pressure sensor) were incorporated in this stage.

III. Production of mono-layer, composite and multilayered coatings. In this stage, the knowledge and solutions implemented in stages one and two are used.

IV. Facilitating titanium diboride for arc evaporation. Stage four involved a deep understanding of the challenges associated with TiB$_2$ arc evaporation. After careful literature research, certain sintering additives are selected which are meant to help overcome problems related to TiB$_2$ arc evaporation such as arc spot sticking to a specific location on the cathode surface.

V. TiB$_2$ cathodes assessment and parameters optimisation. The cathodes produced based on the information obtained in stage four are assessed

regarding the arc spot behaviour (stability, mobility). The deposition parameters such as magnetic field distribution and arc current were precisely optimised.

VI. Characterisation and testing of the deposited coatings and evaluation of the results. This stage covers the characterisation of the microstructure, thickness, tribological and mechanical properties of coatings produced.

VII. Machining testing. The last stage involves testing the coated tools by AlSi face milling, corresponding the results to the observations made in stage six and comparing to the performance of the commercial TiB_2 coated tools.

1.4 Thesis content and structure

The journal paper format has been used for this thesis with chapters 3-5 being either published already or submitted for publication. Although this format requires distinct chapters to contain all aspects needed to describe that specific package of work the papers (chapters 3-5) were streamlined to limit repetitions within the thesis. The thesis starts with an introduction and literature review providing the background information which are not covered within introduction sections for papers in chapters 3-5; then the structure follows the stages discussed in the previous section. Each chapter discusses the different family of coatings being deposited and tested. At the end of the thesis, the general discussion and conclusions chapters wrap up the whole work and demonstrate how the individual paper chapters connect together. The contents of the specific chapters are:

Chapter 1.   An introduction is describing the motivation of the work, structure and objectives.

Chapter 2.   Provides background to help understand the challenges associated with machining and justification for the coatings selected. The foundation of PVD deposition technique is laid as well as the more in-depth elaboration on the magnetron sputtering and filtered vacuum arc methods that were used in this project.

Chapter 3.   This chapter discusses an innovative approach to deposit Ti-MoS$_2$ by hybrid deposition (combining arc evaporation and magnetron sputtering). Deposition, characterisation, and testing of the deposited coatings are studied in this chapter covering stages II, VI and VII.

Chapter 4.   Production of DLC monolayers and DLC-WS$_2$ multilayered coatings. This chapter consists of two sections; depositing and optimising DLC monolayer and incorporating the best performing DLC monolayer into the DLC-WS$_2$ multilayer structure to further improve the performance. Covers stages II, VI, and VII.

Chapter 5.   Facilitating TiB$_2$ for arc evaporation. In this chapter, sintering additives are used to allow stable and reproducible deposition of TiB$_2$ using FCVA. The arc behaviour is assessed, and deposition parameters optimised as well as a coating deposited and tested — covers stages IV-VII.

Chapter 6.   General discussion. Discusses in greater detail the outcomes of stages VI and VII from all of the coatings deposited.

Chapter 7.   Conclusions.

Chapter 8.   Recommendations and future work.

1.5 Project constrains, industrial requirements and materials selection

Some aspects of this PhD thesis project have been driven by the industrial requirements. Most of the deposition systems used for hard tool coating in Kennametal are arc evaporators thus the use of a hybrid FCVA-MS deposition system has been proposed to allow a wide range of coatings with a variety of properties to be investigated. Cathodic arc evaporation is one of the oldest PVD technique, used for depositing dense coatings with exceptional adhesion to the substrate and high deposition rates due to the production of highly charged ions [38,39]. The high energy concentrated into the tiny arc spot limits its usage for deposition of brittle materials, e.g. ceramics [40] and produces macroparticles being droplets of partially molten materials. Those droplets are undesired in the

coating as increasing its roughness and have lower adhesion than the rest of the coating [41]. In contrast, magnetron sputtering is widely considered as the most versatile PVD technique as it allows deposition of the wide range of materials, including isolators [35]. The limitations come from low deposition rate and adhesion being not as high as for arc evaporation [42].

The combination of these two techniques potentially plots advantages of both methods to produce a multilayered or composite coating. Also, simultaneous deposition from both sources will allow observation of plasma interactions and the investigation of the potential of such combination, as it was not used commonly by other researchers or widely studied [40].

Application of a thin lubricious layer on top of currently used commercial TiB_2 coating (known under commercial name Camecon) has been proposed to decrease the wear in the first stage of the machining. The high hardness of the TiB_2 makes it prone to extensive wear when the tool part adaptation takes place [13]. The literature reviewed in chapter 2 indicated that the additional lubricious layer should also have a high hardness to provide wear resistance [43], a low coefficient of friction and provide lubrication facilitating this phase of the machining process [44]. The obvious candidates for these coatings are solid lubricants such as MoS_2 which has been employed as a lubricant for many years [45]. Their layered structure can provide a low coefficient of friction (0.01) due to self-lubricating properties which will be of benefit in the dry machining condition [21]. Once solid lubricants are deposited as a layer, they are often referred as self-lubricating coatings (although this term could also be used for coatings not being made of solid lubricant). The literature review showed that the solid lubricants have to be combined with other material [46] to prevent deterioration of tribological properties in the wet environment [47]. The first decision had been made to deposit $Ti-MoS_2$ composite coating as it was known at the market and available under the commercial name of MoST® [48]. However, a different deposition strategy has been decided taking advantage of exceptional film densification provided by cathodic arc; therefore, it was used to deposit titanium while MoS_2 was sputtered. There is no literature proof of using such a

8

combination to deposit MoST®. As one of the motivations for the work is to prevent aluminium sticking to the tool which requires tailoring the Ti:MoS$_2$ ratio to keep the balance between wear resistance and low coefficient of friction, a combinatorial deposition method has been used. It offers manufacturing flexibility, increasing the speed of sample production under the same process conditions by ensuring that only the influence of the chemical composition is investigated [49,50]. The coatings developed in this stage were tested under dry conditions due to both; industrial requirements and availability of the softer aluminium blocks made of (SAE 6061) alloy. For the other two coatings families due to higher Si content Al-10Si alloy has been used.

The selection of the second coating to be tested was based on the amended industrial requirements – more abrasive Al alloy was meant to be used and under wet cutting conditions. DLC coating has been selected as it provides both a low coefficient of friction and high hardness. Moreover, it allows taking full advantage of arc evaporation as a deposition method resulting in hydrogen-free, extremely hard coatings [51]. The literature review suggested a strong dependence between the tribological properties of DLC and the energy of the incoming ions [52,53]. In FCVA the ion energy can be easily adjusted by changing substrate bias. Therefore, it has been decided to test a variety of negative biases [54]. The best performing DLC monolayer would be combined into the multilayer structure with another solid lubricant WS$_2$ to improve the tribological properties further. A different number of layers would be tested to find the optimum combination.

After the successful adaptation of thin coatings on top of TiB$_2$ the next decision was to modify the chemical composition and structure of the TiB$_2$ to facilitate it for arc evaporation. The number of issues has been reported by other researchers including arc sticking into the specific location at the cathode, cathode fracture, poor arc stability, and cathode destruction [17,18]. The cathode density close to the 100% theoretical density (TD) has been indicated as one of the requirements to overcome these issues [55]. However, sintering additives such as Ni and Co used commonly to provide a high density of TiB$_2$ are not desired for cathode production as they are not suitable for high-temperature

applications and also would change the composition of the resulting films. Therefore TiSi$_2$ sintering additive has been chosen as being compatible with TiB$_2$ (density, thermal and electrical conductivity and thermal expansion coefficient close to the monolithic TiB$_2$ [56]) and was described before to provide density close to 100 % TD [57]. Also, TiB$_2$ cathode with the addition of carbon would be tested as being reported recently to provide stable and repeatable arc evaporation, although was not tested in the configuration with a cone-shaped cathode [17,58]. Due to project time constraints and the readiness of the manufacturers to test new compositions each cathode had to be produced by a different manufacturer.

All of the machining testings has been done externally by project partner McMaster University. As it was part of collaboration there were some constraints in the project methodology. The project sponsor supplied tools for coating and testing and requirements regarding the material to be machined. However, the material itself (Al alloy blocks) were donated by the automotive industry thus its amount was limited. It has been decided to perform short machining tests (30 meters for Al-10Si) for all of the deposited coatings to get comparison rather than performing a full tool life machining test of just one coating composition.

1.6 Thesis dissemination

Publications and conferences talks/posters from this thesis to-date.

Publications:

- Tomasz L. Brzezinka, Jeff Rao, Mohamad Chowdhury, Joern Kohlscheen, German S. Fox Rabinovich, Stephen C. Veldhuis, Jose L. Endrino, Hybrid Ti-MoS$_2$ Coatings for Dry Machining of Aluminium Alloys. Coatings 2017, 7, 149.
- Tomasz L. Brzezinka, Jeff Rao, Jose M.Paiva, Joern Kohlscheen, German S. Fox Rabinovich, Stephen C. Veldhuis, Jose L. Endrino, DLC and DLC-WS$_2$ Coatings for Machining of Aluminium Alloys. Coatings 2019, 9, 192. ***This paper has been selected as the journal issue cover.*** Available: https://www.mdpi.com/2079-6412/9/3.

- Tomasz L. Brzezinka, Jeff Rao, Jose M.Paiva, Joern Kohlscheen, German S. Fox Rabinovich, Stephen C. Veldhuis, Jose L. Endrino, Facilitating TiB_2 for filtered vacuum cathodic arc evaporation. Paper submitted for publication in the MDPI Coatings Journal and is currently undergoing the peer review process.

Conferences:

- T.L. Brzezinka, J. Rao, G. S. Fox-Rabinovich, M. Chowdhury, S.C.Veldhuis, J. Kohlscheen, J.L. Endrino. Investigation of wear behaviour in composite Ti-MoS$_2$ coated mill inserts for aluminium alloys milling. European Conference on Nanofilms (ECNF). 19-21st October 2016, Bilbao, Spain. (Contents of chapter 3 were presented).
- Tomasz Brzezinka. Investigation of the characteristics of cutting tools coated with mono-layer DLC and multi-layered DLC-WS$_2$ PVD coatings. European Conference on Nanofilms (ECNF). 20-22nd March 2018, Cranfield, UK. (Contents of chapter 4 were presented). ***Nomination for the best poster***.
- Tomasz L. Brzezinka, Jeff Rao, Mohamad Chowdhury, Joern Kohlscheen, German S. Fox-Rabinovich, Stephen C. Veldhuis, Jose L. Endrino, Hybrid Ti-MoS$_2$ Coatings for Dry Machining of Aluminium Alloys. Challenges in Tribology IET. 16-17 March 2017. Birmingham, UK. (Contents of chapter 3 were presented).

Other:

- Industrial secondment, Metaestalki, November-December 2017, Bilbao, Spain.

2 Coatings for AlSi machining – review of principles and methods

2.1 Abstract

This review summarises the principles of metalworking, coatings for AlSi machining and deposition methods. The fundamental aspects of cutting; starting from types of tool wear through revising wear stages until tool adaptation are discussed in 2.3. Section 2.4 introduces PVD deposition methods with an emphasis on cathodic arc evaporation. Also, the hard and lubricious coatings for machining of ductile materials and methods to tailor their tribological properties for specific applications are discussed in greater detail in section 2.5. The analysis showed that the use of a unique hybrid FCVA-MS system could potentially help to produce hard coatings with self-lubricating and tribological properties better than the coatings used nowadays. The combination of hard base coating and thin lubricious top layer appears to be the novel solution for AlSi machining.

2.2 Introduction

Aluminium silicon alloys play an essential role in a wide range of industries such as automotive and aerospace [6]. Therefore, the demand for cutting tools used for their machining increases every year. Aluminium alloys despite being softer than most of the tool materials are challenging during machining due to adhesion to the cutting tool edge known as build-up edge (BUE) [5]. When the machined material adheres to the cutting edge of the tool, it changes the geometry of the cutting edge, which increases the cutting forces at the tool interface [59]. The size of the BUE increases until some critical size after which it becomes unstable, with the resulting fractured particles being carried into both the chip and new workpiece surface [60]. In the case of AlSi, in addition to adhesive wear, the silicon particles cause abrasive action on the tool surface. P. Roy et al. [61], compared the machinability of the TiN, TiN, Al_2O_3 and AlON coated tools for dry machining of ferrous materials during Al and Al-12Si cutting. An extensive BUE

13

was observed for all of the coatings for both machined materials. However, on the tools used to machine Al-12Si a notch was formed on the cutting edge [61].

TiB_2 is the most successful coating used to protect the tools during machining of Al alloys [62]. However, its brittleness sometimes makes it prone to extensive wear during AlSi cutting [13]. Alternative coating solutions are therefore researched. DLC is emerging as a promising solution and was already reported by Giovanni R. dos Santos et al. [63], to reduce cutting forces during Al-12Si turning. The well-established coatings with self-lubricating properties such as MoS_2 and WS_2 could be potentially used for this application, though, only if combined with hard underlayer [13].

PVD deposition methods such as magnetron sputtering (MS), and filtered cathodic vacuum arc evaporation (FCVA) have been widely used to coat cutting tools. However, while MS allows deposition of a wide range of lubricating coatings such as TiB_2 and MoS_2, the use of FCVA is more focused on hard coatings such as TiN. Recently the successful synthesis of TiB_2 coating by arc evaporation has been reported by Zhirvov et al. [17], which gives a possibility of FCVA utilisation for deposition of hard, lubricious coating systems. Lastly, the establishment of hybrid FCVA-MS deposition gives the opportunity to develop a composite of multilayer coatings with improved coating density and adhesion, thus facilitating their usage for coating cutting tools.

2.3 Principles of wear during the cutting process and friction control

This section briefly discusses the challenges associated with metalworking, specifically automated cutting processes. The tool adaptation and methods to promote it are introduced.

2.3.1 Wear stages and tool adaptation

Cutting, one of the oldest methods of metalworking, includes few types of machining such as milling, turning, drilling or grinding. All of these operations are a consequence of mechanical and thermal processes involving surface plastic deformation of the workpiece, fracture and chip removal [13]. When the chip

14

leaves the cutting zone in such severe frictional conditions, it carries some particles of the worn tool. Although the real tool wear is small, over a time a change of the cutting-edge profile is high enough for the tool to lose its workability. A schematic of the tool-chip interface is presented in Figure 2-1.
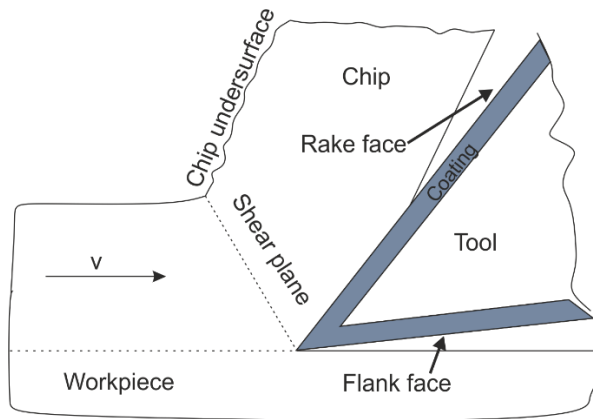
Figure 2-1 Cutting tool-chip contact area.

The wear of both flank and rake surfaces occurs during cutting. The major components of the wear during cutting are [15,64]:

- Adhesive: Junctions between the asperities of the tool surface and chip are formed. Shear forces continuously fracture these junctions; therefore, microscopic fragments of the tool material are torn and adhere to the chip.
- Diffusive or chemical wear: The subsequent process of material transfer between two metals within the interface.
- Abrasive: Scratching of the tool surface by the hard particles.

Typically wear process consists of three stages; running-in stage, steady-state and surface damage stage as presented in Figure 2-2. In the initial and final stages, the surface damage of the tool can be observed (high wear rates) while in the middle stage (steady) stable wear and frictions conditions are typically achieved therefore little or no macroscopic damage of the surface is observed. During the initial (running-in) stage, a complex phenomenon of adaptation process takes place. The adaptation occurs at three levels [65]:

- Macro-level: At this level, a geometrical adaptation of the cutting edge due to friction occurs. Also, dissipative macrostructures such as BUE and flow-zone are formed.
- Micro-level: Formation of debris during contact dynamics.
- Nano-level: Occurs at the very tool-workpiece area by protective tribo-film formation. These films are formed by an interaction of the base material with the environment (mostly oxygen) or by structural modification.
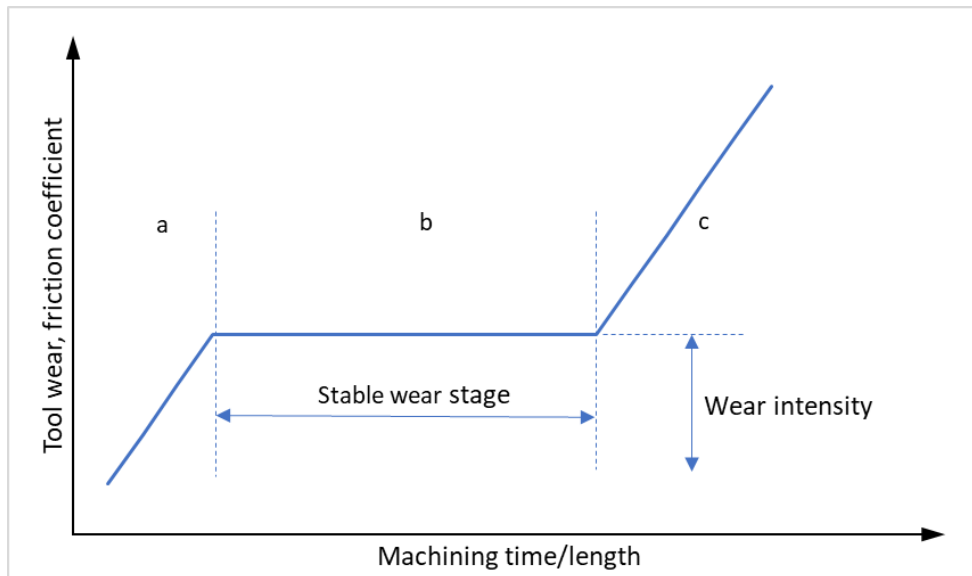
Figure 2-2 Typical tool wear curve: a - running-in stage, b - steady-state, c - catastrophic wear stage.

2.3.2 Tribology control

The primary goal of tool tribology control is to increase the steady-state length and decrease the tool-wear intensity and friction coefficient. This can be realised by "Self-Adaptive coatings" or "smart coatings" which are the new generation of coatings aiming to minimise the surface damage in the initial machining stage [13]. For example, hard coatings due to their brittleness are susceptible to extensive surface damage in the running-in stage. The observed wear rate in the stable stage is still lower as a result of the formation of protective tribofilms. However, most of the hard coating is lost which significantly decreases the machining length/time of this phase [65]. Therefore an additional top layer with

high anti-frictional properties is a critical component especially during machining of ductile materials with abrasive components such as AlSi [66]. This lubricious layer prevents the intensive surface damage of the hard coating during the adaptation stage. Thus more protective compounds such as TiO_2 can form. Finally, when the stable stage starts the overall tool wear is lower, and the tool life is extended.

2.3.3 Lubricants and future trends in machining

Liquids have been employed as sources of lubrication for machining applications for many years [67–69]. Their main purpose is to reduce heat, reduce the cutting forces, change the tool-chip contact area and decrease the BUE formation [70]. However, the costs associated with using the liquids can be high the refrigeration and recycling can be up to four times their purchase costs as most of the lubricants are not bio-degradable [71,72]. Also, in some applications, using a fluid lubricant is limited to avoid contamination or because of its low effectiveness [73]. Hence one of the major tasks in modern cutting applications is the search for alternative "greener" production processes that either minimise or avoid the production of environmentally aggressive liquid residues [74]. One of the processes eliminating most of the liquids' drawbacks is minimum quantity lubricant (MQL) or near dry. In this technique, the used lubricants are minimised by mixing with compressed air to form an aerosol, thus much smaller quantities (10-100ml/h) are needed [75]. The temperature of the process causes the fluid evaporation thereby costs related to disposal and circulating are eliminated [71]. Still, the issue with contamination of the machined materials and possibly hazardous fumes associated with evaporated cutting fluid persist [76]. Dry machining is considered to be a "greener" alternative eliminating the need for any liquid-based lubricants [77]. Howbeit, in the absence of a cooling and lubricating liquid, a significant reduction of uncoated tool life can be expected [78]. Dry machining is a serious challenge for lightweight alloys e.g. aluminium and titanium machining as they have a high degree of plasticity [73]. The higher temperatures that occur during the process facilitate aluminium adhesion to the cutting tool, forming a built-up edge [79]. BUE can be defined as a layer of refined

17

and heavily deformed material sourced from the machined workpiece [80]. To some extent, this layer can serve as protection to the tool surface. However, especially when cemented carbide tools are used [5], the stability of BUE is very low. As the result of adhesive interactions between the carbide grains and build-up layer the subsequent cyclical stress leads to separation of the carbide grains and crack formation [13,61].

2.4 Physical Vapor Deposition (PVD) Methods

This section introduces the main methods and concepts regarding physical vapour deposition. The focus has been made on the filtered vacuum cathodic method as it is necessary for understanding the decisions made and results obtained especially during arc evaporation of TiB_2 (see chapter 5).

2.4.1 Definition and main categories

Physical Vapour Deposition (PVD) processes cover thin film deposition processes in which the material from a solid or liquid source (target) located in the vacuum or low-pressure environment is vaporized into the atomic or molecular form and condensed on to the substrate after being transported in the low-pressure gaseous environment [81]. PVD processes allow deposition of films with thicknesses ranging from few a nanometres to microns which can be arranged into the multilayer or graded composition coatings [40,82,83]. Machining tools are one of the critical applications of the PVD coating technique. The versatility, low deposition temperatures, lack of harmful gasses being produced during the deposition, and higher energy efficiency [84] favours PVD over other common cutting tools deposition technique - chemical vapour deposition (CVD). The substrates can have a range of shapes from flat to complex geometries which, however, require the use of special rotating holders. Generally, PVD processes can be broadly divided into two main categories indicating the way of particles removed from the target: sputtering and evaporation [85]. The evaporation (Figure 2-3 (a)) usually provides dense coatings with excellent adhesion and the high deposition rate. However, it transfers particles having higher mass (larger grains) therefore is preferred for industrial applications of thick coating depositions, where the surface morphology

is not the primary quality requirement [81]. During the sputtering process (Figure 2-3 (b)), the atoms and molecules are ejected from the target surface by transferring the momentum of bombarding gaseous ions [86]. Sputtering has fewer restrictions regarding the target material, but the deposition rates and density of the coatings produced are lower compared to evaporation. Consequently, it is mainly used in the semiconductor industry, reflective coatings production and dry lubricants deposition [87].
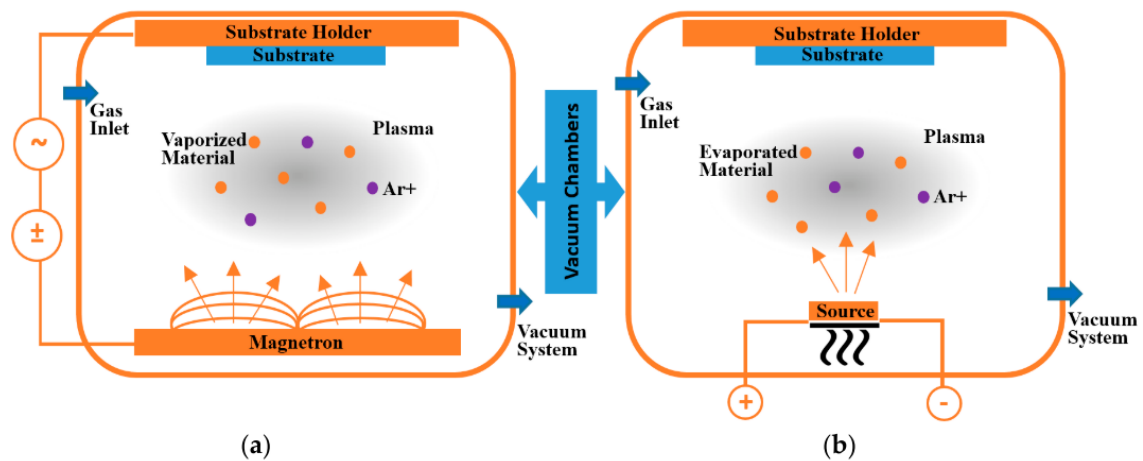
Figure 2-3 Diagram of two conventional PVD processes: (a) sputtering and (b) evaporating using ionised argon (Ar+) gas [85]**.**

The summary of the main differences between evaporation and sputtering is presented in Table 2-1.

Table 2-1 Summary of the main features of evaporation and sputtering [81,88,89]**.**

Process parameter	Evaporation	Sputtering
Pressure	Low (arc evaporation can operate even without assisting gas)	High
Atomised particles	Highly directional	Dispersed
Coating uniformity	Lower	Higher
Grain size	Bigger	Smaller
Deposition rate	High (up to 75 µm/min^{-1})	Low except for pure metals and dual magnetron

19

2.4.2 Filtered cathodic vacuum arc

2.4.2.1 Definition

Commercial vacuum arc evaporators were developed and used in the 1970s in Russia (former USSR) and over the years have become the leading technology to deposit hard coatings on the cutting tools [38,90]. The vacuum cathodic arc is a type of high-current, low voltage electrical discharge in which high-current plasma consists of the material removed from the cathode. The electrical arc operates at low voltage due to the high efficiency of collective electron emission process such as thermionic and field emission at the cathode [91]. The direct electron emission from the cathode is the main factor differentiating arc evaporation from the other discharge deposition methods (e.g., glow discharge) requiring high voltage to produce secondary electrons resulting from the bombardment of the cathode by accelerated ions or excited atoms [92]. The arc current is conducted by the plasma formed of the vapour ionised by the discharge, thus no background gas is required to operate the vacuum arc (in practice to improve stability, control and direct the plasma during deposition, low-pressure inert gas is used) [90].

2.4.2.2 Arc spot and cathode spot control

The natural concentration of the arc current at the surface of the cathode is called an arc spot. These spots are mobile and have an extremely high current density (up to 10^{12} A/m^2) resulting in areal power density of up to 10^{13} W/m^2 [93]. Such conditions allow local phase transformation of solid cathode material into the fully ionised plasma [94]. The degree of ionisation depends on the cathode material, but multiple ionised ions are common, especially for refractory materials. The ions state can range from 1 for Li to 5 for Mo, and there are some publications providing exact charge distribution for certain elements [38,41,95]. Nevertheless, it has been proven that these ion states can be enhanced by magnetic fields [96]. The energy of the ions can range between 14 eV (light elements), and 200 eV (heavy elements) yet can be easily multiplied by the use of substrate bias [54,91]. These high energies of the ions are the main advantage over discharge deposition techniques as they can produce coatings with different properties. In

the absence of an external magnetic field, the arc spots move randomly (called random-walk) around the surface of the cathode. The modelling of cathode spots movements was found to be very challenging. Howbeit, the primary mechanism of spot movement is known. Generally cathode spot "prefer" to ignite on the "contaminated" locations on the cathode surface [94]. The term contaminated is a bit misleading because multiple arc spot can be typically observed during reactive deposition as the cathode surface is poisoned (for example by nitrogen in case of TiN deposition), also sharp grain edges or inclusions are preferred locations of cathode spot ignition [54,93].

Considering the cathode spot "random-walk," it is necessary to control the spot motion to make sure it is kept in the front face of the cathode (facing the substrate) and prevent the destruction of the supporting structure of the cathode [93]. The control should also facilitate spreading the heat flux over the broad area of the cathode. The control of the location and motion can be realised in two ways. The first one, which advantage is simplicity employs the insulating shields, limiting the area of the spot motion, yet, it is possible the conductive coating material from the cathode will condense on the insulator. Therefore, it will serve as an extension for the cathode [91]. The most popular solution uses a magnetic field, which provides more control over the cathodic spot motion [94]. Magnetic steering exploited two phenomena:

a) Retrograde motion – the apparent motion of the spot will happen in the -JxB direction with the velocity being proportional to |JxB| with the saturation value of around 50-150 m/s [54].

b) Acute angle rule – according to Boxman [91] "if the magnetic-field lines cut the cathode surface obliquely, there will be a second-order tendency of the cathode spots to drift in the direction of the opening of the acute angle between the magnetic field line and its projection on the cathode surface."

These two phenomena are applied in the three most popular cathode designs (Figure 2-4):

a) Race track – a permanent or electromagnetic coil is located under a flat cathode (circular or rectangular) and generates an arched, circular field

having a radial component parallel to the cathode surface [91]. The cathode spot is forced to move in retrograde direction by the radial component. The acute angle of the field lines will push the spot to the preferred trajectory in case of cathode stop drifts, e.g. towards the cathode centre. The advantage of such a system is full control of the spot over large area cathodes which are preferred in the industry to cover a large area (many samples) at one deposition [97].

b) Cone-shaped cathode located in an axial magnetic field – for the conical cathode placed an axial magnetic field the retrograde motion of the spots at the tilted face will have azimuthal direction, while secondary drift direction will be towards the apex [91,98]. The advantage is that despite the cathode radius is small, it's thickens is way bigger than for race track configuration. Therefore, they can be used for a long operational time before being changed [99]. Moreover, the utilisation of the cathode is better as it wears uniformly from the front and there is no groove being eroded [54,100]. Also, the deposition rig design can be more straightforward as the steering coils are placed around the anode tube not behind the cathode, which is typically crowded with cooling and high-current connections.

c) Central rod cathode – the central rod cathode can occupy almost the entire length of the deposition chamber. An external magnetic field allows helical motion of the arc spot [91]. The advantage is the high yield of the cathode and substantial area being coated.
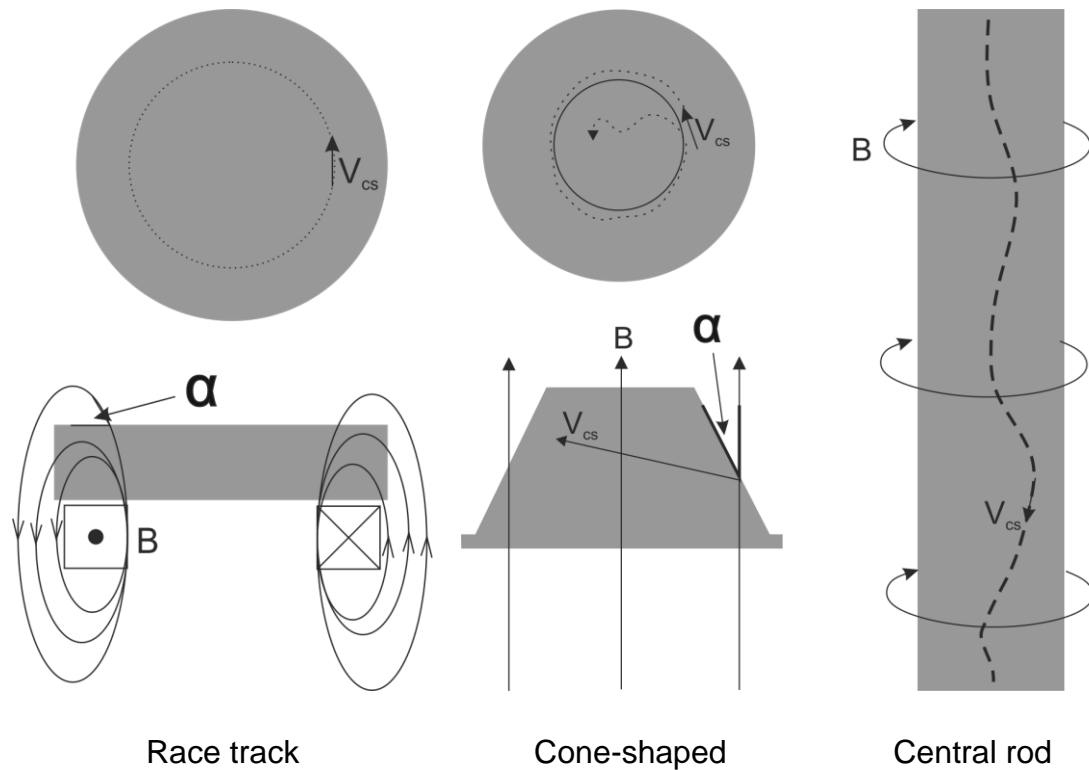
Figure 2-4 Magnetic control of the cathode spot motion on different cathode configurations. The diagram presents magnetic field lines B, acute angle α between B and cathode surface, and the velocity vector V$_{cs}$ of the spot.

2.4.2.3 Macroparticle production and filtering

Boxman [91] describes the process of material removal from the cathode by the arc spots as "a succession of explosions in adjacent locations, in which a small protrusion on the cathode surface is instantly vaporised and ionised." The explosive nature of the cathode spots results in the production of not only highly ionised plasma but also debris particles or droplets commonly called macroparticles, which are the most important issue in a cathodic arc. Although reports describe the distribution of the sizes (0.1-10 μm) and production of macroparticles [100,101] generally this term can be used for any particles more massive than electrons or ions. Due to its large size and the low velocity, the macroparticles are undesired as they have poor adhesion to the substrate, cause the growth of defects and increase the roughness of the resulting coatings [101,102]. Macroparticle production can be limited by appropriate adjustment of the deposition parameters such as:

a) Cathode cooling effectiveness.

b) Decrease the areal current density, e.g. cathodes with larger areas can be employed.

c) Using magnetic steering to control the spot movement, thus minimising the peak temperature at the specific locations on the cathode surface.

d) In case of nitride coatings, high nitrogen pressure can poison the cathode what results not only in creating the thin layer with a higher melting point but also causing multi-arc spot evaporation, which distributes the arc current over the larger area.

For some applications, e.g. nanocomposite coatings [43] incorporation of the macroparticles into the coating is unacceptable. Therefore, some filtering methods to separate the droplets from the plasma were developed [103]. Most of the filtering systems use electromagnetic coils to guide the plasma to the substrate. The trajectories of the macroparticles having large inertia and small charge are almost not affected by electric or magnetic fields [96]. In the simplest filters which have linear geometry (Figure 2-5), the macroparticles are not completely eliminated as for the ones having the high velocity to the substrate direction can reach the substrate. However, the advantage of such a geometry is that while the macroparticles number is significantly reduced the deposition rate is not affected in such a significant way as for the other filtering methods [104]. The most popular filter is 90-degree bend (Figure 2-5) allowing to filter almost 100 % of the macroparticles (some of them can still reflect from the filter walls and reach the substrate) [54]. There are few further filter variations and geometries; some allow 100% filtering rate other improve the deposition rate and are described in detail in some publications [39,54,91,104].

Linear filter   90-degree bend filter
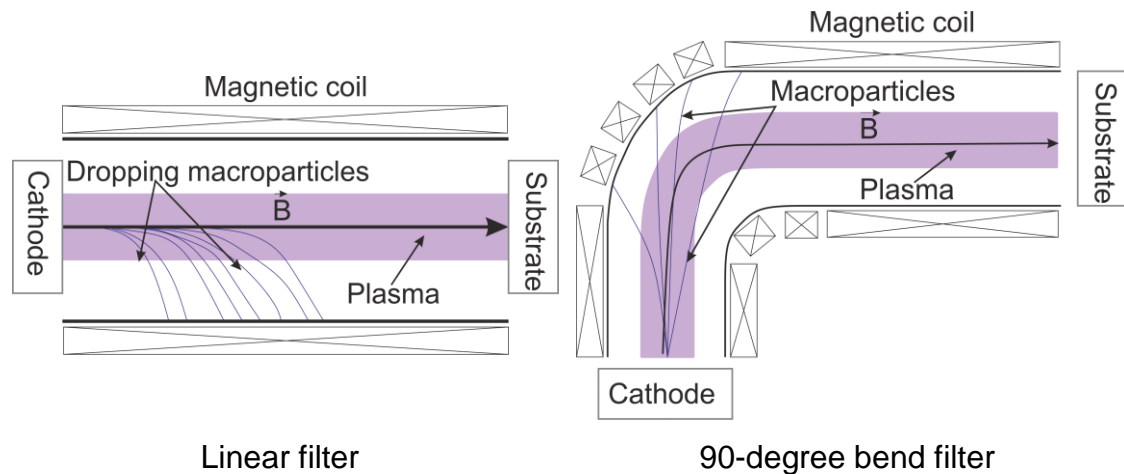
Figure 2-5 Macroparticle filter configurations.

2.4.2.4 Plasma expansion

The cathodic arc plasma expands towards the vacuum or low-pressure region due to pressure gradients and electron coupling [54]. In the absence of an external magnetic field, it can be expected to have a quadratic drop of the density of the particles from the cathode spot [93,105]. The external magnetic field can decrease the plasma expansion and guide it to the substrate. Consequently "focusing coils" are used which create an axial magnetic field what confines the plasma and directs it towards the samples [100]. An example of steering, focusing and filtering coils arrangement in cathodic arc source equipped with the cone-shaped cathode is described in chapter 5.2. D.S. Aksyonov et al. [99], discussed the importance of the proper adjustments of the magnetic fields from the coils in the conical cathode systems, as due to the superposition rule they would add and affect the arc spot motion and stability [99]. Furthermore, the field gradient can influence the ion drift; when streamed to the region with lower B-field the ion kinetic energy will increase, while the decrease can be observed in the opposite situation which was proved by experiments [54].

2.4.2.5 Cathode temperature control

Only 2/3 of the power supplied to the arc is used for material removal [54,91]. The rest of the energy is being dissipated in the cathode increasing it's temperature. Hence to prevent cathode fracture it must be cooled. In most of the cases, either direct or indirect water cooling is used. In case of the metallic cathodes such as

Ti or Cr, the cooling water can be in direct contact with the cathode material which improves the cooling rate. Though, for some materials, e.g. graphite or to simplify the cathode change a backing plate is used to avoid direct contact of cathode material with the cooling water. An example of indirect water cooling is shown in Figure 2-6. The average temperature of the cathode surface (except the area of the cathode spot) T_{cath} can be estimated by [91]:

$$T_{cath} = T_w + P_{cath} T_s \qquad \textbf{(2-1)}$$

where $\qquad P_{cath} = 1/3 P_{arc} \qquad \textbf{(2-2)}$

while the thermal resistance of the cathode-water system

$$R_s = R_c + R_W + R_{it} + R_b. \qquad \textbf{(2-3)}$$

The thermal resistance of the cathode and the backing plate can be estimated

$$R_c = L_c/(k_c A_c) \qquad \textbf{(2-4)}$$

where $\qquad R_b = L_b/(k_b A_b) \qquad \textbf{(2-5)}$

Where L and A are dimensions and k are the thermal conductivity. The thermal resistance of the water – backing plate R_w will depend on the surface condition and the water flow. The interface between the backing plate and cathode R_{it} will have thermal resistance, which is difficult to estimate, still, it will depend strongly on the surface finish. If the contacting surfaces are rough (as presented in Figure 2-6), there will be only a few contact points which can provide solid thermal conduction resulting in high thermal resistance. R_{it} can be significantly reduced by bonding the backing plate to the cathode using thermal conductive glue or solder. The most common solder for metallic bonding is high purity indium [106] (used by, e.g. Plasmaterials). According to (2-4) if the thicker cathode is used while all the other resistances are constant the average temperature of the cathode T_{cath} will be higher. This factor is significant for using conical cathodes made of the materials with low thermal conductivity. In such a case the other resistivities have to be decreased to maintain low T_{cath}; for example, the water flow can be increased to decrease R_w.
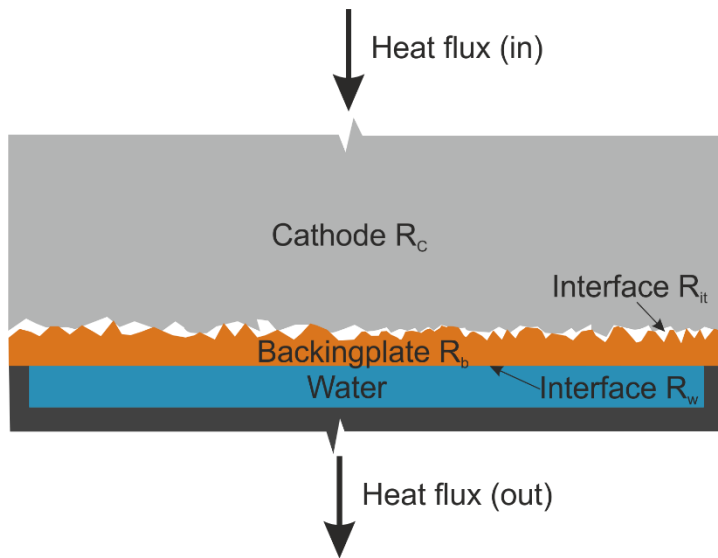
Figure 2-6 Diagram of heat flow in an indirectly cooled cathode.

2.4.3 Magnetron sputtering

Sputtering is a process of physical ejection of the atoms from a solid surface (target) by momentum transfer from energetic particles accelerated in the plasma confined in front of the target [107]. The removed, i.e. "sputtered" particles of the target may condense and form a thin film on the surfaces being placed in the short distance such as substrates or vacuum chamber walls. The ion bombardment also results in secondary electrons being emitted from the target surface and plays a vital role in maintaining the plasma [35]. This basic concept of sputtering has been known and used for many years yet, suffered limitations such as high substrate heating, low ionisation of the plasma and low deposition rates [35]. The above drawbacks were overcome by the development of magnetron sputtering (Figure 2-7) which restricts the secondary electron motion in the vicinity of the target by parallel configuration of the magnetic field to the target surface [81].
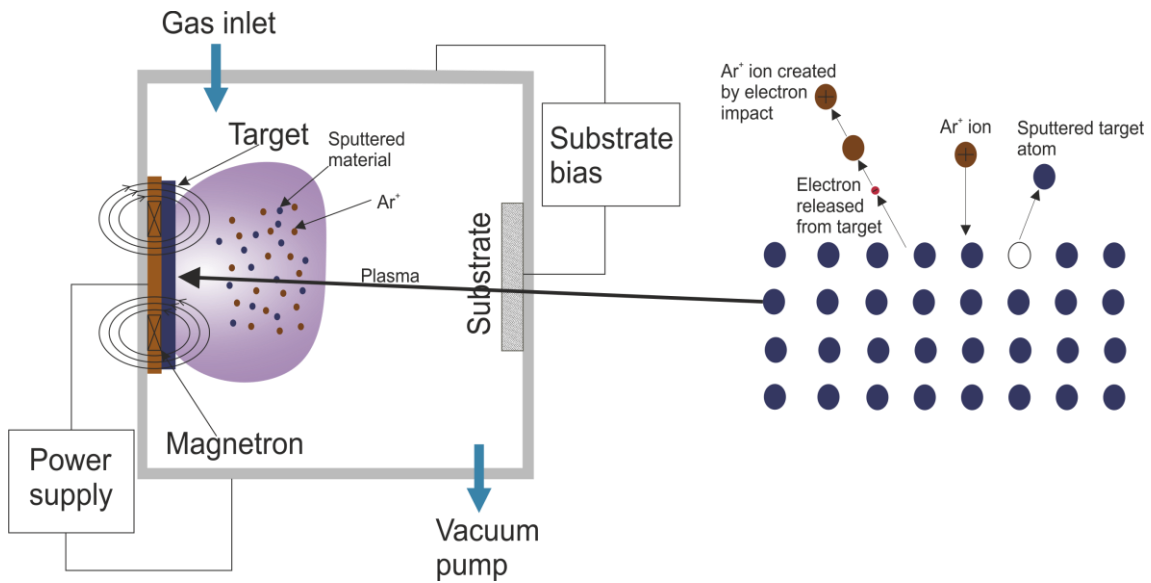
Figure 2-7 Magnetron sputtering process diagram.

The arrangement of the magnet's positions one pole at the central axis of the target, while the second pole is located around the outer edge of the target where ring magnets are placed. As the electrons are trapped in the target region, the likelihood of electron-atom collisions promoting ionisation is greater, thus creates denser plasma [85]. In turn, increased ion bombardment of the target surface occurs resulting in higher sputtering yields (ratio of the number of ejected particles to the number of impinged particles) and therefore higher deposition rates are achieved [87]. Typically, argon is used as an inert gas to produce the plasma in front of the target. Other gases such as nitrogen can be used in addition during reactive deposition producing nitride coatings, e.g. TiN [88,108,109]. Other benefits of employing magnetron include lower operating pressures (around 10^{-3} mbar) and lower operating voltages (-500V compared to up to -3 kV) [35]. The substrates can be negatively biased to improve further the energy of depositing ions thus ensuring better density and adhesion of the resulting films. The cleanness of the sputtering process makes it relevant for many applications, where film stoichiometry, grain size and roughness are more significant than the deposition rate. Also, magnetron sputtering is often implemented to deposit multi-component materials, e.g. W-S-C-TI [110] and materials that are challenging to evaporate such as WC or SiC [40].

Over the years many studies have been carried out to optimise the magnetron sputtering technique in the areas such as deposition rate improvement, target utilisation, plasma ionisation and deposition from insulating targets [81,111–113]. The most popular magnetron sputtering techniques are:

- Direct current (DC) – used for conductive target materials. As requires only DC power supply, it is considered to be the simplest solution to incorporate.

- Pulse Magnetron – employs unipolar or bipolar square waveform operating at 50-250 kHz. This technique allows sputtering of electrically insulating films and can be used during reactive deposition of non-conductive oxide targets.

- High-Power Impulse Magnetron Sputtering (HiPIMS) – it is relatively young PVD technique which has drawn much attention from researchers in the recent decade [82,114–120] as it combines the advantages of a typical sputtering technique with the production of highly charged ions, which are characteristic to arc evaporation. According to Andre Anders [120] "HIPIMS is pulsed sputtering where the peak power exceeds the time-averaged power by typically two orders of magnitude". The improved plasma ionisation caused by high power impulses results in denser coatings with high adhesion and gives a range of improvements for the films which cannot be evaporated. For instance, Babak Bakhit [42] demonstrated deposition of stoichiometric TiB_2 using HiPIMS while Erik Lewin et al. [121], improved the density and hardness of Al-Si-N nanocomposite coatings.

- Radio Frequency Sputtering (RF) – involves alternating the supply power at radio frequencies (typically 13.56 MHz) the electrical potential of the current applied to the target which prevents the charge build-up on dielectric target materials. Therefore, RF sputtering is the primary PVD method used in the semiconductor industry, where thin insulating films are required. Hence, low deposition rate which is the main drawback of RF sputtering is not applicable in this application.

2.4.3.1 Substrate preparation by ion etching

The substrate surface preparation has a significant influence on the adhesion of the deposited coatings using PVD deposition methods. Typical contamination layers such as oils can be removed by adopting chemical methods (ultrasonic cleaning in acetone and Isopropyl alcohol (IPA)), however impurities and oxides would stay on the surface limiting the active interactions between coatings and substrate [54,122]. Plasma etching employs the sputtering concept (physical ejection of the atoms by ion bombardment) to clean the substrate surface consequently providing versatile, environmentally friendly and efficient in situ cleaning method, which can be used prior to deposition process inside the vacuum chamber [107,123]. Generally, two different approaches are applied for plasma etching: Ar gas etching and metal ion etching, e.g. Cr ions [122]. Ar etching due to its practicability and easy implementation is commonly used as it only requires introduction of Ar into the chamber and application a high voltage to the substrate (-300V and more) to create the plasma. As Ar cannot remove all oxide layers effectively, a combination of Ar and hydrogen etching gases has been successfully adopted for copper and stainless steel substrates cleaning [124].

Contrary to inert gas etching, metal ion etching requires a plasma generated from an external source, e.g. magnetron sputtering, although, the cathodic arc is preferred due to a high fraction of highly charged metal ions in the plasma [123,125]. The negative bias (typically 1 kV) is applied to the substrate. Consequently, the plasma condensation on the substrate is overcompensated by sputtering from the substrate surface [54]. Also, some of the incoming metal ions are supplanted and remain in the substrate sub-surface which is desired for some of the coatings (e.g. TiN) as subsequent film growth and adhesion is improved [113].

2.4.4 Hybrid FCVA- MS deposition

The multi-source deposition chambers are commonly used to deposit multi-layered or composite coatings [89]. A few PVD sources can also be used to improve the deposition rate or coat the substrates with complex shapes [87].

However, most sources combine the same PVD technique such as closed field unbalanced magnetron sputtering unit (CFUBMS) used by Teer Coatings Ltd. [126] to deposit $MoS_2/Ti–MoS_2/TiBN–TiBN–TiB_2–Ti$. Another example is VIT-2 set-up combining three FCVA sources to allow Ti-AlN/CrN-TiAlN, Ti-AlN/CrN-TiCrAlN and Zr-AlN/CrN-ZrCrAlN deposition implemented by A.Vereshchaka *et al.* [127].

Combining the same PVD techniques ensures simplification of the deposition parameters such as deposition pressure and plasma interactions. Nevertheless, several research groups have reported hybrid deposition sources to have great potential as they are taking advantage of both the high ionisation of the plasma provided by arc evaporation and the coating uniformity provided by magnetron sputtering [107]. Such a concept was introduced by W.D Munz *et al.* [125], where arc evaporation was adopted for substrate preparation by Ti ion etching. The Ti ions not only removed contaminations but also penetrated the substrate, thus provided better adhesion and higher hardness to the following coating. The surface preparation was followed by TiN deposition performed using reactive unbalanced magnetron sputtering. Hence, obtaining dense, stress-free coatings with no macroparticles typically seen in arc evaporation. A similar solution was employed by C. Schönjahn *et al.* [123], for Cr ion etching which was followed by reactive TiAlN deposition by unbalanced magnetron sputtering. Later Kenji Yamamoto *et al.* [128], took advantage of high deposition rates provided by arc-evaporation and the versatility of the complex targets available for magnetron sputtering. In their work nano-scale multilayered coatings of (Ti, Al)N/SiN, (Ti, Al)N/WN, and CrN/BCN were successfully deposited by cathodic arc evaporation combined with unbalanced magnetron sputtering.

The development of the HiPIMS process generating a mixture of ionised gases (mostly argon) and highly ionised sputtered atoms opened new possibilities for tailoring coating properties [129]. Hybrid DC-magnetron and HiPIMS unit employed by Xiaopeng Qin *et al.* [130], allowed dopping of the MoS_2 by Ti ions. The resulting coating was $Ti-MoS_2$ which is well known lubricious coating (the work and coating described in greater detail in 2.5.3.2) typically deposited by

multi-source magnetron sputtering [131]. Recently J.Vetter *et al.* [40], proposed a new concept of hybrid arc-HiPIMS source for advanced coating architecture deposition. Such solution takes full advantage of both techniques; arc evaporation provides high deposition rate, therefore, can be used to deposit thick base coating (e.g. TiAlN) while HiPIMS is suitable for sophisticated coating compositions with high density that may be used for the deposition of complex top layers (e.g. oxidation protection or friction reduction).

2.4.5 Combinatorial deposition

An increasing need for modern advanced coating systems to meet a wide range of requirements led to the development of deposition methods which enables the production of many samples with variable composition during a single deposition run. The approach called the "multiple-sample-concept" had been suggested by J.Hanak [132] more than three decades ago. Over the years this concept has been incorporated into the modern approaches called "combinatorial" and applied mainly in semiconductors and the hard coating industry [49,50,133,134]. This name covers several methods, allowing rapid development of novel coatings. Although combinatorial deposition had not been used for tool coatings so far, selective masking is commonly used in the semiconductors industry. It enables the production of wedged layers of individual phases [49], while the ternary sputter target, allows deposition of composite coating with gradient composition using a single PVD sputtering source [135]. Another combinatorial deposition method was proposed by R.Cremer at al. [50], and successfully used in the development of hard coatings Ti-Al-Hf-N and Ti-Al-Si-N. Three angled magnetron sputtering sources were used, whereas the silicon wafer was located equidistant from all of them [50]. The chemical composition of the coatings on each sample varies with the distance from the specific sources. Thereby the number of samples with the different chemical composition of the coating is produced in one single run, which not only increases the speed of sample production but also provides the same deposition conditions for all of the coatings assuring that only the influence of the chemical composition is investigated [49,50].

2.5 Low friction coatings for Al alloys machining

This section introduces the coatings which could improve the tool lifetime during Al cutting. The main focus is on the possible improvements on existing TiB_2 and coatings with self-lubricating properties made of solid lubricants.

2.5.1 Titanium diboride

2.5.1.1 Material properties

Titanium diboride is a stable intermetallic compound having a hexagonal close-packed structure with boron atoms forming a two-dimensional covalently bonded network inside the titanium matrix [136] (Figure 2-8).
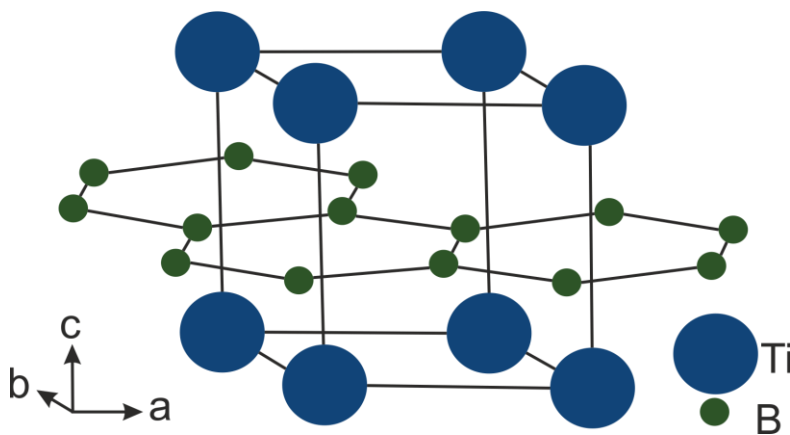
Figure 2-8 Cristal structure of TiB_2.

According to the Ti-B equilibrium phase diagram (Figure 2-9) TiB_2 stoichiometry lies within a range 28.5-30 wt% B with the highest melting point (3225°C) of all Ti-B intermetallic compounds. The atomic bonding and crystal structure provides exceptional properties such as high hardness (25 – 35 GPa), elastic modulus (565 GPa) and chemical stability (all of the TiB_2 material properties are discussed in greater detail in the work of Ronald G.Munro [9]) making it an vital candidate material for wear applications. Moreover, TiB_2 is also an excellent material for electrical applications due to its chemical inertness, low electrical resistivity (13-18^{-8} Ωm) and thermal conductivity properties [57]. However, monolithic TiB_2 as other structural ceramics, e.g. SiC or ZrB_2 suffers from low fracture toughness (~5 MPa $m^{1/2}$) and difficult densification due to low self-diffusion coefficient caused by strong covalent bonding of the constituents [10,137].
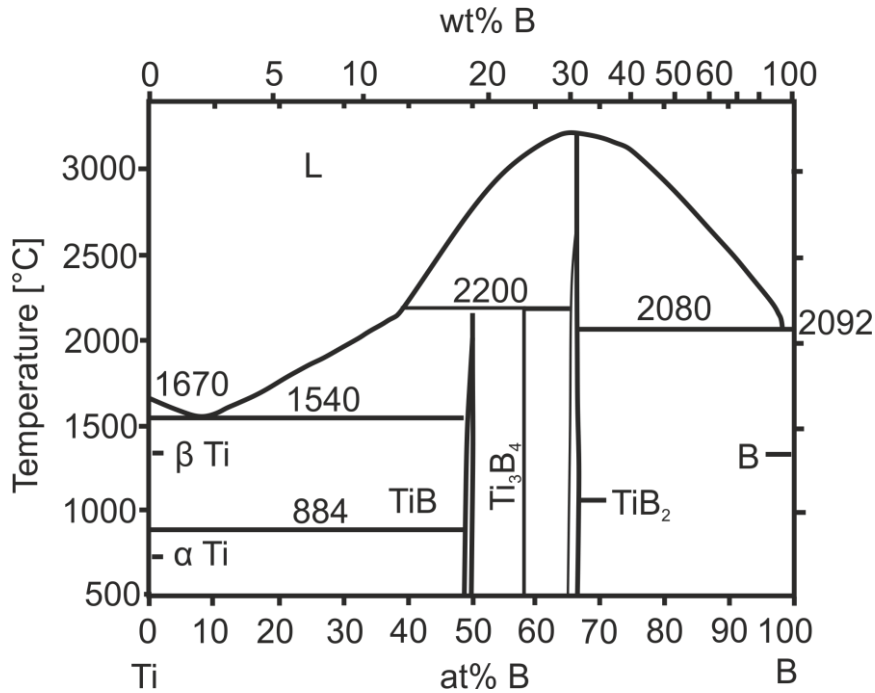
Figure 2-9 Ti–B binary equilibrium phase diagram indicating the possibility of formation of three intermetallic compounds: TiB, Ti$_3$B$_4$ and TiB$_2$ [10].

A variety of methods such as hot pressing, hot isostatic pressing and spark-plasma sintering [138,139] can be used to produce TiB$_2$. However, the full densification had been challenging due to the low self-diffusion coefficient, high melting point and oxygen contamination of the pre-cursor powders. The use of high temperatures (~2000°C) ensures near the theoretical density (TD) of TiB$_2$ [10] is achieved. Although, this leads to extensive grain growth and anisotropy of the hexagonal structure which is associated with internal stress development and correlated microcracking during the cooling phase [140]. It has been further reported that densification and sinterability can be improved by employing a metallic binder/sintering aid such as transition metals Ni, Co, Fe which promotes liquid phase sintering [137]. The boron reacts with transition metals forming metallic borides with a low melting point (900 – 1100°C) such as Ni$_3$B, Co$_3$B, Fe$_3$B which can dissolve Ti [10]. The successful use of metal aid binders has been reported indicating the mass fraction of the sintering aid in the range from 1 % - 10 % can reduce the sintering temperature down to 1425°C [9,10,141]. Although, the use of metallic aids leads also to degradation of hardness and high-temperature properties (due to the low melting point of the binder) of the bulk

material. In case of sintering the cathode for PVD, any degradation of the bulk material properties would potentially affect the properties of deposited coating what is undesired.

Various non-metallic sintering additives were studied such as AlN, SiC, Si_3N_4, CrB_2, B_4C, TaC aiming to provide good densification and fine grain structure while maintaining exceptional high-temperature properties [10]. Special mention should be made to metallic silicides having an excellent oxidation and creep resistance, good thermal conductivity and low melting point [137,141–143]. Metallic disilicates not only lower the sintering temperature but also increase oxidation resistance by forming borosilicate glass and SiO_2 on the surface of TiB_2 which acts as a diffusion barrier to the ingress of oxygen [142]. Those properties together with good thermo-mechanical compatibility with TiB_2 makes metallic disilicide potential sintering additives for high-temperature applications [137]. Among various high-temperature intermetallics, the best combination of keeping good mechanical properties of TiB_2 as well as ensuring high density are $MoSi_2$, WSi_2, and $TiSi_2$. The $MoSi_2$ was firstly assessed for high-temperature applications by Murthy *et al.* [137]. For the 20 % $MoSi_2$ mass fraction in the TiB_2, 98.7 % TD was obtained together with properties such as hardness (25 GPa), thermal conductivity (64.8 $W*(m*K)^{-1}$), electrical conductivity and wear resistance outperforming monolithic TiB_2 [137]. Later G. B. Raju investigated [144,145] the properties of TiB_2-$TiSi_2$ and the influence of the mass fraction. It was concluded that the addition of 5 wt% $TiSi_2$ is optimal as hot pressing at 1650ºC provides 99.6% TD. Moreover results also in a combination of good mechanical properties such as the hardness of 25 GPa, electrical resistivity of 10 $\mu\Omega*cm$ and an indentation toughness of ~6 $MPa*m^{1/2}$ [144]. Crack deflection was identified as the main reason for toughness outperforming monolithic TiB_2 as "a mixed mode of fracture with the dominance of intergranular fracture was observed in the case of composite materials" [144] while monolithic TiB_2 fractured mostly by intergranular crack growth. Ch. Murthy *et al.* [56], confirmed those observations and also observed oxidation resistance superior to TiB_2-$MoSi_2$ composite due to the formation of SiO_2 on the surface. Lastly, Ch. Murthy [142] also studied the WSi_2 as a sintering additive and compared it to previously studied $MoSi_2$ and $TiSi_2$, the

mechanical properties and sinterability are presented in Figure 2-10. The outcome of the work suggests an excellent oxidation resistance of TiB_2-WSi_2 composite superior to those of $TiSi_2$ and $MoSi_2$ as well as good shock resistance in comparison to TiB_2 sintered using conventional metallic sintering aids [142].
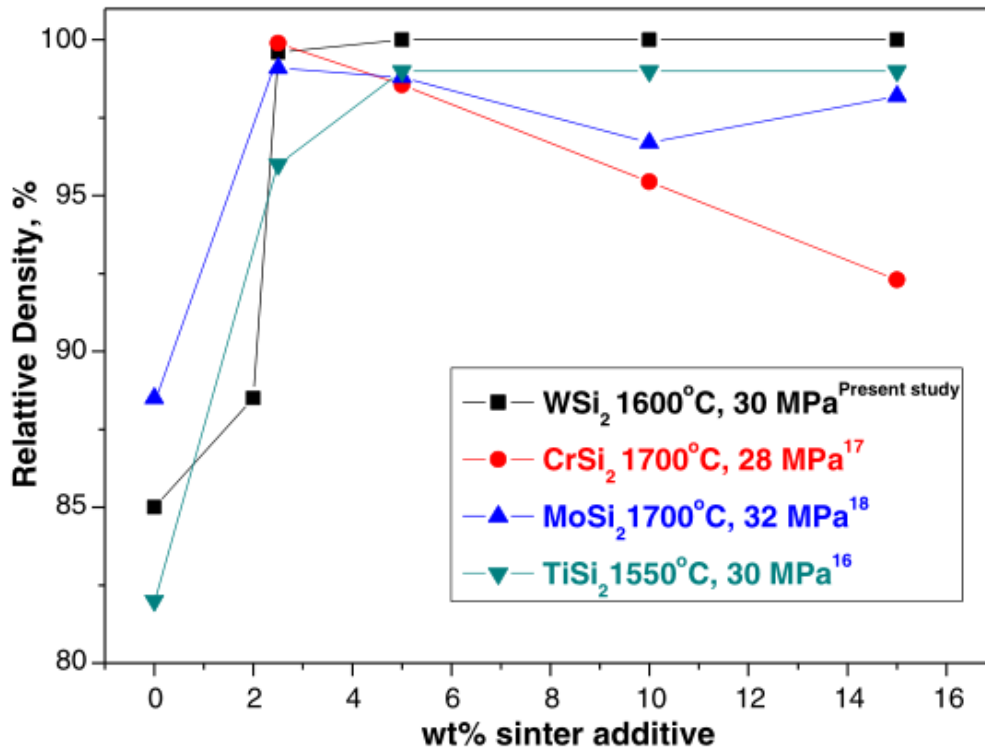
Figure 2-10 Effect of silicide sinter additives on densification of TiB$_2$ and peak K$_{Ic}$ [142].

2.5.1.2 TiB$_2$ applied as a coating

In addition to its exceptional tribological properties, TiB_2 has low chemical inertness to aluminium that is a function of these; low solubility in liquid Al and TiB_2 is a good diffusion barrier for Al [62,146]. These properties make TiB_2 an ideal material for coating the cutting tools not only to improve the wear resistance but also prevent the machined material sticking to the tool when machining Al alloys [14]. As discussed in section 2.3.2 in case of lightweight alloys especially aluminium the BUE has to be addressed as it significantly decreases the tool lifetime. The beneficial adhesion behaviour of TiB_2 comparing to other hard coatings has been demonstrated in some research papers [62,66,80,147]. Berger *et al.* [62,80], showed that concerning the coefficient of friction, pick-up of material

and smoothness of the surfaces, TiB_2 outperforms hard nitride coatings such as TiN, TiCN and TiAlN when sliding against Al. These positive attributes were related to an "exceptionally high chemical resistance against aluminium for TiB_2" [80] as no significant advantage of TiB_2 over the other coatings compared was found when sliding against other ductile materials such as Ti and Ni based alloys. E.Konca *et al.* [66], investigated the TiB_2, TiN, TiAlN, TiCN and CrN as coating candidates for dry machining of aluminium in regards to sliding distance, temperature, environment and coating roughness. The TiB_2 exhibited the least amount of Al adhesion in comparison to the other coatings, independent of the temperature, sliding speed and roughness. High chemical stability of TiB_2 was proved when testing in different environments; for other coatings, the oxygen in air promoted the Al adhesion. However, in case of TiB_2 almost no change in the material sticking was observed when the inert atmosphere was used [66].

TiB_2 coatings can be produced by a variety of CVD and PVD deposition methods although magnetron sputtering appears to be the most suitable for coating cutting tools due to a low temperature of deposition and ability to coat complex shapes [136]. The high compressive stress of deposited coatings has been limiting factor when employing TiB_2 for larger scale. Nevertheless, it has been solved by Berger *et al.* [148], who proposed to apply positive substrate bias, thus "the mobility of adatoms on the growing film surface was enhanced by thermal activation due to increased bulk temperature and also by activation due to electron bombardment" [14]. Later other researchers [8,14,136,149,150] showed that deposition parameters such as substrate bias voltage and deposition temperature allow control of the microstructure, mechanical properties and stoichiometry of resulting TiB_2 coatings. Overall the mechanical properties of TiB_2 coatings can be expected in the ranges: hardness = 30-50 GPa, Youngs Modulus = 450-600 GPa, elastic recovery = 80 % and CoF = 0.5-0.8 [8,14,136,149,150], however the brittle nature of TiB_2 [151] can sometimes limit its usage for use in finishing operations at high cutting speeds [152].

2.5.1.3 Arc evaporation of TiB$_2$

As discussed in 2.4.2 arc evaporation due to its high deposition rate, good adhesion and high density of the produced coatings is a preferred synthesis method for hard coating production. For those reasons researchers have been trying to deposit TiB$_2$ coatings using arc evaporation [18,19,153]; yet, only one successful and reproducible reported attempt [17] was found when researching the papers for this work. Other reported attempts identified extensive cathode cracking, arc instability, problems with arc triggering as well as the tendency of the arc to remain in certain location [18,19,153]. The possible explanation of the arc spot immobilisation was proposed based on the observations made for graphite cathodes, where the arc sticking has been explained by an increase in electrical conductivity of carbon with an increase of its temperature [54]. Figure 2-11 presents the electrical resistivity of TiB$_2$ against the temperature diagram obtained by A. D. McLeod *et al.* [154]. Contrary to graphite TiB$_2$ electrical resistivity increases with the increase of the temperature, though, the electrical conductivity of TiB$_2$ is significantly growing with its density. Hence, if the density of TiB$_2$ cathode is not close to 100% of TD, the arc sticking to the specific location of the cathode, can still be attributed to increase in local electrical conductivity due to material densification at a local area in time of high-temperature treatment by the arc spot [17]. Such an observation suggests that the possible way of improving arc mobility is to produce the TiB$_2$ cathode with 100% TD. As discussed in 2.5.1.1 the silicides are the most promising candidates for sintering additives providing high density while maintaining exceptional mechanical properties of TiB$_2$ and a low mass fraction (5 wt%) still, their use for cathode production was never reported.

The arc stability problems were addressed by Knotek *et al.* [18], who attempted the reactive deposition (nitrogen) of TiB$_2$. Nevertheless, the deposited films were TiBN rather than TiB$_2$. On the other hand, Trelegilo et al. [19], explored arc stability using pulsed bias arc evaporation though the resulting deposition rate was low.
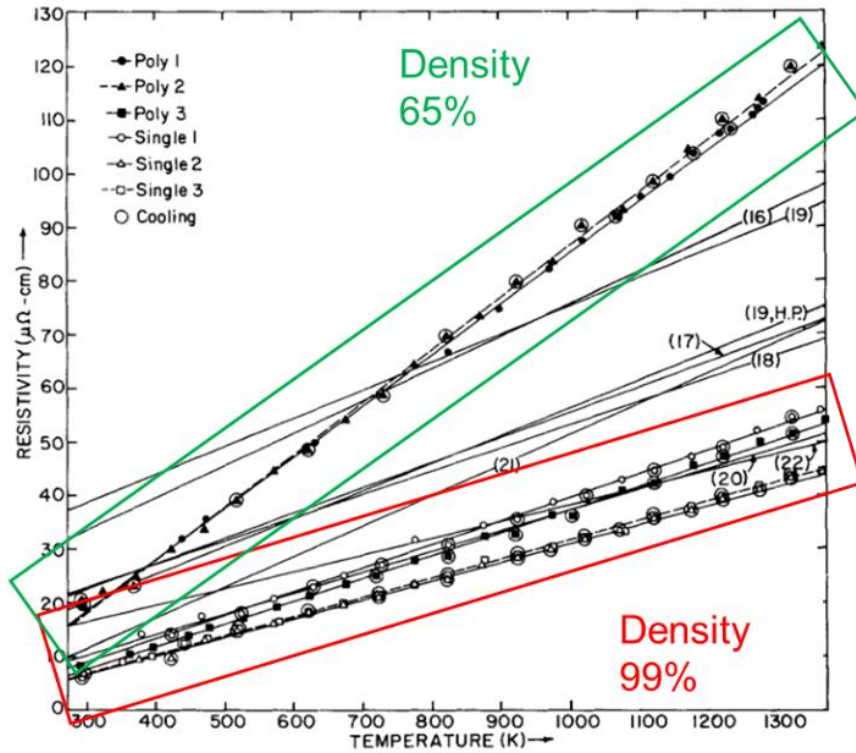
Figure 2-11 Electrical resistivities of polycrystalline and monocrystalline TiB$_2$ [54]**.**

A successful and reproducible solution has been reported by Zhirkov *et al*. [17]. TiB$_2$ cathodes with density close to 100%TD were produced what limited cathode cracking. Avoiding arc sticking was achieved by switching off the external magnetic field (which is used to guide the arc movement, as discussed in section 2.4.2.2). Therefore the arc was dissipated over a larger area, limiting local overheating and cracking [17]. Zhirkov *et al*. [17] proposed also hampering crack propagation as a way to delay the cathode destruction (Plansee Gmbh patents [155,156]). For that purpose, 1 wt% of graphite powder was added into the TiB$_2$ composition before sintering [58]. The SEM analysis of the resulted material showed carbon particles around TiB$_2$ crystals [155]. As it is suggested, carbon inclusions, due to a better temperature shock resistance, can serve as stopping points of propagation of cracks as presented in Figure 2-12. The cathodes so produced allowed stable and reproducible arc evaporation.
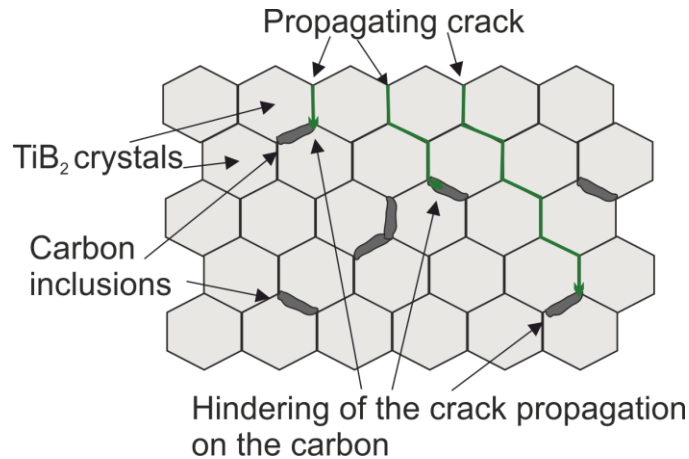
Figure 2-12 Hampering of the crack propagation on carbon inclusions [58].

2.5.2 Diamond-like carbon (DLC)

Diamond-like carbon coating refers to the range of amorphous materials containing a high fraction of sp^3 bonds which are the ones present in the structure of the diamond [157]. Depending on the method used for deposition either hydrogen-free (ta-C) or coatings containing up to 50% hydrogen (a-C:H) can be deposited [158]. Hence DLC can have a wide range of the properties [159]: hardness: 15 – 80 GPa, young modulus: 120 – 900 GPa, compressive stress: 0.5 - 0.7, CoF: 0.02-0.5. The sp^3 fraction of the coating is strongly dependant on the energy of ions forming the coating [34]. As presented in Figure 2-13 the sp^3 bonding fraction can be maximised if the ion-dominated process is used with ion energies of around 100 eV [160]. As discussed in 2.4.2 cathodic vacuum arc deposition produces mostly highly charged ions. Therefore, using this method hydrogen-free DLC coatings containing up to 85% of the sp^3 bonds can be deposited [33,157] (Figure 2-14). Contrary, in a magnetron sputtering only a little fraction of plasma, contains highly charged ions (the rest are neutrals), thereby only low sp^3 fraction can be achieved [161]. As the coating structure has a strong correlation with the energy of impinging ions, it depends on several plasma parameters but mostly gas pressure and substrate bias [160]. Thus, FCVA allows an easy way to control the content of the sp3 bond by applying a negative bias to the substrate and tailoring it to achieve specific ion energy [34]. Natthaphong Konkhunthot [162] concluded that based on the Raman peak evaluation, and XPS analysis that -100V bias applied to the substrate during FCVA deposition

provides 83 % of sp^3 bonds in the coating. Such an easy way of controlling the properties of the resulting films gives the possibility to produce multilayered coating combining hard (high sp^3 content) and soft lubricious (high sp^2 content) layers by simply changing the bias voltage during the deposition [33].

Despite all of the advantages of the DLC coating, there are some limitations. The properties of DLC coatings originate from the high kinetic energies of impinging particles, therefore the film growth is governed by supplantation process rather than by conventional condensation [160]. Consequently, the maximum substrate temperature during the film deposition is limited [163]. S. Reinke [163] reported that if the transition temperature 200°C is exceeded almost all of the sp^3 bonds are lost. Although as reported by J. Robertson [33] if after deposition the coating is annealed in a vacuum, sp^3 bonds can be stable up to 1100°C, is due to the relaxation of the stress in the coating. Another limitation of DLC is attributed to high compressive stress in the coating, which limits the maximum thickness of ta-C to 1 µm [164].
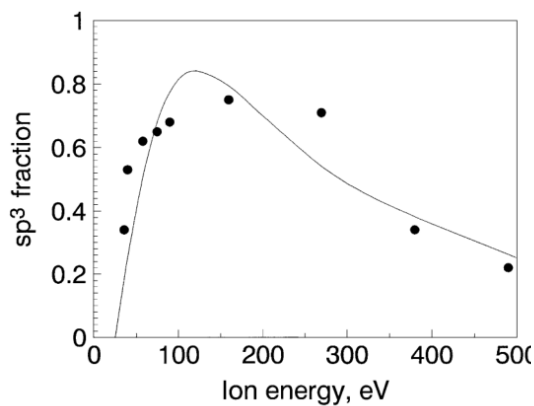
Figure 2-13 Comparison of an sp3 fraction of DLC for different ion energy [33].
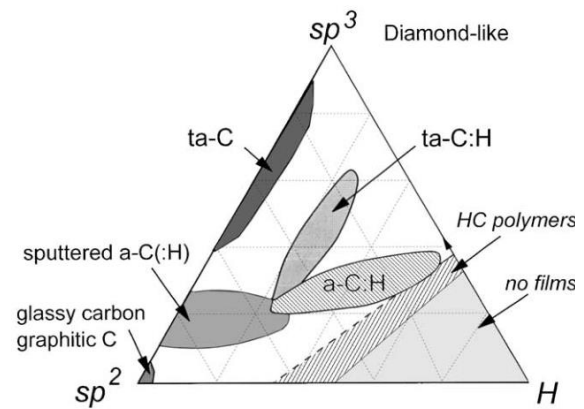
Figure 2-14 Phase diagram of DLC materials [165]**.**

The exceptional tribological properties of DLC together with the possibility to adjust them by just changing deposition parameters make DLC suitable coatings for a variety of applications. Hydrogenated DLC have the broadest range of applications as they provide a lower CoF (0.02) than hydrogen-free DLC (0.4)

while the hardness is still high (50 GPa) [160]. The most widespread applications of hydrogenated DLC are protective coatings for IR optics, sunglasses, wear and corrosion protection of magnetic storage discs (coating thickness <50nm), ferromagnetic recording tapes, razor blades (Gillette) and as a wear-resistant coating for joint implants [160,165]. The non-hydrogenated DLC has exceptional hardness and strong anti-sticking properties and is widely used in the cutting tool industry especially for cutting tools for dry and semi-dry machining of Al [78,166]. Haruyo Fukui *et al.* [167], demonstrated that even thin (100 nm) DLC coating has excellent anti-adherent properties and low CoF (0.1) thus successfully prevents Al build-up and improves machinability.

2.5.3 Solid lubricant coatings

2.5.3.1 Properties and wear mechanism

Solid lubricants are a family of materials with very low CoF, providing lubrication in a variety of conditions [168]. Therefore, they are commonly used either to replace the oil lubricants which reduces environmental impact or in conditions where the use of liquids is undesired, such as in a vacuum, food industry, aerospace, high temperature and medical applications [169]. Lamellar solids such as graphite, MoS_2 and WS_2 are the best-known solid lubricants, and their exceptionally low CoF origins from their anisotropy of mechanical properties in the shear direction parallel to the contact surface. In other words, these lamellar solids have planes of weakness, thus the lamellas can slide one over another with very low shear stress meaning they have self-lubricating properties [168]. Figure 2-15 presents the structure of MoS_2 lamellar solid; lamellas are bonded by weak Van der Waals forces. Consequently, only low stress is needed to slip one over another and this is responsible for the low friction coefficient (0.02) [170]. WS_2 has a similar structure to MoS_2. However, it maintains tribological properties at higher temperatures and in high load applications [15,171].

Solid lubricants are usually applied in the form of the coating into the working surfaces. For some applications where low loads and speeds of counterparts occur, traditional deposition methods such as spraying or painting can be used

[169]. Yet, to ensure good adhesion, e.g. when using MoS_2 and WS_2 on cutting tools PVD magnetron sputtering is preferred [27,172,173].
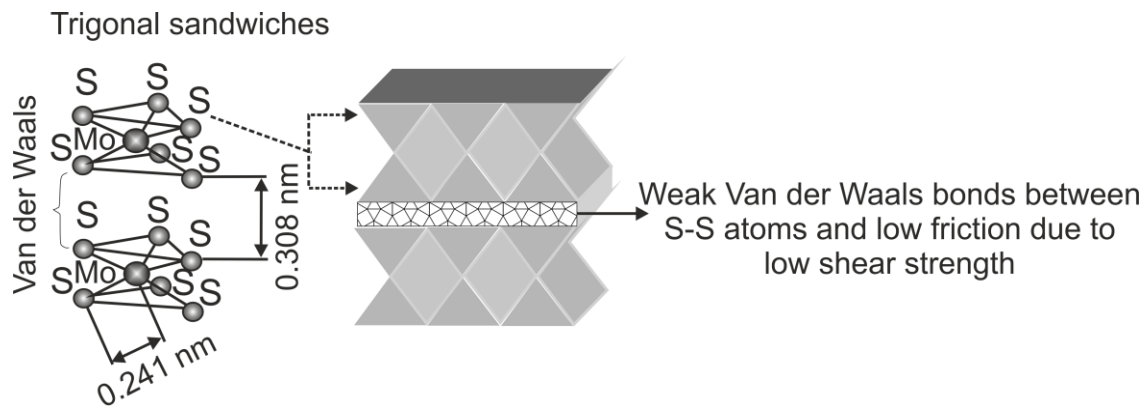
Figure 2-15 The origin of the solid lubrication effect of MoS_2 [170]**.**

The drawback of coatings made of solid lubricant is the dependence of their properties on the service conditions; MoS_2 degrades in humid air, and its CoF equal to 0.02 can increase up to 0.1 [21]. The deterioration of tribological properties of solid lubricant coatings originates from the wear mechanism known as blistering [170] presented schematically in Figure 2-16. Blistering starts with the detachment of circular patches of the lubricant from the substrate. In a vacuum, these patches can be pressed back onto the wearing surface many times before the failure occurs [169].
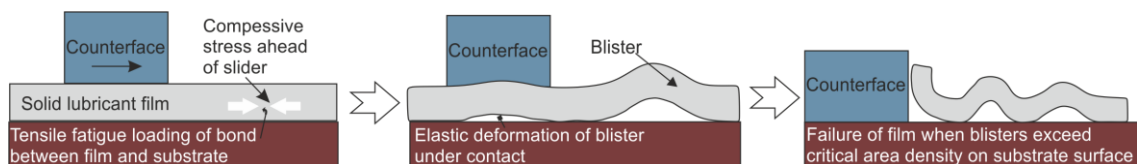
Figure 2-16 Blistering failure mechanism of solid lubricants [169].

However, the presence of oxygen and humidity accelerates the blistering effect [174]. Unoxidised lamellae edges are smooth and allow mutual sliding of one over another. If the oxidation occurs crinkling and pitting of the edges takes place what hinders the sliding movement as presented in Figure 2-17. G.Stachowiak *et al*. [169], describes the oxidation induced failure as "a result of buckling under the compressive stress caused by the hindrance of the lamella movement due to oxidised edges".
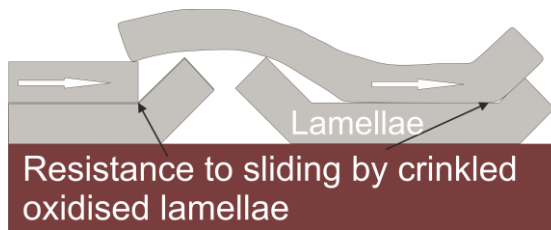
Figure 2-17 Failure of solid lubrication caused by oxidation [169].

2.5.3.2 Solid lubricant coatings for cutting tools

The MoS_2 oxidation can be prevented by co-deposition of a small amount of metals such as Ti, Ag or W [171]. However, the best known is the combination of MoS_2 with Ti which was reported by some researchers [28,29,175]. MoS_2-Ti is known under a commercial name MoST™ developed by Teer [176] and produced by closed-field unbalanced magnetron sputtering. Ti addition not only improves oxidation resistance of MoS_2 lamellas but also significantly improves mechanical properties such as hardness (1000-2000 HV compared to 400 HV for pure MoS_2), wear resistance (factor of 100) and low coefficient of friction of around 0.04 [21]. Further improvement to deposition method of MoS_2-Ti has been proposed by Xiaopeng Qin *et al.* [130], who employed hybrid HiPIMS-Magnetron sputtering system. In their work MoS_2 has been deposited by DC-magnetron sputtering while Ti has been doped into the structure by HiPIMS. As HiPIMS produces a high fraction of energetic ions, the adhesion and density of resulting coatings were improved. The maximum hardness and adhesion have been found for the coatings with 13.5 at% Ti, which also showed excellent lubrication and wear resistance, with consistent CoF of around 0.04 [130].

Similarly to MoS_2 the tribological properties of WS_2 can be significantly enhanced by co-deposition with metals such as Cr [177], Ag [178] and Ti [22]. Fang-er Yang *et al.* [179] demonstrated that improvements can also be achieved by combining WS_x and amorphous carbon (a-C). The multilayered WSx/a-C coatings showed improved tribological properties such as wear resistance and CoF in the various environments (vacuum, humid air and distilled water).

Previous studies indicated that an addition of hard underlayers such as TiN or TiCN can further enhance the tribological properties of lubricating films [21–23].

44

The addition of hard underlayer prevents the outer bodies from penetrating the soft matrix at the top; therefore the contact area is smaller, and ploughing is reduced [22]. N.M. Renevier *et al.* [21], reported a significant increase in milling distance and a reduction in average milling force during dry machining using MoST deposited on top of TiCN. A similar combination of the hard+soft coating was reported to improve other tools used in dry conditions such as; drills and punches [131]. Tushar Banerjee *et al.* [22], demonstrated the improved load-bearing capacity of WS_2-Ti layer with TiN underlayer.

2.6 Conclusions

The primary goal of applying the coatings on the cutting tools is to allow rapid tool adaptation with minimum wear and increase the steady-state duration. The adaptive coating concept proposes introducing of a relatively thin (<1 μm) lubricious layer on top of thick (>1 μm) wear-resistant coating. PVD deposition methods offer a variety of material to be deposited while avoiding the production of toxic gasses which are typical for CVD. FCVA deposition is a well-established PVD method allowing high deposition rates and good adhesion of the produced coatings. However, this method requires control of macroparticle production and arc spot movement. The high energetic nature of the arc spots limit FCVA use for ceramic material evaporation. However, recent reports suggest that with further research, it could be successfully adopted for TiB_2 deposition. Magnetron sputtering is the most versatile PVD method, though suffers from low deposition rates. Hybrid FCVA-MS deposition system would allow the production of composite and multilayered coatings with properties not achievable for each of the individual techniques.

TiB_2 is a well-established coating for machining of AlSi alloys as it addresses both the abrasive nature of Si and the tendency of Al to form a BUE. Although the high brittleness of TiB_2 might sometimes lead to the increased wear in the adaptation phase of machining. Solid lubricants such as MoS_2 and WS_2 could provide the lubrication needed to improve the tribological properties of TiB_2 coated tools. When used in tool application, solid lubricants require the addition of another element to prevent deterioration of their tribological properties, although the ratio

of MoS$_2$ to, e.g. Ti has to be optimised. The combinatorial deposition could speed up the process of chemical composition optimisation and allow evaluation of plasma distribution during hybrid FCVA-MS deposition. The high hardness and low CoF of DLC make them perfect candidate as thin lubricious coatings primarily when deposited by FCVA. DLC combination with WS$_2$ could further improve their lubricating properties.

Cathodic arc deposition is a well-recognized deposition technique used for the production of hard cutting tool coatings, although its application to coat cutting tools for AlSi machining is not commonly reported. Especially the novel concept of FCVA deposition of TiB$_2$ should be further researched. Also, the great potential of hybrid FCVA-MS deposition which takes advantage of both the high ionisation of the plasma provided by FCVA and versatility of MS should be addressed.

3 Hybrid Ti-MoS$_2$ Coatings for Dry Machining of Aluminium Alloys

Tomasz L. Brzezinka, Jeff Rao, Mohamad Chowdhury, Joern Kohlscheen, German S. Fox Rabinovich, Stephen C. Veldhuis, Jose L. Endrino.
Available at: https://doi.org/10.3390/coatings7090149

Abstract: Combinatorial deposition, comprising filtered cathodic vacuum arc and physical vapour deposition PVD magnetron sputtering is employed to deposit MoS$_2$ and Ti thin films onto TiB$_2$-coated tool inserts specifically designed for the dry machining of aluminium alloys. Titanium is deposited by FCVA while MoS$_2$ is magnetron sputtered. The deposition set up allows several compositions of Ti-MoS$_2$ to be deposited simultaneously, with Ti content ranging between 5 and 96 at%, and their machining performances to be evaluated. Milling took place using a CNC Vertical Machining Center at a 877 mm/min feed rate. The effect of different coating compositional ratios on the degree of aluminium sticking when a milling insert is used to face mill an Al alloy (SAE 6061) was investigated using a combination of EDX and XPS analysis. XPS studies suggest that the greater degree of Al sticking on the rake face of the inserts is due to the formation of greater amounts of non-protective Ti-O phases. EDX mapping of the milling inserts after machining reveal that a Ti:MoS$_2$ ratio of around 0.39 prevents Al from sticking to the tool edges. Since we prevent Al from sticking to the tool surface, the resultant machined surface finish is improved thus validating the machining performance of TiB2-coated tools using optimum compositions of Ti:MoS$_2$ thin film coatings.

Keywords: self-lubricating composites; molybdenum disulphide; SEM; EDS; XPS; milling; aluminium

3.1 Introduction

Liquid lubricants are employed as sources of lubrication in machining applications for many years [67–69]. Their main purpose is to reduce the frictional heat of the tool and suppress contact pressure [70]. Lubricants also help to remove cutting chips from the cutting area as well as removing heat during machining [180]. However, the drawbacks with lubricants are their high costs associated with purchasing as well as the costs of refrigeration and recycling [72]. Refrigeration costs can be almost four times their purchasing costs since most lubricants are not bio-degradable [71]. Hence, of importance in modern cutting applications is the search for alternatives which either minimise or avoid the production of environmentally aggressive liquid residues [74]. Dry machining is emerging as a "greener" alternative, eliminating the need for any liquid-based lubricants [77]. Although considered environmentally friendly, its main drawback is the significant impact it has on tool lifetimes due to the lack of fluid to lubricate the tool-chip area and remove heat from the cutting region [78]. Furthermore, dry machining is a serious challenge for lightweight alloys such as aluminium which during machining exhibit a high degree of plasticity [73]. The higher temperatures during machining facilitate aluminium adhesion to the cutting tool forming a built-up edge [79]. BUE results in the machined part surface being rough and tool lifetime reduced [59,71] as described in section 2.2.

Existing cutting tools in dry machining applications are coated to increase their hardness, prevent the tool material from being exposed and reduce friction coefficients [71,180]. A commonly employed solid lubricant coating is molybdenum disulfide, which significantly improves the tribological properties of cutting tools [181], and is also typically employed in many other applications such as precision bearings, release mechanisms and space applications [131] due to its inherent low friction attributes. The characteristics of MoS_2 arise from its layered anisotropic crystal structure [176] where weak bonding between the slip planes allows atoms to slip one over another, producing the low friction coefficients observed. However, the friction coefficients degrade over time in the presence of water and oxygen due to the formation of MoO_3 [182], as a result of oxidation and blistering of the topmost layers. Blistering can be prevented by co-

depositing MoS_2 with a metal [23], which affects not only friction coefficients but lead to higher hardness values and lower wear resistance, not only in the presence of oxygen but also in high humidity [182]. However, the hardness, wear resistance and the lifetime of a coating in a humid environment has yet to be resolved [183].

Currently, cemented carbide mill inserts coated with TiB_2 offer the possibility of dry machining a large variety of structural metallic alloys. TiB_2 has a high hardness (~30GPa) and excellent wear characteristics, but its brittleness and adhesion to the workpiece can sometimes reduce tool longevity [184]. In this study and friction coefficient of thin films of Ti and MoS_2 was studied by the deposition of a thin (200nm) $Ti:MoS_2$ lubricant coating layer on TiB_2 precoated cemented carbides. A combinatorial deposition method comprising a filter cathodic arc deposition of titanium and sputtered deposition of MoS_2 was used. The application of a combinatorial deposition method offers manufacturing flexibility, increasing the speed of sample production under the same process conditions by ensuring that only the influence of the chemical composition is investigated [49,50]. Thus, the specific objectives of this study are to ascertain the degree of combinatorial control offered by FCVA and to sputter, to optimise the metal-solid lubricant ratio, in an attempt to prevent aluminium sticking to the tool rake of a mill insert used to dry-machine an SAE 6061 Al alloy. The full cutting tool life evaluation is outside the scope of this article.

3.2 Materials and Methods

3.2.1 Deposition parameters

The tungsten carbide mill inserts were as-received with 2 μm of TiB_2 (Figure 3-1) which were DC magnetron sputtered using TiB_2 ceramic tiles on a copper backplate by the tool manufacturer. $Ti-MoS_2$ coatings were deposited by combining magnetron sputtering with filtered cathodic vacuum arc techniques. Prior to deposition, the tool inserts were ultrasonically cleaned in an acetone bath for 15 minutes and then rinsed in isopropyl alcohol. The system base pressure was below 0.25×10^{-3} Pa prior to coating, while the system process pressure was set at 1.6 Pa. Substrates were grounded during the deposition. A range of

compositions were deposited by placing a sample holder equidistant to both the Ti (FCVA) and MoS_2 (MS) sources. Substrates closer to the MoS_2 source should exhibit coatings with a higher MoS_2 content contrary to those placed close to the Ti source which should have higher Ti content. Figure 3-2 presents a schematic of the system. Ti was deposited by FCVA using a conical shaped cathode (67mm x 50mm x 50mm), with the arc current set to 65 A. To prevent macro particles in the coatings the plasma was filtered using a linear filter as shown in Figure 3-2. The filtering coil current was set to a maximum current of 10 A. MoS_2 was sputtered from a 3-inch diameter target. Coatings were produced by simultaneously operating both the Ti and MoS_2 sources. Simultaneous deposition on silicon allowed for step and roughness measurements of the mixed coating surfaces. Ion current measurements at the sample surface were made by connecting wires at each sample position a-e which will allow a better understanding of the influence the ion characteristics have on coating properties. Measurements at each position were collected simultaneously for 60 s, using laboratory potentiostat connected to a computer sampling at 5 Hz.
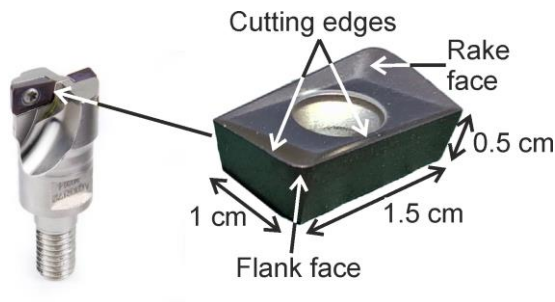
Figure 3-1 A Widia® mill insert dimensions and its position in the milling holder [185]
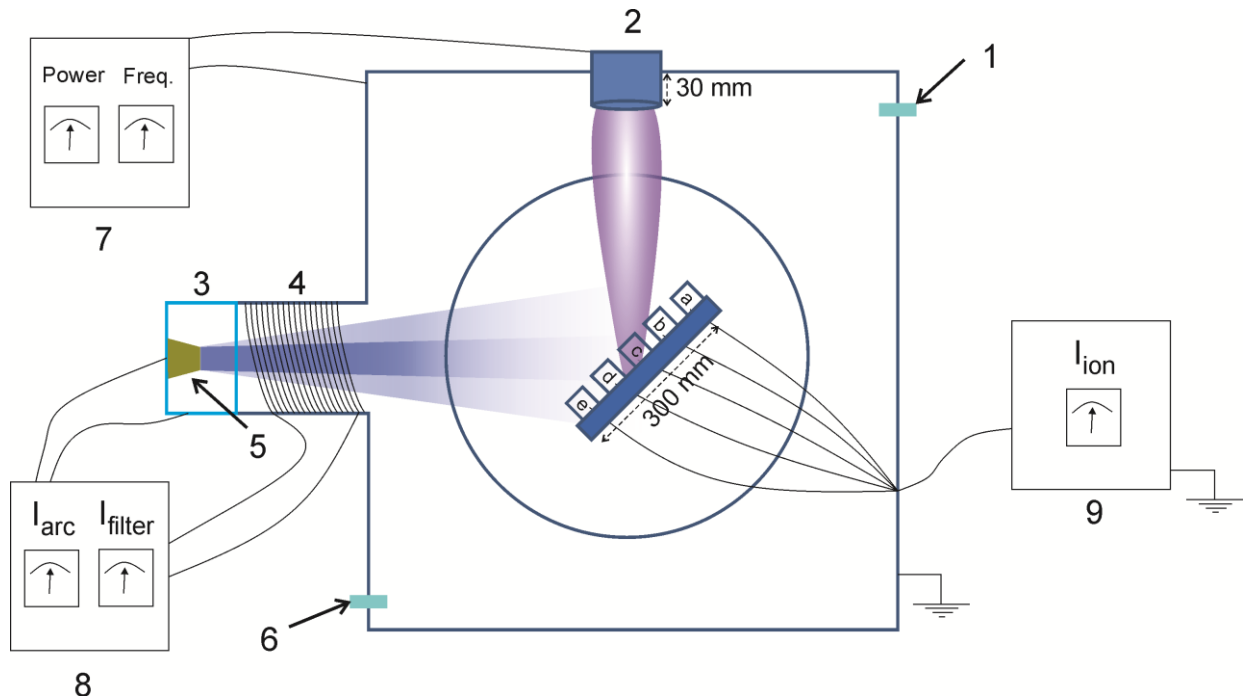
Figure 3-2 Top view of the chamber presenting location of the substrates (1-vacuum cryo pump inlet, 2 – 3" MoS$_2$ sputtering target, 3 – anode, 4 – linear filter, 5 – Ti cathode, 6 – argon inlet, 7 – PVD sputtering power unit, 8 – cathodic arc power unit, 9 – Ametek VersaStat 4 Potentiostat)

3.2.2 Coefficient of friction evaluation

To allow thickness measurements, a small portion of the silicon sample was covered before deposition. The difference in step between the coated and uncoated portion of the silicon was measured by a Dektak stylus profilometer. The same device allowed roughness measurements to be made. The progressive load unidirectional sliding tests were conducted using a ST-3001 Tribo Tester. In this test, an indenter is drawn over a specimen surface with a linearly increasing load until well-defined failure occurs at critical load L_c [186]. Normal force (F_z) and tangential force (F_x) are recorded. The coefficient of friction was measured using a fixed chrome steel 5 mm-diameter ball, applying an increasing progressive load from 5 to 100 N, at a loading rate of 50 N/min and linear velocity equal to 5 mm/min. For each sample, three scratches were obtained, and the measured friction coefficients were averaged. To simulate tool wear during the Al alloy machining additional scratch tests were conducted using the same parameters but with Al ball.

3.2.3 Aluminium milling performance and characterisation tests

Face milling experiments were conducted using an Okuma Cadet Mate CNC vertical machining centre. The coated inserts were assembled on a face milling cutter with Ø 75 mm and five-flutes. The coated mill inserts were used to cut an Al alloy, SAE6061 material. The machining volume was 104400 mm^3. The detailed cutting conditions are presented in Table 3-1. These cutting parameters were selected according to parameters that are widely used in the industry of automotive components manufacturing, such as cylinder head and engine block for semi-finishing operations. Semi finish operations during cutting process reflect extreme frictions conditions for cutting tools.

Table 3-1 Cutting conditions used for Ti-MoS$_2$ coated tools evaluation.

Machine tool	CNC Vertical Machining Centre
Tool speed [RPM]	5827
Feed rate [mm/min]	877
Feed per revolution [mm/rev]	0.15
Depth of cut [mm]	1
Cutting speed V_c [m/min]	464
Total cutting length [m]	1.8
Workpiece material	Al alloy SAE 6061

The surface of the worn inserts and the scratches formed during the tribological tests were examined by scanning electron microscopy (SEM) in secondary electron mode operating at 20.0 kV. Coating composition and element mapping images were determined by using Energy-dispersive X-ray spectroscopy (EDX). X-ray Photoelectron Spectroscopy (XPS) measurements were employed to evaluate the chemical bonding in the coatings.

The structural and any phase transformation at the cutting tool/workpiece interface along with the chemical composition of the tribo-films were studied by X-ray photoelectron spectroscopy (XPS) equipped with a hemispherical energy analyzer, an Al anode source for X-ray generation and a quartz crystal monochromator for focusing the generated X-rays. A monochromatic Al K-α X-ray (1486.7eV) source was operated at 50W-15kV. The system base pressure was no higher than 1.0×10^{-9} Torr with an operating pressure that did not exceed 2.0×10^{-8} Torr. Before collecting any spectra, the samples were sputter-cleaned for 4 minutes using a 4kV Ar^+ beam. Pass energy of 280eV was used to obtain all survey spectra while pass energy of 69eV was used to collect all high-resolution data. All spectra were obtained at a 45˚ take-off angle and a dual-beam charge compensation system employed to ensure the neutralization of all samples. The instrument was calibrated using a freshly cleaned Ag reference foil, where the Ag $3d_{5/2}$ peak was set to 368eV. All data analysis was performed by computer software.

3.3 Results and discussion

3.3.1 Combinatorial effects

3.3.1.1 Ion current measurements

The combinatorial deposition method allows the rapid development of a range of coatings having different chemical compositions [132]. The plasma glow discharge during magnetron sputtering produces material sputtered from the surface of the target (mainly focused around the circular magnetron track) [82], in contrast to the FCVA process where the plasma is focused over a much smaller area typically referred to as cathode spots [54]. FCVA studies propose that in the absence of a magnetic field, the FCVA plasma exhibits a quadratic drop in density of particles from the spot centre [93,105]. Hence, the combination of plasma from these two sources produces Ar+ ions, metal Mo and S atom and FCVA Ti^+ ions colliding in complex elastic collisions in a variety of intensities depending on the distance from the source. In the case, neutral-electron collision the energy transferred to the neutral from the electron is very small [187]. However, if the frequency of the collisions is large, then the collective effect of all these collisions

might be significant. On the other hand, neutral-ion collisions result in charge-exchange producing fast neutral and slow ion [187]. For a large number of collisions, the neutral density in the plasma centre can be depleted significantly [187]. In order to gather some insight, the variations in ion current from the PVD and FCVA sources were collected during deposition (Figure 3-3 (a)). The current was averaged for each sample position and measured for 60 seconds at each individual source and with both sources started. There was little or no variation in the measured ion current when only the PVD MS source was in operation. This is due to the stability of the glow discharge typical for MS producing species with similar energies generated [188]. On the contrary, arc discharge plasmas produce ions more dynamically over the entire surface of the cathode. This produces ions with variable charge states: Ti^{1+}, Ti^{2+}, Ti^{3+}, Ti^{4+} and its distribution [189]. E. M. Oks. *et al* [189] found that for their arc ion source the distribution of the ion states was: 5% Ti^{1+}, 35% Ti^{2+}, 54% Ti^{3+} and 6% Ti^{4+}. That is reflected in the greater differences in the ion currents measured in this experiment. As expected, the currents generated from the FCVA ions are greater than the ions from PVD sputtering [54]. For MoS_2 the highest average current can be found at sample position labelled b, falling gradually with increasing distance from the MoS_2 target. However, when only the FCVA source is operational, for Ti, the highest currents were found on the sample positions a, b, and e, which indicates the tendency of the ionised plasma to expand towards the chamber walls once it is away from the linear magnetic filter [105]. Other factors influencing the spread of the plasma plume generated by FCVA include pressure gradients, shape and the size of the anode, the concentration of neutrals and external magnetic flux present in the chamber [54,94]. As magnetron includes permanent magnets the magnetic field from them might have affected plasma expansion and ion charge [189]. In case of combinatorial deposition FCVA was found to dominate the deposition rate as the Ti-MoS_2 graph shape matches the shape of the Ti graph (Figure 3-3 (a)). However, it is worth noting that the average current for samples a and b located the closest to the MoS_2 source drops when both sources are running. Interactions between neutrals and ions in this region near the MS source could result in high intensity collisions between the Ar+ and Ti ions and neutrals

resulting in some of the ionized Ti ions losing their energy due to charge-exchange with neutrals in the region near samples a and b when the MS source is running. After collision the fast neutrals are able to escape from the plasma centre [187]. This would also explain the increase in ion currents in samples d and e.

3.3.1.2 Chemical composition

Research studies show that the greatest tribological properties have MoS_x compositions at S to Mo ratio of around 2 [26,174,175,190] as the chemical composition of thin films of MoS_2 are significantly affected by the substrate bias voltage and working pressure during deposition [170], which in turn affects the tribological and oxidation characteristics [191]. Oxygen atoms are smaller than sulphur atoms, therefore, they can easily substitute in any sites deficient in sulphur forming Mo-O-S, leading to degradation of tribological properties of MoS_2 films in the air [190]. The co-deposition with Ti prevents MoS_2 degradation as Ti goes into interstitial or substitutional sites in MoS_2 and act as a barrier for oxygen diffusion, thereby stabilising MoS_2 [26]. The chemical composition as a function of the sample position of the as-deposited coatings is shown in Figure 3-3 (b). Given the 200 nm thickness of these films, the EDX-SEM technique was used to quantify the Ti and MoS_2 contents in the samples. Figure 3-3 (b) shows that the Ti content in the coatings increases relative to the position with the cathodic arc source. In fact, the measured chemical compositional variations follow the changes in measured ion currents. For samples at positions a and b, are dominated by the plasma from the MoS_2 source, while the samples at positions c, d and e have higher Ti contents. Moreover, samples at positions d and e seem to be more influenced by the short distance to the source (similar composition ~96 at% Ti) than the samples positioned at both a and b. Position c, being equidistant from both MoS_2 and Ti sources, the Ti content in this sample is 3 times, greater than the Mo content. This is attributed to the greater deposition rate of the cathodic arc source compared to magnetron sputtering [192].
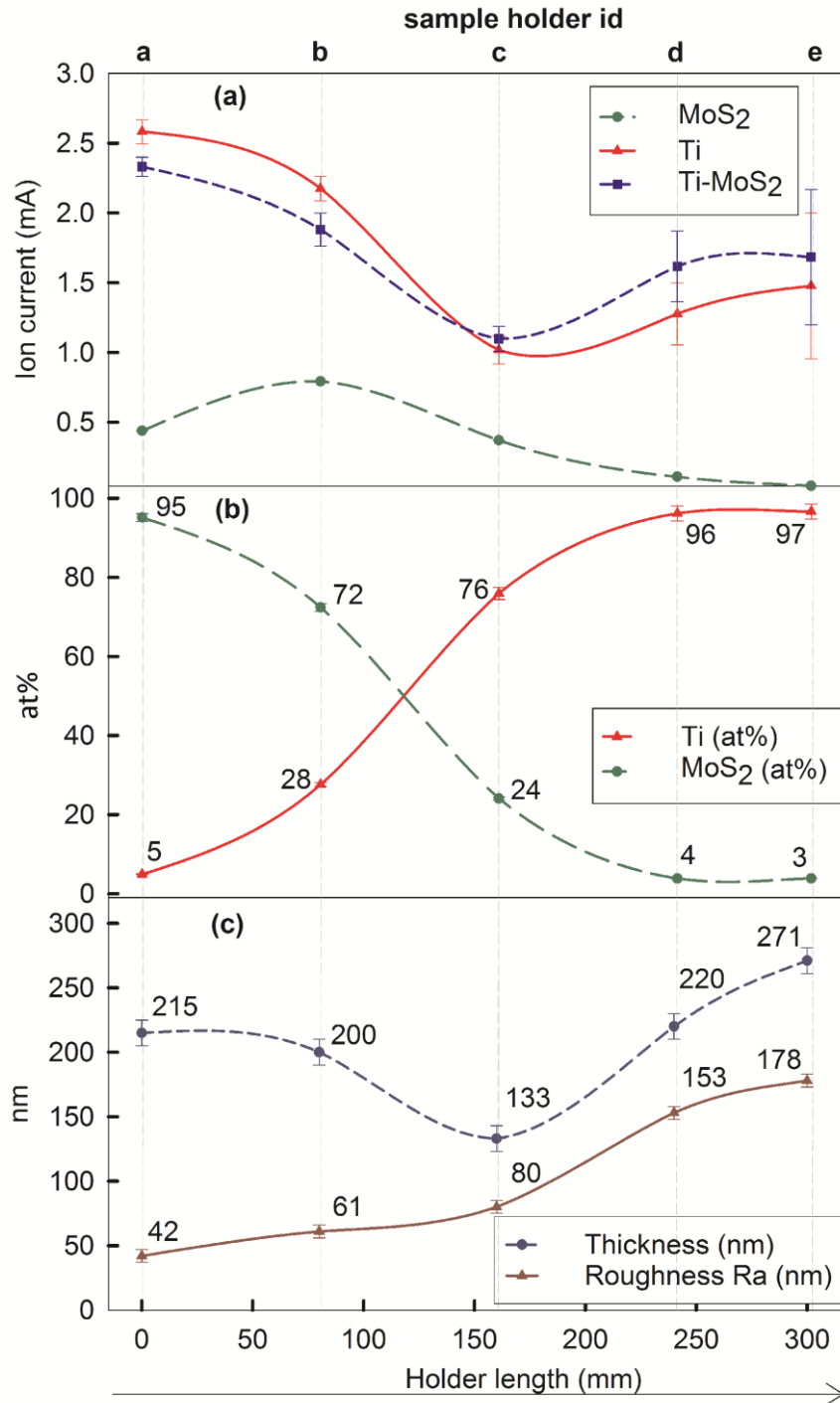
Figure 3-3 (a) Ion current measured on each of the five samples (a-e) during deposition from MS and FCVA separately, as well as during combinatorial deposition. Each measurement made for 60s with 5Hz sampling speed. (b) Ti and MoS$_2$ contents (at%) in Ti-MoS$_2$ coatings on five samples (a-e). Measurements obtained by EDX mode of SEM. (c) Roughness and thickness for the five samples (a-e) deposited with Ti-MoS$_2$ coating. Measurements were done on silicon slides using Dektak® profilometer.

3.3.1.3 Thickness and roughness

Figure 3-3 (c) shows the thickness and roughness values for all the deposited samples. The lowest thickness value (135 nm) was measured for the sample c positioned equidistant to the MS and FCVA sources which was also the sample with the lowest measured ion current. There are also notable differences in the thicknesses between samples d and e despite having similar compositions. This difference is likely due to the proximity of position e to the FCVA source since the plasma density is greater in the vicinity of the front of the cathode. In fact, the ion current profile across the holder follows to a great extent the measured profile thickness. During deposition, besides the charged ionised plasma from the FCVA source, macroparticles of molten cathode material created at the cathode surface [54] could pass through the linear filter and adhere to the substrate. In some cases can decrease the density and adhesion which is undesired as it decreases the lifetime of the coating [39]. Figure 3-3 (c) shows that the Ra increases with increased proximity to the Ti target. The maximum roughness of 178 nm was found for sample e, which is furthest from the MoS_2 target and has a Ra that is almost 5 times greater than sample a. This shows a direct correlation between the deposition technique and the roughness values of the deposited sample.

3.3.1.4 Frictional properties

Figure 3-4 shows average friction coefficient for the 5 deposited samples as a function of increasing load. For loads above 50 N, a coefficient of friction (CoF) ranging from 0.07 to 0.15 was obtained. The measured values are similar to other studies for MoST coatings [193]. For hybrid MoS_2/Ti coatings deposited using combined dc sputtered by high power impulse magnetron sputtering (HiPIMS) methods, the reported CoF values between 0.05 and 0.23 depending on Ti content [130]. In the present study, the lowest CoF (equal to 0.07) was obtained for the sample at positions a and b having a Ti content of around 5 and 28 at% respectively, in good accordance with other reported values on samples with comparable chemical composition [191]. In fact, it is worth noting that the CoF for this composition also had only little variation during ball on flat test independently of the load. The low CoF for this particular chemical composition has been related

to the formation of thin MoS$_2$ lamellas with good adhesion to the hard titanium phase present in these coatings [26]. In this line, other research studies [26,175] concluded that the Ti to MoS$_2$ ratio has to be optimised for certain applications as too high Ti content may lower the tribological properties due to segregation of metallic titanium [175], while too low Ti content will also result in degradation of tribological properties over time due to oxidation of MoS$_2$ [174]. Optical microscope studies (Figure 3-5) of the scratches support these findings. Coatings with high (98 at%) Ti contents (sample d and e), did not provide sufficient lubricating properties therefore, material transferred from the ball can be observed. The wear track on the sample a reveals coating failure at the start of the scratch occurs due to high MoS$_2$ content which is soft therefore fails easily under load [174].
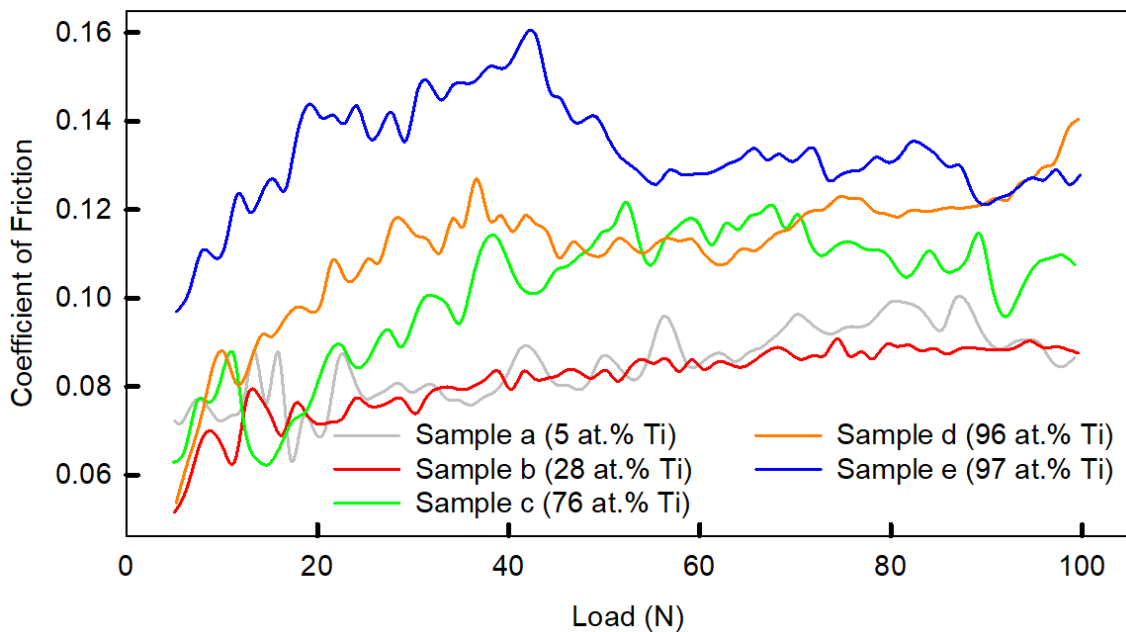
Figure 3-4 Average friction coefficient vs load applied for Ti-MoS$_2$ coatings on five samples (a-e). Tests conducted by progressive load unidirectional sliding tests using fixed chrome steel ball with 5mm diameter ball sliding against a coated sample. Progressive load 5 N-100N applied with 50N/mm loading rate.
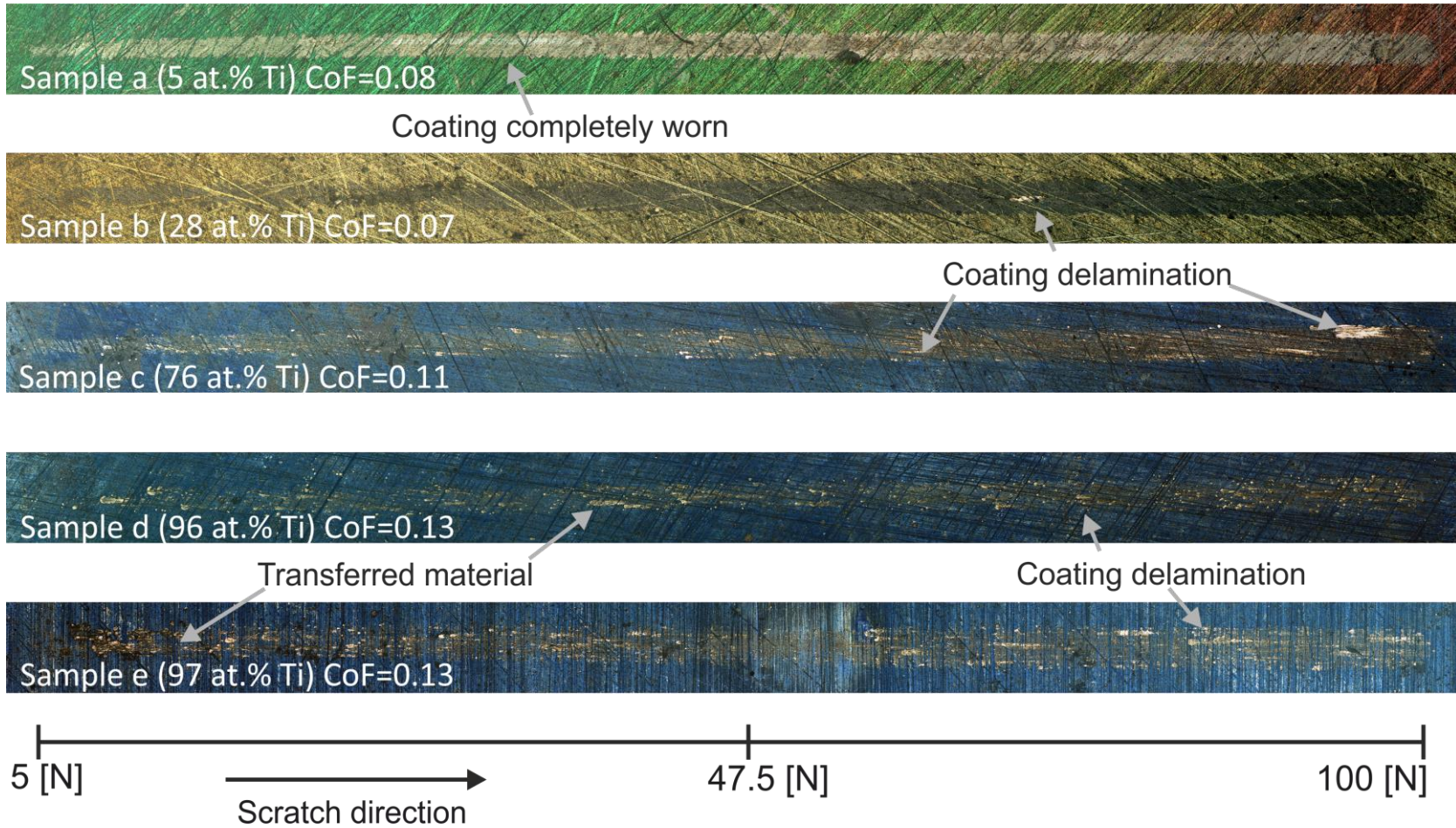
Figure 3-5 Optical microscope images of scratches after progressive load unidirectional sliding tests with Cr steel ball for increasing progressive load 5 N -100 N.

Although as the sliding direction does not change the worn coating material piles up in front of the ball providing low friction (around 0.08) for the whole length of the scratch. However, in case of the machining process where chips are constantly removed, and the cutting direction varies the worn coating would not be able to provide low friction on the interface tool-machine part. Contrary on the coating on sample b, while the scratch is visible confirming a transfer layer was formed. Only little delamination (base material exposed) can be observed for loads above 80 N, confirming the conclusions drawn from progressive load unidirectional sliding CoF vs load graph observed in Figure 3-4. It also proves this chemical composition of the coating can successfully provide self-lubricating properties of MoS_2 while over exceeding its wear resistance.

3.3.1.5 Progressive load unidirectional sliding tests with Al ball

To support the milling tests a series of progressive load unidirectional sliding tests were performed on all samples using Al balls. This test aimed to simulate to some extent the contact between the tool edge and Al in the range of loads (5-100 N) and asses the Al sticking to the tool surface. The trials were performed in room temperature due to equipment limitations and the degree of Al transferred to the insert was determined using an optical microscope. Although this test does not fully reflect conditions during dry machining of Al, as the temperatures between 200°C and 300°C can be expected [20] on the tool-chip interface it still provides useful information about the material transfer for different loads. Higher temperatures would increase Al plasticity; thus the transfer layer can be expected to increase, and this is tested during machining trials in section 3.3.2.1.

The slightly lighter areas in Figure 3-6 correspond to a transfer layer of Al within the wear track. Comparing to other samples a large amount of Al transferred to the insert can be found on the sample a for lower loads (<50 N). This can be attributed to a high content of soft MoS_2 in this coating, therefore, the coating debris accumulating in front of the ball becomes entrapped and serves as a self-lubricating layer at higher loads. There was little Al transferred observed for sample b over the entire range of loads, and the Al transferred from the ball is present in the form of small discontinuous 'clumps'. These observations suggest

that the composition of sample b is optimum to prevent Al sticking during Al-alloy machining, although higher temperatures generated during machining can promote more intense Al sticking. Compare and contrast this with samples d and e containing a high amount of Ti, where a large amount of Al can be found for both compositions, proving poor protection against Al sticking of Ti even in room temperature.
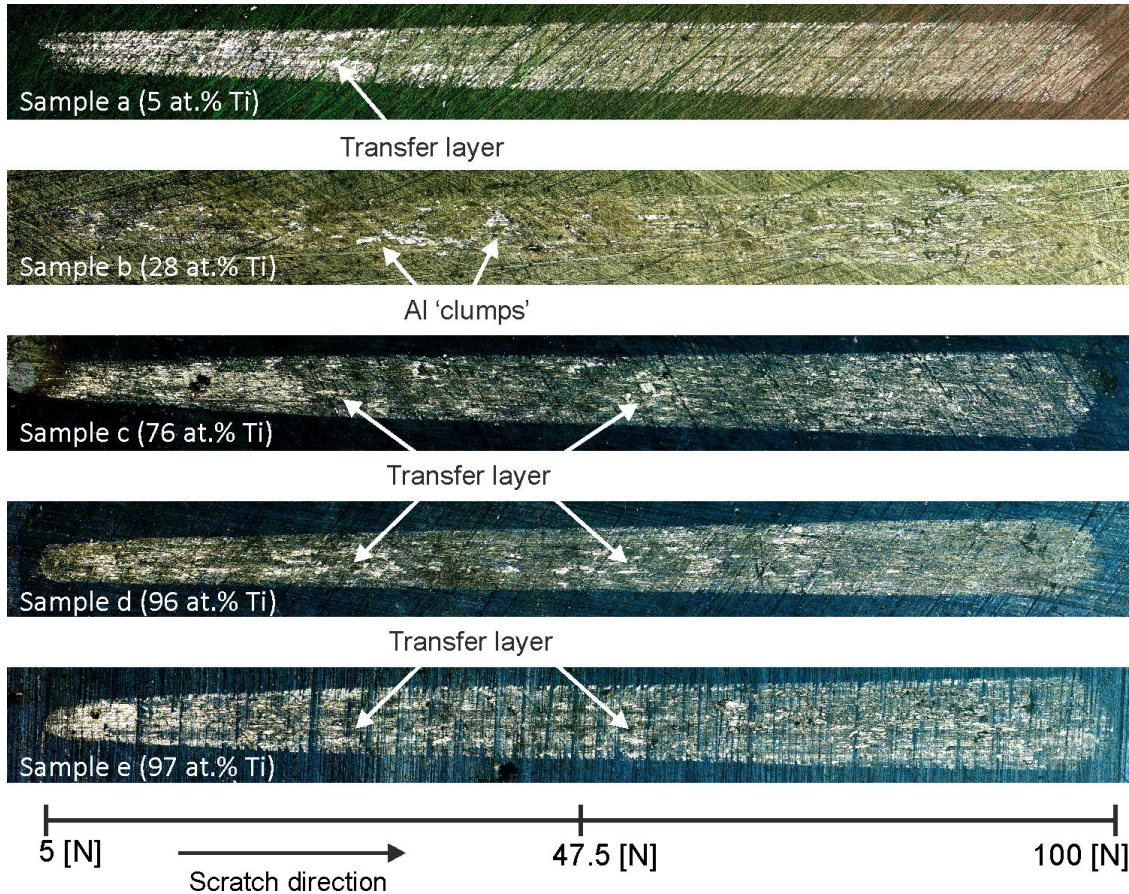
Figure 3-6 Optical microscope images of scratches after the progressive load unidirectional sliding tests with an Al ball, for progressive increasing load 5 N - 100 N.

3.3.2 Machining results

Cutting tests were performed under the conditions specified in Table 1. The available number of SAE 6061 Al alloy test blocks was limited thus the total length of the cut was initially set to 1.8 m. Due to the low cutting length, this test could asses the wear only in the first stage (running-in stage) of machining process (Figure 2-2). The tools showed no visible flank wear after cutting 1.8 m of Al alloy.

After that test was continued up to the length of cut of 3.6 m and still no visible flank wear of the tool was observed during optical microscope studies.

3.3.2.1 EDX element mapping

EDX mapping was conducted to ascertain an optimum Ti-MoS$_2$ ratio which prevented Al sticking to the rake face after dry-machining an Al alloy. The bright areas in Figure 6 correspond to Al adhesion sticking to the tool rake face. No signs of Al are observed on sample b (28 at%). Sample a, having 5 at% Ti and sample c 76 at% Ti, has no aluminium adhering to the tool edge, yet, a thin layer of aluminium can be observed on the rake face. It suggests that the composition of sample b is optimum to prevent Al sticking to the tool rake face as it keeps the best balance between low CoF of the MoS$_2$ and oxidation protection provided by Ti which could act as barriers for oxygen diffusion [26]. As there is no material adhered to the sample b the surface finish of the machined part, as well as tool lifetime, would be improved compared with other samples where BUE is present [59,60]. The worst performance was indicated by sample d and e both having almost the same composition – around 96 at% Ti. Bulk Ti does not have lubricating properties, therefore, coatings on sample d, and e could not provide any sufficient protection against aluminium sticking [174].

Similar results were obtained after the length of cut of 3600 mm (double length of cut). This indicates a good tool life of the coated tool. The only difference observed between different coatings was the intensity of rake wear due to build-up edge formation.
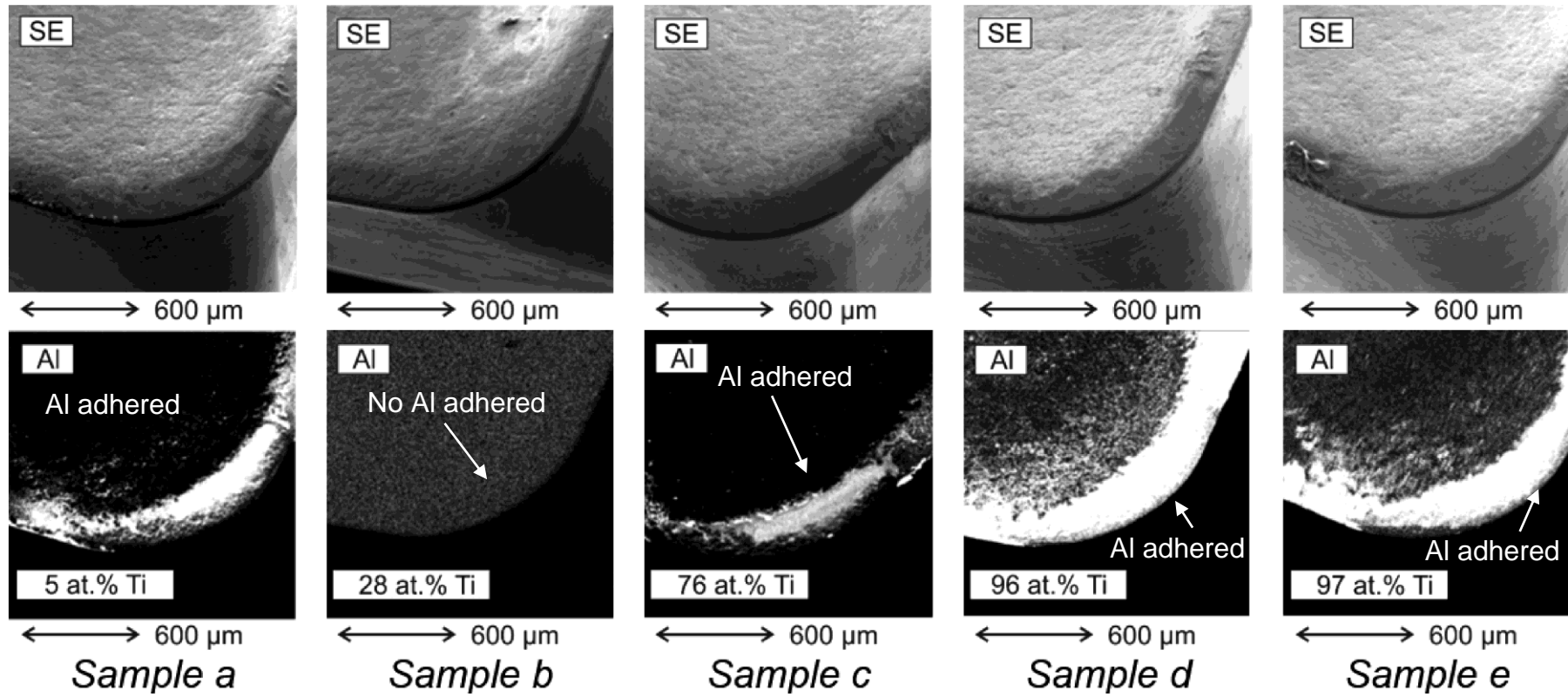
Figure 3-7 Aluminium element mapping images of flank face of mill inserts with Ti-MoS$_2$ coating after turning of 1.8 m. Element mapping obtained with EDX mode of SEM

3.3.2.2 XPS analysis

Samples b and c were chosen for XPS analysis as having almost opposite chemical composition, to investigate chemical bonding of tribofilms and how it impacts on the degree of sticking of the workpiece material to the rake surface. An analysis of the phases formed during the running-in stage can be used to determine the differences in performances (protection against aluminium sticking) of the sample b and c. The B 1S, Ti 2P and Mo 3d peaks associated with B, Ti and Mo were fitted using a Gaussian-Lorentzian function as shown in Figure 3-8. To allow a direct comparison between the results, the percentage of atomic concentrations have been calculated by representing the ratio of the intensity to the total intensity of the electrons of the measurement.

Figure 3-8 (e) and (f) shows that the amount of MoO_2 is greater in sample c compared with sample b. $Mo-O_2$ is highly undesired as it decreases lubricating properties due to volume mismatch between MoO_3 and MoS_2, which leads to the disintegration of MoS_2 blisters [182].

However, in Figure 3-8 (a) and (b) higher amounts (8.2 %) of B_2O_3 can be observed in sample b. B_2O_3 is known as a solid-lubricant, having a similar lamellar structure to the graphite and MoS_2 [194,195], which is the reason why it is believed this particular composition offered the best performance in terms of preventing Al sticking to the rake face. Ti_2O_3 has doublet binding energy at 457.2 and 462.2 in sample b. As can be seen in Figure 3-8 (c) and (d), sample c has a greater degree of TiO bonding compared to sample b and therefore, forms a greater TiO tribo-oxide layer which is believed to be the main reason of poorer wear resistance in Ti-based alloys. It is considered that this tribo-oxide is not adherent to the substrate, is also brittle and tends to be fragmented therefore does not have any protective role during machining [196,197]. Although at temperatures above 600°C tribo-oxides can play a protective role [196], machining in this study was performed at temperatures below 300°C. Therefore it is most probably the formation of greater amounts of Ti-O tribo-phase in sample c and significantly lower amount of lubricating B_2O_3 (4.7 % while 8.2 % for sample b causes a poor wear performance (more intensive sticking of Al on the rake face) than found in sample b.
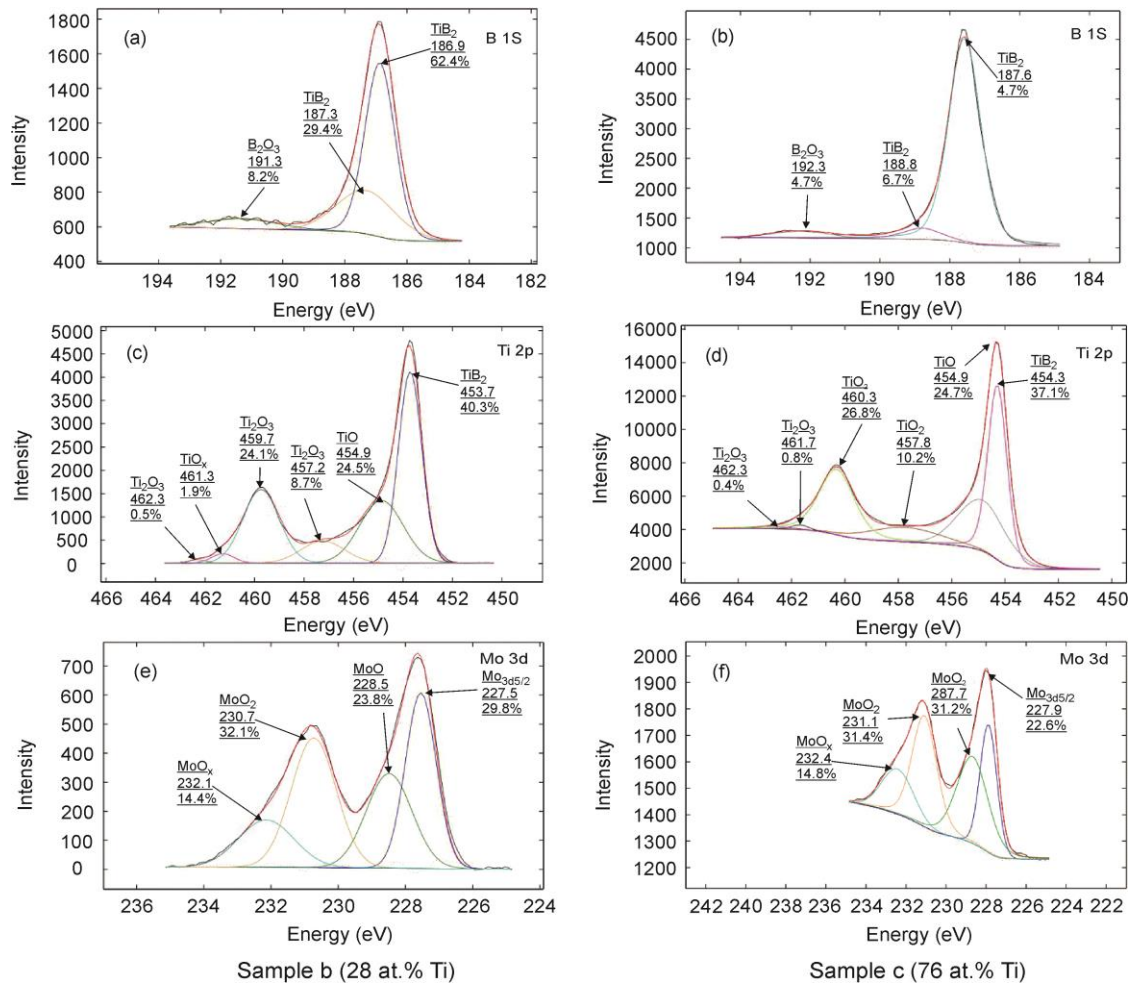
Figure 3-8 Sample b (left) and sample c (right) photoelectron spectra of B 1s, Ti 2p and Mo 3d on rake face after total 1800 mm of milling.

3.4 Conclusions

A hybrid filtered vacuum cathodic arc - magnetron sputtering system was successfully used to deposit composite Ti-MoS$_2$ on five TiB$_2$-coated milling inserts with Ti contents ranging from 5 to 97 at% which varied according to the distance from both Ti and MoS$_2$ sources. Tool inserts placed close to Ti source produced at% Ti higher to those placed close to MoS$_2$ that had a mixture of Ti and MoS$_2$ contents. Ion current measurements revealed that FCVA dominated the deposition rate through the plasma expansion towards the chamber walls. Interactions between neutrals from MS and ions from FCVA led to the lowest ion current being measured on the sample placed equidistant from both Ti and MoS$_2$ sources. There is a correlation between the measured changes in the ion current during deposition and variations in thickness, which increased with increasing titanium content. The roughness increased with increasing proximity to

FCVA source due in part to the influence of unfiltered macroparticles during deposition, correlating with large variations ion currents measured on samples placed the closest to the Ti source. Combinatorial deposition of Ti with MoS_2 led to reduced frictional properties of inserts with Ti:MoS_2 ratios between 0.05 and 3. Progressive load unidirectional sliding tests, EDX mapping and aluminium alloy face milling machining tests indicated that a coating with around 28 at% of Ti had the lowest friction coefficient 0.07 for loads between 40 and 100 N. This particular composition successfully prevented aluminium sticking to the rake of the tool after cutting length of 3.6 m. This result was confirmed after the ball on flat frictional test with aluminium ball for the 20N load as only a little Al was found to be adherent to the scratch. XPS studies revealed greater sticking of Al on the rake face with different Ti:MoS_2 ratios, and is likely caused by the formation of slightly higher amounts of non-protective Ti-O phase significantly lower amount of lubricating B_2O_3. Overall, this study demonstrates the potential of combinatorial deposition for rapid development of hard lubricant coatings.

4 DLC and DLC-WS$_2$ Coatings for Machining of Aluminium Alloys

Tomasz L. Brzezinka, Jeff Ra, Jose M.Paiva, Joern Kohlscheen4, German S. Fox Rabinovich, Stephen C. Veldhuis, Jose L. Endrino.
Available at: https://www.mdpi.com/2079-6412/9/3/192/pdf

4.1 Abstract

Machine-tool life is one limiting factor affecting productivity. The requirement for wear-resistant materials for cutting tools to increase their longevity is therefore critical. TiB$_2$ coated cutting tools have been successfully employed for machining of AlSi alloys widely used in the automotive industry. This paper presents a methodological approach to improving the self-lubricating properties within the cutting zone of a tungsten carbide milling insert precoated with TiB$_2$, thereby increasing the operational life of the tool. A unique hybrid Physical Vapor Deposition system was used in this study, allowing DLC to be deposited by FCVA while PVD magnetron sputtering was employed to deposit WS$_2$. A series of ~100-nm monolayer DLC coatings were prepared at a negative bias voltage ranging between −50 and −200 V, along with multilayered DLC-WS$_2$ coatings (total thickness ~500 nm) with varying number of layers (two to 24 in total). The wear rate of the coated milling inserts was investigated by measuring the flank wear during face milling of an Al-10Si. It was ascertained that employing monolayer DLC coating increased the tool steady-state by ~60% compared to a TiB$_2$ benchmark. Combining DLC with WS$_2$ as a multilayered coating further improved tool life. The best tribological properties were found for a two-layer DLC-WS$_2$ coating which decreased wear rate by ~75% compared to TiB$_2$, with a measured coefficient of friction of 0.05.

Keywords: self-lubricating coatings; tungsten disulphide; DLC; SEM; EDS; XPS; milling; aluminium

4.2 Introduction

Cutting, also called machining, is one of the oldest methods of metalworking, comprising three main processes: surface plastic deformation, fracture and chip removal [13]. Tool wear is obviously associated with any cutting process, though it is a complicated phenomenon; when a chip leaves the cutting zone, it carries with it a small number of particles from the worn tool. This causes a progressive change in the tool's cutting edge profile over time, finally reducing the efficiency of the tool [13]. Moreover, machining of lightweight alloys, such as aluminium with its high degree of plasticity, leads to what we term a built-up edge (discussed in depth in 2.2). In case of carbide tools, BUE significantly increases wear due to adhesive interactions between grains in the structure of the tool and the workpiece, which form microcracks in the tool. These cracks are generated at the interface of the WC phases because of the cyclical stress action at the points of adhesion with the workpiece. This leads to the separation of carbide grains from the tool surface [13].

AlSi machining, in particular, requires addressing both high abrasions of the silicon particles and BUE formation, thus, most milling inserts for AlSi machining are coated with TiB_2 (specific properties of TiB_2 discussed in 2.5.1) [12]. However, TiB_2 brittleness sometimes makes it prone to extensive surface damage during the running-in stage of wear [184]. Often a large fraction of the hard coating can be worn away at this phase prior to the start of the stable wear stage which results from the geometrical adaptation of the cutting edge and overall self-organisation of the tribosystem in the running-in stage [13]. Self-organisation during friction can be associated with the formation of surface tribo-films (secondary structures) such as protective or lubricating oxides [65]. From the thermodynamic perspective during self-organisation, the two bodies (tool and the surface of machined material) which initially were under different conditions achieve equilibrium thus energy and matter flows stops, as well as the thermodynamic forces of the system, become equal [13]. The tribo-films can store up to 90% of the total friction energy hence serve as a stable zone of a dominating dissipation of energy. Once the stable stage is achieved the tool wear rate can decrease by an order of magnitude. Because the extensive wear of the coating can limit tool longevity, a low-friction layer can be deposited on top of the hard coating to protect its surface [180].

Protecting the surface of the hard coating is one of the most important goals of wear-resistant coatings, especially at low and moderate cutting speeds [198] and during the cutting of hard-to-machine materials when adhesive and attrition wear modes dominate [13]. Combining the top layer into the multilayer structure can further increase the tool lifetime [25].

Diamond-like carbon (DLC) is made up of a range of amorphous bonds which, depending on the method used for its production, can consist of different types of carbon-based materials, either hydrogen-free (ta-C) or containing up to 50% hydrogen (a-C: H) [158]. A combination of properties, such as a high hardness of up to 80 GPa, high chemical stability, a low coefficient of friction (0.1), high wear resistance and good anti-adherent properties, make DLC coatings excellent for aluminium machining [167]. Build-up reduction helps to maintain the sharpness of the tool's cutting edge, limit cutting resistance and improve the machinability of aluminium-based alloys with Mg and Si additions [167]. The good mechanical properties of DLC arise from its high proportion of sp^3 bonds, similar to the ones present in the structure of diamond, and strongly depend on the energy of the ions produced during the coating deposition and on the deposition method [162]. FCVA is one of the PVD methods for producing a plasma containing a large fraction of highly charged ions [87]. As the energy of the ions can be easily varied by applying a negative bias to the substrate, the ideal ion energy (100 eV) for high sp^3 content can be achieved [199]. Limitations of DLC and methods to overcome them are discussed in section 2.5.2.

The common solid lubricant used as a low friction coating is tungsten disulphide (WS_2), which has a lamellar structure [200]. The lamellas are held by weak van der Waals bonds, allowing them to slip easily one over one another and resulting in a very low coefficient of friction [45,201]. When operating in a wet environment or conditions, however, their lifetime decreases due to oxidation of the lamellas' edges, which hinders their sliding leading and increases the CoF [22]. Some research studies show that incorporating metallic elements such as Cr and Ti into the WS_2 structure can densify the coating, thus preventing oxide and moisture penetration and increasing the lifetime of the coating [22]. Non-metallic elements such as C can also significantly increase the wear resistance due to the presence of W-C phase [202]. DLC and WS_x were successfully combined before into the multilayer structure to improve the

hardness and wear in the wet environments such as the work presented by Fag-er Yang *et al.* [179], where various layer thicknesses rations of DLC to WS_x were deposited by RF magnetron sputtering and evaluated under various test environments. However, the attempt to use the hybrid deposition system combing FCVA with MS to deposit them was not made before.

In this work, DLC thin film was deposited on a cemented tungsten carbide substrate (precoated with 2 µm TiB_2 coating), by FCVA discharge using a graphite cathode. The objective was to assess the combination of thin DLC films and TiB_2 for tools for cutting AlSi alloys that traditionally require the use of cutting fluids in the machining industry. DLC was then combined in a multilayered structure with WS_2 to study tool lifetime during AlSi machining.

4.3 Materials and Methods

4.3.1 Deposition parameters

Kennametal EDCT milling inserts (KC410M grade) and Widia SNUN120408 turning inserts were used as the substrate material. The tools supplied by Kennametal to be used as substrates were as-received with 2 µm of TiB_2 deposited by DC magnetron sputtering using TiB_2 ceramic tiles on a copper backplate.

The coatings were fabricated in a hybrid FCVA and magnetron sputtering PVD system described elsewhere [203]. The schematic of the specific system is shown in Figure 4-1. It comprises a cathodic arc source equipped with a cone-shaped cathode allowing up to 70 A arc current, a linear filter with adjustable magnetic coil (up to 10 A current), a magnetron sputtering source (ENI RPG-50) and a rotating substrate holder which can be biased (up to 650 V), which can alternate between two PVD sources. Before deposition, the inserts were ultrasonically cleaned in an acetone bath for 15 minutes and then rinsed in isopropyl alcohol. A rotating substrate holder was employed to ensure the uniformity of the deposited coatings. Prior to each coating deposition, the system base pressure was below 3 x 10^{-6} Torr.
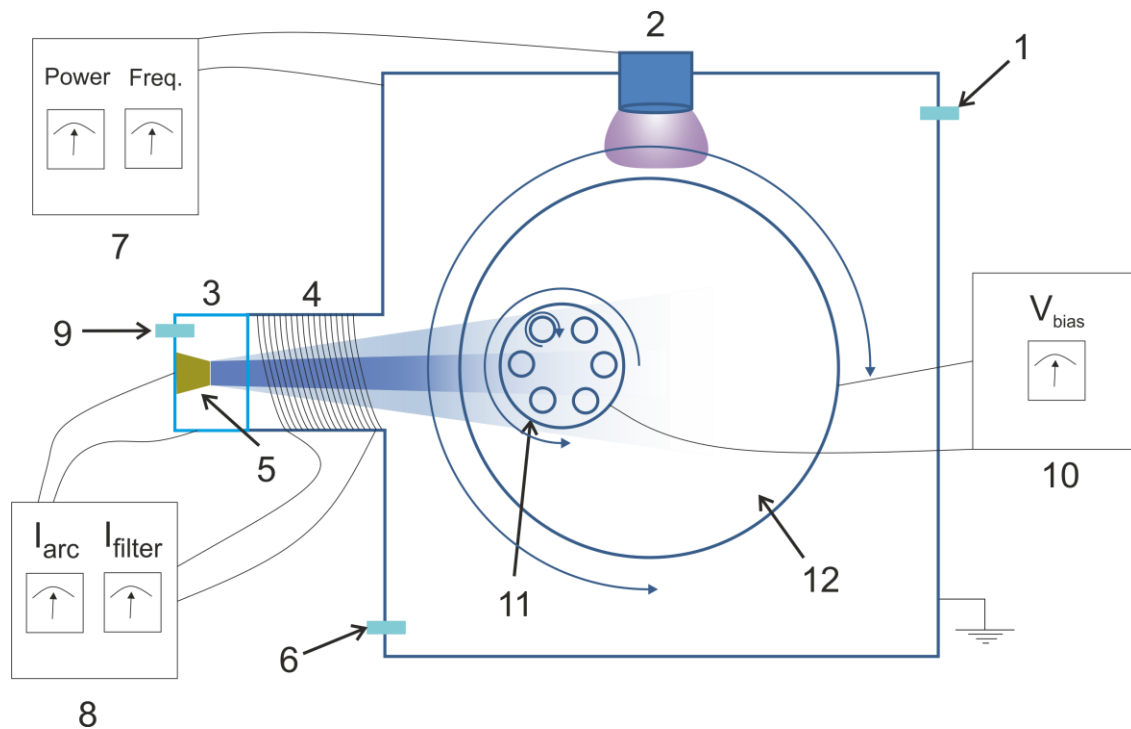
Figure 4-1 Schematic view of the deposition system (1-vacuum cryopump inlet, 2 – 3" WS$_2$ sputtering target, 3 – anode, 4 – linear filter, 5 – graphite cathode, 6 – sputtering argon inlet, 7 – PVD sputtering power unit, 8 – cathodic arc power unit, 9 – cathodic arc argon inlet, 10 – substrate bias power unit, 11 – rotating substrate holder, 12 – substrate table).

4.3.1.1 Monolayer DLC coatings

FCVA was used to deposit DLC films from a cone-shaped graphite cathode supplied by Plasmatechnology (67 mm x 50 mm and 50 mm height). The argon pressure during the deposition was 4.5 x 10^{-3} Torr. A linear filter was used at the exit on the cathodic arc anode. To minimise the macroparticle content in the resulting thin films, the filter magnetic coil current was set to maximum 10 A. Based on previous studies, arc currents during deposition were at 40 A to prevent cathode fracture.

Five sets of coatings were deposited with the substrate bias varied to confirm it has an influence on the DLC coating wear resistance [33]. To avoid substrate overheating (above 200 ºC) that would decrease sp^3 content [165], the maximum deposition times (until the substrate reached 200 ºC) were limited based on previous studies.

4.3.1.2 Multilayer DLC-WS$_2$ coatings

A hybrid FCVA - MS system enabled DLC-WS$_2$ multilayer deposition. Each source was switched on sequentially for specific layer deposition. A rotating table allowed the substrate holder to move between the two sources. To investigate the influence of the number of DLC-WS$_2$ layers on the cutting tool performance during machining trials, the target total thickness of the coatings was fixed at 500 nm. Deposition parameters (pressure, arc and filtering currents) for DLC layers were kept the same as for the monolayers with the substrate bias set to -100 V. WS$_2$ was deposited from a 3-inch diameter target using pulsed DC magnetron sputtering with 80 W power and 100 kHz frequency to avoid arcing. Five sets of samples were deposited – monolayer WS$_2$ and 2, 6, 12 and 24 layers of DLC-WS$_2$ in total. Depending on the number of layers, the deposition time of certain layers was varied, though total time was the same – 36 minutes – and volume fraction was always 50% DLC to 50% WS$_2$.

4.3.2 Aluminium milling performance and characterisation tests

The tool cutting lifetime was studied by conducting face-milling experiments of the test blocks, carried out in an Okuma Cadet Mate CNC vertical machining centre. The DLC- and DLC-WS$_2$-coated mill inserts were used to cut an AlSi alloy material. The performance of these coatings was benchmarked to a commercial TiB$_2$-coated insert. The full cutting conditions are presented in Table 4-1. To observe the tool wear changes, between passes, the inserts were removed from the machine and its' dimensions and edges were measured using an optical toolmaker microscope (Mitutoyo model TM) and then the cutting process was continued. This procedure allowed plotting the graph of tool wear vs machining length. As the milling holder used two tools for machining and both of them were assessed. It has to be noted that this procedure does reflect the machining process only to some extent as the measurements require to stop the machining process thus the tool goes through many heating up/cooling cycles. In industrial machining, the cooling down/heating-up cycles take place as well when the parts are being changed but their number overall is lower. However, this is standard research and industrial practice employed to assess the tool life performance [1,152,204].

Tescan dual-beam focused ion beam (FIB) scanning electron microscopy (SEM) was employed to study the cross-section of the coatings as well as worn inserts and chips collected during the machining. The amount of machined material (Al) adherent to the tool was evaluated using the energy-dispersive X-ray spectroscopy (EDX) mode of SEM (20 kV). Alicona microscope 3D images were employed to determine the wear of the inserts, calculate roughness of the chips, and precisely measure the tool edge geometry to compare with an unworn insert.

Table 4-1 Cutting conditions used for DLC and DLC-WS$_2$ coated tools evaluation.

Machine tool	CNC Vertical Machining Centre
Number of cutting edges	2
Feed rate [mm/min]	1880
Feed per tooth f$_t$ [mm/tooth]	0.05
Cutter diameter [mm]	25.4
Tool speed RPM [rev/min]	6265
Axial Depth of cut a$_p$ [mm]	10
Radial Depth of cut [mm]	1
Cutting speed V$_c$ [m/min]	500
Coolant rate flow [l/min]	44
Coolant concentration [%]	6
Workpiece material	Al-10Si

The CoF was measured using a Teer ST-3001 Tribo Tester during dry reciprocating sliding test with a fixed WC 5-mm-diameter ball, applying a constant 5 N load on a 10 mm distance for 100 cycles. An additional test with ramped load allowed for analysing the response of the multilayer coating under a variety of loads; an increasing progressive load was applied from 5 to 100 N, at a loading rate of 50 N/min and a linear velocity equal to 5 mm/min. The test outcomes include both CoF and wear characteristics – that is, adhesion and coating cracking. A series of images for each scratch trace were collected using an Olympus Lux optical microscope with 20x

magnification. The images were later stitched using Microsoft Image Composite Editor. A Dektak stylus profilometer measured the profile of the scratches from Tribo Tester dry reciprocating sliding test of the coatings.

4.4 Results and discussion

4.4.1 Coating structure and composition

The cross-sectional images of the coatings prepared using FIB are presented in Figure 4-2, and the summary of the main properties of the coatings are presented in and Table 4-3. The deposited DLC coatings are not uniform – the thickness across the sample varies. As the filter used during the deposition was linear, it allowed some of the macroparticles to reach the substrate [54]. Thus they are found as a local increase in the thickness of the coating what influences the average film thickness measured for each of the biases. For the coatings deposited from -50 V to 125 V the thickness is in the range 70-100 nm. The coating deposited with -200 V has a significantly lower thickness equal to 45 nm, which results from shorter deposition time rather than from the bias voltage itself. The WS_2 monolayer, by contrast, is seen to have a uniform thickness and a columnar microstructure similar to that observed by other researchers [179,202]. The images of DLC-WS_2 coatings do not allow us to clearly distinguish separate layers, although the DLC macroparticles can be noticed. The combination of energetic deposition by FCVA and magnetron sputtering resulted in the DLC layers being doped into the structure rather than combined into the multilayer. This can have a positive effect on the hardness of the coatings, as F. Yang, Y. Lu *et al.* [179] suggested that destroying the columnar morphology of WS_2 can improve the adhesion and hardness, leading to better wear resistance. Nevertheless, while the total deposition time was the same for all of the DLC-WS_2 coatings, the total thickness varies and it is the lowest for the highest number of layers. The most probable reason is re-sputtering of WS_2 caused by bombardment of energetic particles – mostly highly charged ions depositing DLC coating [202].
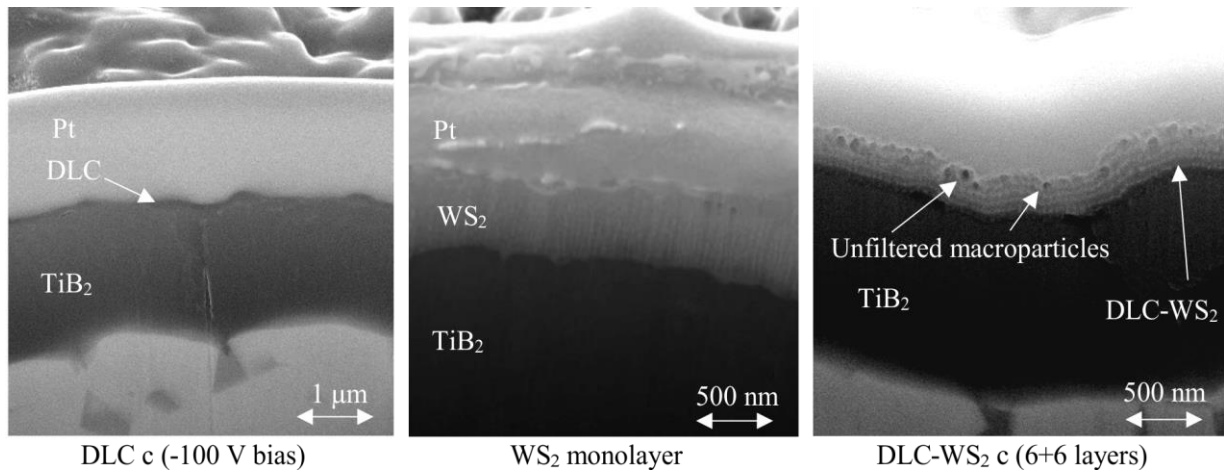
Figure 4-2 SEM images of coatings cross-sections prepared using FIB.

Table 4-2 Monolayer diamond-like carbon (DLC) deposition times, bias and thickness.

Sample ID	Dep time [min]	Substrate bias [V]	CoF after 100 cycles	Coating thickness [nm]	Roughness Ra [nm]
DLC a		-50	0.22	70 ± 20	230
DLC b		-75	0.21	80 ± 20	400
DLC c	11	-100	0.22	100 ± 18	410
DLC d		-125	0.22	80 ± 21	230
DLC e	5	-200	0.37	45 ± 8	380
TiB$_2$ benchmark	-	-	0.4	2000 ± 100	230

4.4.2 Coating hardness

The results of the coating hardness measurement obtained using nanoindentation (average of 10 indents) are presented in Table 4-3. The hardness of around 2.4 GPa found for the WS$_2$ monolayer is slightly higher than the one measured by other researchers [179], yet, those measurements were done on Si and for 3 µm thick coating. The coating deposited in this work is just 0.5 µm thus the substrate could have affected the hardness results. With the addition of DLC layers, the hardness increases to 6.6 GPa for DLC-WS$_2$ d, which suggests the positive effect of the interface strengthening [179].

Table 4-3 Deposition times and properties of DLC-WS 2 multilayers.

Sample name	DLC		WS$_2$		CoF after 100 cycles	Total coating thickness [nm]	Roughness Ra [nm]	Hardness [GPa]
	Number of layers	Deposition time of each layer [min]	Number of layers	Deposition time of each layer [min]				
WS$_2$	-	-	1	36	0.32	450 ± 50	239.33	2.4 ± 1.1
DLC - WS$_2$ a	1	12	1	24	0.18	320 ± 40	123.00	2.7 ± 0.5
DLC - WS$_2$ b	3	4	3	8	0.19	310 ± 40	237.00	4.3 ± 1.2
DLC - WS$_2$ c	6	2	6	4	0.50	290 ± 24	159.00	5.1 ± 1.1
DLC - WS$_2$ d	12	1	12	2	0.49	250 ± 28	214.33	6.6 ± 1.9

4.4.3 Coefficient of friction evaluation

4.4.3.1 DLC monolayers

Figure 4-3 shows the dry reciprocating sliding test results for five DLC-coated samples together with measurements for TiB_2 as a function of a number of cycles. It is important to note that the roughness of the films exceeded the DLC coating thickness (~100 nm). The origin of such a roughness comes mostly from TiB_2 coated substrate, which already prior to deposition had R_a=230 nm. Also, the macroparticles created during DLC deposition increased it further for some of the coatings, e.g. for DLC c was almost doubled (R_a=500 nm). The surface roughness can have a significant influence on the friction coefficient, as reported by other researchers [204–210]. If two rough surfaces are in contact, the interlocking of "asperities" summits representing the surface roughness occurs, what can significantly increase the CoF measured at the beginning of the sliding process [210]. In the case of the sliding test smooth WC ball serves as a counter-face, thus the interlocking is not significant; however, the exact area of contact is limited to the asperities [209]. For the first cycles, the ball surface is in contact just with the peaks of the asperities, and "the friction properties depend on the distribution of asperities, their height, and their deformation during the process. With the flattening of asperities, the contact with the tool gets larger, and this leads to varying friction properties" [211]. As reported by J. Takadoum *et al.* [209] typically, CoF increases gradually for a certain sliding distance (or a number of cycles), after it can be expected for the CoF to remain constant as a steady-state is achieved.

CoF equal to 0.25 was measured for TiB_2 for the first 16 cycles and then progressively increased to 0.4. Similar behaviour has been observed by other researchers [143,212] during short-length (100 μm) wear tests. They found that the running-in period lasted for around 3000 cycles until a steady-state value of approximately 0.8 was achieved. Therefore, based on previous research studies, we assume that the slow adaptation of TiB_2 will extend the running-in stage of the coated tool during cutting.

DLC coatings are known for their low CoFs, which are below 0.1 for ta-C [33] and also usually form a transfer layer consisting of wear debris with low shear strength [167,213]. A transfer layer is typically composed of disordered carbon wear debris from the DLC coating, as well as wear debris from the counterface and from any reactive

environmental species [166]. In case of the cyclic sliding on rougher surfaces, this transfer layer leads to filling in the valleys between the roughness peaks [209]. Therefore, this layer typically governs the friction in DLC coatings. As the thickness of DLC e was found to be below 50 nm, it may not have been enough to form such a transfer layer and affect CoF. As a result, the measured values are close to those of the TiB_2 underneath. It can be noticed that for the other DLC coatings, the steady-state CoF is similar and equal to 0.2. However, the adaptation of DLC d is quicker and occurs before the end of 20 cycles. The friction of DLC coatings can be considered as the sum of adhesive, abrasive and shear mechanisms [213]. While adhesive friction is related to the coating microstructure, sliding environment and counter-face, the abrasive contribution to DLC's friction is related closely to the coating roughness [166]. Consequently it can be concluded that due to the combination of various factors such as high roughness which governs the sliding process, low coating thickness and macroparticle presence the measured CoF is higher than the one reported by other researchers for ta-C [33].
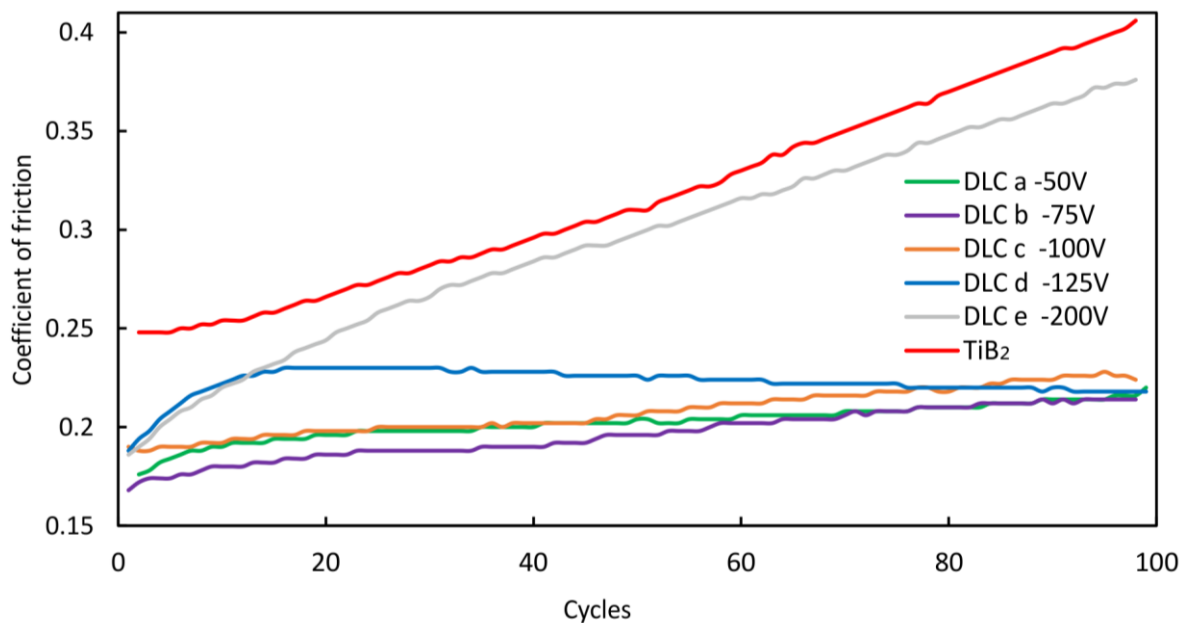
Figure 4-3 Friction coefficient vs a number of cycles for DLC coatings and reference TiB_2 coated samples. Test conducted by a dry reciprocating sliding test using a fixed WC ball with 5 mm diameter sliding against a coated sample. Constant load 5 N applied for 10 mm distance.

4.4.3.2 DLC-WS$_2$ multilayers

DLC-WS$_2$ coatings deposited with different numbers of layers were tested during the dry reciprocating sliding test with a WC ball under a constant 5 N over 100 cycles. The evolution of friction against a number of cycles is presented in Figure 4-4. The progress of the CoF curve indicates that, due to the low hardness of WS$_2$, it failed under the 5 N load. For the first 20 cycles, the friction actually decreased, as the coating that was constantly removed piled up in front of the indenter, filling up to valleys between the roughness peaks [209] and forming a low-friction transfer layer [186]. After, between 45 and 50 cycles, the WS$_2$ was completely worn on the roughness peaks. Therefore, the CoF achieved a steady-state equal to the average of the CoF of TiB$_2$ on the smoothened peaks and WS$_2$ which accumulated in the valleys. SEM image of the wear tracks (Figure 4-5) confirms that coating spallation occurred, which can be noticed on the sides of the track. Also, most of the track surface appears to have a darker colour representing the exposed TiB$_2$ coating.
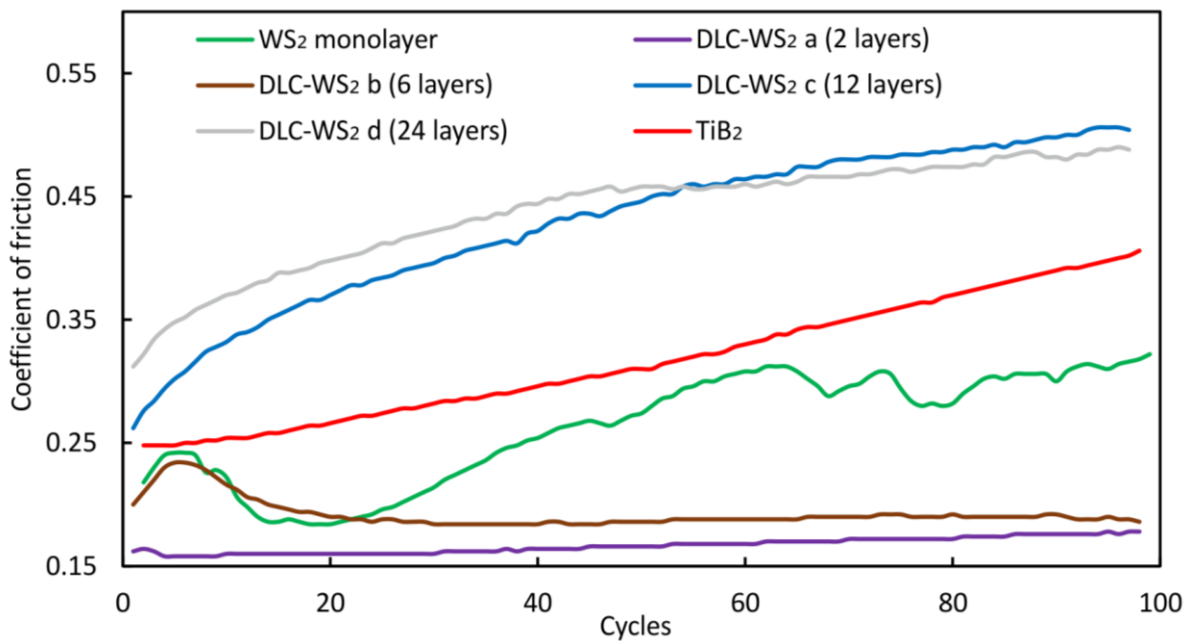
Figure 4-4   Friction coefficient vs a number of cycles for DLC-WS$_2$ coatings and reference TiB$_2$ coated samples. Test conducted by a dry reciprocating sliding test using a fixed WC ball with 5 mm diameter sliding against a coated sample. Constant load 5 N applied for 10 mm distance.

79

The EDX analysis proved almost complete wear of the coating in those locations, as little WS_2 can be recognised. However, there are also some scratches visible, in appearance having a similar colour as a WS_2 coating, which indicates that the debris of WS_2 coating remained in the roughness valleys. Also, scratch profiles obtained using profilometer shows almost complete penetration through the WS_2 coating thickness, as the depth of the formed track was of around 480 nm. The introduction of an additional DLC layer on top of WS_2 (sample DLC-WS_2 a) to form a bilayer had a significant impact on the frictional properties of the coating system. The CoF measured was low (0.15) and only very small increase is observed after 100 cycles. Hard DLC serves as a protective layer, while WS_2 provides lubrication. Good tribological performance is confirmed on the SEM image in Figure 4-5; the track width is narrower than for WS_2 monolayer, no coating spallation can be observed and EDX compositional analysis confirms the presence of WS_2 on the track. The rapid adaptation of this coating should significantly improve cutting performance when applied to the tool, which would be evident especially during the running-in stage of the machining. Increasing the number of layers to 6 (DLC-WS_2 b) led to an increase in the time of indenter-coating system adaptation and for the first 20 cycles the CoF curve matches the one of WS_2 indicating also for this coating smoothening of the roughness peaks occurred. However, it continuously decreased to match a CoF of DLC-WS_2 a after 100 cycles. This is opposite to what is observed for WS_2 monolayer confirming the incorporation of DLC layers between WS_2 successfully increases it's wear resistance. However, for DLC-WS_2 coatings having the highest number of layers (12 and 24), a progressive increase of the CoF was recorded up to the value 0.5, indicating the rapid failure of these coatings. Introducing a high number of layers can prevent crack propagation by stopping it on the interfaces between layers; however, it can also increase the intrinsic stress in the coating [214], moving their failure mode from ductile into brittle [186], which could be observed for DLC-WS_2 c and d. The high value of the measured CoF for those two coatings can be attributed again to the influence of the roughness and the poor adhesion of the coating to the sharp roughness peaks [209].

A ramped scratch load test can analyse the response of the coating to a variety of loads, giving information about the friction, wear characteristics and microcracking [12]. Figure 4-6 presents the evolution of CoF between the coating material and WC

ball for a progressive load of 5–100 N applied over a 10 mm distance. The CoF for WS$_2$ monolayer and the DLC-WS$_2$ a bilayer progressively decreased as the load and scratch distance increased. Given the assumption that the friction coefficients are related to the roughness of the summits [210] progressive decrease of CoF can be associated with smoothening the tops of those summits. As the direction of the scratch was constant, the small portions of the worn coating accumulated continuously in front of the ball, forming a low-friction lubricious layer that can be noticed in the optical image of the WS$_2$-coated sample scratch in Figure 7. However, it can be observed that at the end of the scratch some coating detachment occurred leading to base material (TiB$_2$ coating) exposure. The moment when TiB$_2$ exposure starts is confirmed by increased acoustic emission (AE) in Figure 4-8. Contrary, for DLC-WS$_2$ a bilayer no significant change of AE can be noticed. For the maximum load, the CoF for WS$_2$ monolayer was as low as 0.05, which matches the findings made by other researchers [22,25,179]. The DLC-WS$_2$ bilayer ensured a very low CoF of around 0.07, which together with previous results from a dry reciprocating sliding test and with no evidence of any coating spallation or delamination over the whole 10–100 N range of loads (Figure 4-7), confirms its excellent adhesion and lubricious properties. By contrast, it can be observed that for DLC c, TiB$_2$ and DLC-WS$_2$ d the roughness governs the CoF measurements. It is known that for rough surfaces typically the coating adhesion (defined by the smallest load at which the coating is damaged called the critical load) is lower [209]. Significant variations of CoF occur as a consequence of constant breakage of the roughness peaks [209,215]. The influence of those peak smoothening on the CoF depends on the mode of deformation [216]. It can be considered that in the case of WS$_2$ monolayer and DLC-WS$_2$ a, the mode is rather plastic thus the CoF variations are lower. DLC-WS$_2$ with 24 layers, shows clear signs of coating spallation, which can be recognised by peaks on the CoF graph and exposure of the material underneath visible in the optical image in Figure 4-7 which corresponds to increased AE in Figure 4-8 at around 20 N load. At around 57 N load, the coating is completely worn, the coefficient of friction rapidly increases, and the material underneath is exposed for the whole width of the scratch. In comparison, the DLC b monolayer spalls at around 40 N load.
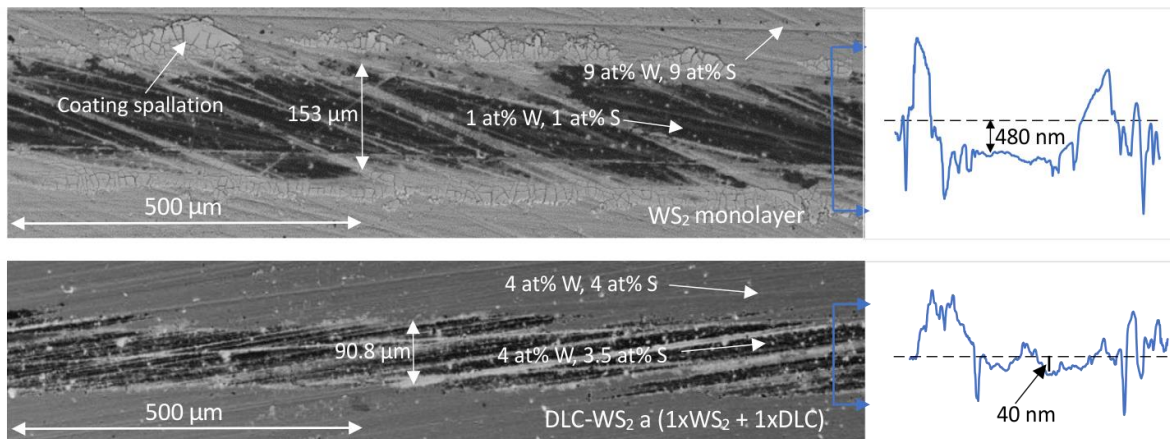
Figure 4-5 SEM image and profile of the scratches after 100 cycles of the dry reciprocating sliding test under constant 5 N load.
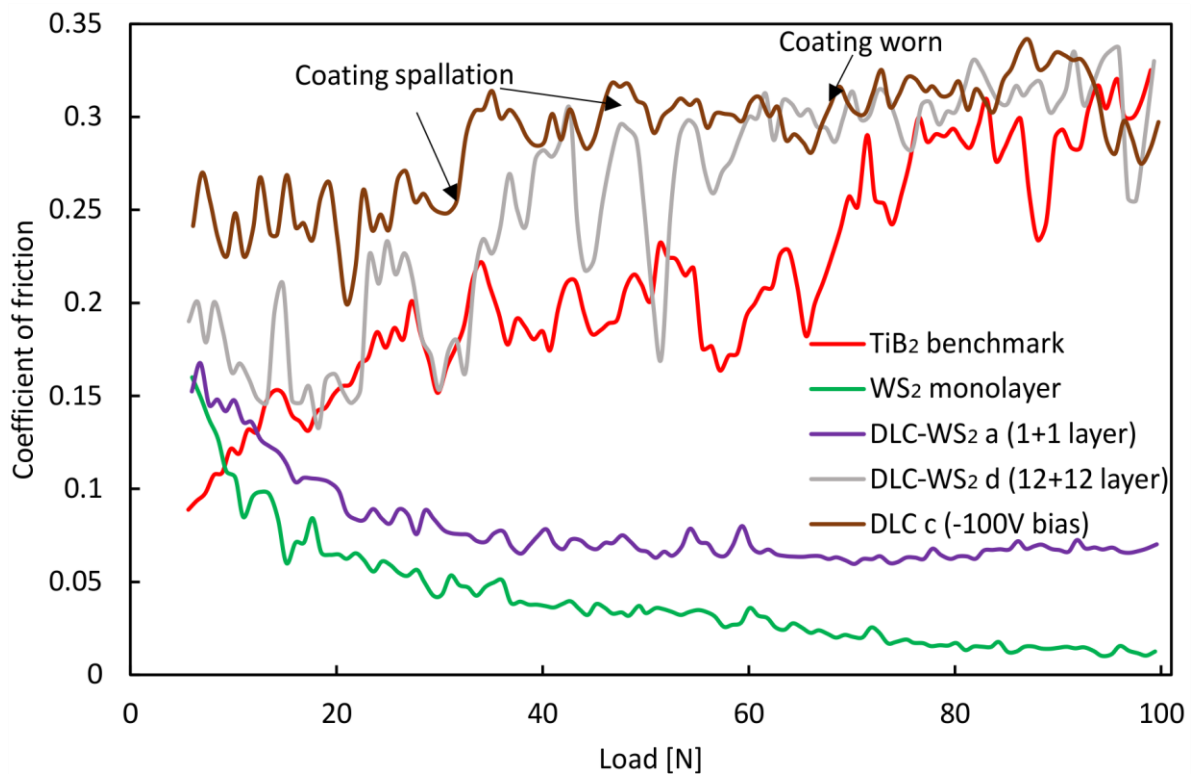
Figure 4-6 Friction coefficient vs load applied for DLC monolayer, DLC-WS$_2$ multilayers, and reference TiB$_2$ and WS$_2$-coated samples. Tests conducted by progressive load unidirectional sliding test using fixed WC ball with 5 mm diameter ball sliding against a coated sample. Progressive load 5 N–100 N applied with 50 N/mm loading rate.

82
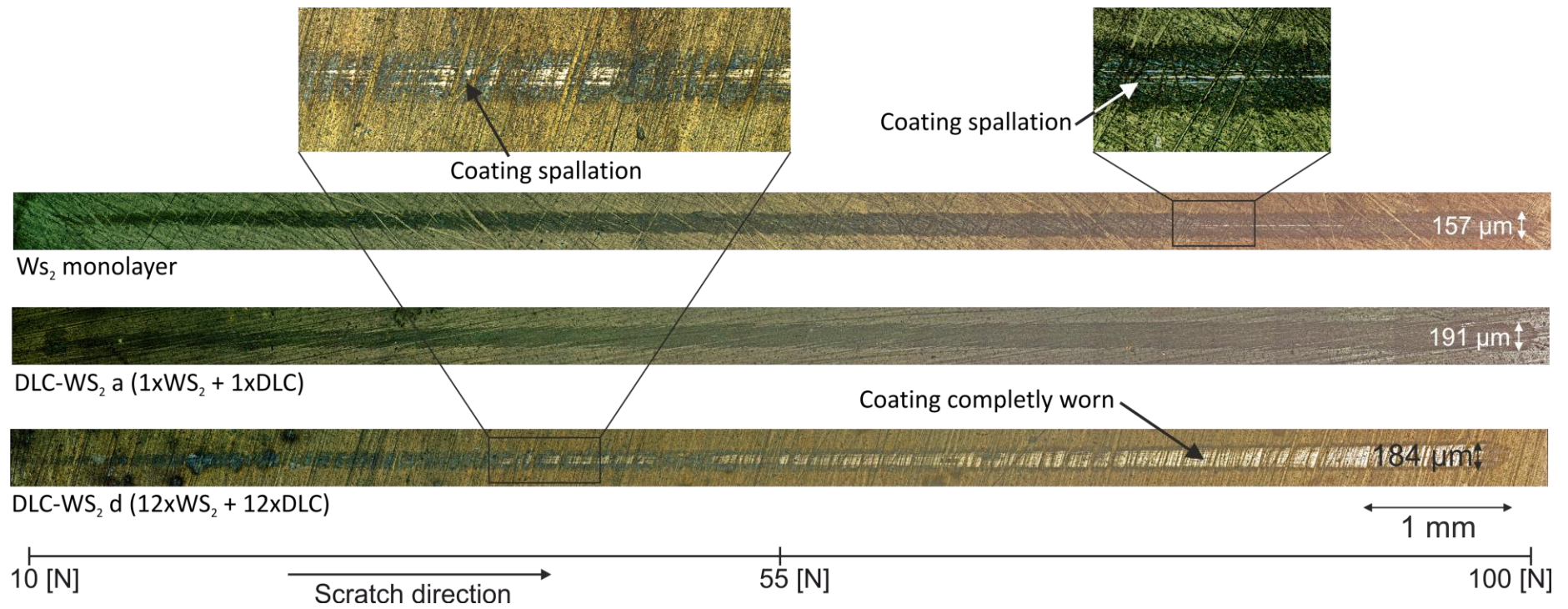
Figure 4-7 Optical microscope images of scratches after the progressive load unidirectional sliding test with WC ball for progressive increasing load 5 N -100 N
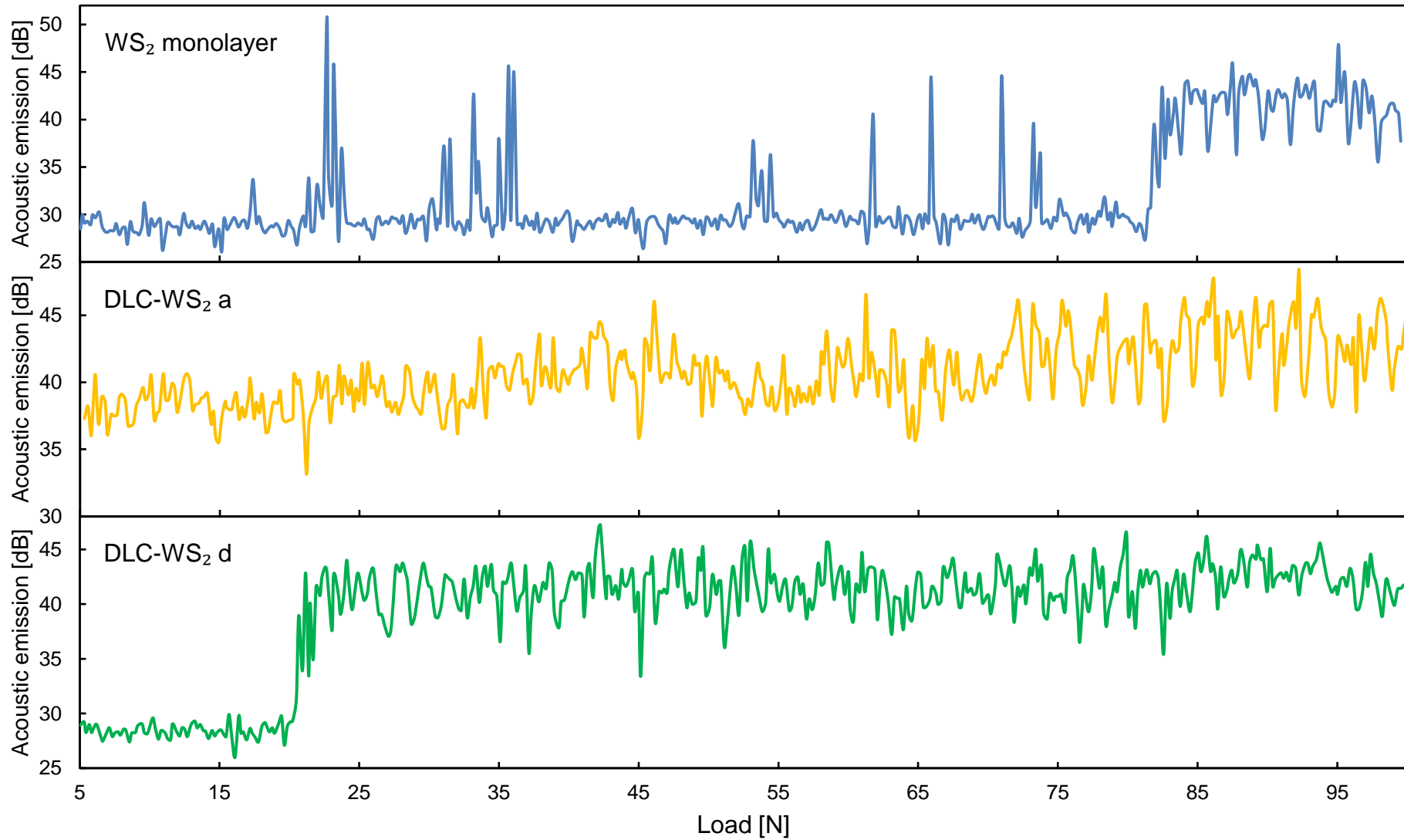
Figure 4-8 Acoustic emission recorded during progressive load unidirectional sliding test with WC ball for progressive increasing load 5 N -100 N.

4.4.4 Machining studies

Typically, the wear process consists of three stages: the running-in stage, the steady-state stage and the surface damage stage. In the initial and final stages, the surface damage of the tool can be observed, while during the steady-state stage, stable wear and friction conditions are typically achieved and, therefore, little or no macroscopic damage of the surface is visible [13]. The main goal of tool tribology is to increase the time during which the tool is in steady-state and thus decrease tool wear and reduce the CoF. These improvements eventually will lead to tool-life enhancement and improved workpiece quality (surface finish and dimensional accuracy) [5,13].

4.4.4.1 DLC monolayer

Figure 4-9 shows the change in flank wear of DLC- and TiB_2-coated tools concerning the cutting length during AlSi milling. TiB_2 presents a typical wear curve with a running-in stage for the first 10 metres, then a stable state up to 24 metres, after which catastrophic failure occurs leading to high tool wear. All of the DLC coatings outperform the benchmark TiB_2 coating. For DLC a, the wear curve follows the TiB_2 curve, with a small decrease in tool wear in the steady-state. Nevertheless, while coatings on samples DLC b, d and e significantly decreased the wear during the running-in stage, only DLC b also limited the machining length needed to achieve steady-state, thereby improving the surface finish of the machined parts [59]. Still, the width of the stable wear is overall shorter than it is for the TiB_2-coated tool. For DLC c, on the contrary, which was deposited with -100 V, the wear in the first stage decreased compared to TiB_2. Moreover, the steady-state stage continues up to 38 metres of machining length, giving 60% improvement compared with TiB_2 and other DLC coatings. This DLC coating is found to ensure the best protection on the microlever during the running-in stage when the geometrical adaptation of the cutting edge happens [13]. This can be attributed to high sp3 content expected for -100 V biased samples according to the work of Konkhunthot *et al.* [162] who based on Ramman and XPS analysis concluded 83% of sp3 bonds in the DLC coatings deposited by FCVA with -100V bias. Sp3 bonds provide both high hardness of the films and low CoF [217]. When the steady-state is achieved, the TiB_2 coating

underneath can protect the tool material, and thereby the tool life is significantly improved.
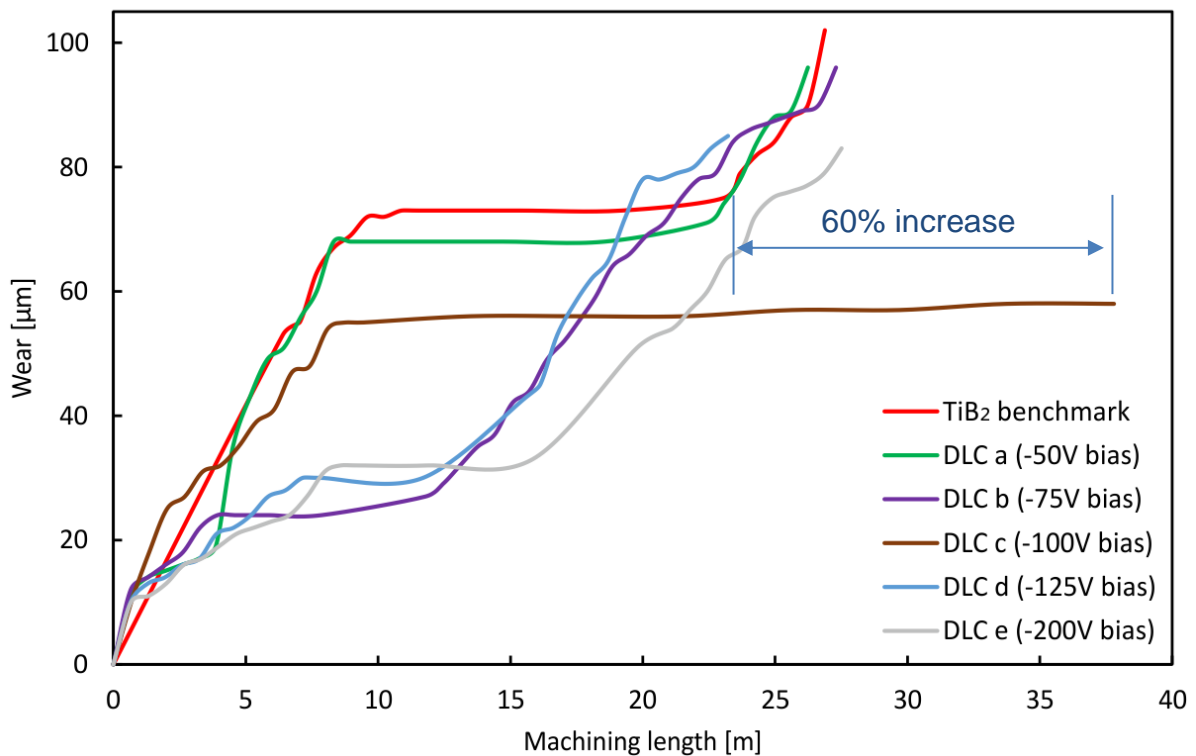
Figure 4-9 Tool wear curves of KC410M milling inserts with DLC coatings (cutting parameters: V_c: 500 m/min, a_p = 10 mm, f_t: 0.05 mm).

4.4.4.2 DLC-WS$_2$ multilayers

The changes in flank wear with respect to the cutting length are presented in Figure 4-11. changes in flank wear concerning the cutting length are presented in Figure 9. The wear curve of the WS$_2$ monolayer confirms the observations made during the dry reciprocating sliding test: for the first 12 metres of machining, the WS$_2$ serves as a source of lubrication, therefore, the tool wear is lower compared to TiB$_2$, and the running-in stage is longer. However, once the WS$_2$ coating wears out, the tool wear increases and typical steady state with little wear cannot be observed. Instead, a flat part of the curve can be noticed between 16 and 24 metres, after which the rate of the tool fracture grows. Similarly, DLC-WS$_2$ d does not present a steady-state but rather constant rapid wear. Possibly, as suggested in section 4.4.3.2, a large number of layers (24 in total) and microparticles generate high stress in the coating, causing its instant failure, with greater wear at the very beginning of the cutting process. As a

result of the rapid wear, the cutting forces increase and lead to elevated wear of the tool.
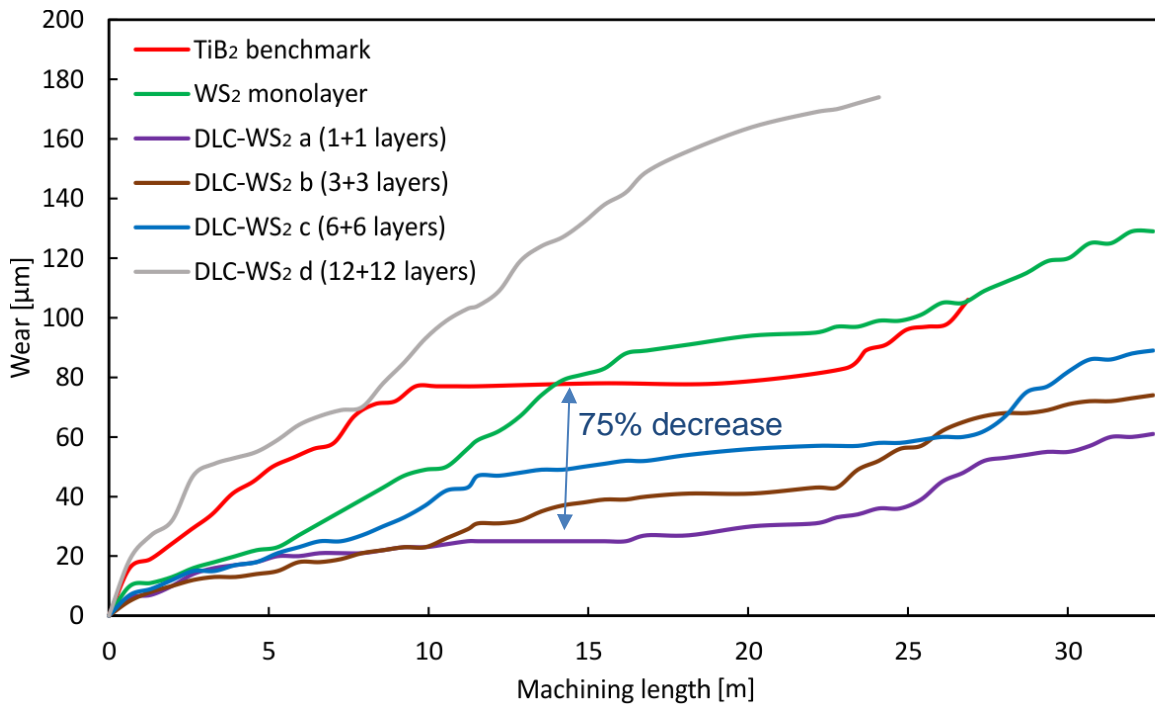
Figure 4-10 Tool wear curves of KC410M milling inserts with DLC-WS$_2$ coatings (cutting parameters: V$_c$: 500 m/min, a$_p$ = 10 mm, f$_t$: 0.05 mm).

On the other hand, DLC-WS$_2$ a, b and c all outperform both TiB$_2$ and monolayer DLC coatings. Interestingly, only DLC-WS$_2$ c, which combines 12 layers in total, presents the typical three-stage wear curve with sharp changes between the stages. It is noticeable that the machining length was extended up to 28 metres as compared to TiB$_2$. In the case of the 2- and 6-layer coatings, the transition between the running-in stage and the steady-state is not as pronounced as a TiB$_2$ benchmark sample. The DLC-WS$_2$ a curve in particular, flattens after just 5 metres of machining, what indicates this multilayer combination of DLC with WS$_2$ ensures rapid adaptation of the tool at the very beginning of the cutting process, thereby limiting the initial wear. In spite of this, the total machining length was not extended, and the tool wear is just 25% that of the TiB$_2$. A rapid adaptation of the tool is essential, especially during finish machining when surface finish and dimensional accuracy are essential.

4.4.5 EDX element mapping

The amount of aluminium that adheres to the cutting edge was assessed using EDX element mapping. The Image J software allowed calculation of the area covered by the adherent material. SEM images using secondary electrons allowed determination of tool wear.

4.4.5.1 DLC monolayer

Figure 4-11 presents the SEM micrographs along with EDX elemental analysis Al dot maps of the rake surfaces of the DLC-coated milling inserts after machining of Al-10Si. Aluminium adhering to the rake edge can be observed in all the samples, however, its shape and amount differ, which is more visible on the SEM images.

Significant Al sticking can be observed for samples DLC a and DLC d. The adherent layer is thick and uniform across the edge, which indicates that after a certain machining length and elevated tool wear, this DLC coating failed and continuous build-up of material occurred. For samples b and e, on the other hand, despite the Al sticking occurs, it can be observed especially on SEM images that Al splats and thin layers are formed rather than large uniform Al build-ups. The amount of Al adhered is lower than for the DLC a and d. Especially for DLC b, it is located at the very edge of the tool, confirming slightly better performance during the matching test (Figure 4-9). This indicates better protection against aluminium sticking provided by these coatings, as the Al build-up could partially detach from the tool surface even at the very end of the machining process.

Even though the machining length was longer for sample DLC c, the smallest Al build-up can be noticed. It forms only a thin layer close to the tool edge. The amount is only around 30% of that on the other coated tools, proving that -100 V bias is optimum for producing thin DLC coating that facilitates tool adaptation during the running-in stage and prevents aluminium adhesion to the tool edge better than does the TiB2 coating. This matches the results obtained from machining tests and CoF measurements.

SE
↔ 250 μm
Al
107021 μm² Al
↔ 250 μm
DLC a (-50V bias)

SE
↔ 250 μm
Al
71584 μm² Al
↔ 250 μm
DLC b (-75V bias)

SE
↔ 250 μm
Al
20311 μm² Al
↔ 250 μm
DLC c (-100V bias)

SE
↔ 250 μm
Al
104015 μm² Al
↔ 250 μm
DLC d (-125V bias)

SE
↔ 250 μm
Al
75485 μm² Al
↔ 250 μm
DLC e (-200V bias)
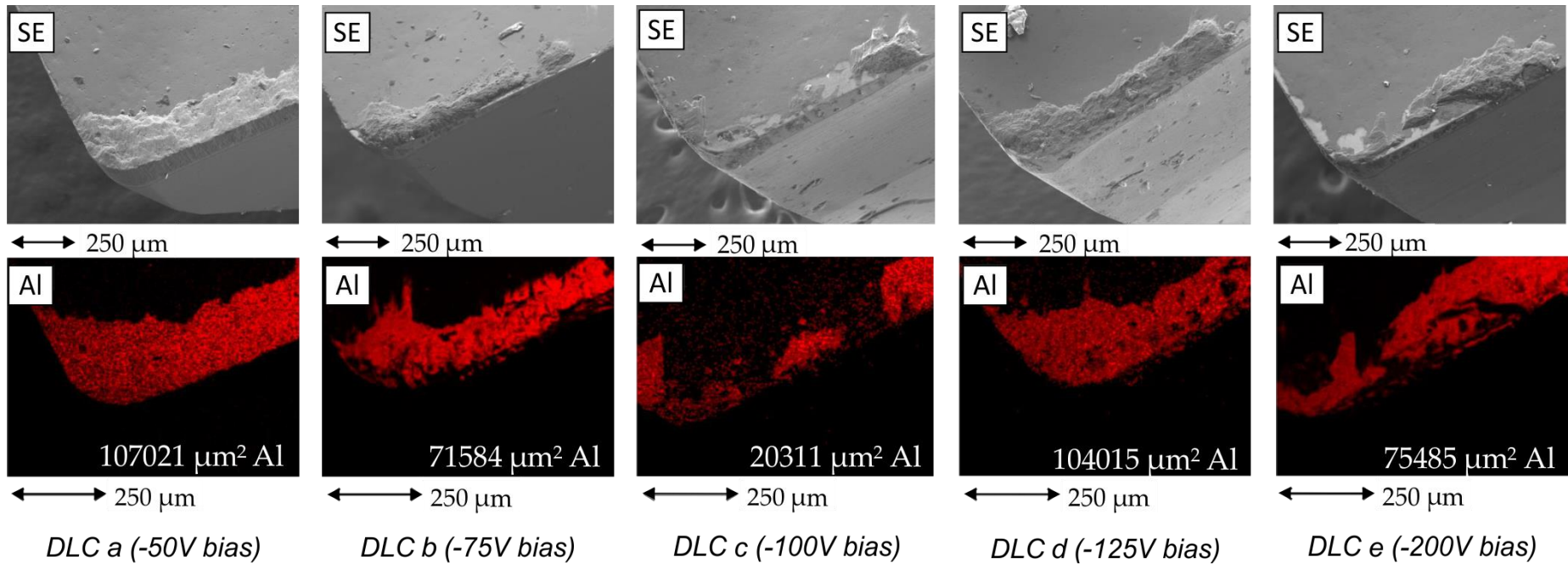
Figure 4-11 Aluminium element mapping images of the flank face of mill insert with DLC coating after face milling AlSi alloy. Element mapping obtained with EDX mode of SEM.

4.4.5.2 DLC-WS$_2$ multilayers

The Al elemental maps and SEM images of the rake faces of the milling inserts coated with the multilayer DLC-WS$_2$ are presented in Figure 4-12. Except for the WS$_2$ monolayer and DLC-WS$_2$ d, it can be observed that the amount of the Al is lower than for DLC. A larger amount of Al adherent can be noticed for the WS$_2$ monolayer, confirming the degradation of its tribological properties in the wet environment [202] and rapid wear caused by hard AlSi alloy. For DLC-WS$_2$ c and d, crater and abrasive flank wear occurred. This indicates that a build-up edge occurred, leading to microcrack formation. As a consequence of the cyclical stress, separation of the grains from the surface of the tool occurred, which is a typical consequence of the adhesive interaction of tungsten carbide grains with the machined material [13,218]. A thin layer of Al adhered on the rake face can also be noticed beside the build-up at the very flank edge of the tool coated with DLC-WS$_2$ c.

The lack of crater wear on sample DLC-WS$_2$ a and only slight Al adherent in the form of a thin layer indicates that adding DLC into the WS$_2$ film can significantly increase tool lifetime [22]. The WS$_2$ provides good lubrication of the tool-chip area, while DLC adds wear resistance and prevents oxidation of the WS$_2$ lamellas [179].

Increasing the number of layers while maintaining the same volume fraction of DLC and WS$_2$ could prevent crack propagation and increase the failure resistance of the coating [67]. Even though such an attempt was successful for fabrication of WS$_x$/a-C coatings using magnetron sputtering [179], in this study applying a deposition method as energetic as cathodic arc combined with pulsed DC magnetron sputtering for multilayer deposition may have introduced too much stress into the coating. As a result, the best tribological performance was achieved for monolayers of DLC and WS$_2$ combined into a bilayer structure.
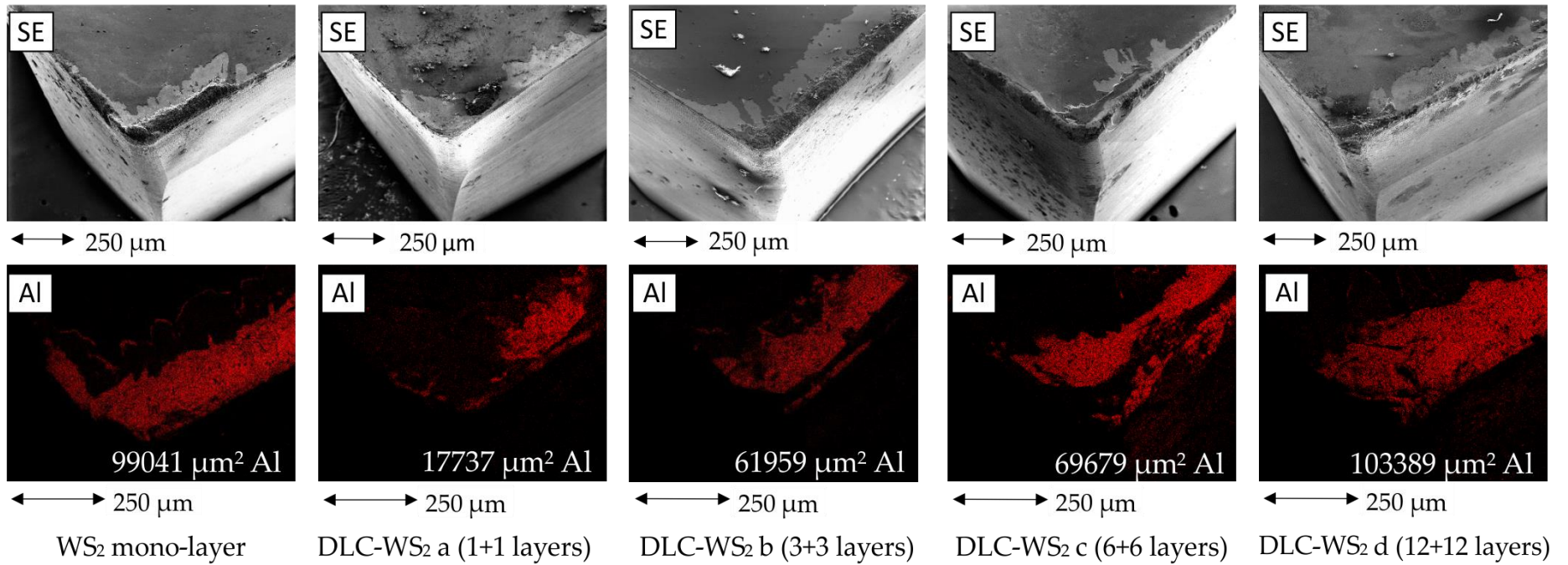
Figure 4-12 Aluminium element mapping images of the flank face of mill insert with multilayered DLC-WS$_2$ coating after face milling of AlSi alloy. Element mapping obtained with EDX mode of SEM.

4.4.6 Chip formation

Figure 4-13 shows the chip material removed during the running-in stage, and the chip surfaces after Al-10Si milling using tools coated with TiB_2, DLC and $DLC-WS_2$ coatings, respectively.
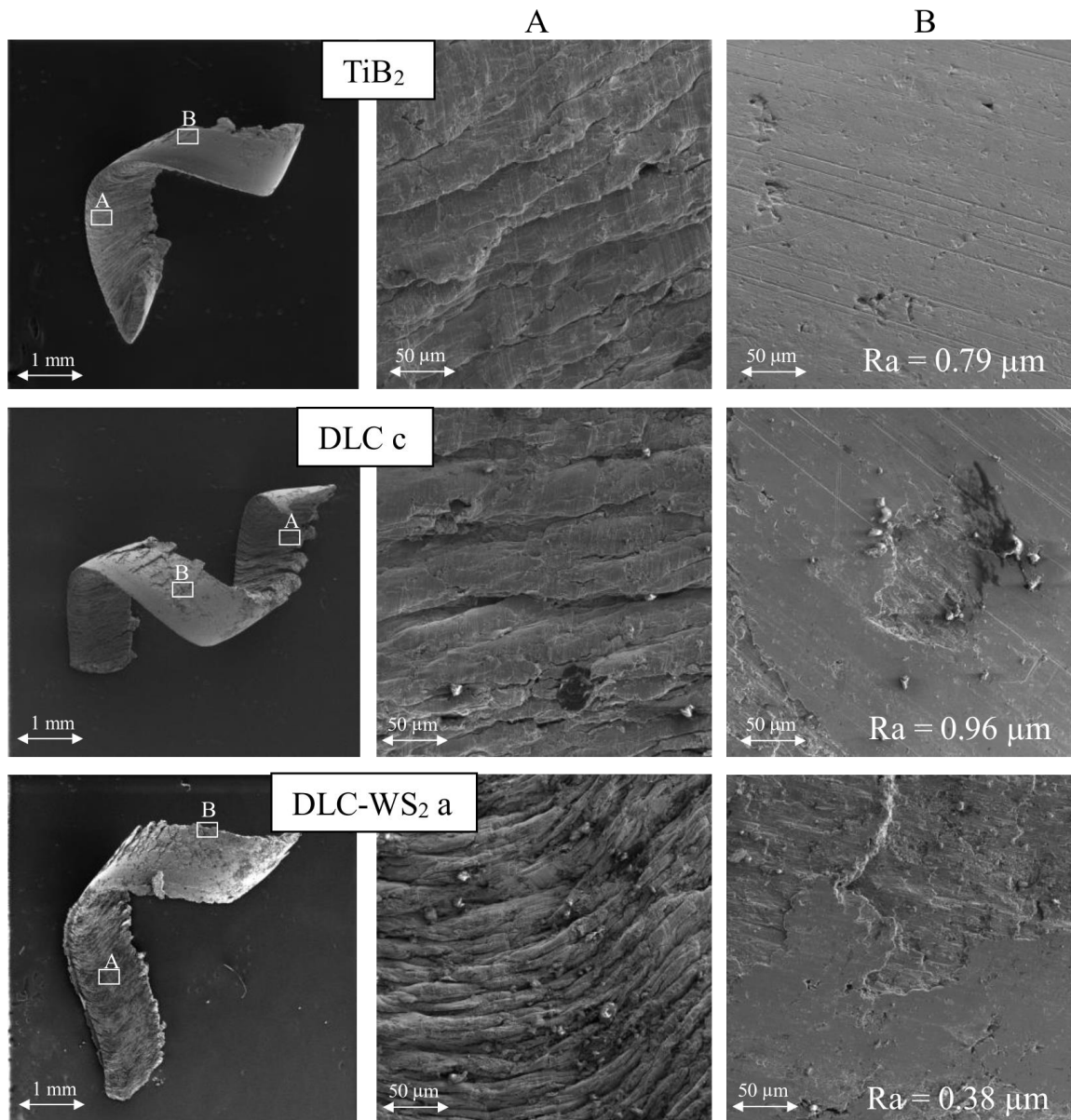
Figure 4-13 SEM images of the chip shapes and surfaces.

To confirm the hypothesis that $DLC-WS_2$ provides better lubrication of the tool-chip area than the DLC coating, the roughness of the chips from machining with TiB_2, DLC

C and DLC-WS$_2$ a was measured using the Alicona 3D digital microscope. As all of the chips were collected at the running-in stage when the coatings had not worn, the sizes of all of the chips are similar. In appearance, TiB$_2$ chips look smoother, indicating this particular coating ensured lubrication and limited Al sticking, thus chip flow could be smooth resulting in a smoother surface under the produced chips [167].

The results indicated that Ra for TiB$_2$ and DLC chips was 0.79 µm and 0.96 µm, respectively. The higher roughness of chips from machining using DLC-coated tools confirms the observation made during the dry reciprocating sliding test in Figure 4-3 Nonhydrogenated amorphous carbon films typically have higher CoF than ones containing hydrogen [33]. However, their high hardness and anti-adherent properties [13] make them perfect for Al alloy machining. Therefore the tool lifetime was improved in Figure 4-9. Contrary to the roughness of the chips from cutting with DLC-WS$_2$ a coated mill have Ra = 0.38 µm. Friction-reduction and increased wear-resistance can be attributed to the formation of a transfer lubricant layer of WS at the tool-chip interface during the cutting process [22]. The low roughness of the chips indicates not only improved tool longevity (Figure 4-13) but also a better surface finish on the machined material.

4.5 Conclusions

A hybrid cathodic arc – magnetron sputtering system was successfully used to deposit nonhydrogenated thin DLC films and DLC-WS$_2$ multilayers on TiB$_2$ precoated (KC410 grade) milling inserts. The volume fraction of each multilayered coating was maintained while the number of layers was varied. The substrate bias during the DLC deposition was found to have a significant influence on the cutting performance of the tools. All of the coatings decreased the tool wear compared to TiB$_2$-only coatings. However, it was found that a coating produced at -100 V bias could improve machining length by 60%. The post-machining tool investigation using an SEM microscopy and EDX elemental mapping also revealed that in addition to improved machining length also Al adherence to the tool was limited, as only a very low Al BUE was found. Combining the DLC deposited at -100 V with WS$_2$ resulted in improved frictional performance, as a CoF below 0.2 was recorded for bilayer DLC-WS$_2$ during the progressive load unidirectional sliding test. While a low friction coefficient was

measured for monolayer WS_2 (0.25), its low hardness did not allow it to decrease tool wear during the machining process. By contrast, a significant influence on tool wear was observed for 2, 6 and 12 layers of DLC-WS_2. The best performance was found for a two-layer coating which shortened the running-in stage to just 5 metres and lowered the tool wear in the stable state four-fold compared to the TiB_2-coated tool. Friction reduction and increased wear resistance can be attributed to the formation of a transfer lubricant layer at the tool-chip interface during the cutting process, as is typical for solid lubricants coatings.

5 Facilitating TiB$_2$ for filtered vacuum cathodic arc evaporation

This chapter was submitted for publication in the MDPI Coatings Journal and is currently undergoing the peer review process. See Appendix C for copyright permission to use as a chapter.

Tomasz L. Brzezinka, Jeff Ra, Jose M.Paiva, Joern Kohlscheen, German S. Fox Rabinovich, Stephen C. Veldhuis, Jose L. Endrino.

5.1 Abstract

The use of hard lubricious coatings for cutting tools has grown considerably in the last decades. The development of the aerospace and automotive industries requiring lightweight alloy machining has placed increased demands on coatings to improve tool lifetime during machining of alloys such as AlSi. TiB$_2$ is well established as a superhard coating with a high melting point and a low coefficient of friction. Although borides can be successfully deposited by a variety of Physical Vapour Deposition and Chemical Vapour Deposition methods, their brittle nature means they cannot be utilised with arc evaporation, which is commonly used for the synthesis of hard coatings as it provides a high deposition rate, fully ionised plasma and good adhesion. In this work, TiB$_2$ conical cathodes with non-standard sintering additives (carbon and TiSi$_2$) were produced, and the properties of the base material, such as grain structure, hardness, electrical resistivity and composition, were compared to those of monolithic TiB$_2$ using nanoindentation, Scanning Electron Microscopy and Energy-dispersive X-ray spectroscopy analysis. The dependence of the produced cathodes' electrical resistivity on temperature was evaluated in a furnace with an argon atmosphere. Their arc-evaporation suitability was assessed in terms of arc mobility and stability by visual inspection and by measurements of plasma electrical potential. Also, shaping the cathode into a cone allowed investigation of the influence of an axial magnetic field on the arc spot. It has been found that adding C ensures exceptional arc-spot stability and mobility compared to monolithic TiB$_2$, however, poor cathode utilisation results due to the steady generation of cathode flakes. The TiB$_2$

cathode containing TiSi$_2$ provided the best balance between arc-spot behaviour and cathode utilisation. The cathodes were also used to deposit coatings on milling inserts, and their structure, friction and thickness were assessed, as was their tribological performance during Al-10Si machining. Despite high observed rates of particle and flake generation, the deposited films had low roughness values and showed good machining potential when compared to commercial TiB$_2$ and TiAlN-coated tools.

Keywords: TiB$_2$; TiB$_2$-C; TiB$_2$-TiSi$_2$; SEM; EDS; XPS; milling; aluminium

5.2 Introduction

Aluminium silicon alloys are widely used in various industries, such as aerospace, military and construction [219]. These materials are difficult to machine, however, because aluminium's metallic matrix has high adhesive interaction with a tool, and silicon's particles are highly abrasive [61].

Titanium diboride has a hexagonal structure with boron atoms being covalently bonded within the titanium matrix [8]. Its excellent properties, such as high hardness (up to 30 GPa) [9], high chemical stability at elevated temperatures, and inertness to liquid aluminium [10], make it an ideal material for coating tools to provide high abrasion resistance and to reduce built-up edge [11,12]. Different CVD and PVD deposition methods can be used to deposit TiB$_2$ coatings. Magnetron sputtering is one suitable method for low-temperature deposition of TiB$_2$ without the use of explosive or toxic gasses, and it is appropriate for coating tools with complicated geometries [136]. Cathodic arc deposition (CAD), however, may be a better choice. One of the oldest PVD deposition methods, CAD ensures high density and adhesion of coatings and provides significantly higher TiB$_2$ deposition rates than MS.

Reports describing successful and reproducible attempts at cathodic arc evaporation of TiB$_2$ are limited [17]. Arc running on TiB$_2$ cathodes is associated with several challenges. Compared to classic metallic cathode materials such as Ti or Cr, the arc spot on TiB$_2$ tends to stick to a specific location leading to local

96

overheating, cracking and disintegration of the cathode [18]. In addition, arc triggering is difficult, and arc stability (time until the arc spot disappears and has to be triggered again) is very low [19]. Finally, despite TiB_2's high melting point, a high rate of macroparticle generation is observed [18,19]. Two routes have been proposed to overcome some of the arc stability issues. Knotek *et al.* [18] subjected reactive deposition (nitrogen); however, the films they deposited were TiBN rather than TiB_2. They also stated that sintering additives had an influence on arc behaviour, but they did not present the exact chemical composition of each cathode tested [18]. Trelegilo *et al.* [19], on the other hand, attempted to overcome these problems by using pulsed-arc evaporation. Others who had used DC-bias reported that high compressive stress in the deposited coatings led to coating fracture. Pulsed high-voltage bias allowed Trelegilo *et al.* to overcome this problem, yet, the physical nature of this solution remains unknown [19].

TiB_2 electrical resistivity studies performed by other researchers [154] suggest that local densification of the cathode material caused by the arc temperature is the primary reason for the arc's sticking to a specific location on the cathode [17]. Therefore, to facilitate arc running, TiB_2 cathodes should have a density close to 100 % of their theoretical density (TD). Recently Zhirkov *et al.* [17] presented the first successful and reproducible method to synthesise TiB_2 from arc evaporation. In their industrial-scale work, a DC arc source was used with cathodes 63 mm in diameter. The TiB_2 cathodes were produced using a hot pressing method by Plansee Composite Materials with a density close to 100% TD. They observed that the dissipation of the arc spot improved significantly when there was no external magnetic field [17]. In addition, Zhirkov *et al.* [17] suggested that an addition of 1 wt% of carbon powder added into the TiB_2 composition before sintering can hamper the crack propagation thus further delay the cathode destruction. This concept was adopted and reported in the conference proceedings [58]. Zhirkov *et al.* [58] confirmed carbon inclusions serve as stopping points for crack propagation as almost no visible cracks were observed on the surface of the cathode in comparison to TiB_2 cathodes with no carbon addition tested before [17].

Producing high-density sintered bulk TiB_2 is difficult, however, as it requires high pressure and pressing temperatures of up to 2,000 ºC [10,143]. Metallic sintering additives such as Ni, Co and Cr have been reported to successfully enhance TiB_2's density by forming borides with a low melting point (900–1,100 ºC) and good wetting behaviour [10]. Nevertheless, they are not suitable for high-temperature application [57,137], as the low melting point of metallic additives leads to incipient fusion. Based on the studies referred to above, we can conclude that the sintering additive for TiB_2 cathode production should also meet the following requirements: 1) its thermal and electrical conductivity should be similar to or higher than that of pure TiB_2 (to improve arc dissipation), 2) its thermal expansion coefficient should be similar to that of TiB_2 (to avoid cathode fracture), and 3) it should not change significantly the final composition of the cathode (to allow pure TiB_2 to be deposited). The most promising non-metallic additives meeting some of the above requirements, which were also reported in [56,57,137,141,142] for successful application under high temperatures, are silicides such as $TiSi_2$, $MoSi_2$ and WSi_2. These enhance the liquid phase sintering by promoting the formation of $TiSi_2$ [10]. $TiSi_2$, in particular, appears to have significant potential for use in cathode production, as its density, thermal and electrical conductivity, and thermal expansion coefficient are all close to those of monolithic TiB_2 [56]. Moreover, the addition of just 5 wt% of $TiSi_2$ is enough to ensure a cathode relative density of greater than 99 % during sintering at 1,550 ºC, while maintaining the fracture resistance and hardness of the monolithic TiB_2 [56].

In work described in this paper, we compared the material properties and arc behaviour during cathodic arc evaporation of monolithic TiB_2, TiB_2-C (1 wt%), and TiB_2-$TiSi_2$ (5 wt%). Our testing equipment used cone-shaped cathodes, which allowed for an axial magnetic field configuration rather than the arched circular field configuration of typical flat racetrack cathodes. As a result, different arc behaviour could be expected, and the previous observations on monolithic TiB_2 [18] and TiB_2-C [17] could be confirmed. To benchmark the overall potential of new TiB_2 cathode compositions for coating deposition, the coatings were

deposited on cemented carbide milling inserts, and their performance was assessed against commercial magnetron-sputtered TiB_2 and TiAlN coatings.

5.3 Experimental procedure

5.3.1 Cathode production and testing

The cathodes used were produced by three companies: Plasmtechnology (monolithic TiB_2), Plansee (TiB_2-C) and Plasmaterials (TiB_2-$TiSi_2$). As materials other than metals require indirect cooling, a backplate had to be used to avoid direct contact between the cooling water and the cathode material. For the TiB_2 and TiB_2-$TiSi_2$ cathodes, Cu backplates were used. The roughness of the TiB_2-C material created additional thermal resistance at the interface between the cathode and backplate [91]; therefore, the TiB_2-C was fastened to a Mo backplate with highly thermally conductive glue.

5.3.1.1 Cathode testing

We used a filtered cathodic vacuum arc deposition system for the cathode testing and coating deposition (Figure 5-1). The system featured a cone-shaped cathode (67 mm x 50 mm and a 50-mm height) which dimensions were recemented by the FCVA source manufacturer, and the spot motion around the cathode was controlled by focusing and steering magnetic coils wrapped around the anode. An additional magnetic coil was used as a linear filter placed between the end of the anode and the substrate to minimise the number of macroparticles reaching the substrate. The power source allowed control of the arc current (up to 70 A), focusing coil (FcC) 3–7 A and filtering coil (FtC) 1–10 A, while the steering coil was fixed at 1 A. Prior to each test and deposition, the chamber pressure was pumped down to below $3*10^{-6}$ Torr.

5.3.1.1.1 Arc running

The sample holder was removed, and a mirror was placed at 45º in the middle of the chamber to allow direct observation of the cathode during operation through the viewport. Each of the cathodes was tested, and parameters such as chamber pressure, Ar flow, magnetic field (coils current), and arc current were optimised

to allow stable arc running after triggering and good spot mobility (fast motion in front of the cathode).
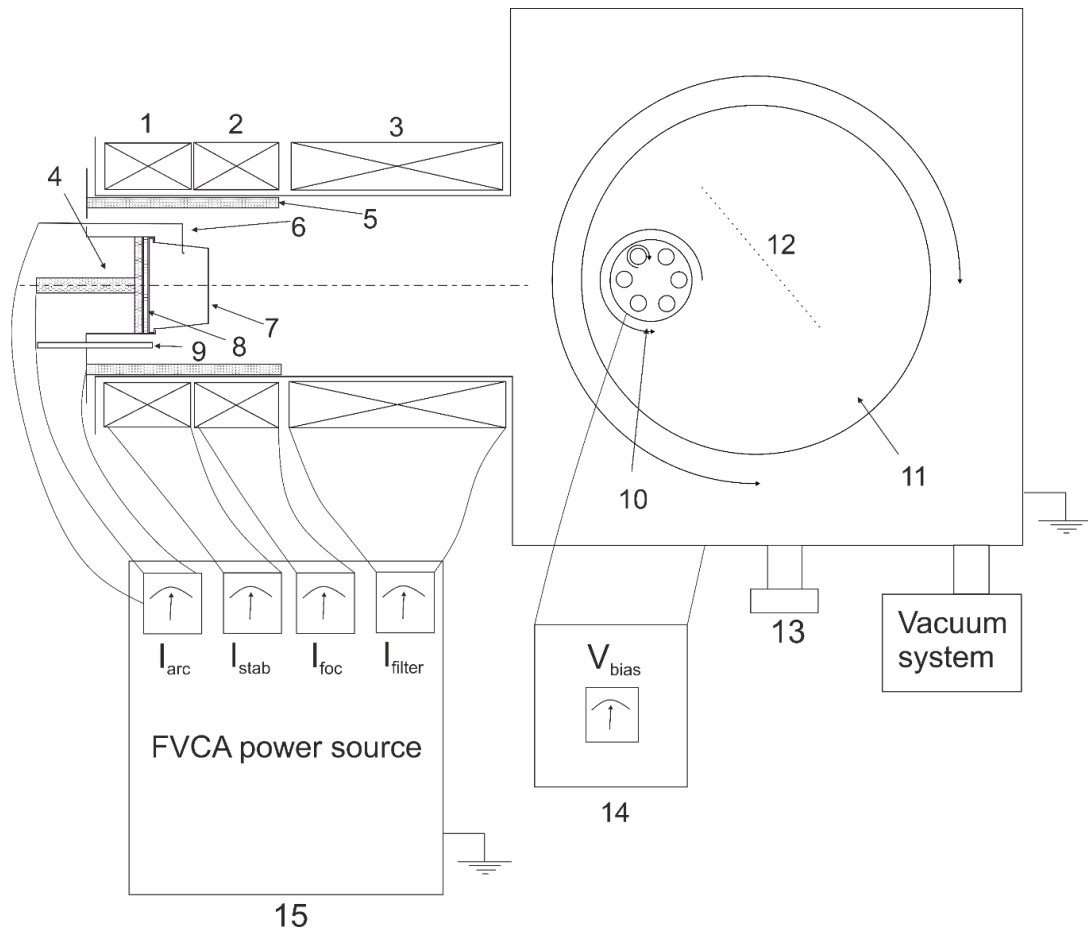
Figure 5-1 Schematic view of the filtered vacuum cathodic arc deposition system (1-stabilising coil, 2 – focusing coil, 3 – filtering coil, 4 – cooling pipe,5 – anode, 6 – trigger, 7 – cathode, 8 – , 9 – argon inlet,10 – rotating substrate holder, 11 – substrate table, 12 – mirror, 13 – viewport, 14 – substrate bias power unit, 15-FCVA power source).

The cathode fracture was assessed after arc running; fractured cathode parts were collected from around the anode, filter and chamber, and cathode height was measured.

To assess the influence of the magnetic field on the arc spot motion, the substrate holder presented in Figure 5-1 was replaced by an insulated metal plate (10 cm x 10 cm), and the electric potential between the plate and the ground was

measured using a Versastat potentiostat. The data was collected for 60 s for each setting. We anticipated that if we observed arc running at the side of cathode and a high frequency of arc triggering this would result in a lower potential generated by the ions hitting the metal plate, whereas stable arc running at the front face of the cathode would result in a higher potential generated at the plate.

5.3.1.1.2 Electrical resistivity measurements

As the focus of this work was to produce and test the cathodes, and resources were limited, dedicated samples for comparing the electrical resistivity of the cathode materials could not be produced. However, the cathode parts that were removed after the initial arc-running tests were collected and used to measure the dependence of electrical resistivity on temperature. We assembled a special rig to do this, consisting of a Versastat potentiostat, tube furnace and platinum wire (to limit the influence of oxidation on the measurement). Each cathode part was measured and placed on the ceramic base wrapped by platinum wires with 1 cm between them as presented in . To secure the part in place, additional nickel wires were used. The wires were connected to the Versastat potentiostat, allowing resistance measurements at regular intervals to be recorded in the computer. Before each measurement, the air was evacuated from the furnace using the rotary pump. An argon atmosphere was introduced with a flow of 200 sccm. The temperature was progressively increased from room temperature at a rate of 5 ºC/min up to 1,000 ºC. DC current was applied to the sample, and the resistance was measured. For each cathode material, two samples were measured to ensure correct values. As the resistance (R) depends on the cross-section of the sample (s) and its length (l) the resistivity (ρ) was calculated based on equation (1) to allow comparison between the samples:

$$\rho = R\frac{s}{l} \qquad \textbf{(5-1)}$$
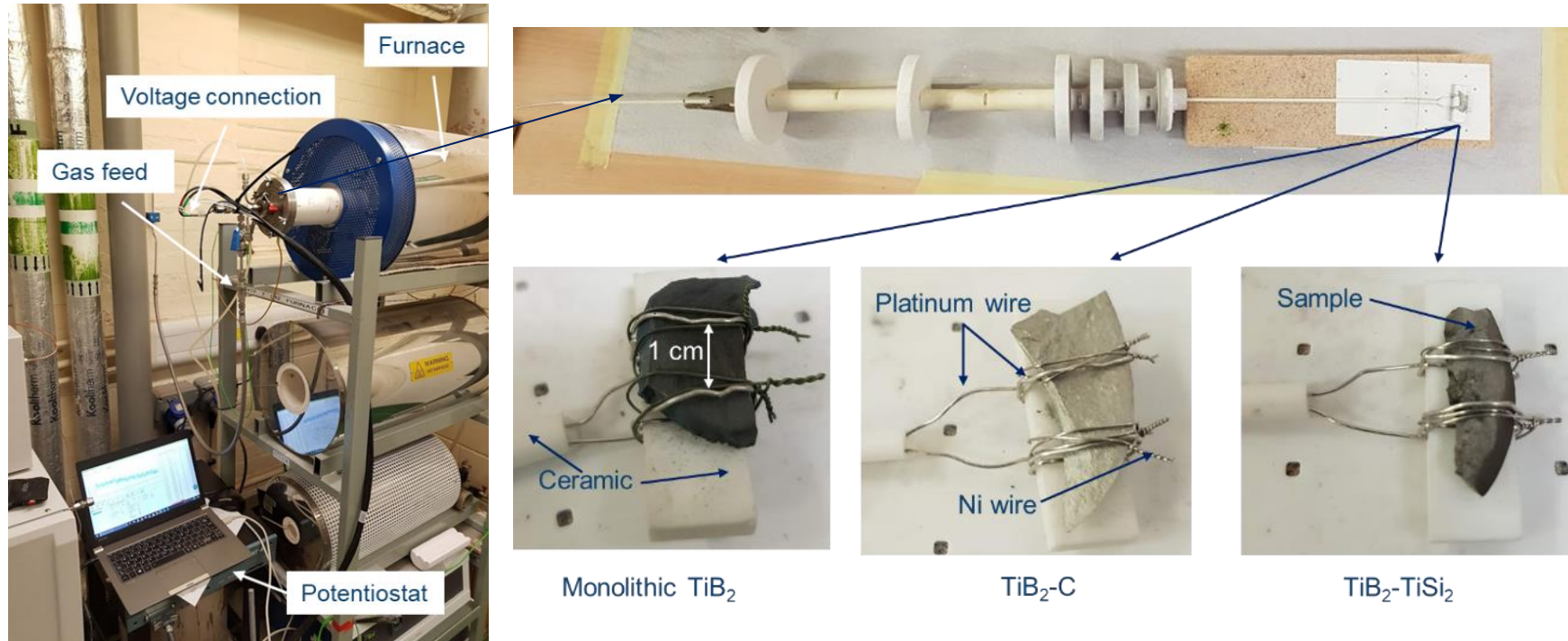
Figure 5-2 Resistivity rig assembly and sample fixture.

5.3.2 Coating deposition and testing

5.3.2.1 Deposition parameters

Pieces of silicon wafers, Kennametal EDCT milling inserts and Widia SUN120408 turning inserts were used as substrate materials. The substrate cleaning prior to each deposition included ultrasonic cleaning in an acetone bath for 15 min followed by rinsing in isopropyl alcohol. The substrates were then loaded on the rotating substrate holder, and the system was pumped down to below 3×10^{-6} Torr. The substrates were cleaned in situ by Ar etching; a negative 450 V bias was applied to the substrate for 10 min under a 10^{-1} Torr process pressure and a 100-sccm Ar flow.

The coating parameters for deposition on the cutting inserts were chosen based on initial cathode trials to ensure stable arc running (although, the arc running on the monolithic TiB_2 cathode was too unstable to allow any coating deposition). The argon pressure was 4.5×10^{-3} Torr, the focusing coil current was equal to 5 A and the filtering coil was set to 10 A, and the substrates were grounded. For TiB_2-C, the cathode arc current was set to 45 A, while for TiB_2-$TiSi_2$ it was set to 50 A. The deposition time was 2 hours.

To investigate the influence of substrate pre-heating, and cathode cooling on coating thickness, another series of coatings were deposited on silicon samples partially covered by Kapton tape. Deposition parameters were kept as described above except for the time intervals. The step height was later measured using Dektak profilometer. The possibility of cathode overheating during plasma generation was investigated. Therefore, the coating was deposited in fixed intervals: 5-min deposition intervals alternated with 5-min breaks (substrate temperature during this phase was maintained using the heater to avoid additional stress being generated in the coating) for 20-, 40- and 100-min total deposition times.

5.3.2.2 Machining testing and characterisation

To assess the potential of the coatings deposited on the new cathodes' faces, we performed milling tests on an Okuma Cadet Mate CNC vertical machining centre. The cutting conditions are presented in Table 5-1 and were similar for both wet and dry machining tests. As the thickness of the deposited coatings was less than 1 µm, they were benchmarked not only to commercial TiB_2-coated (2–3 µm) but also to thinner (1 µm) commercial TiAlN-coated and uncoated tools. The procedure of measuring the tool wear was discussed in detail in section 4.3.2.

A Tescan dual-beam focused ion beam scanning electron microscope (SEM) was employed to study the cross-sections of the coatings. A Philips SEM microscope equipped with energy-dispersive X-ray spectroscopy detector was used to investigate the surface and chemical composition of cathodes, deposited coatings, chips collected during the machining and tools after use. The EDX also allowed also us to explore the aluminium that had adhered to the tool, the area of which we later determined using ImageJ software. The cross-section images of the chips were obtained on an optical microscope.

A Teer ST-3001 Tribo Tester was used to assess both friction coefficient and adhesion of deposited and benchmark coatings. The CoF was determined using a dry reciprocating sliding test with a fixed 5-mm WC ball drawn over the surface of the coating for a 10-mm distance for 100 cycles. The adhesion was measured using increasing loads (5–100 N) at a 50-N/min loading rate applied at a linear velocity equal to 5 mm/min.

The hardness of deposited coatings and cathode material was determined using Micro Materials Ltd. Micro Materials NanoTest nanoindenter. A series of 10 indents with a 100-mN load for cathodes and 25-mN for coatings was obtained, and an average value calculated.

Table 5-1 Cutting conditions used for TiB$_2$ coated tools evaluation.

Machine tool	CNC Vertical Machining Centre
Number of cutting edges	2
Feed rate [mm/min]	1880
Feed per tooth f$_t$ [mm/tooth]	0.05
Cutter diameter [mm]	19
Tool speed RPM [rev/min]	6300
Axial depth of cut a$_p$ [mm]	10
Radial depth of cut [mm]	1
Cutting speed V$_c$ [m/min]	375
Coolant rate flow [l/min]	44
Coolant concentration [%]	6
Workpiece material	Al-10Si

5.4 Results

5.4.1 Cathode material

5.4.1.1 Surface and composition

The SEM images of the unused cathodes are presented in Figure 5-3. The grains of the monolithic TiB$_2$ cathode had sharp edges, and the structure presented a high porosity. The sintering process did not result in a high-density cathode. The addition of C promoted the reduction of oxides which typically inhibit surface mobility. Therefore, rounded grain boundaries can be observed due to improved

surface mobility. Also, carbon inclusions could be noticed at some of the grain boundaries. The surface morphology of the TiB_2-$TiSi_2$ cathode looked dense, and grains did not have sharp edges as they did in the monolithic TiB_2, indicating the $TiSi_2$ additive promoted the formation of a liquid phase during sintering process. The average grain size (7.3 µm) was smaller than that for TiB_2-C (13.1 µm) but slightly larger than that for monolithic TiB_2 cathode (5.6 µm). The chemical compositions of the cathodes and deposited coatings obtained using EDX are presented in Table 5-2. For all cathodes, the stoichiometric composition (B to Ti) 2:1 was achieved. The recognised carbon content for the TiB_2-C cathode was around 13 at% and was lower than the Si content for TiB_2-$TiSi_2$, which was 5 at%. Also, oxygen was present in this cathode at almost 20 at%, which was significantly higher than for the other two cathodes. The most probable reason for this is Si's rapidly forming SiO_2 while exposed to air.
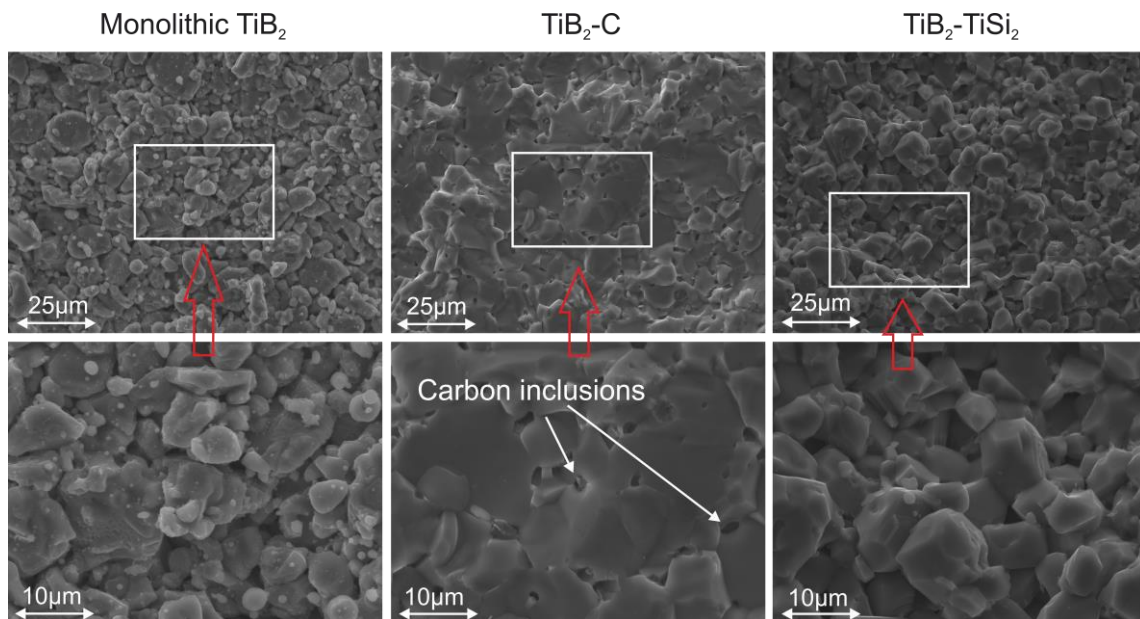
Figure 5-3 SEM images of the virgin cathode surface.

Table 5-2 Chemical composition of the cathodes and deposited coatings obtained using EDX analysis.

	B (at%)	Ti (at%)	C (at%)	Si (at%)	O (at%)
TiB$_2$ cathode	67	31			2
TiB$_2$-C cathode	59	27	13		1
TiB$_2$-TiSi$_2$ cathode	52	23		5	20
TiB$_2$-TiSi$_2$ coating	30	20		8	29
TiB$_2$-C coating	31	15	22		12

The coating deposited from the TiB$_2$-C cathode had TiB$_2$ stochiometric composition. However, the oxygen and carbon contents were relatively higher than those in the cathode itself. Unlike the material of the TiB$_2$-TiSi$_2$ cathode, the deposited coating was TiB$_{1.5}$ rather than TiB$_2$. Also, approximately 7 at% of Si is present in the coating structure.

5.4.1.2 Electrical conductivity

The temperature dependence of electrical resistivity in the cathodes parts is presented in Figure 5-4. Resistivity at room temperature differed for each cathode material. The lowest resistivity was for TiB$_2$-C, while monolithic TiB$_2$ gave a significantly higher measurement. The density of the cathodes, as well as their composition (e.g., the good electrical conductivity of C), would have had a significant influence on these results. Although resistivity remained almost constant up to 100ºC, it increased almost linearly with increasing temperature for all of the cathodes. It is noticeable that the angle of the plot for monolithic TiB$_2$ was significantly steeper (tanα = 5 * 10^{-6}) than the plots for the other two cathodes (tanα = 1 * 10^{-6}), confirming the influence of density on the electrical resistivity of TiB$_2$.
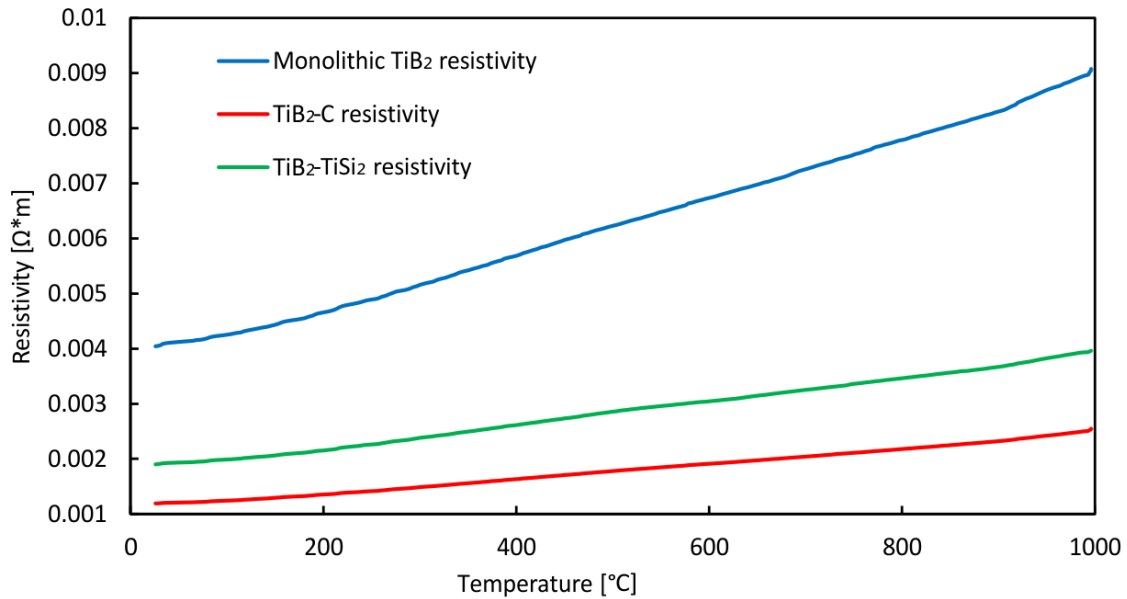
Figure 5-4 Electrical resistivity dependence on temperature of produced TiB$_2$ cathodes.

5.4.1.3 Arc stability

The initial arc-running tests involved parameter optimisation, arc observations and arc stability measurements (number of times the arc had to be triggered during 5 min). With the monolithic TiB$_2$ cathode, it was not possible to trigger an arc with arc currents lower than 65 A (the power source maximum was 70 A). Even when triggered, the arc was not stable; the average time to next triggering was just 10 s. Also, the TiB$_2$ cathode arc tended to stick to a specific location on the cathode, leading to the extensive cathode fracture presented in Figure 5-5. Large cathode chunks could be seen especially in the anode but also around the filter. Arc paths could be observed on the side face of the monolithic TiB$_2$ cathode after use.

By contrast, the TiB$_2$-C cathode experienced exceptional arc stability – once triggered, the arc was running for the entire 5 min. The minimum current required to achieve a stable arc was 40 A, although it was possible to trigger an arc below that current level. During deposition, a constant flow of particles could be observed. These particles appeared to be cathode flakes and could be found in the filter and around the chamber after the deposition (Figure 5-5). The quantity

of particles was significant and led to poor cathode utility; around 9 mm/hour was used, while the rate for the typical metallic cathode, e.g., Cr, is approximately 1–2 mm/hour.

The TiB$_2$-TiSi$_2$ cathode required approximately 50 A arc current for stable deposition. The arc stability was good; arc-spot time was equal to 2 min. Contrary to the other two tested cathodes, multi-spot evaporation could be observed at times), which should have decreased the cathode fracturing, as it leads to a dissipation of the energy between two spots. Particle generation could be observed during arc running, and particles were later collected from the chamber bottom. However, they appeared to have solidified before reaching the substrate, as the resulting coatings were smooth. Some cathode fractures could be found in the anode and filter. Still, the amount was significantly smaller than for monolithic TiB$_2$, and no visible cathode fracture was observed.

Monolithic TiB$_2$ TiB$_2$ + 1wt% C   TiB$_2$ + 5wt% TiSi$_2$
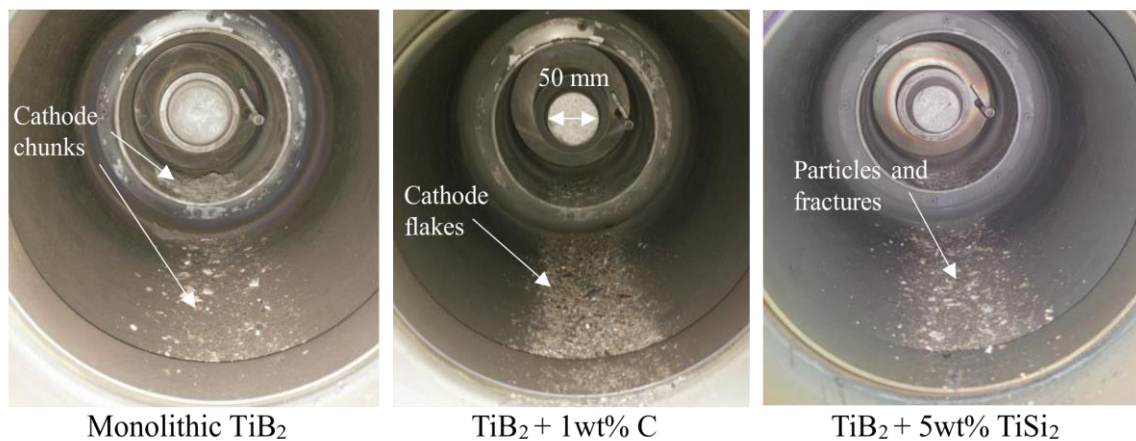
Figure 5-5 Comparison of the cathodes and fractured part in the filter after 60 minutes of arc running.

The influence of the magnetic field from both focusing and filtering coils on the potential of generated plasma is presented in Figure 5-6 (a)-(d). These graphs also represent the overall stability and movement of the arc spot; when the arc was triggered frequently or tended to run along the side face of the cathode, the potential measured during acquisition time was lower.

Reference plots for a Cr cathode are provided (Figure 5-6 (a)), as the Cr cathode was known from previous experiments on this setup to have exceptional arc movement and stability. It can be seen that above the level of 3 A, an increase of the filter coil current (FtC) increased the measured potential, as the filter confined the plasma and more ions reached the metal plate. Similarly, an increase of the focusing coil current (FoC) increased the potential, as the arc was more focused on the front face of the cathode and the plasma was more confined. Interestingly, for the high FtC currents, there was little influence of the FoC. The poor stability of the arc triggered on the monolithic TiB_2 cathode, as ascertained by visual observations, was confirmed experimentally in Figure 5-6 (b). For an FoC set to 3 A, the arc rarely triggered, and when it did so it was running on the side face of the cathode, which resulted in low voltage measured. For higher FoC and FtC currents, the measured potentials were similar. Only an FtC current of 6–8 A with an FoC current at 6 A seemed to allow the arc to be sustained for a longer time at the front face of the cathode.

The influence of the magnetic field on the arc triggered on the TiB_2-C cathode (Figure 5-6 (c)) appeared to be similar to what had been seen with the Cr cathode, as all the lines followed an approximately linear pattern. For minimum settings of both FoC and FtC currents, the measured voltage was low (0.5 V), indicating arc running at the side face of the cathode. However, once the FtC current reached 6–7 A, there was a rapid increase in the voltage measured, which indicated that the arc was running on the front face of the cathode. Overall, we noted that the filtering coil led to the confinement of the plasma, therefore, the higher the FtC current was, the higher was the measured ion voltage. Similar behaviour could be observed with an increase in FoC current. For the TiB_2-$TiSi_2$ cathode, the influence of the magnetic field (Figure 5-6 (d)) was less noticeable than for TiB_2-C and Cr. For FtC current values from 1 to 4 A and FoC current from 4 to 7 A, similar ion voltages were measured, indicating the arc was running at the side face of the cathode.
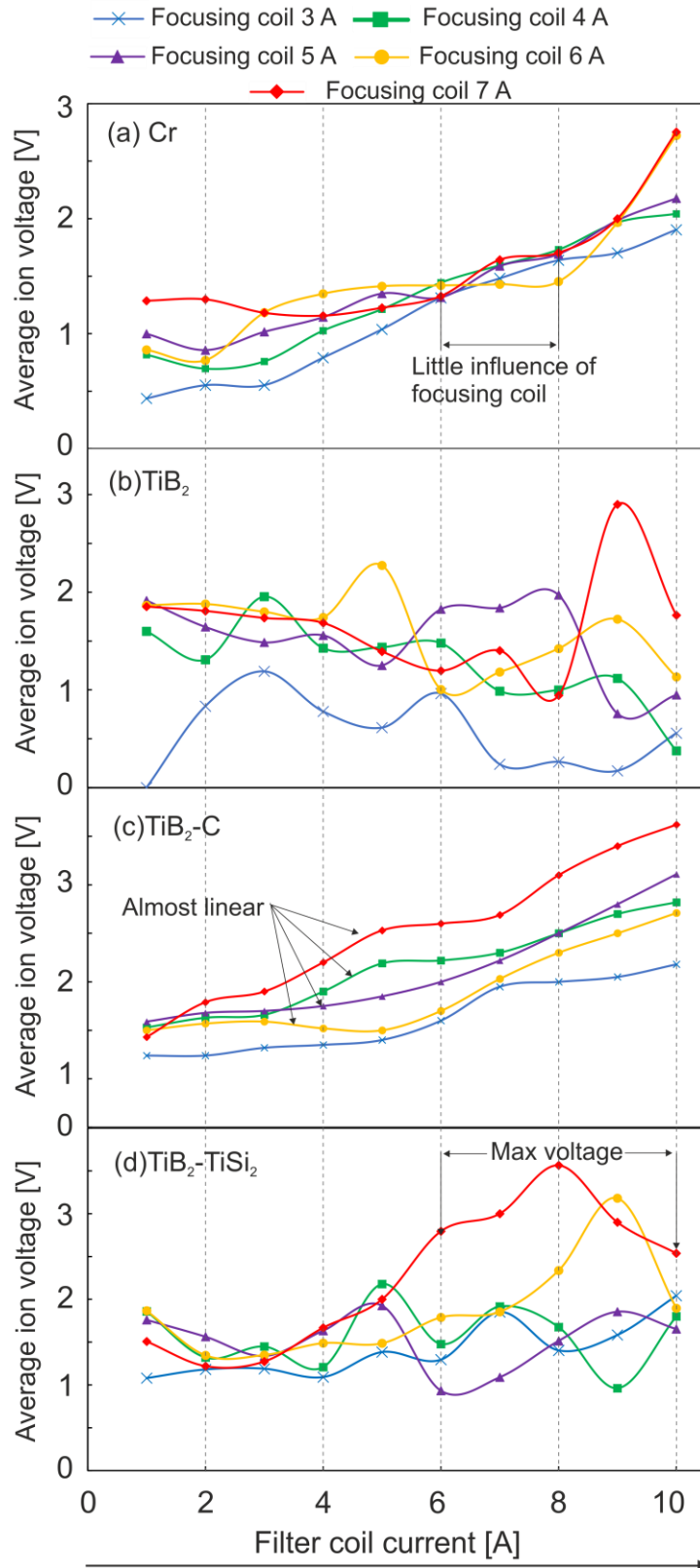
Figure 5-6 Ion voltage measured for different electric currents of focusing and filter coils for (a) Cr, (b) monolithic TiB$_2$, (c) TiB$_2$-C, (d) TiB$_2$ -TiSi$_2$ cathode.

Once the FtC current was increased, the ion voltage varied. However, significantly higher values were achieved when FoC current was 6 to 7 A and FtC current was 6 to 9 A, indicating that such a magnetic field combination ensured good plasma confinement and arc running only at the front cathode face.

5.4.2 Coating analysis

The TiB_2 cathodes were used to deposit trial series of coatings to assess their overall potential for replacing the commercial TiB_2 coatings. The initial trials of 20 min of deposition produced coatings from both TiB_2-C and TiB_2-$TiSi_2$ with a thickness of approximately 300 nm (Figure 5-7).
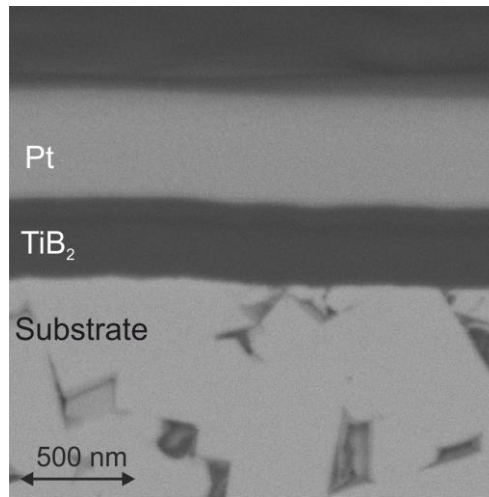
Figure 5-7 SEM cross-sectional image of TiB$_2$ coating deposited from TiB$_2$-C cathode.

To obtain thicker coatings, a 2-hour deposition was performed, including a study to determine the influence of a -100 V bias applied during deposition, determining whether it could provide better adhesion of the films and result in higher coating densities. Figure 5-8 presents the SEM images of deposited films. Despite the high particle generation observed from both TiB_2-C and TiB_2-$TiSi_2$ cathodes, films produced appeared smooth, with roughnesses of R_a = 15 nm and 18 nm, respectively. Some particles with dimensions of 5–7 µm could be found on the samples, but they were rare. Despite increased deposition time, the thickness of

the deposited films was 500 nm for the TiB_2-C cathode and 300 nm for the TiB_2-$TiSi_2$ cathode.
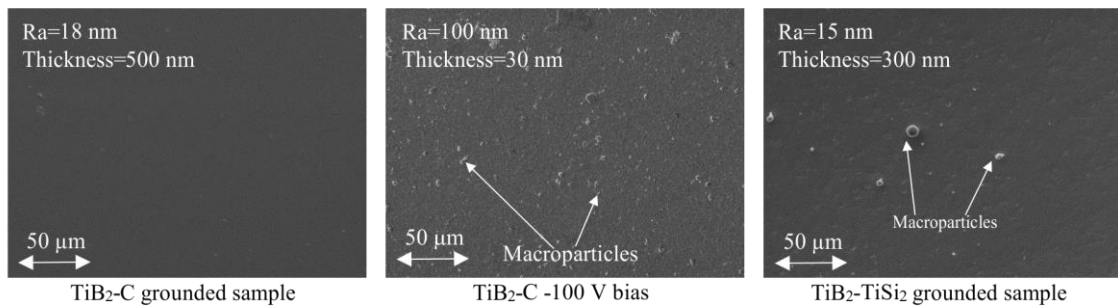
Figure 5-8 SEM images of coatings deposited from different cathodes for 2 hours deposition time.

The coating produced with a -100 V bias had a very low thickness (26 nm) and high roughness (R_a = 100 nm) compared to the other coatings. The coating SEM image appeared to be rough, with many particles on the surface of the coating. The lower thickness than expected was potentially a result of overheating of the cathode. To confirm this effect, interval coating deposition tests with running periods of 5 min were carried out (as described in the 'Experimental Procedure' section), which should have allowed for maintaining a low temperature at the cathode. Three coatings were deposited using this method, with varied total deposition time. The results (Table 5-3) of 20-, 40- and 100-min deposition times were coatings with thicknesses of 200, 400 and 780 nm, respectively. Such results confirmed that a cathode overheating problem was a critical barrier that needs to be addressed.

Table 5-3 Thickness of the TiB_2 coating deposited during interval deposition test.

Deposition time	Coating thickness [nm]
20 min	200
40min	400
100 min	780

113

5.4.2.1 Coefficient of friction evaluation

The CoF measurements obtained from dry reciprocating sliding test under a 5-N load for 100 cycles on the produced and commercial TiB_2 films are presented in Figure 5-9.
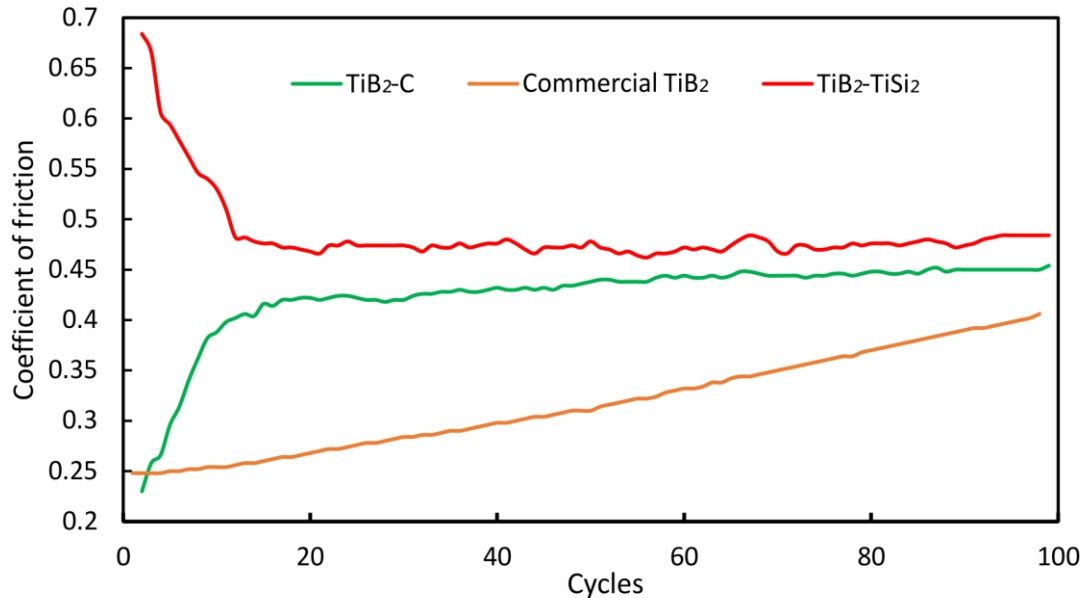
Figure 5-9 Coefficient of friction results obtained for the dry reciprocating sliding test under 5-N load.

For the sputtered TiB_2 coating, a CoF of 0.26 was measured for the first 16 cycles, which increased to 0.4 by the time 100 cycles had been completed. Similar behaviour has been observed by other researchers [143,212] during short-length (100 µm) wear tests. They found that the running-in period lasted for around 3000 cycles, until a steady-state value of approximately 0.8 was achieved. By contrast, both arc-deposited TiB_2 coatings from TiB_2-C and TiB_2-$TiSi_2$ cathodes adapted during the first 15 cycles, at which point they achieved steady CoFs of 0.43 and 0.47, respectively.

5.4.2.2 Hardness

Nanoindentation allowed the hardness values of cathode materials and coatings to be measured. The highest value for cathode hardness (Figure 5-10) was obtained for monolithic TiB_2 and was ~24 GPa. The cathodes with C and $TiSi_2$

114

additions displayed slightly lower hardnesses of ~23 GPa, which is however within the error limit. The hardness of the produced coatings was compared to that of commercial TiB_2 (Figure 5-11).
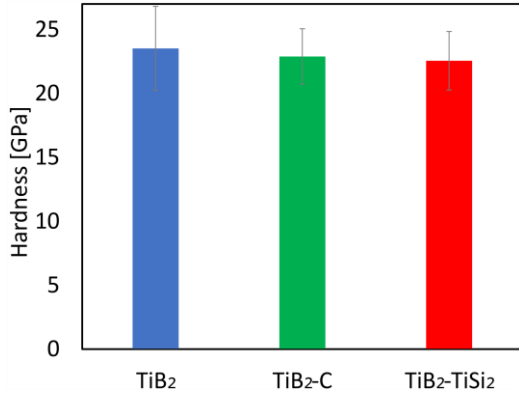
Figure 5-10 Hardness of the cathodes (average of 10 indents for 100 mN load).
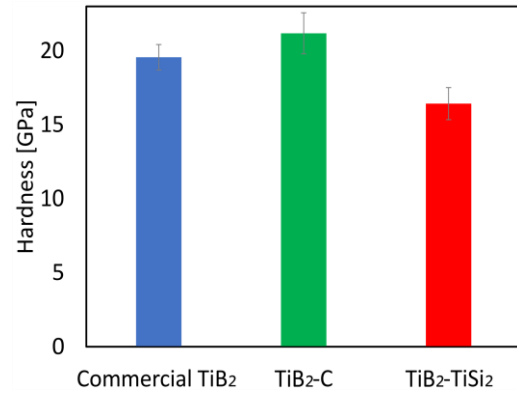
Figure 5-11 Hardness of the deposited films (average of 10 indents for 25 mN load).

The declared hardness of the commercial TiB_2 should be between 20-25 GPa [220]. The value obtained during the nanoindentation was equal to 19.9 GPa. The TiB_2-C cathode displayed a slightly harder coating (~21.1 GPa) than that of commercial TiB_2, however, the standard deviation of the indents was also greater. By contrast, the coating from the TiB_2-$TiSi_2$ cathode displayed a lower hardness value (~16.4 GPa), although it was still within the acceptable range, considering no coating optimisation (e.g., interlayer or substrate heating) had been applied.

5.4.2.3 Machining

In the wear process, three stages can typically be identified: the running-in stage, the steady-state and the surface-damage stage. The initial stage allows the tool-machined part adaptation process, and therefore, it is typically associated with increased wear, while once the tool reaches the surface-damage stage, it has to be replaced [13]. In the middle, steady-state stable, tool wear and friction are achieved, consequently, the tool wear is restricted. To reduce tool wear, it is necessary to have a rapid tool adaptation that results in a prolonged steady-state stage. Such conditions result in better machined-surface finish and tool-life

enhancement [5,13]. Figure 5-12 shows a comparison of the change in flank wear of uncoated, TiB_2-coated, and TiAlN-coated inserts in terms of cutting length during AlSi milling with coolant. Up to ~18 m of machining, the lowest amount of tool wear was observed for the TiAlN coating. This coating experienced a running-in stage for the first 5 m, then a stable state started and continued up to 8 m, after which elevated tool wear could be observed. The uncoated tool, by contrast, experienced constant wear through 25 m of machining, after which the wear speed decreased significantly, indicating the tool was in the stable state, which continued until the machining process was stopped at 30 m. A similar path was followed by both the commercial TiB_2 tool and the tool coated from the TiB_2-$TiSi_2$ cathode. TiB_2-C, however, allowed significantly faster tool adaptation, as the stable state could be observed after 12 m of machining, while the tool wear was lower than for the uncoated tool.

The uncoated and coated tools from these trials were also tested during dry AlSI machining as a way to represent the most extreme conditions. The wear curves are presented in Figure 5-13. In dry machining, in the absence of a lubricant, the coating serves as a source of lubrication, thus significantly higher wear is expected.
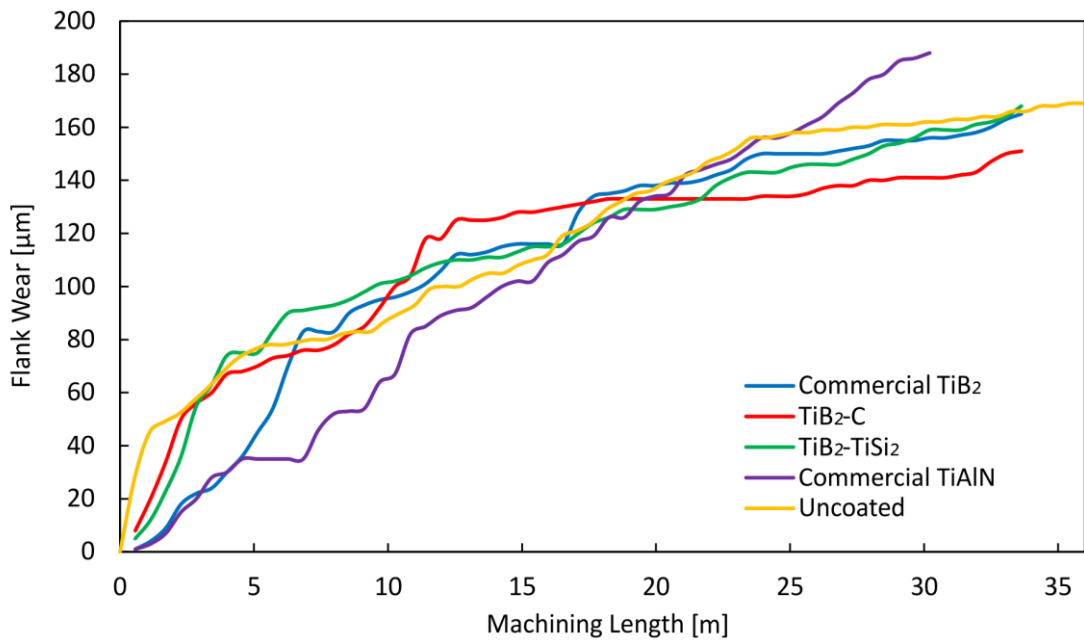
Figure 5-12 Tool wear curves of KC410M milling inserts with different coatings (cutting parameters: cutting speed Vc: 375 m/min, RPM = 6300, feed = 1880 mm/min).
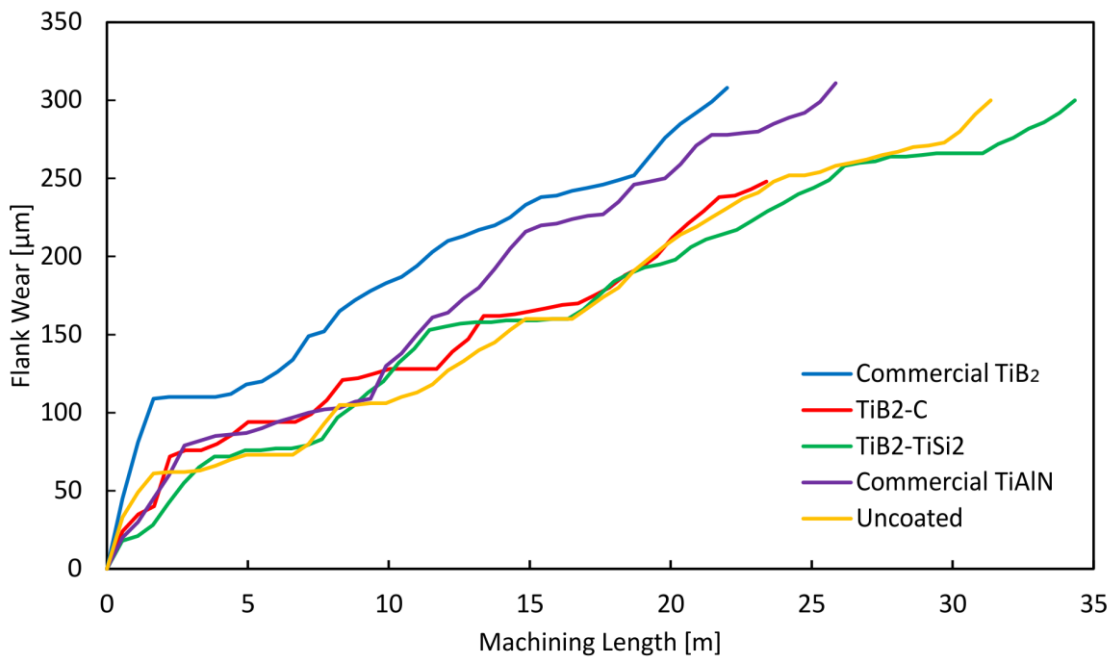
Figure 5-13 Tool wear curves of KC410M milling inserts with different coatings (cutting parameters: cutting speed Vc: 375 m/min, RPM = 6300, feed = 1880 mm/min, conditions: dry).

Commercial TiB$_2$ experienced elevated wear during the running-in stage, after which no increase in wear was observed up to 5 m. Thereafter, steady tool wear could be seen until wear reached 300 μm, when machining was stopped. The TiAlN-coated tool followed a wear curve similar to that of commercial TiB$_2$. However, the tool wear in the adaptation phase (first 3 m) was lower, and then, rather than going into the stable state, the tool experienced significantly lower wear up to 10 m, after which the wear progressed quickly until the cutting process was stopped at 25 m of total machining length. The adaptation phase for uncoated and TiB$_2$-coated tools required approximately 2 m of machining as well; however, the stable state continued up to 8 m. This phase was followed by elevated tool wear, although periodic (e.g., for TiB$_2$-C from 8–12 m and 14–16 m) stable states were observed.

5.4.2.4 Tool investigation

Figure 5-14 and Figure 5-15 present the SEM micrographs and EDX elemental analysis (Al represented in green) of the rake surfaces of the worn tools after wet and dry Al-10Si machining. The area covered by Al was calculated using ImageJ software, and the values added to the images. Al adhering to the rake edge could be noticed for all of the samples in Figure 5-14; it was concentrated close to the tool edge, and no aluminium was observed at the flank face. The amount of Al differed by the tool; the highest could be seen for commercial TiB$_2$, the lowest for uncoated and TiB$_2$-TiSi$_2$-coated tool.

The rake faces of the tools after dry machining differed significantly from those rake faces used in the presence of a lubricant. Extensive BUE could be observed on all the tools tested (Figure 5-15). Chipping could be noticed for the uncoated tool and for TiB$_2$-C, while slightly less was seen for TiAlN and TiB$_2$-TiSi$_2$. The uncoated tool had the greatest amount of adhered Al, forming a thick layer on both rake and flank faces. In appearance, the smallest amount of BUE was present on the TiB$_2$-TiSi$_2$ sample, although the area covered was slightly larger than that for TiB$_2$-C.
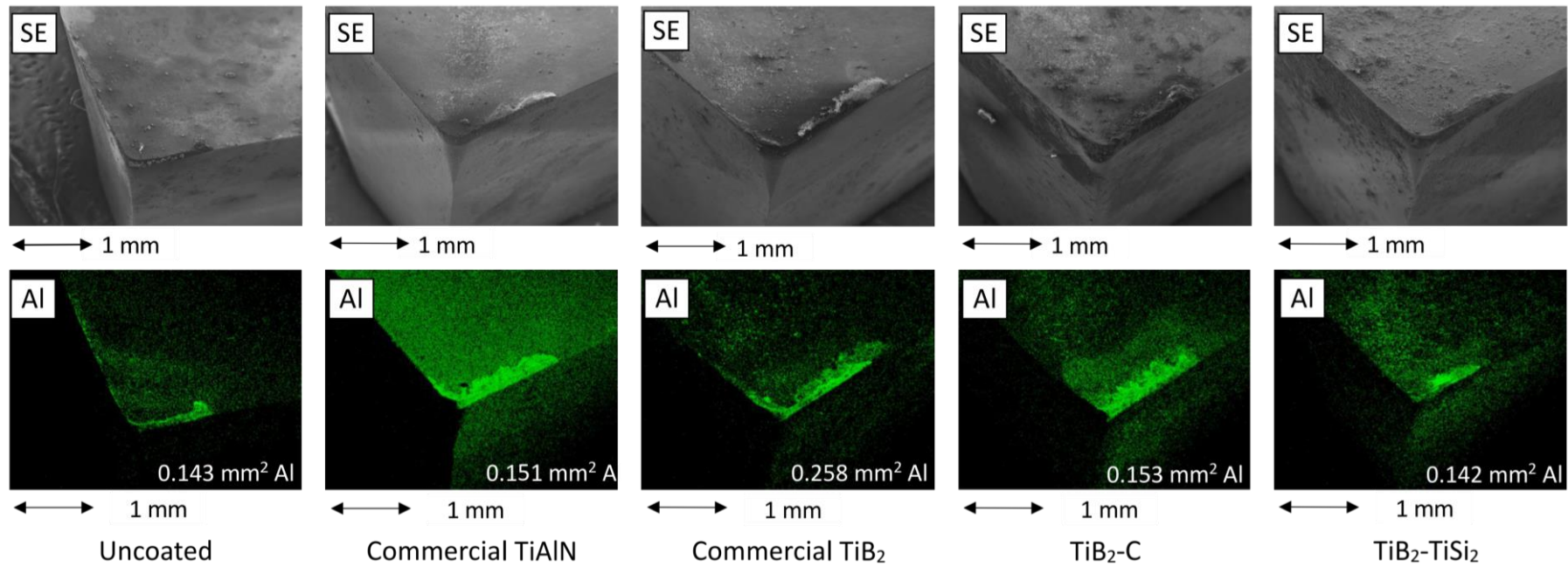
Figure 5-14 Aluminium element mapping images of the rake face of coated mill insert after wet face milling of Al-10Si alloy. Element mapping obtained with EDX mode of SEM.
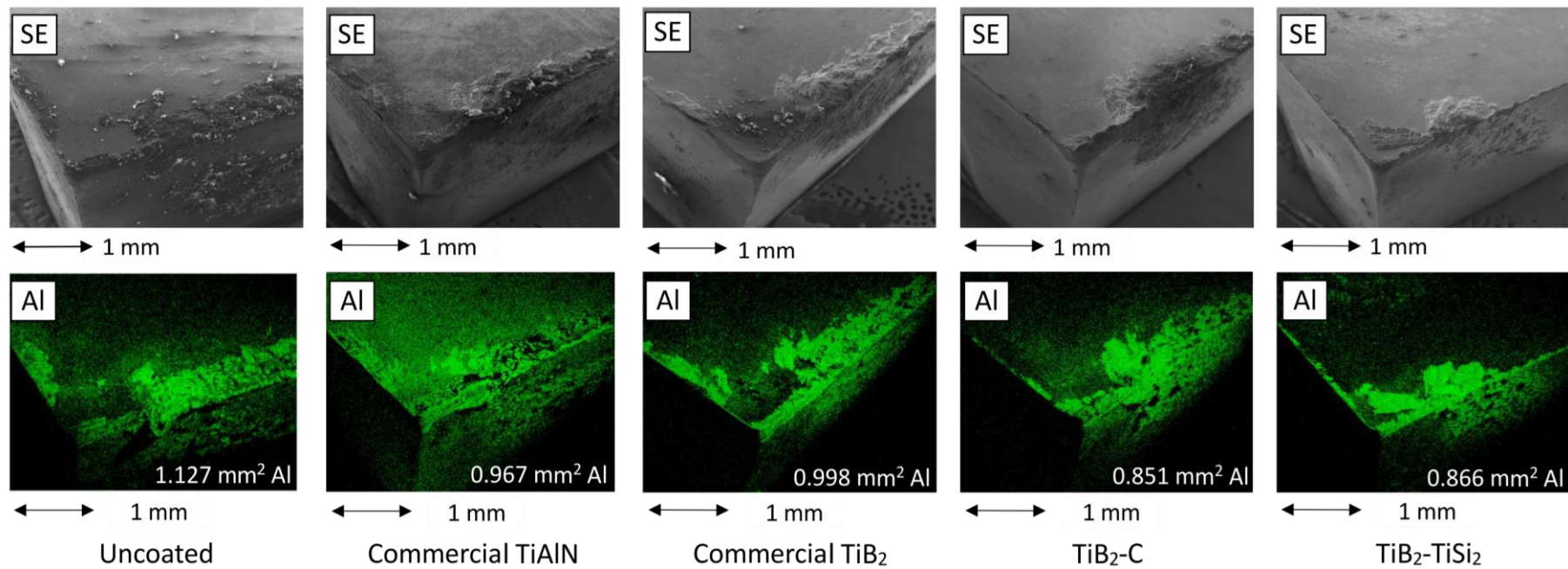
Figure 5-15 Aluminium element mapping images of the flank face of coated mill insert after dry face milling of Al-10Si alloy. Element mapping obtained with EDX mode of SEM.

5.4.2.5 Chip comparison

Analysis of the chips resulting from machining with TiAlN and TiB$_2$-C-coated tools indicated those tools had the greatest and the least flank wear, respectively, after 30 m of wet AlSi machining. Optical images of the chip cross-section displaying the chip microstructure as well as a secondary electron image of the under surface are presented in Figure 5-16. Systematic chip segmentation could be recognised on the TiB$_2$-C chip undersurface, confirming good chip-tool lubrication [221] was provided; therefore, continuous chip flow had taken place.
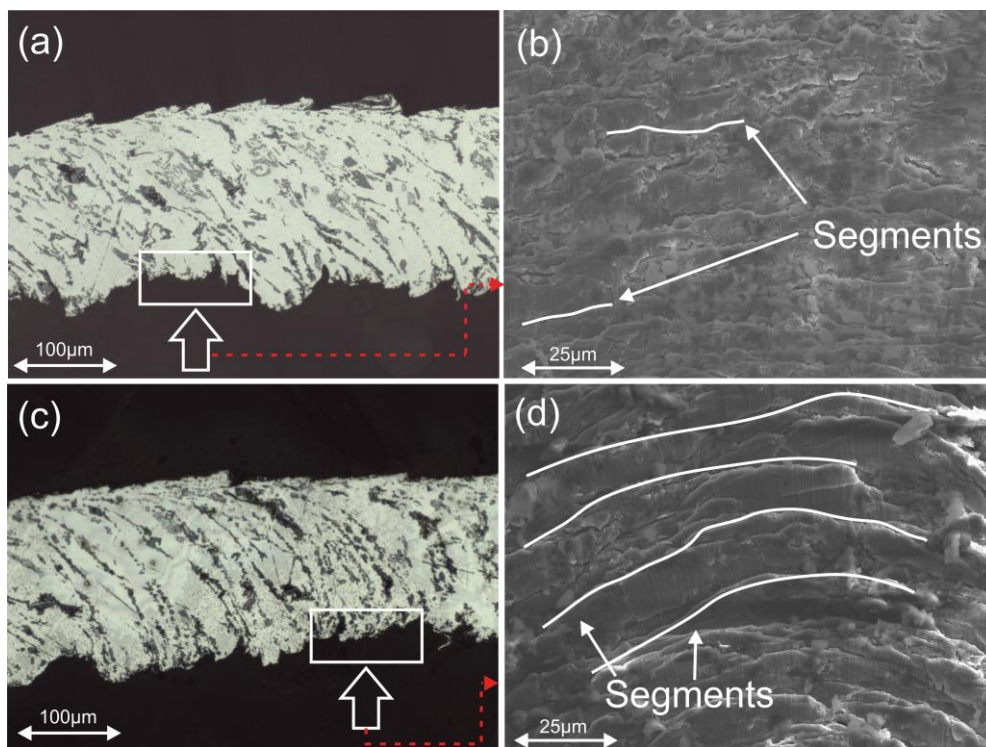
Figure 5-16 Optical images of the chip microstructure after machining with coolant: (a) TiAlN and (c) TiB$_2$-C coated tools. SEM images of the chip under surface: (b) TiAlN (d) TiB$_2$-C coated tools.

By contrast, although some chip segments could be recognised on the TiAlN chip, those segments were irregular, which indicated the chip flow was not continuous and no plastic deformation had occurred [198].

The microstructure and undersurface of the chips obtained from dry machining with uncoated, TiB$_2$ and TiB$_2$-TiSi$_2$ coated tools are presented in Figure 5-17. Regular segments could be observed on all of the chips. However, the segments from the uncoated tool were several times larger than those from other tools. Such chips can be observed when ploughing action takes place instead of cutting, as lubrication is not provided [219,222,223]. Lack of lubrication on uncoated tools resulting in limited plastic deformation could be observed on the chip microstructure as well; many of the grains were undeformed. On the other hand, grain elongation typically associated with good chip-tool area lubrication [221,224], which improves chip flow speed, was observed on chips from both TiB$_2$ and TiB$_2$-C.
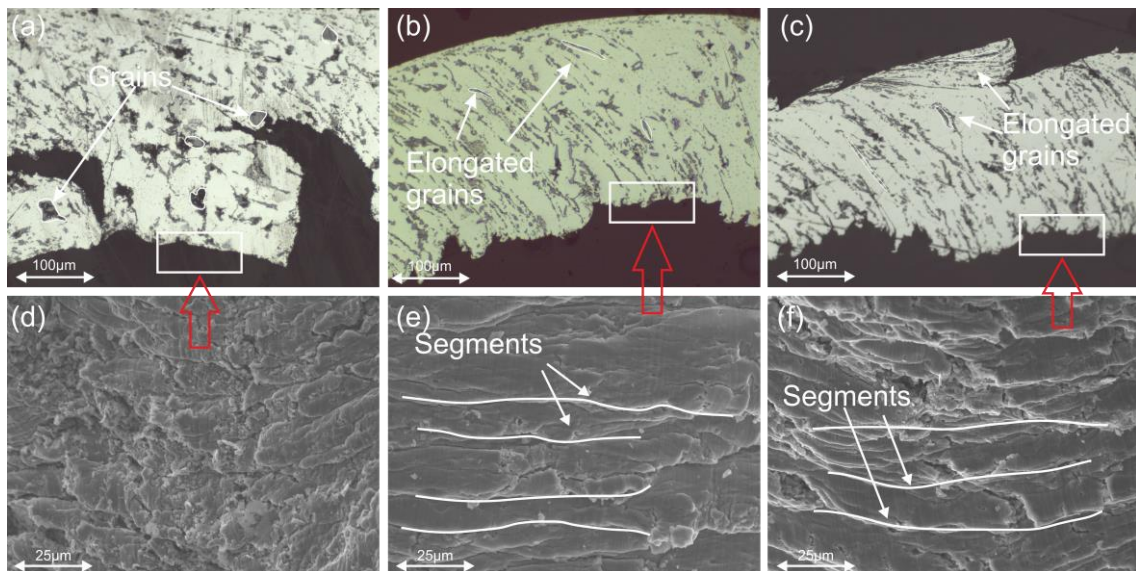
Figure 5-17 Optical images of the chip microstructure after dry machining: (a) uncoated and (b) commercial TiB$_2$-coated and (c) TiB$_2$-TiSi$_2$-coated tools. SEM images of chip under surface: (d) uncoated and (e) commercial TiB$_2$-coated and (f) TiB$_2$-TiSi$_2$-coated tools.

5.5 Discussion

5.5.1 Cathode material

5.5.1.1 Monolithic TiB$_2$

The hardness of the virgin cathode material is equal to 24 GPa and is consistent with previous observations [9]. However, the grain structure observed on SEM micrograph (Figure 5-3) indicated that sintering in the liquid phase was not achieved, as mostly sharp grain edges are present. No sinter additives that could promote liquid-phase sintering [143] were used; therefore, considering the low self-diffusion coefficient of TiB$_2$, which makes it difficult to densify [10], high density was not achieved. The electrical resistivity of this cathode (Figure 5-4) at room temperature is significantly higher than for the other cathodes produced in this work, and it grows more quickly with increasing temperature. This observation matches the results of other researchers [154] who studied the influence of the structure and density of TiB$_2$ on its resistivity. They concluded that good densification could decrease the effect of increasing temperature on TiB$_2$ resistivity. The high temperatures created by the arc can locally melt TiB$_2$ [18], leading to its densification. Zhircov *et al.* [17] proposed that if the density of the virgin cathode was not high, this local densified cathode area could have significantly lower electrical resistivity. The specific arc motion depends on a variety of factors (magnetic fields, local impurities, phases) [94]. However, the increased conductivity caused by densification can lead to the arc spot sticking to a specific location on the TiB$_2$ cathode. Such behaviour was observed when running the arc on the produced monolithic TiB$_2$ cathode; observations by eye confirmed the arc was sticking to a particular location. Also, a very high (compared to other cathodes) arc current (65 A) was required to trigger the arc. The need for high arc current confirms lower electrical conductivity, which correspondingly resulted in poor arc stability and significant cathode fracture caused by high local temperature (more energy carried by the arc spot). The dependence of the thermal expansion coefficient of boride on its temperature can be considered as one of the main reasons for the cathode destruction [9].

Cathode spots can move randomly around the cathode, and spot motion has to be controlled to prevent erosion of supporting structures [54]. The spot motion can be restricted by insulating shields; however, much more definitive control can be ensured only by applying a magnetic field [91]. Typically in industry, a racetrack configuration is used with an arched circular field produced by a magnetic coil [225] or permanent magnet [100]. Previous studies [18] suggested, however, that in the case of arc evaporation of TiB_2, the removal of the magnetic field can decrease cathode fracturing by preventing overheating of a certain area (circular race track) on the cathode [102]. Zharkov *et al.* [17] completely removed the magnetic field, which resulted in a stable and reproducible plasma generation. For the cone-shaped cathode used in this work, the focusing coil applies an axial magnetic field that focuses the arc spot on the front face of the cathode [93]. The filter coil is used mainly to confine the plasma and guide it towards the substrate, but it also influences the arc spot [99]. As the fields coexist, their elimination would result in arc stability problems and spot movement mostly on the side face (where it is triggered) [54,91]. This concept is confirmed by ion voltage measurements on a Cr cathode. When the minimum coil current settings allowed in this system are used, the measured voltage is very low. Also, the magnetic field of the focusing coil has the greatest influence on the average ion voltage, and above 6 A of FtC current, the effect of the FoC is limited. For these reasons, limiting the magnetic field when using a monolithic TiB_2 cathode does not improve arc stability, as it did for other researchers [17,18]. In fact, for FoC, arc triggering is almost impossible. For the highest FoC and FtC currents, the arc is triggered but its high instability throughout the range of currents is the main influence on the measured ion voltage.

5.5.1.2 TiB₂-C

The TiB_2-C produced cathode has a well-densified structure (99.9% TD according to the manufacturer specification), though the grains are larger than for the other cathodes. To achieve good densification without using sintering additives, temperatures close to 2000ºC were used. Extensive grain growth at high temperatures has been reported before and is typical for boride materials

124

[140,226]. The good densification of the cathode resulted in higher room-temperature conductivity (compared to the other cathodes produced) and significantly lower dependence of conductivity on temperature. Also, the hardness of the virgin cathode is found to be close to that of monolithic TiB_2, indicating the addition of C did not have a negative effect on the mechanical properties. The arc stability was substantially improved over the monolithic TiB_2; the minimum arc current needed was just 40 A, and optical observations confirmed good arc mobility. For low FoC and FtC currents, the arc tends to run on the side face of the cathode, resulting in low measured ion voltage. However, increasing currents of both the FoC and the FtC increases the measured ion voltage, and ion voltage is greatest when both of these coils are set to their maximum values. We noticed that an FtC current of 4–5 A is required to confine the plasma to the metal plate used for measurement, as increasing the FoC current above this level results in a significant increase of measured ion voltage.

Densification and the addition of C lead to arc stability. The carbon inclusions locate around TiB_2 crystals and, having better stress resistance, can serve as stopping points for propagating cracks [156,227], although this does not stop completely the destruction of the cathode during arc operation. As evidence of this, constant generation of cathode flakes could be observed when running the arc, no matter what parameters were used. The flakes could be found everywhere around the chamber, though their highest concentration was in the anode and filter tubes. Possibly, the flakes are created as follows: A crack forms and propagates at the cathode surface because of the thermal shock created by the arc spot, but, it stops at the carbon inclusion [31]. Due to the explosive nature of the arc spot [97], a weakly attached flake is released, the spot moves to a different location, and the process repeats. This constant generation of flakes is also the reason for exceptional stability of the arc on this particular cathode, as the tiny volume of the material affected (melted) by the arc is being constantly removed, thus the spot is pushed to start at the new, virgin location. Although the arc movement and stability are improved, the utilisation of the cathode as a result of flaking is poor, with approximately 9 mm of the cathode being consumed per hour.

The same cathode (same composition and manufacturer) was used by Zhircov *et al.* [58] in their work; they, however, do not describe such high cathode consumption. The high cathode consumption in our work may be due to the different arc source configuration used (i.e., a cone-shaped cathode). Zhircov *et al.* [17], used the typical racetrack cathode equipped with a protective stainless steel ring [17], which possibly limited wear. Also, better cathode cooling could be providedd, as their cathode is thinner than the cone-shaped one.

5.5.1.3 TiB$_2$-TiSi

The grain structure of TiB$_2$-TiSi$_2$ indicates good densification, and no extensive grain growth can be observed. The electrical resistivity at room temperature is slightly higher than that observed with the TiB$_2$-C cathode. However, resistivity does grow with increasing temperature in a manner similar to that of TiB$_2$-C, confirming good densification [154]. TiSi$_2$'s phase is liquid at temperatures below 1,700 ºC, therefore, it can wet TiB$_2$ [141]. Despite TiSi$_2$ having a lower hardness (8–10 GPa) [228], its addition did not affect the hardness of the TiB$_2$-TiSi$_2$. A hardness of 23 GPa was measured, which is close to the hardness of monolithic TiB$_2$ (24 GPa). Arc stability and mobility are improved over those seen with monolithic TiB$_2$, and the minimum arc current required is 50 A. Unlike other cathodes tested, multi-spot evaporation (many small spots distributed over a larger area) can be observed. This behaviour is typically observed on poisoned cathodes (deposition in a reactive gas atmosphere), as the ion bombardment charges the contaminants, thereby creating an electric field that enhances the emission of electrons [54]. The rate of charging and the field enhancement and emission onset are very fast, and several emission centres switch on simultaneously [17]. TiSi$_2$ crystals can serve as 'contaminants', the energy per spot is reduced, and a more extensive area is heated by the arc current. As a result, local overheating is reduced, which stabilizes the arc and limits the thermal shock, which in turn limits cathode cracking [54].

The high abundance of particles seen during the arc evaporation is typically associated with a material having a low melting point [54]. Since TiB$_2$ has a high

126

melting point (~3,500 K) [140], it is expected to produce an insignificant number of droplets. However, once the arc is triggered, extensive particle emission can be observed visually as a glowing spark, and these are also found around the chamber after deposition. Similar observations of intense emission of visible droplets have been reported by other researchers [17,18]. Another mechanism for particle generation from materials with a high melting point has been proposed, one that differs from the generally accepted mechanism that is based on the presence of a molten bath and varied plasma pressure [54]. Given the high degree of flaking of the TiB_2-C cathode, we can suggest that particles are produced due to the constant destruction of the thin surface layer of the cathode caused by explosive nature of the arc spot. The layers are smoothed by the high temperature of the arc. As a result, new crystals can be accessed, which decreases the chance that the spot will be immobilised at a single location.

The ion voltage measurements indicate that the stable arc running at the front face can be achieved, although it requires a certain distribution of the magnetic field generated by filtering and focusing coils. Similarly to the TiB_2-C cathode, for FtC currents below 4–5 A, low ion voltage is measured. The optimum currents appear to be an FtC of 8–9 A and an FoC of 6–7 A.

5.5.2 Analysis of deposited coatings

There is no reflection of the intensive flux of glowing particles on the film surfaces. As expected, most of those particles are solid and too big for possible attachment. The film surfaces are smooth, with roughness R_a = 15–18 nm, and only a few droplets are measured. The stoichiometric composition of the coating produced using the TiB_2-C cathode is close to that of monolithic TiB_2. The hardness of the produced coating is slightly higher (21 GPa) than commercial TiB_2 (19GPa) confirming the addition of C did not deteriorate mechanical properties of the TiB_2. For the TiB_2-$TiSi_2$ cathode, the depletion of B can be observed and may be explained by the previously shown dependence of spatial plasma distribution on ion mass [17]. It is known that lighter elements typically have a wider distribution, and a reduced intensity along the cathode normal can be expected for lighter ions

127

as compared to heavier elements [229]. This is consistent with the observed reduction of B, compared with Ti, in a film. The lower B content results in lower hardness (16.4 GPa) compared to commercial TiB_2 obtained for this coating. However even though this hardness value is lower than for commercial TiB_2 it is still high and can be considered as success, since it was obtained for the very first coating deposited from the cathode with novel composition. When used for wet machining, both coatings provide good lubrication and decrease tool wear. In fact, TiB_2-C seems to achieve a steady-state after 13 m and shows little wear increase up to 30 m, exceeding all other coatings tested. In the absence of a lubricant, higher temperatures are achieved, and the coating serves as a source of lubrication [230]. As the thickness of deposited films from our cathodes was lower than 1 µm, they were not able to prevent tool wear. Extensive built-up edge occurred, which can be observed on EDX element maps. Although BUE is undesirable, it can serve as a protective layer that detaches once reaching a certain size [71]. The BUE growth can be observed on the plot as a flat segment that rapidly increases once the BUE detaches.

The initial trials on grounded samples indicated the deposition rate should be equal to 900 nm/hour. However, when the deposition time was raised, it resulted in coatings having just 300 nm and just 26 nm for the biased sample. Application of bias increases the energy of the ions. Therefore, higher compressive stress is introduced in the coating [82]. Treglio *et al*. [19] reported that a -75 V bias applied during pulsed arc TiB_2 deposition leads to fracture and flaking of the coating, which becomes thin and rough. The high roughness of the coating deposited with a -100 V bias in our work supports this conclusion. When a range of biases from 0 to -100 V was applied during a 5-min deposition of thin film, no difference in thickness was observed, confirming that at least a certain thickness has to be achieved to cause coating destruction by compressive stress [19]. As for the grounded substrates, Knotek *et al*. [18] and Zhirkov *et al*. [17] do not report observing thickness limitation, although they also do not report their actual coating thicknesses.

The following parameters were considered as potentially contributing to the unexpectedly thin coatings: low thermal conductivity of TiB_2 (25 W/m*K); greater length of the cathode compared to racetrack configurations; indirect cooling, consequently, an interface with a certain thermal resistance was created between the cathode and Cu backplate. Considering these, we propose cathode overheating as the primary reason for the low thickness of the resulting coatings. Only 10 % of the arc current is transformed into the ion energy [54], while the rest is used to heat the cathode. In case of an insufficient cathode cooling rate, the front face of the cathode becomes seriously overheated, which leads to an increase in electrical resistivity (see Section 3.1.2 Electrical conductivity), which in turn increases the temperature even further. Such behaviour can increase the number of droplets being produced, and as it was found these droplets solidify before reaching the substrate rather than becoming part of it, coating deposition rate decreases drastically. The solution we proposed in this paper was to preheat the substrate before the deposition to 200 ºC (the maximum for the system) and to perform deposition in 5-min evaporation steps, leaving 5-min breaks to cool down the cathode (with the substrate temperature being maintained by heaters to avoid coating stress). This method allowed us to successfully deposit a 780-nm-thick film during 100 min total evaporation time. Our method was a proof-of-concept and indicated that good cathode cooling is essential for TiB_2-coating deposition. In the case of this system configuration with cone-shaped cathodes, higher-flow, very-low-temperature coolant should be used, and the height of the cathode could be decreased to limit the thermal gradient.

5.6 Conclusions

We evaluated the use of TiB_2 for arc evaporation after first densifying its structure and adding non-metallic sinter additives such as C and $TiSi_2$. We successfully tested a cylindrical cone-shaped cathode configuration and compared its attributes to those of monolithic TiB_2 cathodes. The additives did not significantly affect the material hardness. The cathodes have a bulk hardness of 23–24 GPa. Arc was difficult to trigger in monolithic TiB_2 cathodes and required high arc currents of 65 A. Arc spots were found to stick at certain locations, leading to

extensive local fracturing of the cathode. We found TiB_2-C required the lowest current setting (40 A) to trigger an arc and provided the best arc-spot stability and mobility. Carbon inclusions successfully prevented crack propagation, although they did not stop crack initiation, which resulted in high cathode flaking and poor target utilisation. Good densification of both TiB_2-C and TiB_2-$TiSi_2$ cathodes limits the influence of temperature on the conductivity of the cathode material. We observed multi-arc evaporation when operating a TiB_2-$TiSi_2$ cathode and found it decreases the fracturing of the cathode. The currents required to trigger a TiB_2-$TiSi_2$ cathode are slightly higher (50 A) than for TiB_2-C. Contrary to previous reports, appropriate distribution of magnetic fields from filtering and focusing coils was found to be essential for maintaining stable and mobile arc spots on TiB_2-C and TiB_2-$TiSi_2$ cathodes.

Only TiB_2-C and TiB_2-$TiSi_2$ provided arc stability allowing deposition of coatings on the cutting tools. Despite an intense flux of microparticles, the deposited films are smooth with $R_a = 15$–18 nm, indicating the droplets solidify before reaching the substrates. TiB_2-C cathode produced films with TiB_2 stochiometric composition and hardness comparable to the commercial TiB_2. Flank wear assessment during AlSi machining revealed that this TiB_2-C coating provides better protection against abrasive wear than a commercial coating over the course of 35 m of machining. The deposition from TiB_2-$TiSi_2$ resulted in coatings that have a understoichiometric composition. This depletion of boron results in lower measured hardness. However, the machining tests showed good wear protection, resulting in decreased tool wear. We also found that overheating leads to extensive particle generation, which significantly decreases the deposition rate. Deposition in 5-minute steps allowed deposition of 780-nm-thick films, indicating coating cathode temperature has to be controlled and kept low.

6 General discussion

This chapter expands the discussions covered within each chapter by drawing general conclusions, comparing the results and their impact on the current knowledge. Except "Contribution to knowledge" the sub-sections of the discussion are directly related to the three coating systems investigated.

6.1 Combinatorial deposition for rapid optimisation of lubricious coatings for cutting tools

MoS_2-Ti coatings were reported to be successfully implemented for coating cutting tools (section 2.5.3), especially when combined with hard undercoating. Also, previous publication [130] adopted hybrid HIPIMS-MS deposition method for synthesising these coatings. The deposition methods successfully adopted in this thesis expand this concept by using even more energetic FCVA with MS for Ti-MoS_2 deposition on top of hard TiB_2 coating. The Ti:MoS_2 ratio has to be optimised to ensure the balance between the lubricating properties of soft MoS_2 and protective role of Ti. To ensure fast sample production the use of combinatorial deposition was proposed. Although the concept is not new, so far it has been used mostly in the semiconductor industry, with just one approach of using for optimisation of hard coatings (section 2.4.5), still, the silicon wafer was used as a substrate. No studies were found to use this technique for optimisation and deposition on cutting tools. In the proposed solution the samples are placed on the sample holder located equidistant from both FCVA and MS sources. To assess the degree of combinatorial control and understand the relation between the sample composition, roughness and thickness with plasma interactions, novel approach incorporating measurements of ion current by potentiostat has been implemented (Figure 3-2).

The experiments show that the chemical composition of the coatings changes relative to the distance from each deposition source (Figure 3-3). Nevertheless, the FCVA tends to dominate the deposition as the Ti content in the sample placed equidistant from both sources was three times greater than MoS_2 content. In other setups, when only MS sources were employed for combinatorial deposition,

the reported ratio of the components in the canter point of the Si wafer was around 1:1:1 [50]. This observation confirms that FCVA plasmas contain much more energetic ions, which dominates the neutrals from MS. The results show the combinatorial deposition using hybrid FCVA - MS produces samples with chemical composition ranging from few at% to almost 100 at% for each of the components used.

The measurements of the ion current provide an important knowledge about the plasma interaction and distribution when hybrid deposition is used (Figure 3-3 (a)). For the MS the ion current drops gradually with the increasing distance from the source. However, the experiment with only FCVA operating showed that the highest ion current is measured on the sample located the furthest from the source. This unexpected observation can be explained by the tendency of the plasma to expand towards the walls and pressure gradients generated by the pressure plume [105]. Although, as the magnetic field strongly affects the plasma (section 2.4.2.2) the proximity of magnetron's permanent magnets influences the plasma distribution. A large fraction of the ions produced by FCVA is bent towards the magnetron direction, while the samples located close to the FCVA source are more likely to be reached by the non-energetic macroparticles. For this reason, the ion current close to the FCVA is lower than close to MS. This would be an important factor when adopting combinatorial deposition for other geometries of the hybrid deposition chamber. Primarily the industrial coating chambers commonly use multiple sources (e.g. few magnetrons) thus their influence on the plasma distribution can be even higher and will have to be considered when designing the deposition chambers.

When both sources were operating simultaneously, the average current measured for the two samples located with high proximity to MS was lower than when only FCVA was operating. The region close to MS is saturated with neutrals. Therefore Ti ions could lose their energy due to high-intensity collisions with neutrals [187]. Because of charge-exchange, the neutrals can escape from the plasma centre. The ion current profile across the holder was found to reflect the profile of the coating thickness (Figure 3-3 (c)) to a great extent, while the

roughness reflected the proximity to the FCVA source. The FCVA source used in this thesis employs linear filter which due to its geometry allows some of the macroparticles to reach the substrate [54]. As the highest roughness was found for the sample located the closest to the FCVA, it indicates not all the macroparticles were filtered. Due to low energy compared to the ions, the microparticles cannot reach the samples located further from the FCVA source, thus, the roughness decreases.

To evaluate the frictional properties of the produced coatings, progressive load unidirectional sliding test method was used. The typical test employing chrome steel ball and progressive load allowed CoF and adhesion measurements. The CoF was in the range between 0.07 and 0.14, similar to the one reported for HiPIMS-MS deposition method (section 3.3.1.4). From the optical images of the wear tracks (Figure 3-5), it can be concluded the best lubrication and adhesion were provided by the sample having 28 at% (sample b) of Ti. Higher MoS_2 (sample a) content can provide better lubrication, yet, the coating wears completely above 7 N load. On the other hand, very high Ti content does provide excellent adhesion, though little lubrication, therefore, materials transfer from the sliding ball occurs. To evaluate the protection against Al sticking provided by the deposited coatings additional progressive load unidirectional sliding tests were carried out with Al ball serving as an indenter. Only a little Al transfer was observed on the wear track of sample having 28 at% of Al and more for the compositions with higher Ti content what confirmed this composition is optimal for both ensuring low CoF and prevent Al sticking.

The real-life application of the deposited coatings was assessed by dry machining of Al alloy using coated milling tools. Due to limited availability of the blocks to be machined (as explained in section 1.5) the machining length had to be limited to 1.8 m. Nevertheless, for the coatings produced, it allowed assessing the level of protection against Al sticking provided in higher temperatures (typically 200-300ºC during dry machining [20]) than during the sliding tests. Also, the protective tribo-oxides, which form at the beginning of the machining process could be studied. With a help of element maps of the tool edge obtained using EDX after

133

machining tests, it was found that while for samples d and e having high Ti at% content the Al sticking was significant, for samples a and c only thin layer of Al was found on the tool edge. In accordance with the conclusion from the sliding tests sample b appeared to have an optimum composition preventing Al sticking as no Al adhering to the edge could be seen. Even though the machining length was doubled (up to 3.6) for the sample b, still no Al adhered was observed on the EDX Al mapping image of the tool flank face.

The lubricious and protecting tribofilm formation is desired during the running-in stage of machining to promote tool adaptation (section 2.5.3.1). Tribofilms are self-organised patterns which result from the transformation of existing surface layers by means of interaction with the environment [204]. They can carry our protective and lubricating functions. MoS_2 coating typically wears when MoO_2 is formed, which due to volume mismatch with MoO_3 which promotes disintegration of MoS_2 blisters. XPS analysis revealed that sample b had a lower content of MoO_2 comparing to sample c, which performed worse during the tribological tests. More intense sticking of Al to sample c can also be justified by the higher content of brittle, TiO tribo-oxide, which does not play protective a role in the machining temperatures used in this study (below 300 °C) [196,197] and significantly lower amount of lubricating B_2O_3 (4.7 % while 8.2 % for sample b).

To sum up; the experiments showed that combinatorial deposition could be successfully adopted for coating cutting tools using hybrid FCVA-MS. This combination of methods has vast potential for optimisation of tool coatings as proved to provide manufacturing flexibility of multi-sample production under the same process condition but with varying chemical composition. The tribological tests confirmed Ti-MoS_2 coating improves the protection against the Al sticking to the milling inserts precoated with TiB_2. The best results were found for the sample containing 28 at% of Ti.

6.2 Lubricious hard coatings for AlSi machining

Deposition of thin lubricious Ti-MoS_2 layer optimised using combinatorial deposition proved its effectiveness for preventing BUE and improving frictional

properties. Another solution studied in this project attempted to employ for similar purpose DLC coating, which takes full advantage of the energetic nature of FCVA plasma (section 2.5.2). A high fraction of ions in the plasma allows not only to deposit hydrogen-free DLC but also tailor the energy of bombarding particles by substrate bias adjustment. When specific ion energy is used (around 100 eV), the resulting films contain more than 85 % of sp^3 bonds. The experiments performed in this part of the thesis attempted to optimise the DLC coating for wet machining of Al-10Si alloy by substrate-bias adjustment. This alloy is more abrasive than SAE 6061 used for Ti-MoS$_2$ testing due to the higher content of abrasive Si.

An important limitation of hydrogen-free DLC is the operating and deposition temperature which should not exceed 200 ºC [33]. The initial measurements indicated such temperature is achieved after 5 - 11 minutes depending on the substrate bias applied. The high heating rate of the substrate can be related to small dimensions of the milling inserts used and small diameter of the substrate holder (comparing to the industrial holders), what limits the possibility of the substrate to cool down by radiation. As a result of deposition time limitation, the deposited coatings were found to be in the thickness range between 45 and 100 nm. Another study [167] confirmed DLC coating with 100 nm thickness could decrease the roughness of the machined AlMg2.5 and AlCu4.5Si12 alloys comparing to the uncoated tool. The purpose of DLC deposition in this thesis was to prevent severe damage to the tool in the initial stage of the machining. Base on "smart" multilayer coating design [13] the sufficient thickness of the interaction volume in the running-in stage is between 0.1 to 1 μm. Therefore, it was expected for the thin DLC film to improve the tool life.

To avoid material transfer from the ball due to abrasive nature for Si (nanohardness of around 10 GPa [231]), harder WC-Co (nanohardness of 12-20 GPa depending on carbide volume fraction [232]) has been used during the sliding tests. The measurements of the CoF indicated significant improvements in the frictional properties; most of the deposited DLC coatings provided rapid adaptation (CoF increasing for only 20 cycles), with the CoF equal to around 0.22 compared to 0.40 for TiB$_2$ after 100 cycles (Figure 4-3). However, due to the

combination of various factors such as high roughness which governs the sliding process, low coating thickness and macroparticle presence the measured CoF is higher than the one reported by other researchers for ta-C [33]. Ideally, the roughness of the substrate should have been lower to decrease the influence of the roughness on the CoF. Although the samples were as-received TiB_2 coated therefore pre-deposition polishing was not an option. In addition, the sliding tests were carried in dry conditions (due to testing equipment limitations) while the further AlSi milling tests were done in wet conditions. The addition of cooling liquid decrease the influence of roughness as the liquid containing also some sort of lubricant would fill the roughness valleys [71]. The machining tests revealed that most of the coatings decreased the wear in the running-in stage of the machining comparing to TiB_2 benchmark tool. Moreover coating deposited with -100V not only significantly increased the stable state up to 38 meters, but also limited the overall tool wear in this stage. Following EDX Al element mapping confirmed the lowest amount of Al adhered to this particular tool. The outstanding improvements provided by the coatings deposited with -100 V bias can be attributed to the high sp^3 bond content expected for this value of the bias which other studies found to be of around 83 % [162].

Next experiments examined if hybrid FCVA-MS deposition system can be successfully employed for hard, lubricating coating deposition. A previous report [179] indicated that amorphous carbon could be combined with solid lubricant WS_2 to improve its wear resistance in various environments. However, no studies of using hybrid deposition method for this purpose could be found. The experiments performed in this project combined the best performing DLC monolayer (deposited with -100 bias) with sputtered WS_2 layers. CoF measurements were obtained during the dry reciprocating sliding test and showed the drawback of solid lubricants such as WS_2 which is the wear by blistering (section 2.5.3.1). Although the CoF after 20 cycles is low (around 0.17) and then progressively increases up to 60 cycles where it stabilises and matches the CoF of TiB_2. The decrease in friction is caused by filling up the valleys between the roughness peaks [209] and forming a low-friction transfer layer [186].

Though, as the direction of the ball changes in the middle of each cycle part of the transfer layer is left behind. The spalled coating is well visible on the SEM images of the wear tracks (Figure 4-5). Contrary when WS_2 is combined with one DLC layer, the initial CoF is low (around 0.14), only minor increase can be seen after 100 cycles, and no spalled coating can be observed on the SEM image. The adhesion testing during progressive load unidirectional sliding test revealed that both of WS_2 and DLC-WS_2 (2 layers) ensured good adhesion and lubrication in the whole range of the loads applied. Better performance of WS_2 in adhesion test comparing to wear test can be attributed to the fact, that the adhesion test is unidirectional. Thus, the transfer layer is kept in front of the ball, and the increasing load pushes it back to the substrate [186]. Contrary DLC-WS_2d having 24 layers shows clear signs of coating spallation by exposure of the material underneath visible in the optical image in Figure 4-7 and a corresponding increase of AE in Figure 4-8.

The objective of combining DLC with WS_2 was to further improve the adaptation of the tool due to the lubricating properties of WS_2. The AlSi milling test shows that this attempt was successful (Figure 4-10). DLC-WS_2 multilayer coatings having two, and six layers significantly decreased both the wear and the length of the running-in stage. Two-layer DLC-WS_2 also resulted in decreased tool wear in the stable state which is just ¼ of the benchmarked TiB_2 coated tool. Further chip evaluation indicated lower distances between chip segments visible on the chip undersurface comparing to DLC monolayer and TiB_2 benchmark tools. More frequent chip segmentation typically indicates proper tool-chip area lubrication which increases the chip flow speed [222]. It should be recognised that for a full assessment of the performance of produced coatings the surface finish (e.g. roughness) of the machined blocks should have been checked. However, as the machining trials for this project were done externally such investigation could not be undertaken for this occasion.

The coating solutions discussed in this section expand the knowledge about the application and deposition methods of DLC and DLC-WS_2 multilayers. It is shown that if the deposition parameters are tailored, just 100 nm DLC layer can almost

double the stable state length of TiB_2 coated tool what can lead to material saving and machining cost reduction. This finding meets the research question and proves FCVA can be successfully employed to improve mill inserts coating solution for AlSi machining application. Due to the low thickness of the coating required, the overall cost of the tool production should not increase significantly. Combining DLC with WS_2 can further decrease the tool wear by decreasing the length of the running-in stage. The lower tool wear in the stable state should result in a better surface finish of the machined part.

6.3 Arc evaporation of TiB_2

Following the development of coatings improving existing TiB_2 pre-coated tools, this PhD project attempted to employ FCVA for deposition of TiB_2 itself. As arc evaporation of TiB_2 cathodes was known to be challenging these trials were done in the last stage of the project. Therefore, extensive knowledge and experience with the FCVA coating system could be gained during the trials with less challenging Ti and graphite cathodes used for preceding coatings from the project. Consequently, it was significantly easier to understand the challenges of TiB_2 arc evaporation and propose possible solutions. Limited reported attempts indicate the following issues [17–19]:

- Arc spot is sticking to a specific location on the cathode surface.
- Low arc stability (must be triggered very).
- Difficulties with triggering.

No studies were found of the arc spot behaviours on TiB_2 cone-shaped cathodes. The shape is dictated by the different geometry of the source which employs an axial magnetic field, thus the distribution of the magnetic field is different and the cathode utilisation is typically better than in racetrack cathodes (section 2.4.2.2). For the reported attempts, which adopted racetrack cathodes the absence of an external magnetic field improved arc spot movement due to dissipation of the arc energy over a larger area [17–19]. To assess if similar phenomena occur when cone shape is used, the experiments were initially performed on monolithic TiB_2 cathode. Results show that in this configuration strong magnetic field is

necessary to not only keep the arc spot on the front face of the cathode but also allow its triggering (Figure 5-8). Although, the arc spot tends to stick to a specific location and high arc currents (65 A which is almost the maximum of the system) were required to trigger it. This arc spot behaviour also confirmed that exceptional densification of TiB_2 is essential to facilitate stable arc evaporation what was suggested before in the published work [17]. The full densification during hot pressing is challenging due to the low self-diffusion coefficient, high melting point and oxygen contamination of the precursor powders [144]. The use of high temperatures (~2000°C) ensures near the theoretical density of TiB_2 [10] although, this leads to extensive grain growth and anisotropy of the hexagonal structure which is associated with internal stress development and associated microcracking during the cooling phase [140]. The use of conventional sintering aids such as Ni, Co, Fe which decrease the sintering temperature by promoting liquid phase sintering is not applicable for production of cathodes for FCVA, as the use of metallic aids leads also to degradation of hardness and high-temperature properties (described in depth in the section 2.5.1.1). One of the option options is to employ Hot Isostatic Method (HIP) which employs the simultaneous application of heat and hydrostatic pressure thus produces near 100% TD materials while limiting the grain growth. However, both equipment and tooling are more complex, the operation is inherently batch rather than continuous, and the processes overall are more expensive than the sequential approach of compaction followed by conventional sintering [233].

Based on the above observations two additional cathodes were produced using hot pressing method; TiB_2-C and TiB_2-$TiSi_2$. They represent two different approaches to solve the issues; TiB_2-C uses high sintering temperatures to provide the 100 % TD, while the addition of carbon stops the crack propagation. The addition of $TiSi_2$ was carefully decided base on the thermal compatibility with TiB_2 and ability to decrease sintering temperature when used in quantities no higher than 5 wt%. Such addition of $TiSi_2$ improves sinterability of TiB_2 two ways; firstly $TiSi_2$'s phase is liquid at temperatures below 1,700 ºC, thus it can wet TiB_2 [141]. Also, it is well known that nonoxide powders are inherently contaminated by a

thin oxide layer – in case of TiB_2 it is: TiO_2 and B_2O_3. G.Raju *et al.* [144] reported that the presence of such a surface oxide layer adversely affects the densification of the TiB_2 materials by surface diffusivity. The results of experiments conducted by G.Raju *et al.* [144] indicate that if $TiSi_2$ is added to the powder mixture it reacts with the TiO_2 surface layer of the TiB_2 particles and forms Ti_5Si_3 and SiO_2 phases consequently enhancing the densification of TiB_2 by grain shape accommodation.

Ideally, all three cathodes should have been produced by the same manufacturer to limit the influence of equipment and overall production methods on the condition of produced cathodes. Although due to project timescale constraints and overall readiness of the manufacturers to test new compositions, it was not possible to achieve for this PhD thesis project.

For the initial assessment of the cathode performance, the arc spot behaviour was evaluated by eye through the mirror placed in the middle of the chamber. These observations reviled exceptional mobility and stability of the arc on TiB_2-C cathode. Although high flux of cathode flakes was generated, which results in a significant consumption of the cathode – around 9 mm per hour. Similar behaviour was reported by Zhirkov *et al.* [17,58], although the exact cathode utilisation was not described. TiB_2-$TiSi_2$ cathode ensured good arc stability, with spontaneous macroparticle emission. Though, these droplets solidified before reaching the substrate, therefore, do not affect the coating roughness.

The ion voltage measurements provided quantitative data to support this optical observation. The TiB_2-C cathode is similarly influenced by the magnetic field as Cr cathode. Ion voltage increases with an increasing magnetic field (Figure 5-6 (a)), which not only confines the plasma but focuses the arc spot in the front face of the cathode. Other researchers reported before that for the FCVA configuration with the conical cathode, the external magnetic field cannot be eliminated entirely [91]. Instead it has to be tailored for specific cathode material what can be observed especially for TiB_2-$TiSi_2$ cathode. High ion voltage is achieved only for a specific combination of magnetic fields from filtering and focusing coils (Figure 5-6 (d)). Lastly, for monolithic TiB_2 none of the magnetic field configurations

provided high ion voltage, indicating the arc spot was not stable and could not be sustained on the front face of the cathode.

Typically, spot immobilisation on TiB$_2$ is explained by the dependence of the resistivity of TiB$_2$ on density (section 2.5.1.3). High temperature from the arc spot locally densifies the cathode, thus, decreases its electrical resistivity promoting the spot immobilisation as it "prefers" the area with good electrical conductivity. Similar observations were made before on graphite cathodes as the electrical resistivity of graphite decreases with the temperature [54]. The measurements of TiB$_2$ cathodes material resistivity obtained in this study confirm the conclusions made by other researchers [154]; the rate of the resistivity increase with temperature is significantly greater for monolithic TiB$_2$ comparing with both TiB$_2$-C and TiB$_2$-TiSi$_2$.

This PhD thesis also conducted brief study of initial coating, limited by the resources and time, to asses if TiB$_2$ coatings deposited using FCVA can potentially be used to coat cutting tools. Therefore, it was not expected for these coatings to outer perform the commercial TiB$_2$ coating (as it would require further optimisation coating deposition parameters such as temperature or interlayer), rather than indicate the capability. Base on the step-deposition experiments (section 5.4.2) it was found that the cathode overheating limits the maximum thickness of the coatings, which can be deposited (section 5.4.2). Such limitation was not reported for the race track TiB$_2$ cathodes, having significantly lower thickness thus better cooling rate. Only 2/3 of the power supplied to the arc is used for the material removal [91]. Hence, essential changes in the cooling system such as decreasing the temperature of the coolant or increasing the flow are therefore suggested to overcome this issue. Section 2.4.2.5 describes in great detail the heat flow within the cathode-coolant interface.

Even though the thickness of the deposited coatings was below 500 nm, they provided good lubrication of the tool-chip area and improved the chip flow what resulted in decreased tool wear (section 5.4.2.3). In case of the wet machining, the best performance was achieved for TiB$_2$-C coated tool which after 35 m

reached stable phase (Figure 5-12). The studies of chips showed systematic segmentation, which was not observed on the TiAlN coated tool. Regular chip segmentation typically indicates proper lubrication of the tool-chip area as the chip flow is continuous [221].

Dry machining requires an excellent lubrication to prevent BUE and allow tribofilms to form [13]. All of the tested tools were still in the running-in stage after 35 m of machining. Although the wear curves of uncoated tool suggest its outstanding performance especially compared to commercial TiB_2 coated tool (Figure 5-13) the chip flow significantly differs. Lack of lubrication resulted in limited plastic deformation. This is observed in the chip microstructure (Figure 5-17); for the uncoated tool no elongated grains can be noticed. Contrary to chips produced by TiB_2-$TiSi_2$ and commercial TiB_2 coatings show systematic chip segmentation and many elongated grains which typically indicate good tool-chip area lubrication [221,224]. Therefore, based on the findings of other researchers, it can be expected that for longer machining lengths (up to 5000 m) extensive flank edge chipping would occur on uncoated tool due to BUE detachment [13,152]. Contrary coated tools would develop lubricious and protective tribo-oxides, thus providing stable state and extending the machining length [204].

The experiments and solutions proposed in this section contribute to the knowledge of arc evaporation of TiB_2 and highlight different arc spot behaviour on the cone-shaped cathodes. TiB_2-C cathodes were before successfully adopted for racetrack configuration. Yet, when cone shape is used the poor cathode utilisation prevents its use for large scale. Also, adjustment of the magnetic field was found to be essential to ensure good arc stability, what differs from the suggestions made for other cathode shapes. The proposed addition of $TiSi_2$ provides significant improvement and allows stable arc evaporation of TiB_2. Also, the produced films indicate after further research arc evaporation could be used for large scale production of TiB_2 coatings.

6.4 Contribution to knowledge

The findings of this thesis contribute to the current knowledge concerning TiB_2 and its usage for coating cutting tools. The original contribution of this project is summarised below:

- Providing first analysis of the plasma ion current generated during hybrid FCVA-MS deposition, based on chamber configuration.
- Prove that the combinatorial depostion can be succesfully employed to deposit lubricious Ti-MoS$_2$ coatings.
- Unique study of the influence of substrate distance from magnetron and FCVA on the chemical compositio thickness and roughness of advanced Ti-MoS$_2$ coatings.
- First use of hybrid FCVA-MS deposition to produce DLC-WS$_2$ composite coatings.
- Prove that the lifetime of TiB_2 coated milling inserts can be improved by deposition of various thin (<500 nm), lubricious top layers: Ti-MoS$_2$, DLC and DLC-WS$_2$.
- Original use of $TiSi_2$ sintering additives to produce cathodes for FCVA and facilitate arc spot movement during evaporation.
- Unique study of the magnetic field influence on the substrate ion voltage of plasma produced from Cr, monolithic TiB_2, TiB_2-C and TiB_2-$TiSi_2$ cathodes.
- Indication that TiB_2 can be succesfully deposited using FVCA on milling inserts.
- Although the FVCA deposition parameters has to be optimised it was the first study comparing the machining pertofmance of milling inserts commercially coated by MS TiB_2 with the ones coated using FVCA.

Part of the contribution to the knowledge of this project is also expanding the ideas previously reported in the literature:

- TiB$_2$-C previously reported to be used in the arc evaporation sources with 2D geometries of the cathode (see section 5.1) was successfully employed in the source having a cone 3D geometry (cone).
- The knowledge about the magnetic field influence on the arc spot movement was expanded by the studies of its behaviour on TiB$_2$ cone-shaped cathodes.
- DLC was effectively applied to improve WS$_2$ coating tribological performance in machining processes, only use of soft amorphous carbon was reported previously (see section 4.1).

Finally, some of the findings confirm the observations reported previously in the literature:

- Electrical resistivity and its changes in elevated temperatures strongly depends on TiB$_2$ density.
- TiB$_2$ densification is essential to facilitate the arc movement on the cathode surface.
- Negative substrate bias can influence the tribological properties of the deposited DLC coating.

7 Conclusions

This project aimed to produce hard, low friction coatings increasing tool lifetime during lightweight alloy machining by adopting filtered vacuum cathodic arc and its combination with magnetron sputtering. The aim has been accomplished, and the main conclusions from this thesis are:

1. Hybrid FCVA-MS deposition method was for the first time successfully employed for the deposition of lubricating coatings. The machining testing and analysis revealed that from all of the investigated coatings compositions, three can be recommended for AlSi milling:

   1.1. Ti-MoS$_2$ coating having around 28 at% of Ti content for dry machining applications. This particular composition successfully prevented Al sticking to the tool edge after cutting 3.6 m of Al alloy and was found to have lowest CoF of 0.07 for the loads between 40N and 100 N. XPS studies revealed that higher amount of non-protective Ti-O phase could be possibly identified as a reason for greater sticking of Al to the coated tools having different Ti:MoS$_2$ ratios.

   1.2. Thin (100 nm) DLC film deposited with -100 V bias as it increases the machining length of TiB$_2$ precoated milling inserts by around 60% and decreases the BUE effect due to better wear protection of the tool during the running-in stage of the machining.

   1.3. DLC-WS$_2$ bi-layer combining the DLC layers deposited with -100 V bias and sputtered WS$_2$ layers into a total of ~500 nm thick coating. This particular combination shortened the running-in stage to 5 meters. The total tool wear in the stable state was found to be four times lower than for benchmarked TiB$_2$ coated insert which occurred likely due to improved lubrication of the tool-chip area provided by WS$_2$ layer. Also, CoF of 0.2 was measured for this coating.

2. Necessary hybrid FCVA-MS deposition system upgrades such as implementation of planetary rotation of the substrate holders, new gas flow controllers and substrate biasing allowed combinatorial and multilayer coating

deposition. The following conclusions can be made from the trials with coatings produced using this system:

2.1. The combinatorial deposition can be effectively employed to deposit Ti-MoS$_2$ coatings with Ti content ranging from 5 to 97 at %. Ion current measurements indicated a correlation between the variation of the thickness and roughness of the coatings in terms of the ion current.

2.2. The incorporation of rotating substrate holder designed based on the industrial solution allowed for the deposition on DLC monolayers with different substrate biases. By alternating the holder between FCVA and WS$_2$ sources, composite DLC-WS$_2$ coatings can be deposited.

3. TiB$_2$ can be facilitated for arc evaporation in the deposition system with cone-shaped cathode if appropriate sintering additives are used followed by deep understanding of deposition parameters influencing the arc behaviour:

3.1. Unless densified close to 100% TD monolithic TiB$_2$ is not suitable for arc evaporation; triggering the arc requires very high arc currents (65 A), while the arc tends to stay at a specific location on the cathode surface leading to fracture.

3.2. Producing cathodes with densities close to 100 % TD was identified as the primary factor in promoting the arc spot movement.

3.3. TiB$_2$-C cathode provides an exceptional arc spot stability and mobility with a triggering current of 40 A even if low magnetic field is used to steer the arc spot.. The addition of 1 wt% prevents crack propagation into the cathode material. However, the explosive nature of the arc spots still generates cracks on the working surface of the cathode. Therefore an extensive cathode "flaking" occurs resulting in poor utilisation. The resulted hardness is similar to monolithic TiB$_2$ (24 GPa).

3.4. TiB$_2$-TiSi$_2$ cathode ensures the best balance between the arc stability and cathode utilisation with the triggering current of 50 A. Optimising magnetic field distribution was found to be essential to promote the arc spot movement at the front face of the cathode and for our system optimum focusing coil current was equal 7 A to while for filtering coil 8 A.

4. The developed TiB_2 cathodes allowed coating deposition, which was analysed and tested. The main conclusions are:

4.1. Although extensive flux of microparticles is observed for TiB_2-C cathode, the deposited coatings are smooth (R_a=18 nm) and have a stoichiometric composition. The flank wear of the coated tool was lower than for commercial TiB_2 coating during both wet and dry machining.

4.2. The EDX measurement indicate that the coating produced from TiB_2-$TiSi_2$ cathode has an under stochiometric composition. This composition decreased the tool wear and improved the chip flow during dry machining.

4.3. Arc evaporation can produce TiB_2 coatings with hardness close (21 GPa from TiB_2-C cathode and 16.4 GPa from TiB_2-$TiSi_2$ cathode) to that of commercial TiB_2 coating (20 GPa).

4.4. The cathode cooling is essential for TiB_2 deposition in FVCA sources quipped in cone-shaped cathodes. Thick coating deposition was achieved by depositing in 5-minute steps with short breaks to allow cathode cooling. This method allowed to deposit 780 nm thick film in 40 minutes.

8 Recommendations for future work

The present project demonstrated the possibility of improving the tool lifetime by thin lubricious coating and indicated how to facilitate TiB_2 for arc evaporation. However, there is still a room for future work:

1. Optimise further Ti-MoS$_2$ coatings for dry machining. This coating proved to effectively prevent Al sticking to the tool, however an extensive wear studies should be performed to allow use in larger scale.

    1.1. Deposit wider range of chemical compositions. To fully understand the relation between coating composition and preventing BUE, larger number (>10) of samples should be coated using the multi-sample concept.

    1.2. Perform full scale machining tests. The machining length should be extended to reflect the real-life usage and proof the effectiveness of proposed coating solution.

    1.3. Evaluate the Ti-MoS$_2$ coated inserts during wet machining to understand if the cutting performance of the coated tool is improved also in the wet conditions.

2. Further studies of DLC and DLC-WS$_2$ coatings.

    2.1. Deposit the DLC coatings using 90-degree bend filter. This filter should eliminate the microparticles, therefore the resulting films will be uniform.

    2.2. Evaluate the sp^2 and sp^3 bonds in coatings obtained depending on the bias using e.g. EELS or AES and relate it with the machining performance of the samples.

    2.3. Attempt to double the DLC coating thickness and evaluate its influence on tribological properties.

    2.4. Evaluate the influence of certain DLC or DLC-WS$_2$ lubricious coating on the roughness of the matching surface. The tests performed in this thesis showed the significant improvement on the tool wear curve, however better lubrication should also decrease the roughness of the machined surface, what would be an important factor for commercialisation.

    2.5. Deposit and characterise DLC-WS$_2$ coatings with different DLC to WS$_2$ ratios to further optimise the tribological characteristics.

3. Further development of TiB$_2$ cathodes for arc evaporation into a commercial product. TiB$_2$-TiSi$_2$ cathodes showed potential, however, to be used in large scale, further research and optimisation has to be performed:

   3.1. Sinter monolythic TiB$_2$ cathodes using spark-plasma sintering. The results show that densifying the cathodes close to 100% of TD is essential. Recent developments in spark plasma sintering suggest using this method TiB$_2$ can be fully densified without using sinter additives while maintaining the fine grain structure. Potentially if this production method was found to be successful new additives could be searched to improve the thermal conductivity, what could completely prevent cathode fracture.

   3.2. Produce and test TiB$_2$-TiSi$_2$-C cathode. This is an exciting concept as TiB$_2$-C showed an exceptional arc stability, while TiB$_2$-TiSi$_2$ presented much better cathode utilisation. Possibly these two cathode compositions combined could result in TiB$_2$ material ideal for arc evaporation, as TiSi$_2$ addition would improve sinterability while addition of graphite would stop crack propagation.

   3.3. Improve the cathode cooling. Solving the cathode overheating issue is essential for a commercialisation. There are various possibilities; increase the coolant flow and decrease its temperature, decrease the thickness of the cathode or bond the backing plates with a bonding material having good thermal conductivity.

   3.4. Optimise the coating deposition. Substrate heating could be used to decrease the excessive coating stress. Also, an interlayer e.g. Ti would significantly improve the coating adhesion. Substrate bias voltages and polarity should be also extensively studied to ensure good coating adhesion with minimum compressive stress and coating stoichiometry.

   3.5. Produce and test TiB$_2$-TiSi$_2$ cathode with different geometry. Commercial evaporators commonly use flat, rectangular racetrack cathodes rather than cone shaped. As the magnetic field distribution is different therefore the arc behaviours can vary as well.

REFERENCES

1. López de Lacalle LN., Lamikiz A., Sánchez JA., Cabanes I. Cutting conditions and tool optimization in the high-speed milling of aluminium alloys. Proceedings of the Institution of Mechanical Engineers, Part B: Journal of Engineering Manufacture. 2001; 215(9): 1257–1269. Available at: DOI:10.1243/0954405011519312

2. Uhlmann E., Reimers W., Byrne F., Klaus M. Analysis of tool wear and residual stress of CVD diamond coated cemented carbide tools in the machining of aluminium silicon alloys. Production Engineering. 2010; 4(2): 203–209. Available at: DOI:10.1007/s11740-010-0213-x

3. Trent EM., Wright PK. Metal Cutting. Butterworth-Heinemann Ltd., 1991,. 2000. 311–337 p. Available at: DOI:10.1016/B978-075067069-2/50015-2

4. Chen NC., Sun FH. Cutting performance of multilayer diamond coated silicon nitride inserts in machining aluminum-silicon alloy. Transactions of Nonferrous Metals Society of China (English Edition). The Nonferrous Metals Society of China; 2013; 23(7): 1985–1992. Available at: DOI:10.1016/S1003-6326(13)62687-4

5. List G., Nouari M., Géhin D., Gomez S., Manaud JP., Le Petitcorps Y., et al. Wear behaviour of cemented carbide tools in dry machining of aluminium alloy. Wear. 2005; 259(7–12): 1177–1189. Available at: DOI:10.1016/j.wear.2005.02.056

6. Wain N., Thomas NR., Hickman S., Wallbank J., Teer DG. Performance of low-friction coatings in the dry drilling of automotive Al-Si alloys. Surface and Coatings Technology. 2005; 200(5–6): 1885–1892. Available at: DOI:10.1016/j.surfcoat.2005.08.016

7. M. B., M. L., S. H. Evaluation of magnetron-sputtered TiB_2 intended for tribological applications. Surface and Coatings Technology. 2000; 124(2–3): 253–261. Available at: DOI:10.1016/S0257-8972(99)00638-6

8. Mikula M., Grančič B., Buršíková V., Csuba A., Držík M., Kavecký Š., et al. Mechanical properties of superhard TiB$_2$ coatings prepared by DC magnetron sputtering. Vacuum. 2007; 82(2 SPEC. ISS.): 278–281. Available at: DOI:10.1016/j.vacuum.2007.07.036

9. Munro RG. Material properties of titanium diboride. Journal of Research of the National Institute of Standards and Technology. 2000; 105(5): 709. Available at: DOI:10.6028/jres.105.057

10. Basu B., Raju GB., Suri AK. Processing and properties of monolithic TiB$_2$ based materials. International Materials Reviews. 2006; 51(6): 352–374. Available at: DOI:10.1179/174328006X102529

11. Berger M., Larsson M., Hogmark S. Evaluation of magnetron-sputtered TiB$_2$ intended for tribological applications. Surface and Coatings Technology. 2000; 124(2–3): 253–261. Available at: DOI:10.1016/S0257-8972(99)00638-6

12. Chowdhury MSI., Chowdhury S., Yamamoto K., Beake BD., Bose B., El A., et al. Wear behaviour of coated carbide tools during machining of Ti6Al4V aerospace alloy associated with strong built up edge formation. Surface and Coatings Technology. 2017; 313: 319–327. Available at: DOI:10.1016/j.surfcoat.2017.01.115

13. German Fox-Rabinovich GET. Self-organization during friction : Advanced surface-engineered materials and systems design. Journal of Chemical Information and Modeling. 2013. 1689–1699 p. Available at: DOI:10.1017/CBO9781107415324.004

14. Berger M., Coronel E., Olsson E. Microstructure of D.C. magnetron sputtered TiB$_2$ coatings. Surface and Coatings Technology. 2004; 185(2–3): 240–244. Available at: DOI:10.1016/j.surfcoat.2003.12.029

15. Rao J., Rose T., Craig M., Nicholls JR. Wear coatings for high load applications. Procedia CIRP. Elsevier B.V.; 2014; 22(1): 277–280.

Available at: DOI:10.1016/j.procir.2014.07.005

16. Kelesoglu E., Mitterer C. Structure and properties of TiB_2 based coatings prepared by unbalanced DC magnetron sputtering. Surface and Coatings Technology. 1998; 98(1–3): 1483–1489. Available at: DOI:10.1016/S0257-8972(97)00397-6

17. Zhirkov I., Petruhins A., Naslund LA., Kolozsvári S., Polcik P., Rosen J. Vacuum arc plasma generation and thin film deposition from a TiB_2 cathode. Applied Physics Letters. 2015; 107(18). Available at: DOI:10.1063/1.4935152

18. Knotek O., Loffler F., Bohmer M., Breidenbach R., Stobel C. Ceramic cathodes for arc-physical vapour deposition: development and application. Surface and Coatings Technology. 1991; 49(1–3): 263–267. Available at: DOI:10.1016/0257-8972(91)90066-6

19. Treglio JR., Trujillo S., Perry AJ. Deposition of TiB_2 at low temperature with low residual stress by a vacuum arc plasma source. Surface and Coatings Technology. 1993; 61(1–3): 315–319. Available at: DOI:10.1016/0257-8972(93)90245-J

20. Nouari M., List G., Girot F., Coupard D. Experimental analysis and optimisation of tool wear in dry machining of aluminium alloys. Wear. 2003; 255(7–12): 1359–1368. Available at: DOI:10.1016/S0043-1648(03)00105-4

21. Renevier NM., Hampshire J., Fox VC., Witts J., Allen T., Teer DG. Advantages of using self-lubricating , hard , wear-resistant MoS_2 -based coatings. Surface and Coatings Technology. 2001; 142(144): 67–77. Available at: DOI:http://dx.doi.org/10.1016/S0257-8972(01)01108-2

22. Banerjee T., Chattopadhyay AK. Structural, mechanical and tribological properties of WS_2-Ti composite coating with and without hard under layer of TiN. Surface and Coatings Technology. Elsevier B.V.; 2014; 258: 849–

860. Available at: DOI:10.1016/j.surfcoat.2014.07.072

23. Bhaduri D., Kumar R., Jain AK., Chattopadhyay AK. On tribological behaviour and application of TiN and MoS_2-Ti composite coating for enhancing performance of monolayer cBN grinding wheel. Wear. Elsevier B.V.; 2010; 268(9–10): 1053–1065. Available at: DOI:10.1016/j.wear.2010.01.013

24. Watanabe S., Noshiro J., Miyake S. Friction properties of WS_2/MoS_2 multilayer films under vacuum environment. Surface and Coatings Technology. 2004; 188–189(1-3 SPEC.ISS.): 644–648. Available at: DOI:10.1016/j.surfcoat.2004.07.029

25. Li-na Z., Cheng-biao W., Hai-dou W., Bin-shi X., Da-ming Z., Jia-jun L., et al. Microstructure and tribological properties of WS_2/MoS_2 multilayer films. Applied Surface Science. Elsevier B.V.; 2012; 258(6): 1944–1948. Available at: DOI:10.1016/j.apsusc.2011.06.148

26. Kyu S., Hwan Y., Ho K. MoS_2 -Ti composite coatings on tool steel by d.c. magnetron sputtering. 2003; 170: 428–432.

27. Spalvins T. Morphological and frictional behavior of sputtered MoS_2 films. Thin Solid Films. 1982; 96(1): 17–24. Available at: DOI:10.1016/0040-6090(82)90208-5

28. Renevier N., Fox V., Teer D., Hampshire J. Performance of low friction MoS_2/titanium composite coatings used in forming applications. Materials & Design. 2000; 21(4): 337–343. Available at: DOI:10.1016/S0261-3069(99)00083-7

29. Hilton M. Microstructure of cosputter-deposited metal-and oxide-MoS_2 solid lubricant thin films. Journal of materials Research. 1998; 13(4): 1022–1032. Available at: http://journals.cambridge.org/abstract_S0884291400043806

30. Voevodin AA., Neill JPO., Zabinski JS. WC / DLC / WS_2nanocomposite coatings for aerospace tribology. Tribology Letters. 1999; 6: 75–78.

31. Anders A., Fong W., Kulkarni A V., Ryan FW., Singh Bhatia C. Ultrathin diamond-like carbon films deposited by filtered carbon vacuum arcs. IEEE Transactions on Plasma Science. 2001; 29(5 I): 768–775. Available at: DOI:10.1109/27.964472

32. Ren Y. Diamond-like carbon coatings deposited by vacuum arc in artificial hip joints. University of Wuppertal; 2013. Available at: http://nbn-resolving.de/urn/resolver.pl?urn=urn%3Anbn%3Ade%3Ahbz%3A468-20131023-124239-7

33. Robertson J. Diamond-like amorphous carbon. Materials Science and Engineering: R: Reports. 2002; 37(4–6): 129–281. Available at: DOI:10.1016/S0927-796X(02)00005-0

34. Robertson J. Deposition mechanisms for promoting sp3 bonding in diamond-like carbon. Diamond and Related Materials. 1993; 2(5–7): 984–989. Available at: DOI:10.1016/0925-9635(93)90262-Z

35. Kelly P. J., Arnell R. D. Magnetron sputtering: a review of recent developments and applications. Vacuum. 2000; 56(3): 159–172. Available at: DOI:10.1016/S0042-207X(99)00189-X

36. Christy R. Sputtered MoS_2 lubricant coating improvements. Thin Solid Films. 1980; 73(2): 299–307. Available at: DOI:10.1016/0040-6090(80)90493-9

37. Brzezinka T. Investigation of the Cathodic Arc as a Manufacturing Method of CoNiCrAlY overlay coatings. Cranfield Univeristy; 2015.

38. Lindfors P a., Mularie WM., Wehner GK. Cathodic arc deposition technology. Surface and Coatings Technology. 1986; 29(4): 275–290. Available at: DOI:10.1016/0257-8972(86)90001-0

39. Sanders DM. Review of cathodic arc deposition technology at the start of the new millennium. Environmental science & technology. 2000; 34(1): 7A.

40. Vetter J., Kubota K., Isaka M., Mueller J., Krienke T., Rudigier H.

Characterization of advanced coating architectures deposited by an arc-HiPIMS hybrid process. Surface and Coatings Technology. Elsevier B.V; 2018; 350(2017): 154–160. Available at: DOI:10.1016/j.surfcoat.2018.05.075

41. Datta S., Das M., Balla VK., Bodhak S., Murugesan VK. Mechanical, wear, corrosion and biological properties of arc deposited titanium nitride coatings. Surface and Coatings Technology. Elsevier B.V; 2018; 344: 214–222. Available at: DOI:10.1016/j.surfcoat.2018.03.019

42. Bakhit B., Petrov I., Greene JE., Hultman L., Rosén J., Greczynski G. Controlling the B/Ti ratio of TiB_x thin films grown by high-power impulse magnetron sputtering. Journal of Vacuum Science & Technology A: Vacuum, Surfaces, and Films. 2018; 36(3): 030604. Available at: DOI:10.1116/1.5026445

43. Mayrhofer PH., Mitterer C., Hultman L., Clemens H. Microstructural design of hard coatings. Progress in Materials Science. 2006; 51(8): 1032–1114. Available at: DOI:10.1016/j.pmatsci.2006.02.002

44. Panjan P., Drnovšek A., Kovač J. Tribological aspects related to the morphology of PVD hard coatings. Surface and Coatings Technology. 2018; 343(September): 138–147. Available at: DOI:10.1016/j.surfcoat.2017.09.084

45. CLAUSS FJ. Solid Lubricants and Self-Lubricating Solids. Academic Press. 1972; : 268. Available at: DOI:10.1016/B978-0-08-010018-0.50007-3

46. Chien HH., Ma KJ., Vattikuti SVP., Kuo CH., Huo CB., Chao CL. Tribological behaviour of MoS_2/Au coatings. Thin Solid Films. 2010; 518(24): 7532–7534. Available at: DOI:10.1016/j.tsf.2010.05.040

47. Films TS., Essen UGH. Thin Solid Films, 198 (1991) 157-167. 1991; 198: 157–167.

48. V. Bellido-Gonza´lez, A.H.S. Jones a, J. Hampshire T.J. Allen, J. Witts,

D.G. Teer, K.J. Ma DU. Tribological behaviour of high performance MoS$_2$ coatings produced by magnetron sputtering. Surface and Coatings Technology 97. 1997; 97: 687–693. Available at: DOI:http://dx.doi.org/10.1016/S0257-8972(97)00546-X

49. Lengsfeld CS., Shoureshi RA. (19) United States (12). 2008; 1(19). Available at: DOI:US 2010/0311130 Al

50. Cremer R., Neuschütz D. A combinatorial approach to the optimization of metastable multicomponent hard coatings. Surface and Coatings Technology. 2001; 146–147: 229–236. Available at: DOI:10.1016/S0257-8972(01)01472-4

51. Takikawa H., Izumi K., Miyano R., Sakakibara T. DLC thin film preparation by cathodic arc deposition with a super droplet-free system. Surface and Coatings Technology. 2003; 163–164: 368–373. Available at: DOI:10.1016/S0257-8972(02)00629-1

52. Ha PCT., McKenzie DR., Bilek MMM., Kwok SCH., Chu PK., Tay BK. Raman spectroscopy study of DLC films prepared by RF plasma and filtered cathodic arc. Surface and Coatings Technology. 2007; 201(15): 6734–6736. Available at: DOI:10.1016/j.surfcoat.2006.09.048

53. Vetter J. 60years of DLC coatings: Historical highlights and technical review of cathodic arc processes to synthesize various DLC types, and their evolution for industrial applications. Surface and Coatings Technology. Elsevier B.V.; 2014; 257: 213–240. Available at: DOI:10.1016/j.surfcoat.2014.08.017

54. Anders A. Cathodic Arcs Fom fractal spots to energetic condensation. New York: Springer Inc.; 2008. 555 p. Available at: DOI:10.1007/978-0-387-79108-1

55. Zhirkov I., Polcik P., Kolozsvári S., Rosen J. Macroparticle generation in DC arc discharge from a WC cathode. Journal of Applied Physics. 2017;

121(10). Available at: DOI:10.1063/1.4978306

56. Murthy TSRC., Subramanian C., Fotedar RK., Gonal MR., Sengupta P., Kumar S., et al. Preparation and property evaluation of TiB_2 + $TiSi_2$ composite. International Journal of Refractory Metals and Hard Materials. 2009; 27(3): 629–636. Available at: DOI:10.1016/j.ijrmhm.2008.10.001

57. Schultes G., Schmitt M., Goettel D., Freitag-Weber O. Strain sensitivity of TiB_2, TiB_2, $TaSi_2$ and WSi_2 thin films as possible candidates for high temperature strain gauges. Sensors and Actuators, A: Physical. 2006; 126(2): 287–291. Available at: DOI:10.1016/j.sna.2005.05.023

58. Igor Zhirkov, Szilard Kolozsvári, Peter Polcik JR. Vacuum arc plasma generation and thin film synthesis from a TiB2 cathode. Process Systems Engineering. Linkoping; 2016.

59. Ramaswami R. The effect of the built-up-edge(BUE) on the wear of cutting tools. Wear. 1971; 18(1): 1–10. Available at: DOI:10.1016/0043-1648(71)90059-7

60. Schaefer A., Reichenbach M., Fey D. IAENG Transactions on Engineering Technologies. Lecture Notes in Electrical Engineering. 2013. 345–358 p. Available at: DOI:10.1007/978-94-007-4786-9

61. Roy P., Sarangi SK., Ghosh A., Chattopadhyay AK. Machinability study of pure aluminium and Al-12% Si alloys against uncoated and coated carbide inserts. International Journal of Refractory Metals and Hard Materials. Elsevier Ltd; 2009; 27(3): 535–544. Available at: DOI:10.1016/j.ijrmhm.2008.04.008

62. Berger M., Hogmark S. Evaluation of TiB_2 coatings in sliding contact against aluminium. Surface and Coatings Technology. 2002; 149(1): 14–20. Available at: DOI:10.1016/S0257-8972(01)01361-5

63. dos Santos GR., da Costa DD., Amorim FL., Torres RD. Characterization of DLC thin film and evaluation of machining forces using coated inserts in

turning of Al-Si alloys. Surface and Coatings Technology. 2007; 202(4–7): 1029–1033. Available at: DOI:10.1016/j.surfcoat.2007.07.100

64. Hutchings, Ian PS. Tribology Friction and Wear of Engineering Materials. Second. Cabridge: Elsevier Ltd; 2017. 386 p. Available at: https://www.mendeley.com/catalogue/tribology-friction-wear-engineering-materials-1/

65. Totten GE., Xie L., Funatani K. Modeling and Simulation for Material Selection and Mechanical Design. New York; 2005. 474 p.

66. Konca E., Cheng YT., Weiner AM., Dasch JM., Erdemir A., Alpas AT. Transfer of 319 Al alloy to titanium diboride and titanium nitride based (TiAlN, TiCN, TiN) coatings: Effects of sliding speed, temperature and environment. Surface and Coatings Technology. 2005; 200(7): 2260–2270. Available at: DOI:10.1016/j.surfcoat.2004.10.008

67. Vereschaka AA., Grigoriev SN., Vereschaka AS., Popov AY., Batako AD. Nano-scale multilayered composite coatings for cutting tools operating under heavy cutting conditions. Procedia CIRP. Elsevier B.V.; 2014; 14: 239–244. Available at: DOI:10.1016/j.procir.2014.03.070

68. Aoyama T. Development of a Mixture Supply System for Machining with Minimal Quantity Lubrication. CIRP Annals - Manufacturing Technology. 2002; 51(1): 289–292. Available at: DOI:10.1016/S0007-8506(07)61519-4

69. Obikawa T. Machining with Least Quantity Lubrication. Comprehensive Materials Processing. Elsevier; 2014. pp. 255–281. Available at: DOI:10.1016/B978-0-08-096532-1.01114-6

70. Itoigawa F., Childs THC., Nakamura T., Belluco W. Effects and mechanisms in minimal quantity lubrication machining of an aluminum alloy. Wear. 2006; 260(3): 339–344. Available at: DOI:10.1016/j.wear.2005.03.035

71. Shokrani A., Dhokia V., Newman ST. Environmentally conscious

machining of difficult-to-machine materials with regard to cutting fluids. International Journal of Machine Tools and Manufacture. Elsevier; 2012; 57: 83–101. Available at: DOI:10.1016/j.ijmachtools.2012.02.002

72. Braga DU., Diniz AE., Miranda GWA., Coppini NL. Using a minimum quantity of lubricant (MQL) and a diamond coated tool in the drilling of aluminum-silicon alloys. Journal of Materials Processing Technology. 2002; 122(1): 127–138. Available at: DOI:10.1016/S0924-0136(01)01249-3

73. Dosbaeva J., Fox-Rabinovich G., Dasch J., Veldhuis S. Enhancement of wet- and MQL-based machining of automotive alloys using cutting tools with DLC/polymer surface treatments. Journal of Materials Engineering and Performance. 2008; 17(3): 346–351. Available at: DOI:10.1007/s11665-008-9209-5

74. Sreejith PS. Machining of 6061 aluminium alloy with MQL, dry and flooded lubricant conditions. Materials Letters. 2008; 62(2): 276–278. Available at: DOI:10.1016/j.matlet.2007.05.019

75. Sharma VS., Dogra M., Suri NM. Cooling techniques for improved productivity in turning. International Journal of Machine Tools and Manufacture. 2009; 49(6): 435–453. Available at: DOI:10.1016/j.ijmachtools.2008.12.010

76. Li KM., Liang SY. Performance profiling of minimum quantity lubrication in machining. International Journal of Advanced Manufacturing Technology. 2007; 35(3–4): 226–233. Available at: DOI:10.1007/s00170-006-0713-1

77. Fox-Rabinovich G., Dasch JM., Wagg T., Yamamoto K., Veldhuis S., Dosbaeva GK., et al. Cutting performance of different coatings during minimum quantity lubrication drilling of aluminum silicon B319 cast alloy. Surface and Coatings Technology. Elsevier B.V.; 2011; 205(16): 4107–4116. Available at: DOI:10.1016/j.surfcoat.2011.03.006

78. Ju-Wan Lima H. Ahn, K.-T. Rie J-JL. Dry and semi-dry machining using finely crystallized diamond coating cutting tools. Surface and Coatings Technology. 2003; 174–175: 720–724. Available at: DOI:10.1016/S0257-8972

79. Bhowmick S., Alpas AT. Minimum quantity lubrication drilling of aluminium-silicon alloys in water using diamond-like carbon coated drills. International Journal of Machine Tools and Manufacture. 2008; 48(12–13): 1429–1443. Available at: DOI:10.1016/j.ijmachtools.2008.04.010

80. Berger M., Hogmark S. Tribological properties of selected PVD coatings when slid against ductile materials. Wear. 2002; 252(7–8): 557–565. Available at: DOI:10.1016/S0043-1648(02)00011-X

81. Baptista A., Silva FJG., Porteiro J., Míguez JL., Pinto G., Fernandes L. On the Physical Vapour Deposition (PVD): Evolution of Magnetron Sputtering Processes for Industrial Applications. Procedia Manufacturing. Elsevier B.V.; 2018; 17: 746–757. Available at: DOI:10.1016/j.promfg.2018.10.125

82. Anders A. A review comparing cathodic arcs and high power impulse magnetron sputtering (HiPIMS). Surface and Coatings Technology. Elsevier B.V.; 2014; 257: 308–325. Available at: DOI:10.1016/j.surfcoat.2014.08.043

83. Vetter J., Burgmer W., Dederichs HG., Perry AJ. The Architecture and Performance of Compositionally Gradient and Multi-Layer PVD Coatings. Materials Science Forum. 1994; 163–165(iii): 527–532. Available at: DOI:10.4028/www.scientific.net/MSF.163-165.527

84. A, Martina Gassner, Marisa Rebelo de Figueiredo , Nina Schalk, Robert Franz, Christian Weiß, Helmut Rudigier, Helga Holzschuh, WernerBürgin, Markus Pohler, Christoph Czettl CM. Energy consumption and material fluxes in hard coating deposition processes. Surface & Coatings Technology. Elsevier B.V.; 2016; 299: 49–55. Available at: DOI:10.1016/j.surfcoat.2016.04.062

85. Baptista A., Silva F., Porteiro J., Míguez J., Pinto G. Sputtering Physical Vapour Deposition (PVD) Coatings: A Critical Review on Process Improvement and Market Trend Demands. Coatings. 2018; 8(11): 402. Available at: DOI:10.3390/coatings8110402

86. Musil J., Vlček J. Magnetron sputtering of hard nanocomposite coatings and their properties. Surface and Coatings Technology. 2001; 142–144: 557–566. Available at: DOI:10.1016/S0257-8972(01)01139-2

87. Mattox DM. Handbook of Physical Vapor Deposition (PVD) Processing: Film Formation, Adhesion, Surface Preparation and Contamination Control. Materials and Manufacturing Processes. 1998. 943 p. Available at: DOI:10.1080/10426919908907566

88. Martin PM. Hand Book of Depositions techniques for films and coatings science, applications and technology. Journal of Chemical Information and Modeling. 2013. 912 p. Available at: DOI:10.1017/CBO9781107415324.004

89. Tracton AA. Coatings Technology Handbook. JUNGERMANN E (ed.) Taylor & Francis; 2005. 936 p.

90. Brown IG. Cathodic Arc Deposition of Films. Annual Review of Materials Science. 1998; 28(1): 243–269. Available at: DOI:10.1146/annurev.matsci.28.1.243

91. Boxman RL., Zhitomirsky VN. Vacuum arc deposition devices. Review of Scientific Instruments. 2006; 77(2). Available at: DOI:10.1063/1.2169539

92. Takikawa H. Review of Cathodic Arc Deposition for Preparing Droplet-Free Thin Films. Thin Films. 2006; : 525–530.

93. Jütner B. Characterization of the cathode spot. IEEE Transactions on Plasma Science. 1987; 15(5): 474–480. Available at: DOI:10.1109/TPS.1987.4316740

94. Anders A. The fractal nature of vacuum arc cathode spots. IEEE

Transactions on Plasma Science. 2005; 33(5 I): 1456–1464. Available at: DOI:10.1109/TPS.2005.856488

95. Oks EM., Anders A. Measurements of the ion species of cathodic arc plasma in an axial magnetic field. IEEE Transactions on Plasma Science. 2011; 39(6 PART 1): 1272–1276. Available at: DOI:10.1109/TPS.2011.2106518

96. Sanders DM. Review of cathodic arc deposition technology at the start of the new millennium. 2000; : 78–90.

97. Liu H., Li L., Gu J., Wang Q., Huang K., Xu Y. Research on unusual cathode erosion patterns in the process of filtered cathodic vacuum arc deposition. International Journal of Advanced Manufacturing Technology. 2018; 96(5–8): 1779–1785. Available at: DOI:10.1007/s00170-017-1152-x

98. Karpov DA. Cathodic arc sources and macroparticle filtering. Surface and Coatings Technology. 1997; 96(1): 22–33. Available at: DOI:10.1016/S0257-8972(98)80008-X

99. Aksyonov DS., Aksenov II., Zadneprovsky YA., Loboda AM., Mel SI., Shulayev VM. Vacuum-Arc Plasma Source With Steered Cathode Spot. Problems of Atomic Science and Technology-Plasma Physics. 2008; (14): 210–212.

100. Davy SH. Handbook of Vacuum Arc Science and Technology. Handbook of Vacuum Arc Science and Technology. 1996; : 709–736. Available at: DOI:10.1016/B978-081551375-9.50026-6

101. Anders S., Anders A., Yu KM., Yao XY., Brown IG. On the Macroparticle Flux from Vacuum Arc Cathode Spots. IEEE Transactions on Plasma Science. 1993; 21(5): 440–446. Available at: DOI:10.1109/27.249623

102. Zhirkov I., Petruhins A., Rosen J. Effect of cathode composition and nitrogen pressure on macroparticle generation and type of arc discharge in a DC arc source with Ti-Al compound cathodes. Surface and Coatings

Technology. Elsevier B.V.; 2015; 281: 20–26. Available at: DOI:10.1016/j.surfcoat.2015.09.030

103. Harris SG., Vlasveld AC., Doyle ED., Dolder PJ. Dry machining - commercial viability through filtered arc vapour deposited coatings. Surface and Coatings Technology. 2000; 133–134: 383–388. Available at: DOI:10.1016/S0257-8972(00)00895-1

104. Bilek MMM., Anders A. Designing advanced filters for macroparticle removal from cathodic arc plasmas. Plasma Sources Science and Technology. 1999; 8(3): 488–493. Available at: DOI:10.1088/0963-0252/8/3/319

105. Ivanov VA., Pursch H. Time-resolved measurements of the parameters of arc cathode plasmas in vacuum. IEEE Transactions on Plasma Science. 1985; (5): 334–336.

106. Plasmaterials I. Bonding. 2018. Available at: https://www.plasmaterials.com/products/bonding/ (Accessed: 8 January 2019)

107. Bunshah RF. Handbook of Hard Coatings. Bunshah RF (ed.) Norwich, New York: WILLIAM ANDREW PUBLISHING; 2002. 560 p.

108. PalDey S., Deevi S. Single layer and multilayer wear resistant coatings of (Ti, Al) N: a review. Materials Science and Engineering: A. 2003; 342: 58–79. Available at: DOI:10.1016/S0921-5093(03)00473-8

109. M. Mattox D. The Foundation of Vacuum Coating Technology. New Mexico: Springer; 2003. 150 p.

110. Sarhammar E. Sputtering and Characterization of Complex Multi-element Coatings. 2014. Available at: http://urn.kb.se/resolve?urn=urn:nbn:se:uu:diva-229207

111. Bobzin K., Brögelmann T., Kalscheuer C., Liang T. High-rate deposition of thick (Cr,Al)ON coatings by high speed physical vapor deposition. Surface

and Coatings Technology. 2017; 322: 152–162. Available at: DOI:10.1016/j.surfcoat.2017.05.034

112. Liu MJ., Zhang M., Zhang Q., Yang GJ., Li CX., Li CJ. Gaseous material capacity of open plasma jet in plasma spray-physical vapor deposition process. Applied Surface Science. Elsevier B.V.; 2018; 428: 877–884. Available at: DOI:10.1016/j.apsusc.2017.09.218

113. Schönjahn C., Bamford M., Donohue LA., Lewis DB., Forder S., Münz WD. The interface between TiAlN hard coatings and steel substrates generated by high energetic Cr+ bombardment. Surface and Coatings Technology. 2000; 125(1–3): 66–70. Available at: DOI:10.1016/S0257-8972(99)00552-6

114. Poolcharuansin P., Bradley JW. Short- and long-term plasma phenomena in a HiPIMS discharge. Plasma Sources Science and Technology. 2010; 19(2): 025010. Available at: DOI:10.1088/0963-0252/19/2/025010

115. Samuelsson M. Fundamental aspects of HiPIMS under industrial conditions, PhD Thesis. 2012.

116. Gudmundsson JT. The high power impulse magnetron sputtering discharge as an ionized physical vapor deposition tool. Vacuum. Elsevier Ltd; 2010; 84(12): 1360–1364. Available at: DOI:10.1016/j.vacuum.2009.12.022

117. Sarakinos K., Alami J., Konstantinidis S. High power pulsed magnetron sputtering: A review on scientific and engineering state of the art. Surface and Coatings Technology. Elsevier B.V.; 2010; 204(11): 1661–1684. Available at: DOI:10.1016/j.surfcoat.2009.11.013

118. Gudmundsson JT., Brenning N., Lundin D., Helmersson U. High power impulse magnetron sputtering discharge. Journal of Vacuum Science & Technology A: Vacuum, Surfaces, and Films. 2012; 30(May): 030801–030834. Available at: DOI:10.1116/1.3691832

119. Lundin D., Sarakinos K. An introduction to thin film processing using high-power impulse magnetron sputtering. Journal of Materials Research. 2012; 27(05): 780–792. Available at: DOI:10.1557/jmr.2012.8

120. Anders A. Discharge physics of high power impulse magnetron sputtering. Surface and Coatings Technology. Elsevier B.V.; 2011; 205(SUPPL. 2): S1–S9. Available at: DOI:10.1016/j.surfcoat.2010.01.016

121. Lewin E., Loch D., Montagne A., Ehiasarian AP., Patscheider J. Comparison of Al-Si-N nanocomposite coatings deposited by HIPIMS and DC magnetron sputtering. Surface and Coatings Technology. Elsevier B.V.; 2013; 232: 680–689. Available at: DOI:10.1016/j.surfcoat.2013.06.076

122. Gassner M., Schalk N., Sartory B., Pohler M., Czettl C., Mitterer C. Influence of Ar ion etching on the surface topography of cemented carbide cutting inserts. International Journal of Refractory Metals and Hard Materials. Elsevier; 2017; 69(March): 234–239. Available at: DOI:10.1016/j.ijrmhm.2017.08.015

123. Schönjahn C., Lewis DB., Petrov I. Shortlisted substrate ion etching in combined steered cathodic arc–ubm deposition system: effects on interface architecture, adhesion, and tool performance. Surface Engineering. 2000; 16(2): 176–180. Available at: DOI:10.1179/026708400101516973

124. Barshilia HC., Ananth A., Khan J., Srinivas G. Ar + H2 plasma etching for improved adhesion of PVD coatings on steel substrates. Vacuum. 2012; 86(8): 1165–1173. Available at: DOI:10.1016/j.vacuum.2011.10.028

125. Münz WD., Hauzer FJM., Schulze D., Buil B. A new concept for physical vapor deposition coating combining the methods of arc evaporation and unbalanced-magnetron sputtering. Surface and Coatings Technology. 1991; 49(1–3): 161–167. Available at: DOI:10.1016/0257-8972(91)90049-3

166

126. Gebretsadik DW., Hardell J., Efeoğlu I., Prakash B. Tribological properties of composite multilayer coating. Tribology - Materials, Surfaces & Interfaces. 2011; 5(3): 100–106. Available at: DOI:10.1179/1751584X11Y.0000000015

127. Vereshchaka AA., Vereshchaka AS., Mgaloblishvili O., Morgan MN., Batako AD. Nano-scale multilayered-composite coatings for the cutting tools. International Journal of Advanced Manufacturing Technology. 2014; 72(1–4): 303–317. Available at: DOI:10.1007/s00170-014-5673-2

128. Yamamoto K., Kujime S., Takahara K. Properties of nano-multilayered hard coatings deposited by a new hybrid coating process: Combined cathodic arc and unbalanced magnetron sputtering. Surface and Coatings Technology. 2005; 200(1-4 SPEC. ISS.): 435–439. Available at: DOI:10.1016/j.surfcoat.2005.02.175

129. Guðmundsson JT. On the Plasma Parameters in the High Power Impulse Magnetron Sputtering Discharge (HiPIMS). 2007; (May).

130. Qin X., Ke P., Wang A., Kim KH. Microstructure, mechanical and tribological behaviors of MoS_2-Ti composite coatings deposited by a hybrid HIPIMS method. Surface and Coatings Technology. Elsevier B.V.; 2013; 228: 275–281. Available at: DOI:10.1016/j.surfcoat.2013.04.040

131. Renevier NM., Lobiondo N., Fox VC., Teer DG., Hampshire J. Performance of MoS_2/metal composite coatings used for dry machining and other industrial applications. Surface and Coatings Technology. 2000; 123(1): 84–91. Available at: DOI:10.1016/S0257-8972(99)00424-7

132. Hanak JJ. The ``multiple-sample concept'' in materials research: Synthesis, compositional analysis and testing of entire multicomponent systems. Journal of Materials Science. 1970; 5(11): 964–971. Available at: DOI:10.1007/BF00558177

133. Xiang Xiao-Dong TI. Combinational Materials Synthesis. New York: Marcel

Dekker; 2003.

134. Vepřek S. The search for novel, superhard materials. Journal of Vacuum Science & Technology A: Vacuum, Surfaces, and Films. 1999; 17(5): 2401. Available at: DOI:10.1116/1.581977 (Accessed: 30 March 2016)

135. Muster TH., Trinchi A., Markley TA., Lau D., Martin P., Bradbury A., et al. A review of high throughput and combinatorial electrochemistry. Electrochimica Acta. Elsevier Ltd; 2011; 56(27): 9679–9699. Available at: DOI:10.1016/j.electacta.2011.09.003

136. Grančič B., Mikula M., Hrubá L., Gregor M., Štefečka M., Csuba A., et al. The influence of deposition parameters on TiB_2 thin films prepared by DC magnetron sputtering. Vacuum. 2005; 80(1–3): 174–177. Available at: DOI:10.1016/j.vacuum.2005.08.013

137. Murthy TSRC., Basu B., Balasubramaniam R., Suri AK., Subramanian C., Fotedar RK. Processing and properties of TiB_2 with $MoSi_2$ sinter-additive: A first report. Journal of the American Ceramic Society. 2006; 89(1): 131–138. Available at: DOI:10.1111/j.1551-2916.2005.00652.x

138. Vlasova M., Bykov A., Kakazey M., Aguilar PAM., Melnikov I., Rosales I., et al. Formation and properties of TiB_2–Ni composite ceramics. Science of Sintering. 2016; 48(2): 137–146. Available at: DOI:10.2298/SOS1602137V

139. Sabahi Namini A., Motallebzadeh A., Nayebi B., Shahedi Asl M., Azadbeh M. Microstructure–mechanical properties correlation in spark plasma sintered Ti–4.8 wt.% TiB_2 composites. Materials Chemistry and Physics. Elsevier; 2019; 223(March 2018): 789–796. Available at: DOI:10.1016/j.matchemphys.2018.11.057

140. Balcı Ö., Burkhardt U., Schmidt M., Hennicke J., Barış Yağcı M., Somer M. Densification, microstructure and properties of TiB_2 ceramics fabricated by spark plasma sintering. Materials Characterization. 2018; 145(April): 435–443. Available at: DOI:10.1016/j.matchar.2018.09.010

141. Biswas K., Basu B., Suri AK., Chattopadhyay K. A TEM study on TiB$_2$ - 20%MoSi$_2$ composite: Microstructure development and densification mechanism. Scripta Materialia. 2006; 54(7): 1363–1368. Available at: DOI:10.1016/j.scriptamat.2005.12.001

142. Murthy TSRC., Sonber JK., Subramanian C., Hubli RC., Suri AK. Densification, characterization and oxidation studies of TiB$_2$ - WSi$_2$ composite. International Journal of Refractory Metals and Hard Materials. 2012; 33: 10–21. Available at: DOI:10.1016/j.ijrmhm.2012.02.002

143. Murthy TSRC., Basu B., Srivastava A., Balasubramaniam R., Suri AK. Tribological properties of TiB$_2$ and TiB$_2$ - MoSi$_2$ ceramic composites. Journal of the European Ceramic Society. 2006; 26(7): 1293–1300. Available at: DOI:10.1016/j.jeurceramsoc.2005.01.054

144. Raju GB., Basu B. Densification, sintering reactions, and properties of titanium diboride with titanium disilicide as a sintering aid. Journal of the American Ceramic Society. 2007; 90(11): 3415–3423. Available at: DOI:10.1111/j.1551-2916.2007.01911.x

145. Raju GB., Basu B., Tak NH., Cho SJ. Temperature dependent hardness and strength properties of TiB$_2$ with TiSi$_2$ sinter-aid. Journal of the European Ceramic Society. 2009; 29(10): 2119–2128. Available at: DOI:10.1016/j.jeurceramsoc.2008.11.018

146. Lubas J. Assessment and application of TiB$_2$ coating in sliding pair under lubrication conditions. Wear. Elsevier; 2012; 296(1–2): 504–509. Available at: DOI:10.1016/j.wear.2012.08.005

147. Park B., Jung DH., Kim H., Yoo KC., Lee JJ., Joo J. Adhesion properties of TiB$_2$ coatings on nitrided AISI H13 steel. Surface and Coatings Technology. 2005; 200(1-4 SPEC. ISS.): 726–729. Available at: DOI:10.1016/j.surfcoat.2005.01.064

148. Berger M., Karlsson L., Larsson M., Hogmark S. Low stress TiB2 coatings

with improved tribological properties. Thin Solid Films. 2001; 401(1–2): 179–186. Available at: DOI:10.1016/S0040-6090(01)01481-X

149. Mikula M., Grančič B., Roch T., Plecenik T., Vávra I., Dobročka E., et al. The influence of low-energy ion bombardment on the microstructure development and mechanical properties of TiB_2 coatings. Vacuum. 2011; 85(9): 866–870. Available at: DOI:10.1016/j.vacuum.2010.12.011

150. Petrov I., Hall A., Mei AB., Nedfors N., Zhirkov I., Rosen J., et al. Controlling the boron-to-titanium ratio in magnetron-sputter-deposited TiB_x thin films. Journal of Vacuum Science & Technology A: Vacuum, Surfaces, and Films. 2017; 35(5): 050601. Available at: DOI:10.1116/1.4982649

151. BULBUL F., EFEOGLU I. STRESS-RELIEF SOLUTIONS FOR BRITTLE TiB 2 COATINGS . Surface Review and Letters. 2012; 19(04): 1250045. Available at: DOI:10.1142/s0218625x1250045x

152. Elfizy A., Stolf P., Bork CAS., Junior EL., Chowdhury M., Chertovskikh S., et al. Tribological and Wear Performance of Carbide Tools with TiB2 PVD Coating under Varying Machining Conditions of TiAl6V4 Aerospace Alloy. Coatings. 2017; 7(11): 187. Available at: DOI:10.3390/coatings7110187

153. Fager H., Andersson JM., Jensen J., Lu J., Hultman L. Thermal stability and mechanical properties of amorphous coatings in the Ti-B-Si-Al-N system grown by cathodic arc evaporation from TiB2, Ti33Al67, and Ti85Si15 cathodes. Journal of Vacuum Science & Technology A: Vacuum, Surfaces, and Films. 2014; 32(6): 061508. Available at: DOI:10.1116/1.4897170

154. A. D. McLeod JSH. Electrical Resistivities of Monocrystalline and Polycrystalline TiB_2. 1984; 67(11): 705–708.

155. Plansee composite materials GMBH. WO 2011/137472 A1: Titanium diboride target. 2011.

156. Plansee composite materials GMBH. WO 2015/031920 A1.: Conductive

target material. 2015.

157. Polo MC., Andú Jar JL., Hart A., Robertson J., Milne WI. Preparation of tetrahedral amorphous carbon films by filtered cathodic vacuum arc deposition. Diamond and Related Materials. 2000; 9: 663–667. Available at: DOI:10.1016/S0925-9635(99)00339-8

158. Schultrich B., Scheibe H-J., Drescher D., Ziegele H. Deposition of superhard amorphous carbon films by pulsed vacuum arc deposition. Surface and Coatings Technology. Elsevier Science S.A.; 1998; 98(1–3): 1097–1101. Available at: DOI:10.1016/S0257-8972(97)00386-1

159. Xu S., Flynn D., Tay BK., Prawer S., Nugent KW., Silva SRP., et al. Mechanical properties and Raman spectra of tetrahedral amorphous carbon films with high sp 3 fraction deposited using a filtered cathodic arc. Philosophical Magazine Part B. 1997; 76(February 2015): 351–361. Available at: DOI:10.1080/01418639708241099

160. Erdemir A., Donnet C. Tribology of diamond-like carbon films: Recent progress and future prospects. Journal of Physics D: Applied Physics. 2006; 39(18). Available at: DOI:10.1088/0022-3727/39/18/R01

161. Anders S., Callahan DL., Pharr GM., Tsui TY., Singh Bhatia C. Multilayers of amorphous carbon prepared by cathodic arc deposition. Surface and Coatings Technology. 1997; 94–95: 189–194. Available at: DOI:10.1016/S0257-8972(97)00346-0

162. Konkhunthot N., Euaruksakul C., Photongkam P., Wongpanya P. Characterization of Diamond-like Carbon (DLC) Films Deposited by Filtered Cathodic Vacuum arc Technique. 2013; 23(1): 35–40.

163. Reinke S., Kulisch W. Mechanisms in ion-assisted deposition of superhard coatings: cubic boron nitride–tetrahedral amorphous carbon. Surface and Coatings Technology. 1997; 97(1–3): 23–32. Available at: DOI:10.1016/S0257-8972(97)00390-3

164. Fallon PJ., Veerasamy VS., Davis CA., Robertson J., Amaratunga GAJ., Milne WI., et al. Properties of filtered-ion-beam-deposited diamondlike carbon as a function of ion energy. Physical Review B. 1993; 48(7): 4777–4782. Available at: DOI:10.1103/PhysRevB.48.4777

165. Grill A. Diamond-like carbon: state of the art. Diamond and Related Materials. 1999; 8(2–5): 428–434. Available at: DOI:10.1016/S0925-9635(98)00262-3

166. Sutton DC., Limbert G., Stewart D., Wood RJK. The friction of diamond-like carbon coatings in a water environment. Friction. 2013; 1(3): 210–221. Available at: DOI:10.1007/s40544-013-0023-1

167. Fukui H., Okida J., Omori N., Moriguchi H., Tsuda K. Cutting performance of DLC coated tools in dry machining aluminum alloys. Surface and Coatings Technology. 2004; 187(1): 70–76. Available at: DOI:10.1016/j.surfcoat.2004.01.014

168. Emad Omrani, Pradeep K. Rohatgi PLM. Tribology and Applications of Self-Lubricating Tribology and Applications of Self-Lubricating Materials Self-Lubricating Materials. CRC Press Taylor&Francis Group. London; 2018.

169. Stachowiak GW., Batchelor AW. Engineering Tribology. 4th edn. Elsevier; 2014. 884 p.

170. Bülbül F., Efeoğlu I., Arslan E. The effect of bias voltage and working pressure on S/Mo ratio at MoS2-Ti composite films. Applied Surface Science. 2007; 253(9): 4415–4419. Available at: DOI:10.1016/j.apsusc.2006.09.059

171. Aouadi SM., Paudel Y., Luster B., Stadler S., Kohli P., Muratore C., et al. Adaptive $Mo_2N/MoS_2/Ag$ Tribological Nanocomposite Coatings for Aerospace Applications. Tribology Letters. 2008; 29(2): 95–103. Available at: DOI:10.1007/s11249-007-9286-x

172. Buck V. Preparation and properties of different types of sputtered MoS2 films. Wear. 1987; 114(3): 263–274. Available at: DOI:10.1016/0043-1648(87)90116-5

173. Dimigen H., Hübsch H., Willich P., Reichelt K. Stoichiometry and friction properties of sputtered MoS_x layers. Thin Solid Films. 1985; 129(1): 79–91. Available at: DOI:10.1016/0040-6090(85)90097-5

174. Arslan E., Bülbül F., Efeoglu I. The Structural and Tribological Properties of MoS_2 -Ti Composite Solid Lubricants. Tribology Transactions. 2004; 47(February 2012): 37–41. Available at: DOI:10.1080/05698190490438987

175. Rigato V., Maggioni G., Boscarino D., Sangaletti L., Depero L., Fox VC., et al. A study of the structural and mechanical properties of Ti-MoS_2 coatings deposited by closed field unbalanced magnetron sputter ion plating. Surface and Coatings Technology. 1999; 116: 176–183. Available at: DOI:10.1016/S0257-8972(99)00312-6

176. Teer DG., Hampshire J., Fox V., Bellido-Gonzalez V. The tribological properties of MoS_2/metal composite coatings deposited by closed field magnetron sputtering. Surface and Coatings Technology. 1997; 94–95: 572–577. Available at: DOI:10.1016/S0257-8972(97)00498-2

177. Deepthi B., Barshilia HC., Rajam KS., Konchady MS., Pai DM., Sankar J., et al. Structure, morphology and chemical composition of sputter deposited nanostructured Cr-WS2 solid lubricant coatings. Surface and Coatings Technology. Elsevier B.V.; 2010; 205(2): 565–574. Available at: DOI:10.1016/j.surfcoat.2010.07.050

178. Zheng XH., Lai DM., Gu B., Tu JP., Hu SB., Peng SM. Microstructure and tribological behavior of WS2–Ag composite films deposited by RF magnetron sputtering. Thin Solid Films. 2007; 516(16): 5404–5408. Available at: DOI:10.1016/j.tsf.2007.07.102

179. Yang F., Lu Y., Zhang R., Zhang X., Zheng X. Microstructure and tribological properties of WSx/a-C multilayer films with various layer thickness ratios in different environments. Surface and Coatings Technology. 2017; 309: 187–194. Available at: DOI:10.1016/j.surfcoat.2016.11.071

180. Rivero A., Aramendi G., Herranz S., De Lacalle LNL. An experimental investigation of the effect of coatings and cutting parameters on the dry drilling performance of aluminium alloys. International Journal of Advanced Manufacturing Technology. 2006; 28(1–2): 1–11. Available at: DOI:10.1007/s00170-004-2349-3

181. Gu L., Ke P., Zou Y., Li X., Wang A. Amorphous self-lubricant MoS_2-C sputtered coating with high hardness. Applied Surface Science. Elsevier B.V.; 2015; 331: 66–71. Available at: DOI:10.1016/j.apsusc.2015.01.057

182. Moskalewicz T., Zimowski S., Wendler B., Nolbrzak P., Czyrska-Filemonowicz A. Microstructure and tribological properties of low-friction composite MoS_2(Ti,W) coating on the oxygen hardened Ti-6Al-4V alloy. Metals and Materials International. 2014; 20(2): 269–276. Available at: DOI:10.1007/s12540-014-2009-6

183. Simmonds M., Savan a., Van Swygenhoven H., Pflüger E., Mikhailov S. Structural, morphological, chemical and tribological investigations of sputter deposited MoSx/metal multilayer coatings. Surface and Coatings Technology. 1998; 108–109(1998): 340–344. Available at: DOI:10.1016/S0257-8972(98)00567-2

184. Rao J., Cruz R., Lawson KJ., Nicholls JR. Carbon and titanium diboride (TiB2) multilayer coatings. Diamond and Related Materials. 2004; 13(December): 2221–2225. Available at: http://dspace.lib.cranfield.ac.uk/handle/1826/990

185. Indexable End Mill, 2 Flute, 17 mm, Center Cut, Tormach. Available at: http://lmscnc.com/4806 (Accessed: 24 October 2016)

186. Bull SJ. Failure modes in scratch adhesion testing. Surface and Coatings Technology. 1991; 50(1): 25–32. Available at: DOI:10.1016/0257-8972(91)90188-3

187. Hori T., Bowden MD., Uchino K., Muraoka K., Maeda M., Hori T., et al. Measurements of electron temperature , electron density , and neutral density in a radio frequency inductively coupled plasma Measurements of electron temperature , electron density , and neutral density in a radio-frequency inductively coupled plasma. 2014; 144(1996). Available at: DOI:10.1116/1.579911

188. Buck V. Structure and density of sputtered MoS2-films. Vacuum. 1986; 36(1): 89–94. Available at: DOI:10.1016/0042-207X(86)90277-0

189. Oks EM., Brown IG., Dickinson MR., MacGill RA., Emig H., Spädtke P., et al. Elevated ion charge states in vacuum arc plasmas in a magnetic field. Applied Physics Letters. 1995; 67(1995): 200. Available at: DOI:10.1063/1.114666

190. Buck V. Lattice parameters of sputtered MoS_2 films. Thin Solid Films. 1991; 198(1): 157–167. Available at: DOI:10.1016/0040-6090(91)90334-T

191. Arslan E., Bülbül F., Efeoglu I. The Structural and Tribological Properties of MoS 2 -Ti Composite Solid Lubricants. Tribology Transactions. 204AD; 47(February 2012): 37–41. Available at: DOI:10.1080/05698190490438987

192. Zhao LR., 0 . Lupandina VVP and RCM. Microstructures of nicraly coating applied on cmsx-4 by cathodic arc deposition. Proceedings of ASME Turbo Expo 2014: Turbine Technical Conference and Exposition. 2014;

193. Donnet C., Martin JM., Le Mogne T., Belin M. Super-low friction coefficient of MoS2 coatings in various environments. Tribology Series. 1994; 27(C): 277–284. Available at: DOI:10.1016/S0167-8922(08)70317-1

194. Burroughs BR., Kim J-H., Blanchet T a. Boric Acid Self-Lubrication of $B_2 O_3$

-Filled Polymer Composites. Tribology Transactions. 1999; 42(3): 592–600. Available at: DOI:10.1080/10402009908982258

195. HU Z biao., LI H jun., FU Q gang., XUE H., SUN G ling. Fabrication and tribological properties of B_2O_3 as friction reducing coatings for carbon-carbon composites. New Carbon Materials. 2007; 22(2): 131–134. Available at: DOI:10.1016/S1872-5805(07)60013-4

196. Zhang QY., Zhou Y., Wang L., Cui XH., Wang SQ. Investigation on tribo-layers and their function of a titanium alloy during dry sliding. Tribology International. Elsevier; 2016; 94: 541–549. Available at: DOI:10.1016/j.triboint.2015.10.018

197. Wang L., Li XX., Zhou Y., Zhang QY., Chen KM., Wang SQ. Relations of counterface materials with stability of tribo-oxide layer and wear behavior of Ti–6.5Al–3.5Mo–1.5Zr–0.3Si alloy. Tribology International. 2015; 91: 246–257. Available at: DOI:10.1016/j.triboint.2015.01.028

198. Kishawy HA., Dumitrescu M., Ng EG., Elbestawi MA. Effect of coolant strategy on tool performance, chip morphology and surface quality during high-speed machining of A356 aluminum alloy. International Journal of Machine Tools and Manufacture. 2005; 45(2): 219–227. Available at: DOI:10.1016/j.ijmachtools.2004.07.003

199. Tsai P-C., Hwang Y-F., Chiang J-Y., Chen W-J. The effects of deposition parameters on the structure and properties of titanium-containing DLC films synthesized by cathodic arc plasma evaporation. Surface and Coatings Technology. Elsevier B.V.; 2008; 202(22–23): 5350–5355. Available at: DOI:10.1016/j.surfcoat.2008.06.073

200. Koçak Y., Akaltun Y., Gür E. Magnetron sputtered WS_2; Optical and structural analysis. 2016; 707(1). Available at: DOI:10.1088/1742-6596/707/1/012028

201. Banerjee T., Chattopadhyay AK. Structural, mechanical and tribological

properties of pulsed DC magnetron sputtered TiN–WSx/TiN bilayer coating. Surface and Coatings Technology. Elsevier Ltd; 2015; 282: 24–35. Available at: DOI:10.1016/j.surfcoat.2015.10.011

202. Särhammar E., Strandberg E., Sundberg J., Nyberg H., Kubart T., Jacobson S., et al. Mechanisms for compositional variations of coatings sputtered from a WS$_2$ target. Surface and Coatings Technology. Elsevier B.V.; 2014; 252: 186–190. Available at: DOI:10.1016/j.surfcoat.2014.04.066

203. Brzezinka T., Rao J., Chowdhury M., Kohlscheen J., Fox Rabinovich G., Veldhuis S., et al. Hybrid Ti-MoS$_2$ Coatings for Dry Machining of Aluminium Alloys. Coatings. 2017; 7(9): 149. Available at: DOI:10.3390/coatings7090149

204. Fox-Rabinovich GS., Gershman I., El Hakim MA., Shalaby MA., Krzanowski JE., Veldhuis SC. Tribofilm formation as a result of complex interaction at the tool/chip interface during cutting. Lubricants. 2014; 2(3): 113–123. Available at: DOI:10.3390/lubricants2030113

205. Podgornik B., Vizintin J., Ronkainen H., Holmberg K. Friction and wear properties of DLC-coated plasma nitrided steel in unidirectional and reciprocating sliding. Thin Solid Films. 2000; 377–378: 254–260. Available at: DOI:10.1016/S0040-6090(00)01302-X

206. Sedlaček M., Podgornik B., Vižintin J. Influence of surface preparation on roughness parameters, friction and wear. Wear. 2009; 266(3–4): 482–487. Available at: DOI:10.1016/j.wear.2008.04.017

207. Li J., Xia L., Li P., Zhu Y., Sun Y., Zuo D. Relationship between coefficient of friction and surface roughness of wafer in nanomachining process. Fourth International Conference on Smart Materials and Nanotechnology in Engineering. 2013; 8793: 87931Y. Available at: DOI:10.1117/12.2027965

208. Svahn F., Kassman-Rudolphi Å., Wallén E. The influence of surface roughness on friction and wear of machine element coatings. Wear. 2003; 254(11): 1092–1098. Available at: DOI:10.1016/S0043-1648(03)00341-7

209. Takadoum J., Houmid Bennani H. Influence of substrate roughness and coating thickness on adhesion, friction and wear of TiN films. Surface and Coatings Technology. 1997; 96(2–3): 272–282. Available at: DOI:10.1016/S0257-8972(97)00182-5

210. Hayward IP., Singer IL., Seitzman LE. Effect of roughness on the friction of diamond on cvd diamond coatings. Wear. 1992; 157(2): 215–227. Available at: DOI:10.1016/0043-1648(92)90063-E

211. Sahin M., Çetinarslan CS., Akata HE. Effect of surface roughness on friction coefficients during upsetting processes for different materials. Materials and Design. 2007; 28(2): 633–640. Available at: DOI:10.1016/j.matdes.2005.07.019

212. Prakash B., Ftikos C., Celis JP. Fretting wear behavior of PVD TiB$_2$ coatings. Surface and Coatings Technology. 2002; 154(2–3): 182–188. Available at: DOI:10.1016/S0257-8972(02)00035-X

213. Fontaine J., Donnet C., Erdemir A. Fundamentals of the tribology of DLC coatings. Tribology of Diamond-Like Carbon Films: Fundamentals and Applications. 2008; (Dlc): 139–154. Available at: DOI:10.1007/978-0-387-49891-1_5

214. Guo CQ., Pei ZL., Fan D., Liu RD., Gong J., Sun C. Predicting multilayer film's residual stress from its monolayers. Materials and Design. Elsevier Ltd; 2016; 110: 858–864. Available at: DOI:10.1016/j.matdes.2016.08.053

215. Qu J., Blau PJ., Zhu D., Cook BA., Elmoursi AA. Tribological Characteristics of AlMgB14 and Nanocomposite AlMgB14-TiB2 Superhard Coatings. 2016; (C): 22–24.

216. Ford IJ. Roughness effect on friction for multi-asperity contact between

178

surfaces. Journal of Physics D: Applied Physics. 1993; 26(12): 2219–2225. Available at: DOI:10.1088/0022-3727/26/12/020

217. Robertson J. Properties of diamond-like carbon. Surface and Coatings Technology. 1992; 50(3): 185–203. Available at: DOI:10.1016/0257-8972(92)90001-Q

218. Heinrichs J., Olsson M., Jacobson S. New understanding of the initiation of material transfer and transfer layer build-up in metal forming—In situ studies in the SEM. Wear. July 2012; 292–293: 61–73. Available at: DOI:10.1016/j.wear.2012.05.032

219. Said MS., Ghani JA., Che Hassan CH., Shukor JA., Selamat MA., Othman R. Chip Formation in the Machining of Al-Si/10% AlN Metal Matrix Composite by using a TiN-coated Carbide Tool. Research Journal of Applied Sciences, Engineering and Technology. 2016; 13(6): 422–426. Available at: DOI:10.19026/rjaset.13.3001

220. Kennametal. End mill grades.

221. Ahmed YS., Veldhuis SC. The study of wear performance and chip formation of coated carbide tools during machining super duplex stainless steels. 6th International Conference on Virtual Machining Process Technology. 2017; (May).

222. Ning L., Veldhuis SC., Yamamoto K. Investigation of wear behavior and chip formation for cutting tools with nano-multilayered TiAlCrN/NbN PVD coating. International Journal of Machine Tools and Manufacture. 2008; 48(6): 656–665. Available at: DOI:10.1016/j.ijmachtools.2007.10.021

223. König W., Fritsch R. Physically vapor deposited coatings on cermets: performance and wear phenomena in interrupted cutting. Surface and Coatings Technology. 1994; 68–69(C): 747–754. Available at: DOI:10.1016/0257-8972(94)90248-8

224. Joshi S., Tewari A., Joshi S. Influence of Preheating on Chip Segmentation

and Microstructure in Orthogonal Machining of Ti6Al4V. Journal of Manufacturing Science and Engineering. 2013; 135(6): 061017. Available at: DOI:10.1115/1.4025741

225. Kaplan L., Zhitomirsky VN., Goldsmith S., Boxman RL., Rusman I. Arc behaviour during filtered vacuum arc deposition of Sn-O thin films. Surface and Coatings Technology. Elsevier Science S.A.; 1995; 76–77: 181–189. Available at: DOI:10.1016/0257-8972(95)02592-8

226. Demirskyi D., Sakka Y. High-temperature reaction consolidation of TaC-TiB$_2$ ceramic composites by spark-plasma sintering. Journal of the European Ceramic Society. Elsevier Ltd; 2015; 35(1): 405–410. Available at: DOI:10.1016/j.jeurceramsoc.2014.08.007

227. Plansee composite materials GMBH. GMBH Patent WO 2011/137472 A1: Titanium diboride target. 2011.

228. Murthy TSRC., Sonber JK., Sairam K., Bedse RD., Chakarvartty JK. Development of Refractory and Rare Earth Metal Borides & Carbides for High Temperature Applications. Materials Today: Proceedings. Elsevier Ltd; 2016; 3(9): 3104–3113. Available at: DOI:10.1016/j.matpr.2016.09.026

229. Nikolaev AG., Yushkov GY., Savkin KP., Oks EM. Angular distribution of ions in a vacuum arc plasma with single-element and composite cathodes. IEEE Transactions on Plasma Science. IEEE; 2013; 41(8): 1923–1928. Available at: DOI:10.1109/TPS.2012.2236363

230. Jianxin D., Tongkun C., Lili L. Self-lubricating behaviors of Al$_2$O$_3$/TiB$_2$ ceramic tools in dry high-speed machining of hardened steel. Journal of the European Ceramic Society. 2005; 25(7): 1073–1079. Available at: DOI:10.1016/j.jeurceramsoc.2004.03.033

231. Jasinevicius RG., Duduch JG., Porto AJ V. Investigation on diamond turning of silicon crystal - generation mechanism of surface cut with worn

tool . Journal of the Brazilian Society of Mechanical Sciences . scielo ; 2001. pp. 241–252.

232. Armstrong RW. The hardness and strength properties of WC-Co composites. Materials. 2011; 4(7): 1287–1308. Available at: DOI:10.3390/ma4071287

233. Francis LF. Powder Processes. Materials Processing. 2016. 343–414 p. Available at: DOI:10.1016/B978-0-12-385132-1.00005-7

APPENDICES

Appendix A Hybrid FCVA – MS deposition setup

In this section the main parts of the system assembly and deposition setups are presented. One of the objectives of this thesis was to upgrade hybrid FCVA - magnetron sputtering deposition system to allow multilayer and composite coatings deposition. Among all the most significant upgrades and approaches are:

- New gas flow controllers and full range vacuum gauge – this allowed better control of the process conditions.
- Rotating substrate holder with individual rotation of each sample. The holder allowed also substrate biasing and could alternate between FCVA and MS sources. This upgrade was essential to allow DLC coating (biasing) and DLC-WS$_2$ multilayer (alternating between sources) deposition.
- Pulsed DC magnetron sputtering power supply – necessary for WS$_2$ deposition.
- Feed-through to allow connection of the cables to samples for ion current measurements.
- Using mirror to observe arc spot movement on the cathode surface.
- Substrate Ar etching capability – ensures good surface preparation prior to deposition.
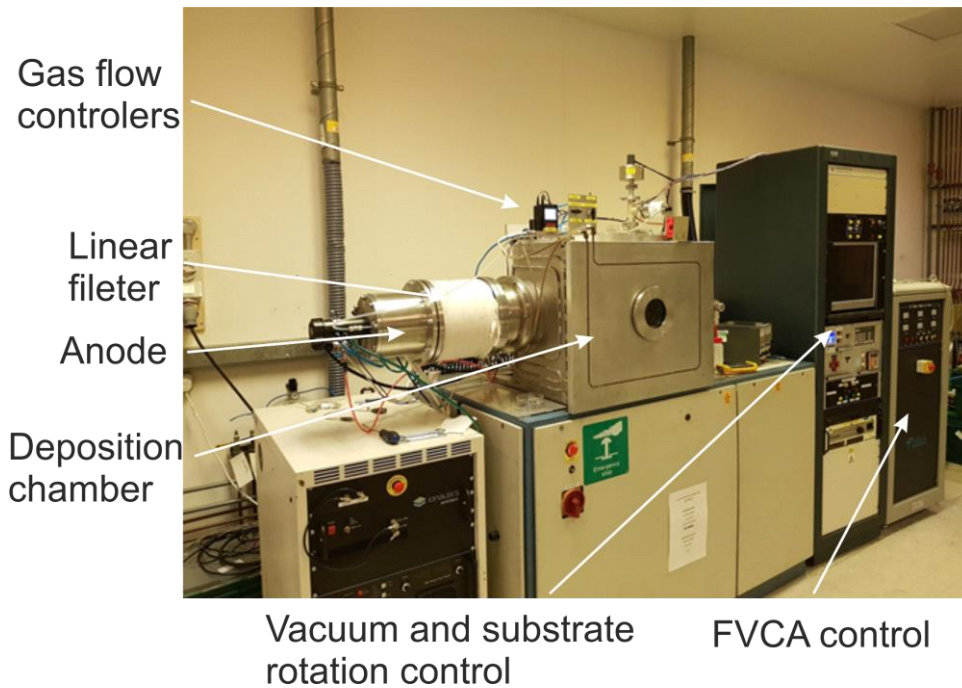
Figure_Apx A-1 Hybrid FCVA-MS deposition setup.
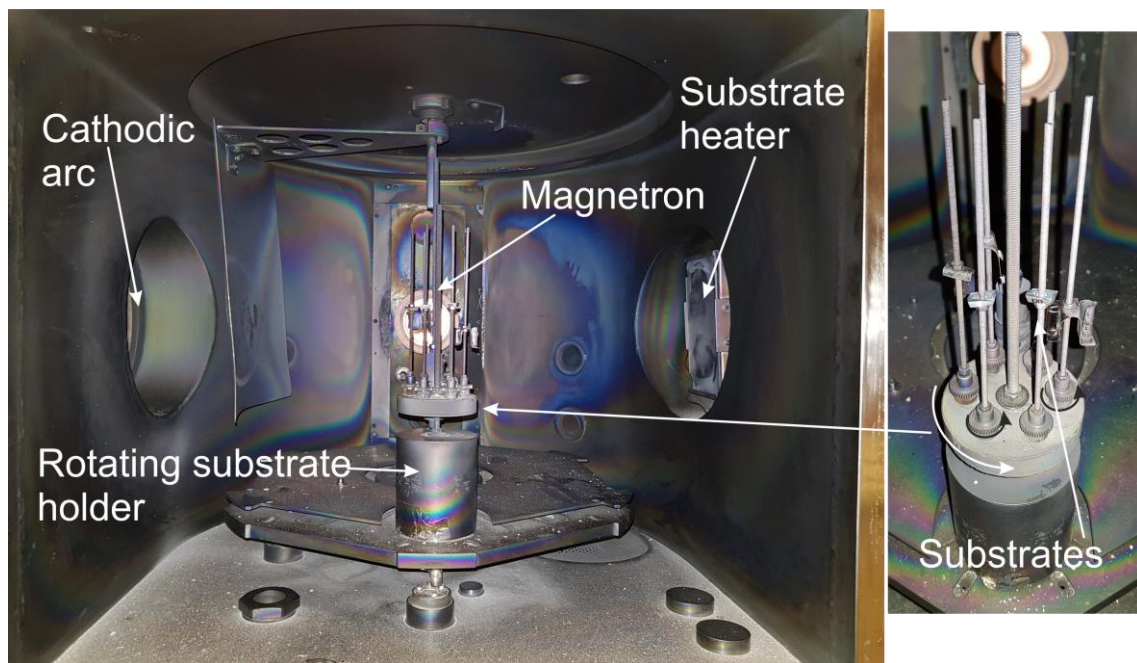
Figure_Apx A-2 Deposition chamber arrangement and rotating substrate holder with individual rotation of each sample.
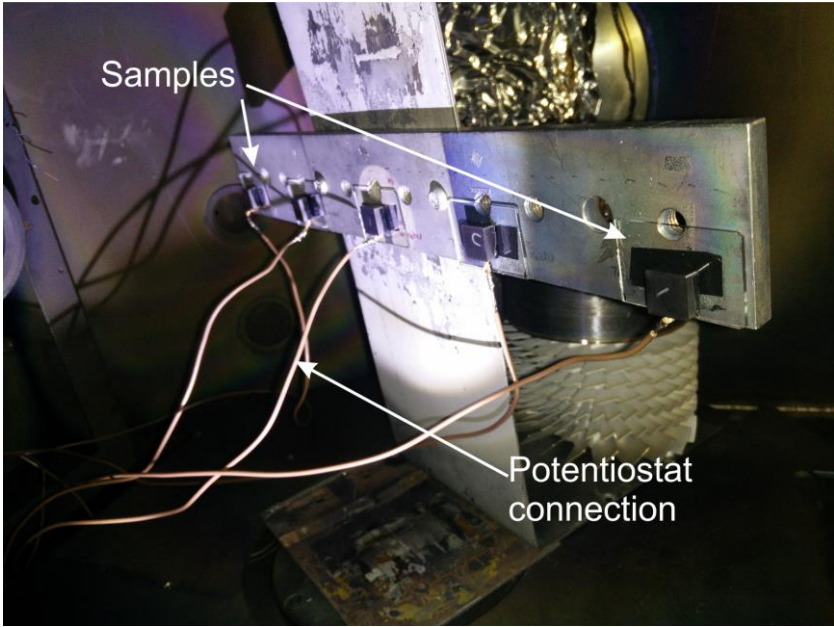
Figure_Apx A-3 Sample arrangement for ion current measurements during combinatorial deposition.
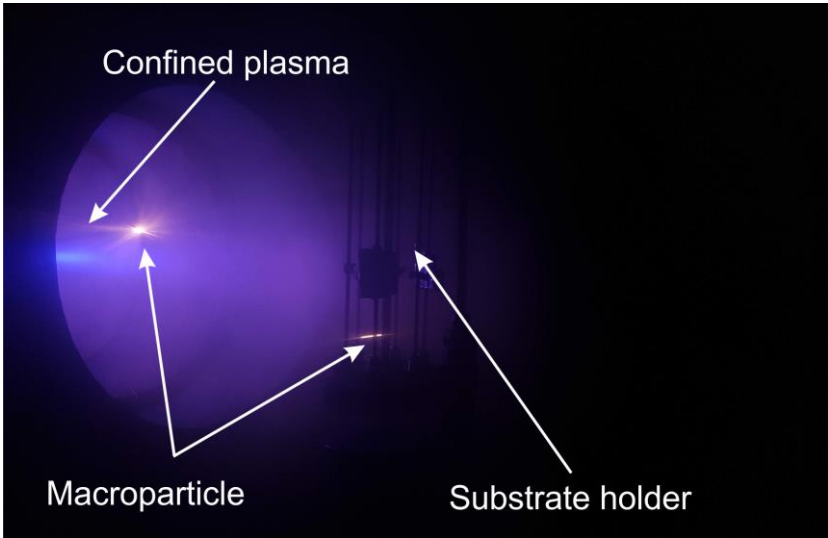
Figure_Apx A-4 Macroparticles observed when running TiB$_2$-TiSi$_2$ cathode
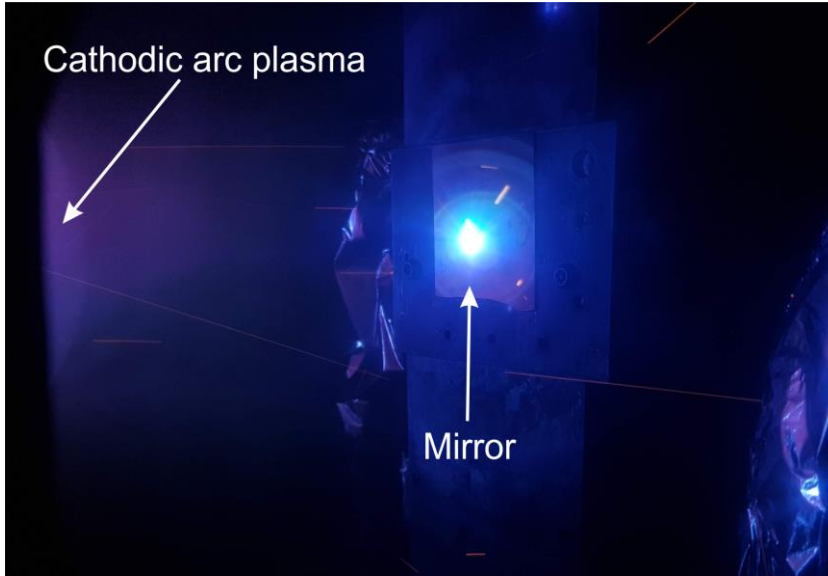
Figure_Apx A-5 Arc spot movement on the cathode observation using mirror placed in the middle of the deposition chamber.

Appendix B Alicona 3D images

This section includes the 3d images of the tool profiles after machining obtained using Alicona 3D. These are supplementary images to the SE and EDX maps of summarised in section 0.
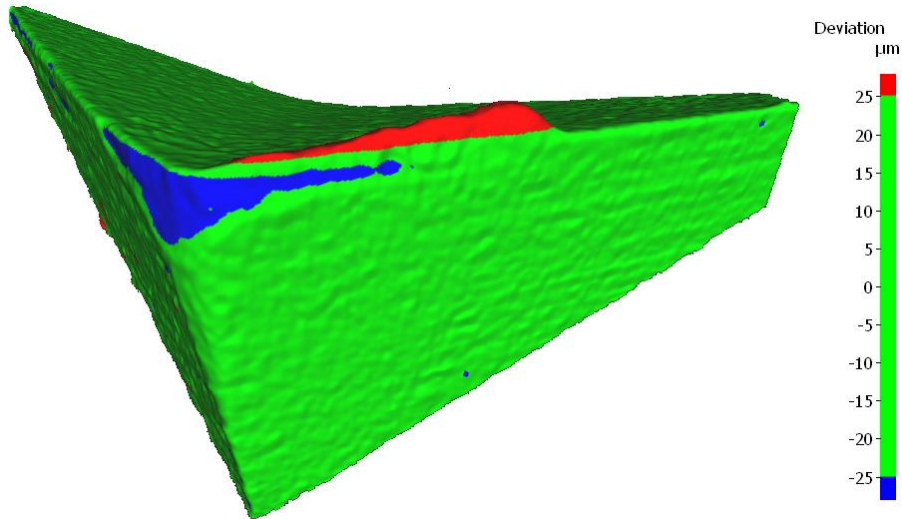
Figure_Apx B-1 Alicona 3D image of TiB$_2$-C coated milling insert after machining 35 m of AlSi with coolant.
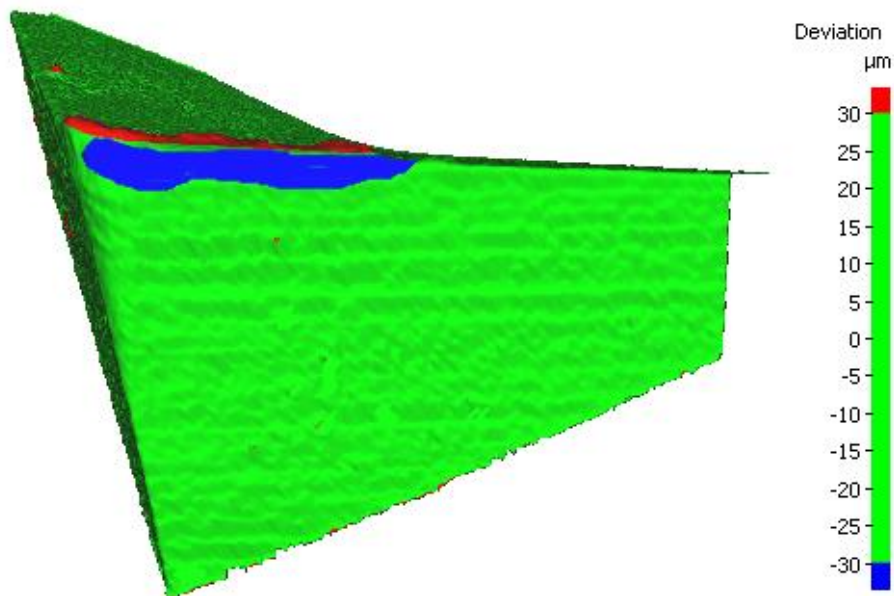
Figure_Apx B-2 Alicona 3D image of TiB$_2$-TiSi$_2$ coated milling insert, after machining 35 m of AlSi with coolant.
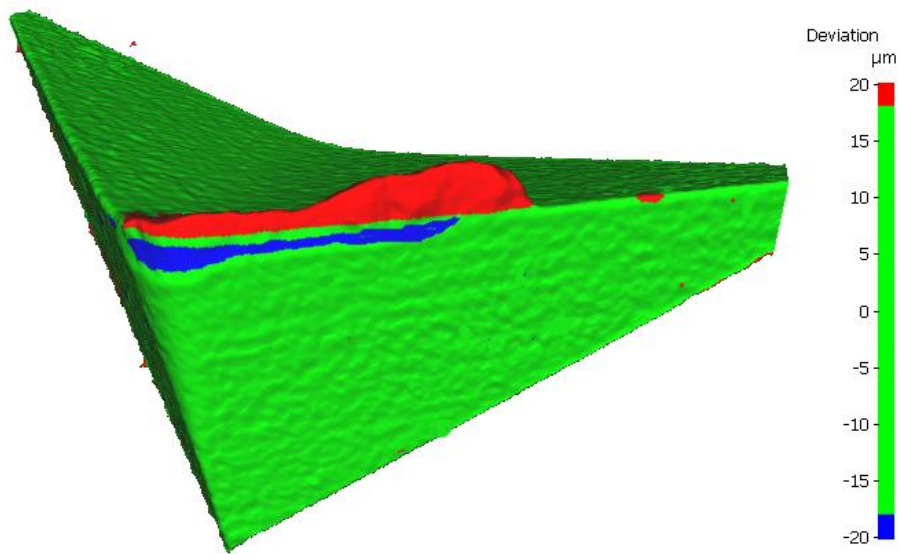
Figure_Apx B-3 Alicona 3D image of TiAlN coated milling insert, after machining 35 m of AlSi with coolant.
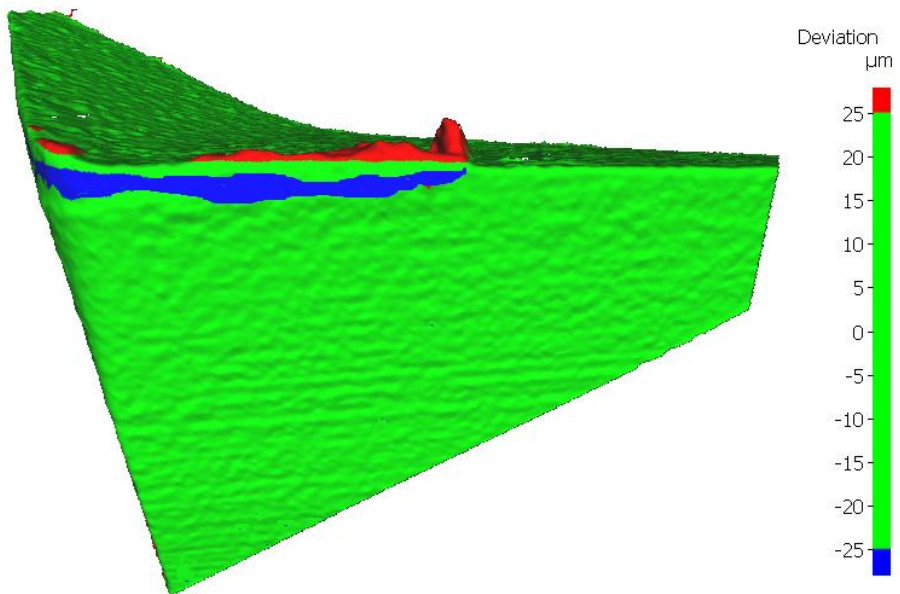
Figure_Apx B-4 Figure_Apx B-5 Alicona 3D image of commercial TiB₂ coated milling insert, after machining 35 m of AlSi with coolant.

Appendix C SEM and optical microscope images of the chips.

This section summarises most of the chip images obtained when writing this thesis. Some of them were analysed in sections 4.4.6 and 5.4.2.5.

Secondary electron (SE) mode of SEM was used to obtain the images of the chips produced during AlSi machining. Figure_Apx C-1 and Figure_Apx C-2 present the whole chips produced with DLC and DLC-WS$_2$ coated tools and 1000 times magnified images free and back surfaces of the chip. In some of the zoomed images, e.g. DLC-WS$_2$ B residues of the coolant which could not be removed during ultrasonic cleaning in acetone bath can be seen.

Figure_Apx C-3 and Figure_Apx C-4 present the whole chip images as well as 50 times zoomed free and back surfaces of the chips produced with uncoated, TiAlN, commercial TiB$_2$, TiB$_2$-C and TiB$_2$-TiSi$_2$ tools during wet and dry machining respectively. Ta o allow better understanding of the chip morphology those chips were later placed into the resin, cut and polished to allow investigation of the cross section, therefore, morphology e.g grain elongation could be studied. Figure_Apx C-5 and Figure_Apx C-6 present the images of the chip cross sections obtained using optical microscope. The pictures produced in back scattered electron (BSE) mode present the same chip cross sections as the optical images, though the chips were etched in the solution of methanol, hydrochloric acid, citric acid and hydrofluoric acid to allow evaluation of the chip segmentation.
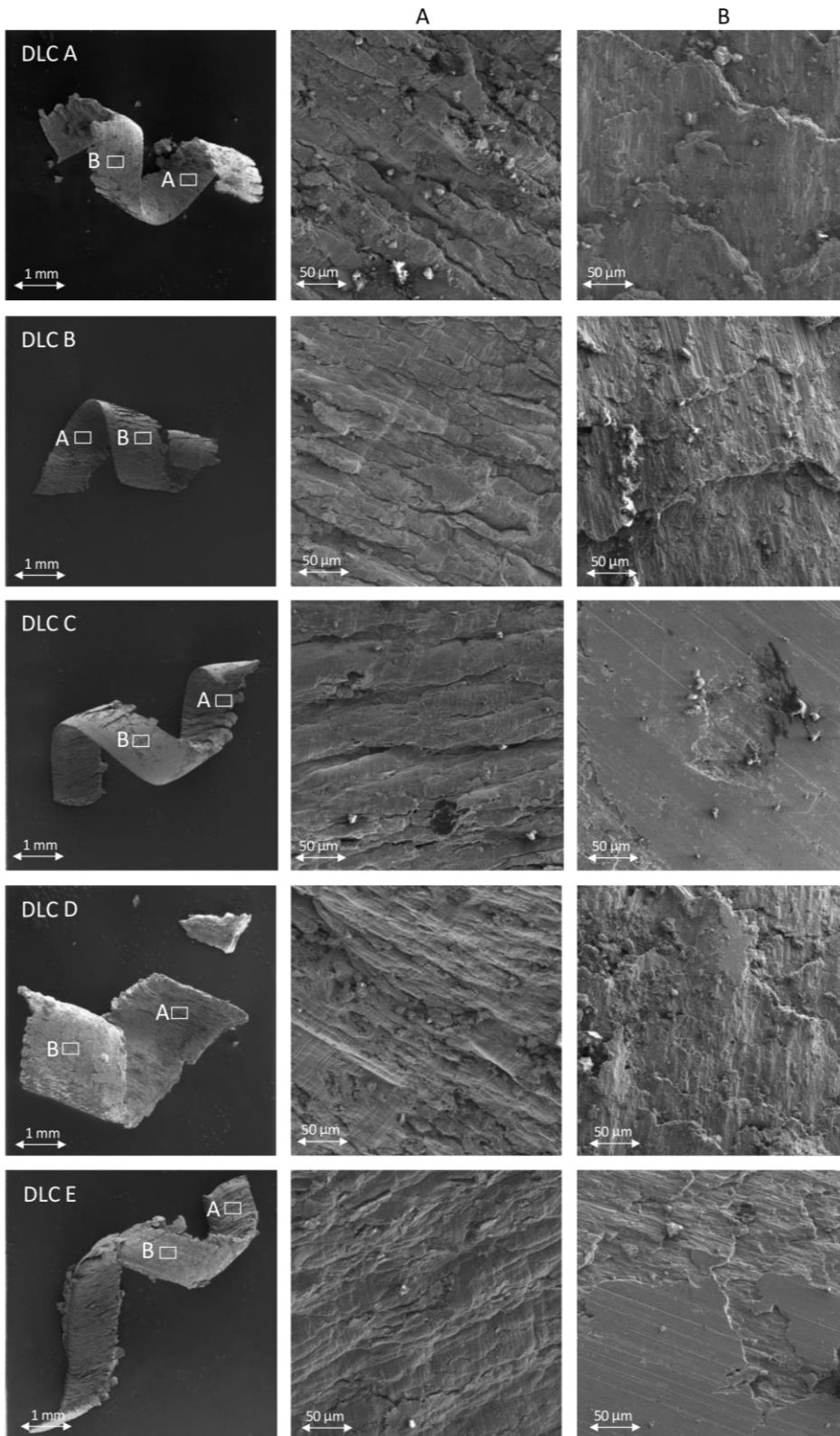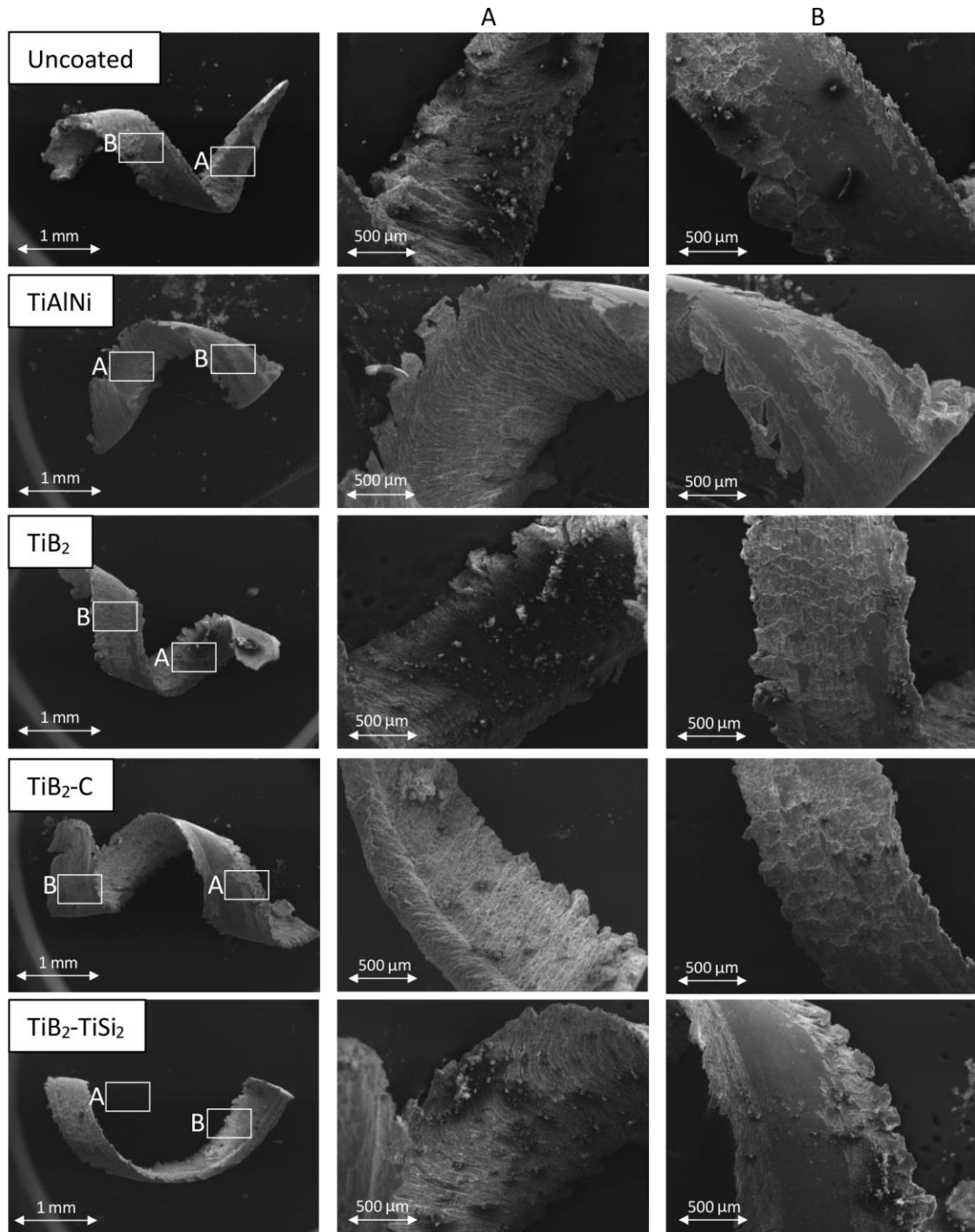
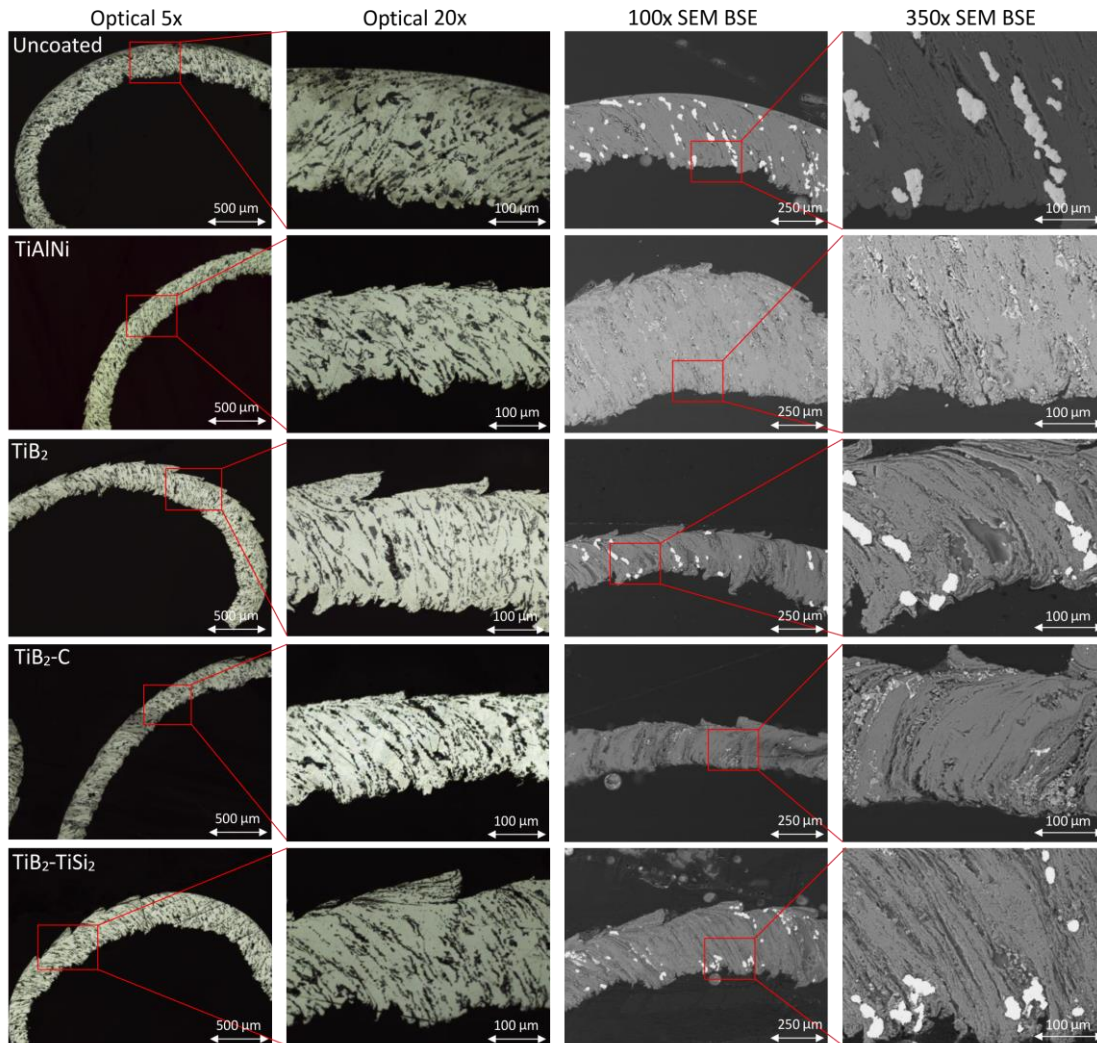**Figure_Apx C-1 SEM images of chips obtained during machining with DLC coated tools.**
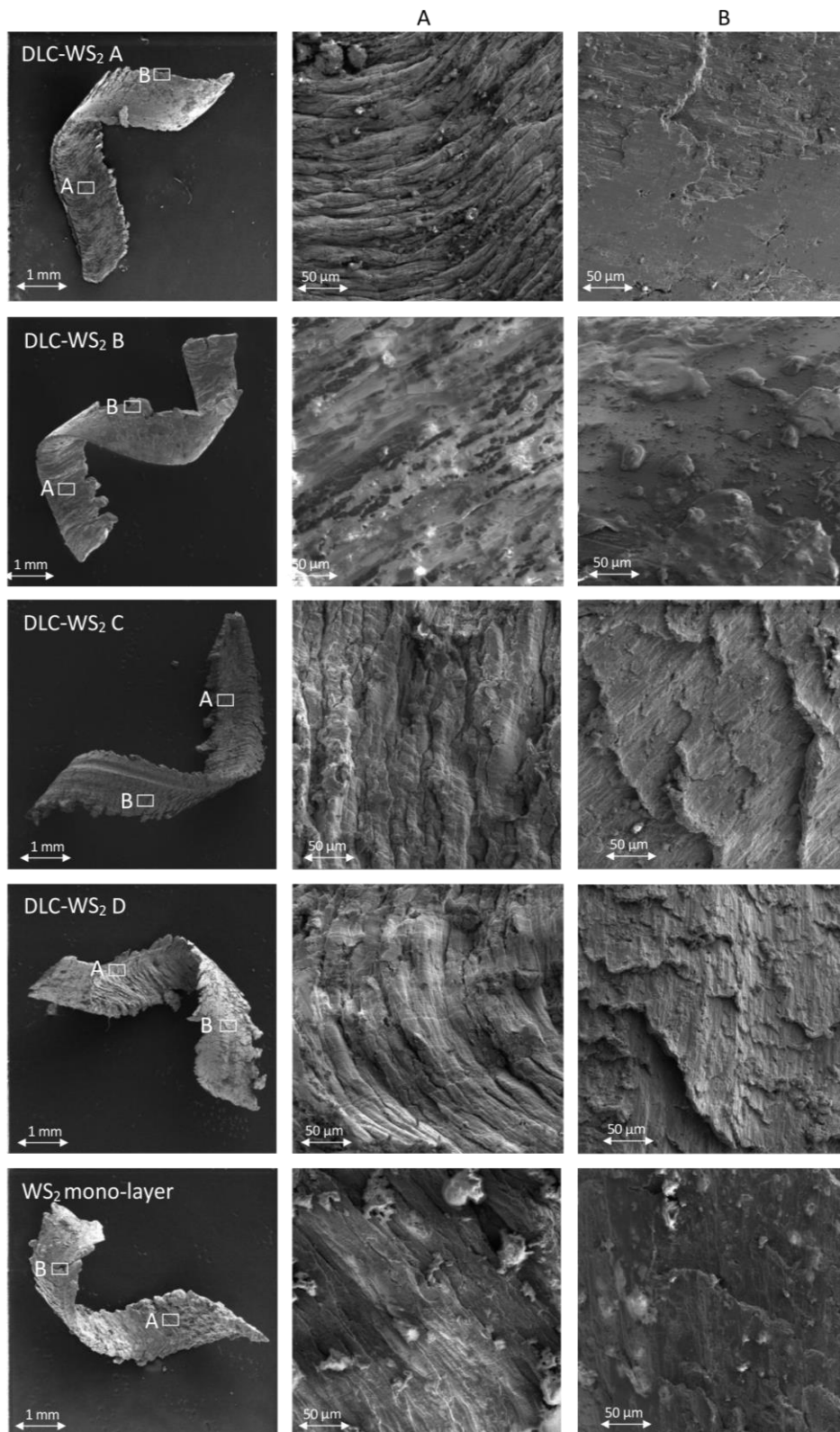
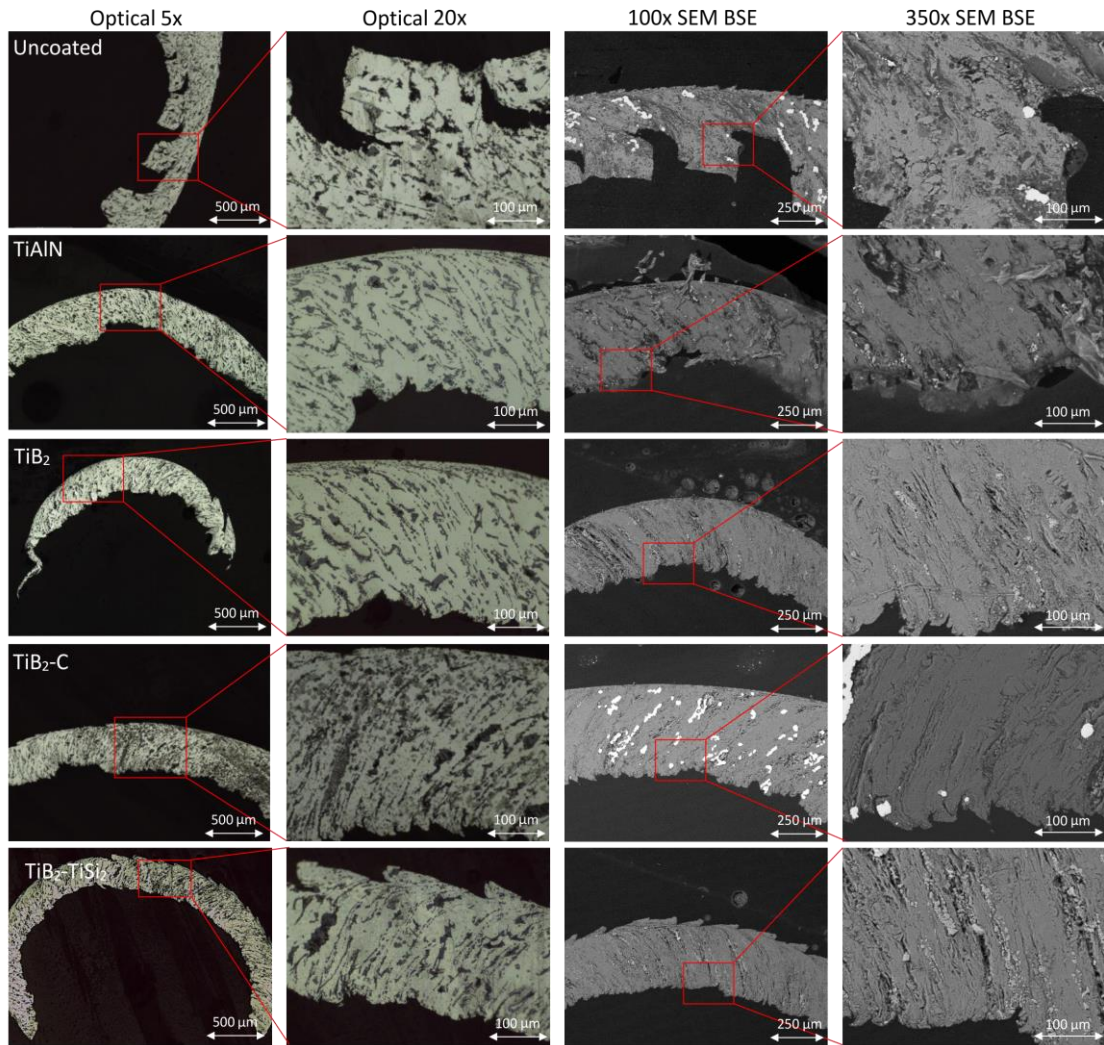**Figure_Apx C-2 SEM images of chips obtained during machining with DLC-WS$_2$ coated tools.**
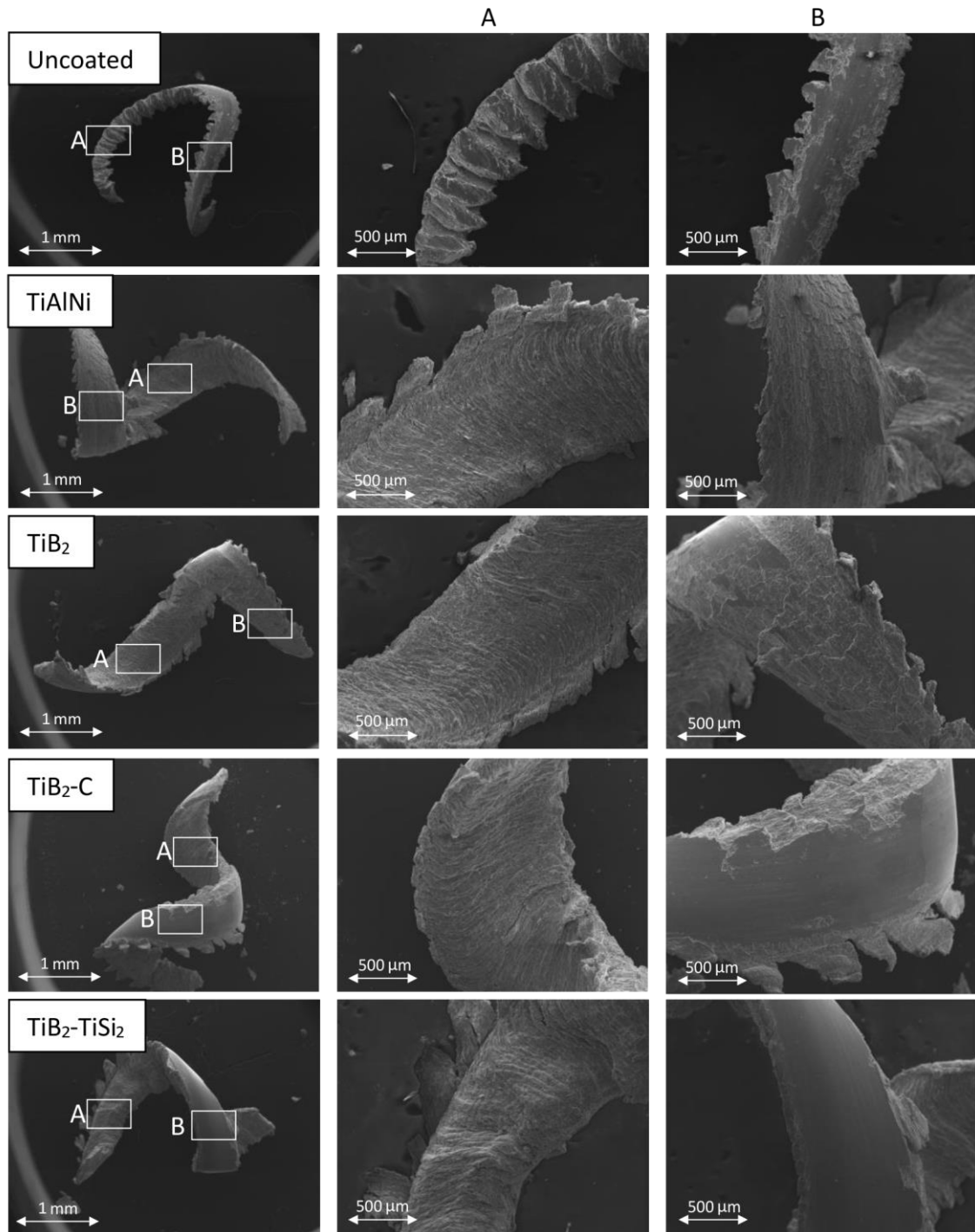
Figure_Apx C-3 SEM images of chips obtained during wet machining with uncoated, TiAlN, commercial TiB_2, TiB_2-C and TiB_2-$TiSi_2$ coated tools.

Figure_Apx C-4 SEM images of chips obtained during dry machining with uncoated, TiAlN, commercial TiB$_2$, TiB$_2$-C and TiB$_2$-TiSi$_2$ coated tools.

Figure_Apx C-5 Optical images of the chip cross sections and their BSE images obtained after etching. Chips produced during wet machining with uncoated, TiAlN, commercial TiB$_2$, TiB$_2$-C and TiB$_2$-TiSi$_2$ coated tools.

Figure_Apx C-6 Optical images of the chip cross sections and their BSE images obtained after etching. Chips produced during dry machining with uncoated, TiAlN, commercial TiB₂, TiB₂-C and TiB₂-TiSi₂ coated tools.

Appendix D Use of the journal articles in the thesis

Chapter 3 and 4 are published journal papers in the MDPI Coatings. They could be used in this thesis in accordance with the open access policy as it falls within the personal use.